SLAC–421
UC–414
(E / I)

SINGLE ELECTRON DETECTION FOR SLD CRID AND MULTI-PION SPECTROSCOPY IN K^-p INTERACTIONS AT 11 GeV/c*

Paul Elliot Rensing

Stanford Linear Accelerator Center
Stanford University
Stanford, CA 94309

August 1993

Prepared for the Department of Energy
under contract number DE–AC03–76SF00515

*Ph.D. Thesis

Abstract

This thesis consists of two independent parts: development of single electron detectors and a pulse finding algorithm for the Cherenkov Ring Imaging Detector (CRID) for SLD; and the analyses of unflavored, light quark meson systems using data from the LASS Spectrometer.

The CRID sections describe the design, construction, and testing of the multiwire proportional chambers used to measure all three co-ordinates of the conversion of UV Cherenkov photons into single electrons in the CRID drift boxes. The detectors use charge division to measure one of the co-ordinates and were carefully designed and built to provide 1 mm resolution. The software algorithm used for CRID to determine the co-ordinates of signals in the digitized data is also described. The algorithm uses knowledge of the fixed pulse shape to deconvolve the amplifier shape from the data, providing good single pulse resolution and excellent double pulse separation.

The spectroscopic analyses are based on data from a 4.1 $(\mathrm{nb})^{-1}$ exposure of the LASS Spectrometer in $\mathrm{K}^-\mathrm{p}$ interactions at 11 GeV/c. The channels $\Lambda\pi^+\pi^-$ and $\Lambda\pi^+\pi^-\pi^0$ are studied in detail. Brief surveys of $\Lambda\pi^+\pi^-\pi^+\pi^-$ and $\Lambda\pi^+\pi^-\pi^+\pi^-\pi^0$ are presented.

The $\Lambda\pi^+\pi^-$ analysis reveals a striking corroboration of ρ–ω interference. A fit to the ρ line shape gives a ρ–ω mass-mixing amplitude of $(2.15 \pm 0.35)\mathrm{MeV/c^2}$, yielding a branching fraction for $\omega \rightarrow \pi^+\pi^-$ of $(2.21 \pm 0.30)\%$, assuming complete coherence of the ρ and ω. A partial wave analysis of the $\pi^+\pi^-$ system provides evidence for a spin 1 resonance at about $1.3\,\mathrm{GeV/c^2}$. A fit of this new state, the $\rho(1300)$, gives a mass of $1290^{+20}_{-30}\,\mathrm{MeV/c^2}$ and a width of $120^{+60}_{-50}\,\mathrm{MeV/c^2}$. The

elasticity of the $\rho(1300)$ is estimated as $\sim 5\%$. Some evidence of $\rho(1690)$ production is seen in the $\pi^+\pi^-$ system.

The $\pi^+\pi^-\pi^0$ system in the $\Lambda\pi^+\pi^-\pi^0$ channel shows clear peaks from ω and η production. The η differential cross section, which dips around $t' \sim 0.4\,(\mathrm{GeV/c})^2$, is reasonably described by the shape predicted by Regge theory. A partial wave analysis of the $\pi^-\pi^0$ system produced against a backward-going $\Sigma^+(1385)$ again shows evidence of $\rho(1300)$ production, with parameters consistent with the $\pi^+\pi^-$ analysis.

The examination of the 4 pion system in the $\Lambda\pi^+\pi^-\pi^+\pi^-$ channel shows evidence of a mass bump at $\sim 1.3\,\mathrm{GeV/c^2}$. However, because of the difficulty of a spin analysis of the system, any possible contribution from the $\rho(1300)$ cannot be distinguished from that of the $f_2(1270)$. The number of events, however, implies a $\pi^+\pi^-\pi^+\pi^-$ branching fraction of less than 3 as compared to the 2 pion channel.

The examination of the charged 4 pion system against a backward $\Sigma^+(1385)$ shows strong production of $b_1^-(1385) \to \omega\pi$, but no evidence of $\rho(1300)$. The $b_1(1385)$ cross section is measured as $(0.61 \pm 0.11 \pm 0.03)\mu\mathrm{b}$, corrected for Λ, $\Sigma(1385)$, and ω visibilities. The upper limit on the $\pi^+\pi^-\pi^-\pi^0$ branching fraction relative to $\pi^-\pi^0$ is approximately 6, depending on the background shape used.

Data for the $\mathrm{K_S^0K^-}$, $\mathrm{K^+K^-}$, and $\overline{\mathrm{K}}^0\mathrm{K}^\pm\pi^\mp$ modes previously analysed by LASS are presented with attention to possible contributions from $\rho(1300)$. No evidence for $\rho(1300)$ is seen.

Acknowledgments

There are many people whom I wish to acknowledge. Without these people, I could not have written this thesis and accomplished what I did.

First of all I would like to thank all the members, past and present, of Group B at SLAC; their work to design and perform such quality experiments made this thesis possible and the research enjoyable. In particular, David Leith, my advisor, gave me a position in the friendly surrounds of Group B and offered help and guidance throughout my time there. Bill Dunwoodie spent countless hours helping with my LASS analysis, teaching me an enormous amount. Blair Ratcliff and David Aston provided advice and assistance both with LASS and CRID. Jaroslav Va'vra taught me about detectors and high voltage. Dick Bierce helped with managing all the tapes and data involved in the LASS analysis.

Tim Bienz helped me enormously with all aspects of my work at SLAC while we shared an office for many years. His friendship is something I hope to maintain. Sridhara Dasu and Joungjoon Kwon were helpful and enjoyable to work with. Working with Tom Pavel and Paul Kunz on UNIX and computer issues at SLAC provided many hours of interesting work and discussion.

The work of Ossie and Dana Millican deserves special acknowledgment. Their many days of hard work on the CRID detectors were indispensable. Dana spent days on end painstakingly stringing the anode wires of the detectors and was cheerful throughout.

The Group B administrative assistants, Eileen Brennan and especially Lilian Vassilian, and secretaries deserve special thanks. Their competence and professionalism made being a member of the group a pleasure. Lilian, in particular, was extremely helpful when dealing with SLAC and the University, and has been a good friend.

Finally, my wife Noa deserves a good part of the credit for this thesis. Her companionship and love throughout our time at Stanford have been big sources of inspiration to me. I dedicate this thesis to her.

Contents

List of Tables

List of Figures

Chapter 1

Cherenkov Ring Imaging

The SLD Detector,[1] shown in Figures 1.1 and 1.2, has been designed to study the properties of the Z^0 particle, produced in 100–200 Hz collisions of 45 GeV/c electrons and 45 GeV/c positrons in the SLC[2] at SLAC. The complete complement of detectors in the SLD includes (moving from the beamline outward) a CCD vertex detector, a drift chamber (DC), a Cherenkov ring imaging detector (CRID), a lead liquid argon calorimeter (LAC), and a warm iron calorimeter (WIC). All subsystems except the WIC are situated inside a 0.6 T solenoidal magnet. The WIC is situated outside the magnet, and utilizes the magnet's iron flux return. For some of the physics that the SLD intends to study, particularly for flavor tagging and heavy quark spectroscopy,[3] good particle identification is vital. Charged particle identification in SLD is provided mainly by the CRID. An example of the importance of the particle identification provided by the CRID is shown in Figure 1.3. The remainder of this chapter discusses the overall design of the CRID, including the readout electronics and online software. Before discussing any of this, however, it is important to review the Cherenkov effect itself.

1.1 Cherenkov Effect

When a charged particle passes through a medium with a velocity greater than the speed of light in that medium, it radiates photons. This effect was first observed

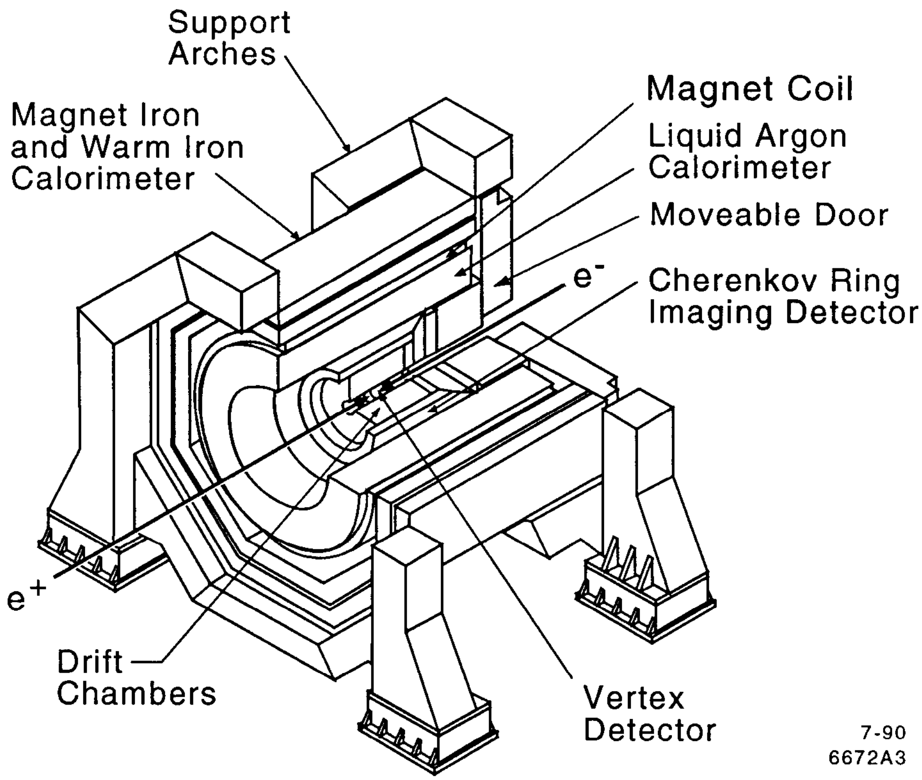

Figure 1.1: Isometric view of the SLD detector.

by Cherenkov in 1934,[4] and explained by Frank and Tamm in 1937.[5] The photons are emitted in a cone, with the angle of emission related to the velocity by[6]

$$\cos\theta_C = \frac{1}{\beta n}. \tag{1.1}$$

In this expression, θ_C is the angle of emission, β is the speed of the particle relative to the speed of light in vacuum, and n is the refractive index of the material through which the particle is passing. If a device is constructed such that the Cherenkov light is emitted in one relatively short path segment, and a photon detector is placed perpendicular to the path in another location further downstream, a ring of Cherenkov photons will impinge on the detector, and the diameter of the ring can be used to determine the velocity of the particle. Combined with measurement of the particle's momentum (for example, from a drift chamber), it is possible to compute probabilities for various mass assignments, and hence various particle

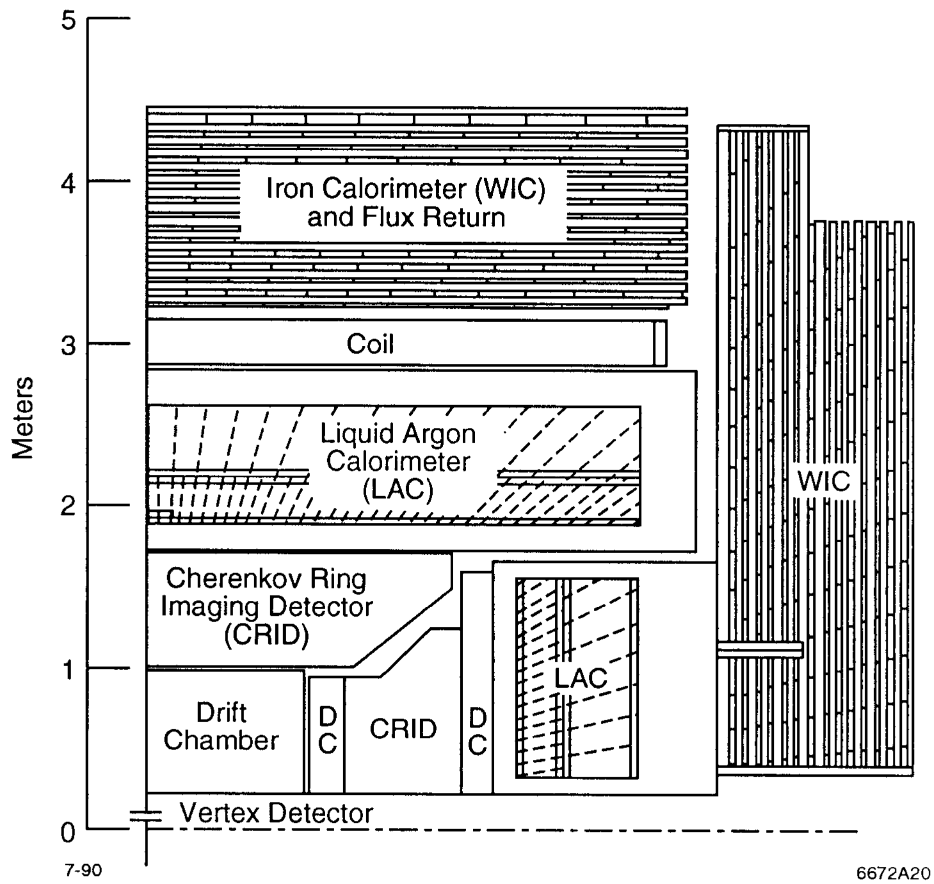

Figure 1.2: Sectional view of the SLD detector.

types. It is important to note that the angle of emission reaches an asymptotic value, so that as the velocity increases from its threshold value, the angle is less and less sensitive to the particle's mass. This has implications for the design of the CRID, as will be seen later.

In order to design a detector, it is also important to know the number of photons expected from the Cherenkov effect, and the wavelength distribution of the emitted light. The number of photons produced can be calculated beginning from the expression for the energy radiated by the Cherenkov effect[7]

$$\frac{d^2E}{dx\,d\omega} = \frac{e^2\omega}{c^2}\left(1 - \frac{1}{\beta^2 n^2(\omega)}\right). \tag{1.2}$$

Here dE is the energy emitted in the frequency interval $d\omega$ from path length

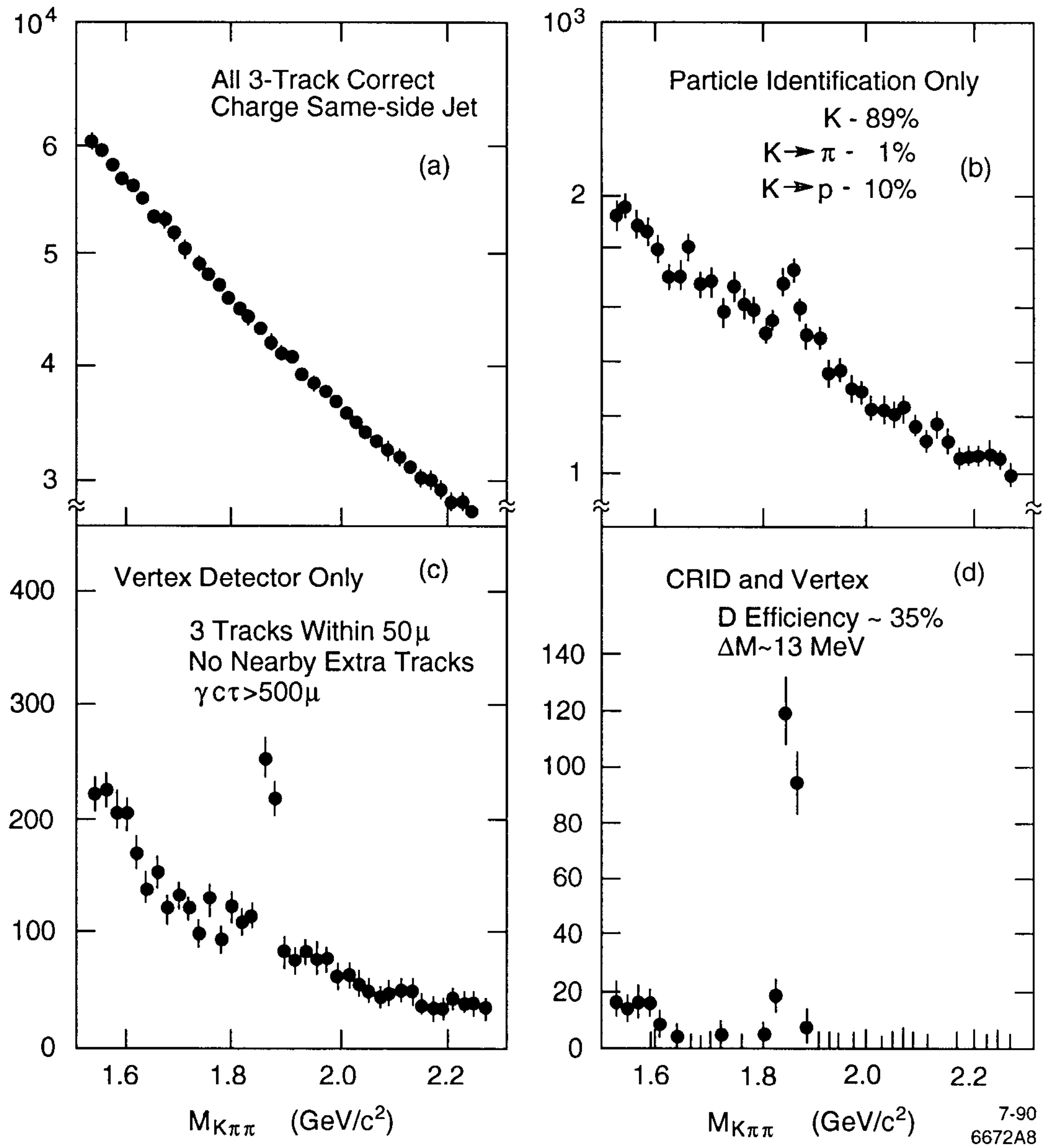

Figure 1.3: Number of events vs. $K\pi\pi$ mass for three particles with total charge ± 1, from a sample of Monte Carlo Z^0 decays. (a) All three-track combinations, (b) CRID used, vertex detector not used, (c) vertex detector used, CRID not used, (d) CRID and vertex detector used. The combination of CRID and vertex detector provides a very clean D signal.

element dx, $n(\omega)$ is the frequency-dependent index of refraction, and β is the velocity of the particle. If the particle radiates over a distance L, the energy radiated is given by

$$\frac{dE}{d\omega} = \frac{e^2\omega L}{c^2}\left(1 - \frac{1}{\beta^2 n^2(\omega)}\right). \tag{1.3}$$

The energy carried by each photon is $\hbar\omega$, so the number of photons produced is

$$dN = \frac{dE}{\hbar\omega} = \frac{e^2 L}{\hbar c^2}\left(1 - \frac{1}{\beta^2 n^2(\omega)}\right) d\omega. \tag{1.4}$$

Hence, the total number of photons is

$$N = \frac{\alpha L}{c}\int\left(1 - \frac{1}{\beta^2 n^2(\omega)}\right) d\omega. \tag{1.5}$$

where $\alpha = e^2/(\hbar c)$ is the fine structure constant.

In order to determine the number of photons that are seen, the efficiency of the photon detector must be taken into account. Real detectors are not completely efficient, and the efficiency is a function of wavelength. Calling the efficiency $\epsilon(\omega)$, the number of observed photons is given by

$$N = \frac{\alpha L}{c}\int \epsilon(\omega)\left(1 - \frac{1}{\beta^2 n^2(\omega)}\right) d\omega. \tag{1.6}$$

Although this gives the expected number of photons, the actual number follows a Poisson distribution with N as the mean value of the distribution.

If we consider the situation in which the light is emitted in a region where n is approximately constant, *i.e.* away from an absorption band, we can rewrite the expression for the number of photons as

$$N = N_0 L \sin^2\theta_C \tag{1.7}$$

where the frequently-used constant N_0 is given by

$$N_0 = \frac{\alpha}{c}\int \epsilon(\omega)\, d\omega. \tag{1.8}$$

Knowledge of the number of photons expected is important in order to set a scale for the required efficiency of the CRID, and because the number of photons emitted can be used to assist in particle identification.

The wavelength distribution of the Cherenkov photons can be obtained by writing the expression for the number of photons in terms of λ instead of ω. Starting with the relation between frequency and wavelength,

$$\omega\lambda = \frac{2\pi c}{n(\lambda)} \tag{1.9}$$

and again considering regions where n varies slowly, so that n can be treated as a constant, it can be seen that the differentials are related through

$$|d\omega| = \frac{2\pi c}{n(\lambda)} \frac{|d\lambda|}{\lambda^2} \tag{1.10}$$

Substituting this into the expression for the number of photons emitted (Equation. 1.5), one obtains the wavelength distribution of the radiated photons

$$N = 2\pi L\alpha \int \left(1 - \frac{1}{\beta^2 n^2(\lambda)}\right) \frac{d\lambda}{n(\lambda)\lambda^2} \tag{1.11}$$

or

$$\frac{dN}{d\lambda} = \frac{2\pi L\alpha}{n(\lambda)} \left(1 - \frac{1}{\beta^2 n^2(\lambda)}\right) \frac{1}{\lambda^2}. \tag{1.12}$$

This shows that the wavelength distribution has a $1/\lambda^2$ shape, and so is peaked towards short, UV, wavelengths. This is important because it places many constraints on the materials and construction techniques that can be used in the CRID. In particular, it requires that all of the material through which the photons pass be transparent to ultraviolet light.

The CRID uses information from the SLD drift chamber on the location and momentum of charged tracks, combined with measurements of the angular dimensions of Cherenkov light cones and the number of Cherenkov photons produced by the tracks, to derive particle identification probabilities. In addition to providing a measurement of a particle's momentum, the drift chamber tracking information is used to determine where to look in the CRID for a Cherenkov ring from a particular particle.

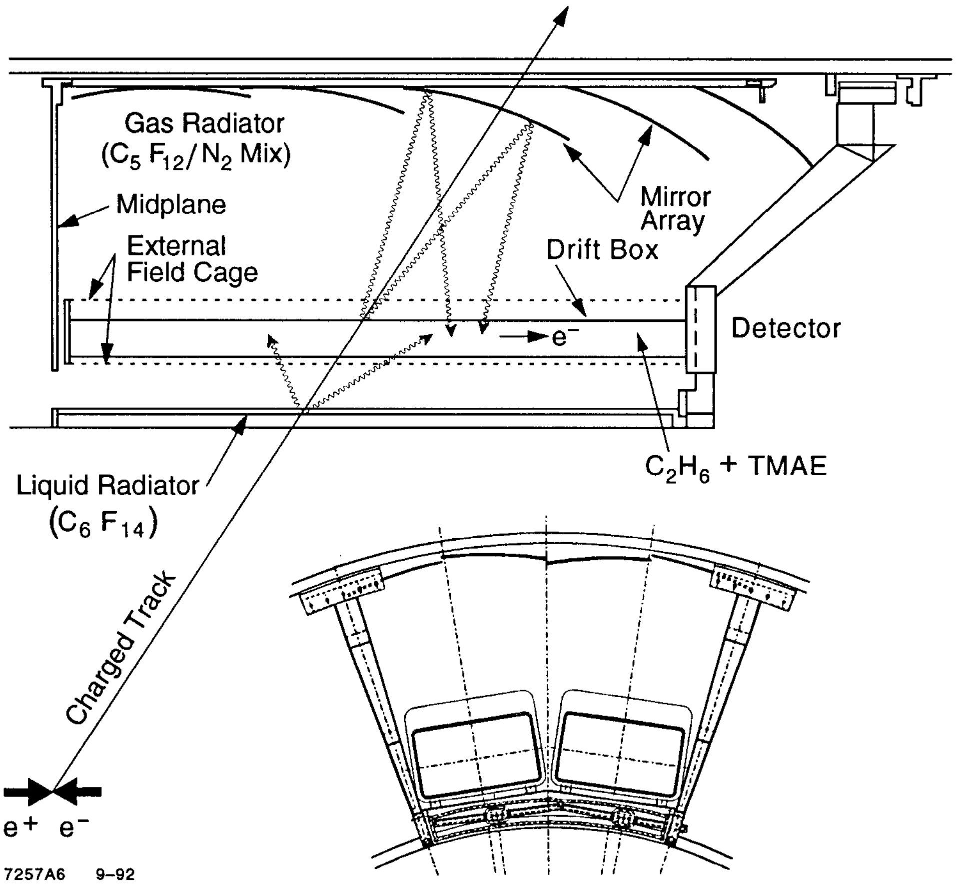

Figure 1.4: Sectional views of the barrel CRID. The upper view shows axial view; the layout is symmetric about the midplane on the left. The lower view shows a radial projection of one CRID sector.

1.2 CRID

Traditional threshold Cherenkov counters look only for the presence or absence of light to help identify particles. The idea for a device that identifies particles by looking not only for the presence or absence of photons, but also at the distribution and number of photons produced by the particle is due to Roberts,[8] while the relatively recent interest in constructing such devices is due in large part to Ypsilantis and Seguinot.[9] Several such devices have been built or are currently under construction, including devices for DELPHI at LEP, the OMEGA Spectrometer at CERN, Fermilab, and the device described here.

The CRID was designed and built in two major sections; the barrel CRID and the endcap CRID. This discussion concerns only the barrel CRID, and while the endcap CRID is conceptually identical, it differs considerably in design. Figure 1.4 shows a cross-sectional view of the barrel CRID. The primary components of the CRID are the liquid radiator, time projection chamber (TPC) with proportional wire plane and readout electronics, gas radiator, and mirrors.

1.2.1 Radiators

In the physics environment of the SLD, it is important to have good particle identification over a wide momentum range. Since the Z^0 decay products are much lighter than the Z^0, particle momenta can be as high as 45 GeV/c (one half the center of mass energy). In order to provide good particle ID capabilities over a wide momentum range, the CRID utilizes two different radiators. A liquid radiator, C_6F_{14},[10] with an index of refraction of 1.277 at a wavelength of 190 nm, is used to cover the low momentum range, and a gas radiator, C_5F_{12}, with an index of refraction of 1.00173 at 190 nm, is used to cover higher momenta. Because C_5F_{12} condenses to a liquid below 30°C, the entire CRID was designed to run at up to 40°C (although during the 1992 run, the barrel was maintained at about 32°C). Figure 1.5 shows the momentum range over which particle identification is provided by each radiator. The combination of the two radiators is expected to provide π/K separation at better than the 3σ level from 230 MeV/c to 28.8 GeV/c, and K/p separation from 800 MeV/c to 46.2 GeV/c.[1]

The relative indices of refraction of the liquid and gas radiators were chosen so that there is no gap in coverage as a function of momentum. These particular materials were chosen for their indices of refraction, their compatibility with other materials used in the CRID, their ability to transmit the primarily short wavelength Cherenkov photons, and their low chromatic dispersion. Another consideration, particularly for the gas radiator, is safety. The radiator gas chosen is much safer than the flammable hydrocarbons which were otherwise acceptable alternatives.

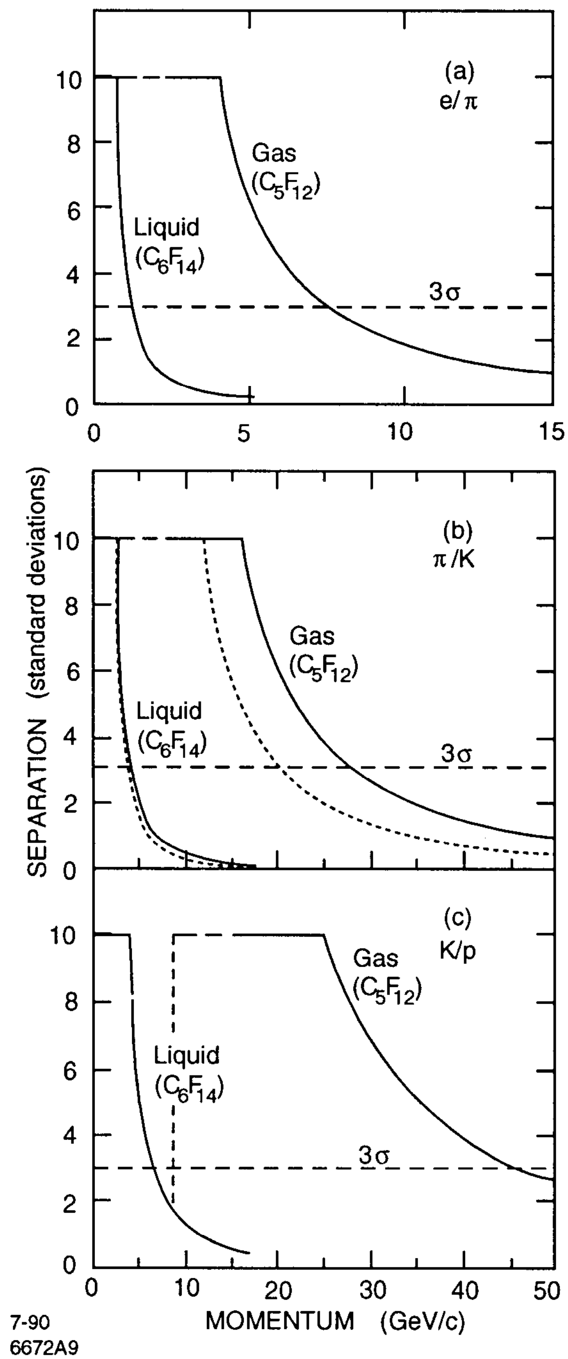

Figure 1.5: Particle separation ability of the CRID at the middle of the barrel. Curves shown are saturated at 10σ. Dashed lines indicate where the heavier particle is below threshold. Dotted line in (b) is for doubled measurement errors.

Because the gas radiator lies outside the radius of the TPC, the photons it produces travel away from the detector. The outer circumference of the CRID is covered with mirrors to reflect these photons back towards the TPC, and to focus the photons so that they produce a ring at the detector's location.

The liquid radiator is contained as a 1.0 cm thick layer in trays situated near the inner radius of the CRID, approximately 10 cm inward from the TPC. The radially outer side of the tray is made from quartz to allow the photons out; the rest of the tray is made mostly from G–10. Since the distance the particle travels in the liquid is short, there is no need to focus the photons to produce a good ring; the liquid thickness is sufficient to produce enough photons to form a good ring.

The gas radiator occupies a 45 cm deep region on the outer side of the TPC. This length is needed because the gas radiator produces few photons per distance. Photons from the gas radiator are both reflected and focussed into a ring by the mirrors placed at the outer circumference of the CRID. For each TPC, there are two rows of 5 mirrors and each of the 10 mirrors has a unique shape.[11]

1.2.2 Detector

A time projection chamber with a proportional wire plane is used as the detector for the photons. A drawing of the TPC/detector combination is shown in Figure 1.6. The drift space inside each TPC is 1.268 m long by 30.7 cm wide, and the thickness tapers from 9.2 cm to 5.6 cm. Forty TPCs are used in the CRID, arranged as twenty in each end of the barrel. The two large surfaces, perpendicular to a radial vector, are made of quartz to allow the UV photons from the radiators to enter the drift volume. The sides of the TPCs are made of G–10 and are double-walled to provide a purge volume to prevent any C_5F_{12} from entering the drift gas or vice versa. Metal traces are placed on the inner and outer surfaces of the quartz faces and sidewalls every 3.175 mm. These traces, whose potentials are set by a resistor ladder, shape the field in the TPC. An additional wire field cage encloses the TPC, to further control the field shape in the TPC.[12]

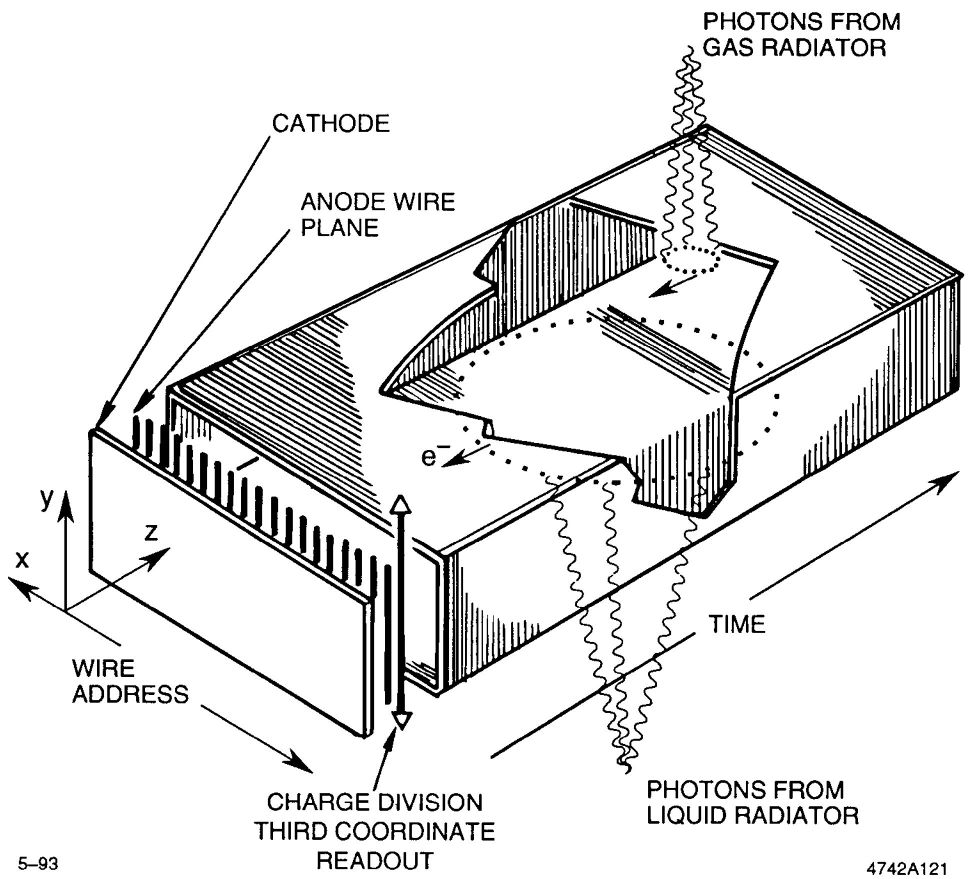

Figure 1.6: TPC and detector for barrel CRID.

The TPCs are filled with a gas mixture that is transparent to ultraviolet photons, has good electron lifetime, has a pulse height spectrum with a peak clearly separated from the noise, and includes a component which efficiently converts photons to single photoelectrons. Good electron lifetime is necessary to minimize losses as single electrons drift up to 1.3 m in the TPC. Pure ethane has been chosen for the TPC gas, with tetrakis di-methyl amino ethylene (TMAE) used as the gaseous photocathode. TMAE has a high quantum efficiency, reaching 50% below 180 nm, and above 10% for wavelengths shorter than 210 nm. The TMAE is introduced into the ethane by bubbling the gas through a bath of warmed liquid TMAE. The quantity of TMAE in the gas is determined by the temperature of the liquid, and is set so that the absorption length for photons is short compared to the thickness of the drift box. This assures that a high percentage of photons are converted before they exit the drift box. The concentration should not be too high, however, or most photons would convert very near their entrance into the TPC near the edges of the box, where electrostatic effects can alter their trajectories and cause losses. During the 1992 run, the bubbler was maintained at 23°C, providing a mean free path of about 2 cm.

The TMAE absorption length is short compared to the thickness of the TPC. Photons preferentially convert near the surface where they enter the detector and so there is a spatial separation between the conversion points of photons from the gas and photons from the liquid radiator. This distinction is be potentially useful to the software that reconstructs the Cherenkov rings.

TMAE is highly reactive, necessitating careful choice and cleaning of materials that come into contact with it. All materials used in the CRID needed to be tested to see if they react with TMAE and to see if any by-products affect electron lifetime. In addition, commercially available TMAE must be carefully cleaned before using it in order to remove contaminants which otherwise ruin electron lifetimes.

The TPC is tapered, widening from 5.6 cm thickness at the end far from the proportional wire plane to a thickness of 9.2 cm. This taper prevents transverse diffusion from causing loss near the faces of the TPC. The taper is not symmetric, but instead, there is more taper on the side facing the gas radiator (the outer radius). This asymmetry is due to the radial component of the SLD magnetic field at the TPC location, and keeps photoelectrons from drifting into the TPC faces due to Lorentz forces.[13]

At the end of the drift box, the single photoelectrons are detected by a proportional wire chamber, which is described in detail in Chapter 2. This chamber is composed of 93 $7\,\mu$m diameter carbon fibers on a 3.175 mm pitch. The diameter and composition of the fibers were chosen because they provide sufficient resistance to minimize electronic noise in the system. The fibers are very difficult to work with, however, since they have a breaking tension of 10.1 ± 2.1 grams, are difficult to see, and are somewhat difficult to attach. The fibers are oriented so that one end is near the TPC face where photons from the liquid radiator enter, and the other end is near the face where photons from the gas radiator enter. The fibers themselves are 10 cm long, which is slightly more than the width of the TPC at this point.

A mechanical blinding structure prevents photons produced in an avalanche from re-entering the TPC, photo-ionizing more TMAE, and drifting onto other wires in the proportional chamber, an effect called photon feedback. In the CRID geometry, photon feedback was measured to be approximately 1%, while an unblinded structure was measured to have feedback of 6–8%.[12]

The proportional chamber is operated at a nominal gas gain of 2×10^5. The operating gas gain is determined by two opposing constraints. On one hand, the gain is pushed down by the need to minimize photon feedback and maximize the operating lifetime of the chamber. On the other hand, the desire to have a pulse height spectrum with a clear peak above the noise favors high gas gain.

1.3 Front-End Electronics

A schematic representation of the CRID electronics is shown in Figure 1.7. Both ends of each carbon fiber are read out into separate preamplifiers, which are located on boards just behind the cathode of the proportional wire plane. Because the charge produced in the avalanche is so small, sensitivity and noise are primary concerns. The design of the preamplifier will be discussed briefly in Section 3.1 and in detail in References [14], [15], and [16]. Both ends of each carbon fiber are read out in order to provide photon conversion depth information via charge-division. This information allows the analysis to correct for parallax error, and provides information on whether a particular photon came from the liquid or gas radiator.

At each beam crossing, the output of each preamplifier is fed into a storage chain consisting of 512 samples stored in two analog sample-and-hold chips, each with the ability to hold 256 samples. These chips are referred to as Analog Memory Units (AMUs). Incoming signals can be digitized at intervals that are integer

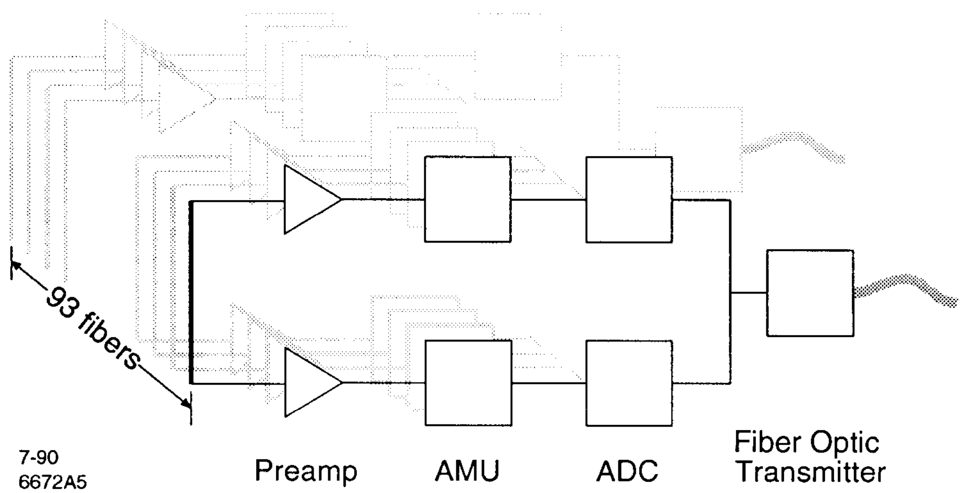

Figure 1.7: Schematic representation of CRID front-end electronics. Each optical fiber, shown as a broad gray line, handles the data from 8 ADCs (two-thirds of a drift box). Each ADC handles the data from 16 preamplifiers (one end of each of 16 chamber fibers).

multiples of the 8.4 ns (119 MHz) SLC clock. A lower bound on the CRID sampling interval can be determined by the simple requirement that the 512 AMU samples must cover the 1.3 m length of the drift box. Using an approximate drift velocity of 5.5 cm/μs, the sampling interval can be no shorter than 46 ns. In reality, the CRID data are digitized at intervals of 67.2 ns. The fact that the interval selected is longer than the minimum is because pulse resolution studies[16] indicated that the sampling interval and preamplifier time constant should be equal. In addition, it was not possible to build 50 ns preamplifiers to tight enough tolerances.

When an event trigger occurs, the AMUs are read out, multiplexed to ADCs, digitized, and sent to processors for analysis. All of the electronics, up to and including digitization, is located on the CRID itself; the digital signals are sent via optical fibers to the outside of SLD, where the processors are located. The AMUs, ADCs, optical fibers, and processors are used not only by the CRID, but by all subsystems in SLD.

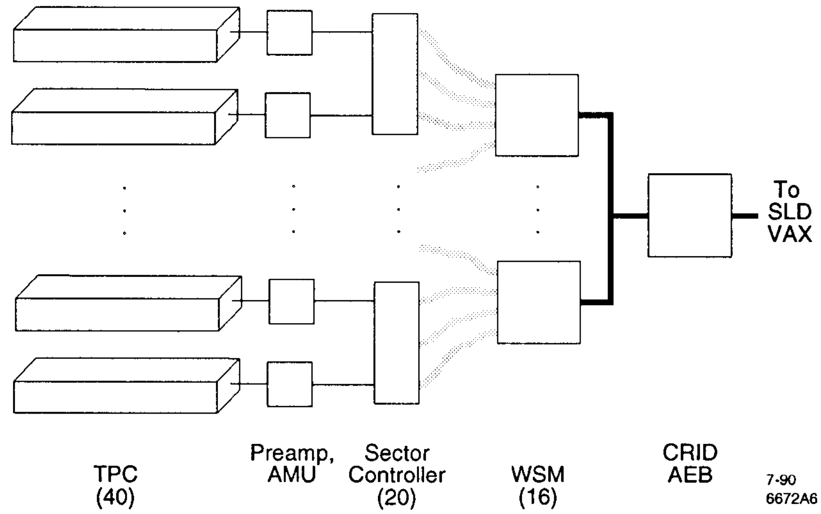

Figure 1.8: Structure of the CRID data acquisition system. Other subsystems in SLD have essentially identical structure. The broad grey bands represent optical fibers. The heavy black lines represent FASTBUS connections. Each WSM accepts four fibers (one per processor). In the CRID, each processor handles data from two-thirds of a drift box. The numbers in parentheses show the quantity of each component in the barrel CRID system.

1.4 Online Processing

The CRID data acquisition system, shown in Figure 1.8, consists of three levels of processors; the Waveform Sampling Module (WSM), the Aleph Event Builder (AEB), and the SLD VAX. Each of these has specific functions, and the three levels are connected together using FASTBUS. The structure of the data acquisition system is essentially the same for all of the subsystems in SLD;[17] variations arise only due to differences in the front-end electronics. For example, it is not appropriate to have a 512 sample readout for the calorimeters. Instead, four samples per calorimeter channel are taken: pedestal and signal at both high and low gain.

Before discussing these modules, it is helpful to get an idea of the amount of data produced by an event in SLD. The barrel CRID will be used as an example. For each event, each preamplifier produces 512 two-byte ADC words. There are two preamplifiers per wire, 93 wires per drift box, and 40 drift boxes in the barrel CRID. Therefore, the barrel CRID produces approximately 7.6 megabytes of data for each event. At a nominal event rate of two Hertz, this is a rate of over 15 megabytes per second. If calibration data are included, the data size is substantially increased. As will be described shortly, each AMU bucket has eight calibration constants associated with it. This means that in the barrel CRID, there are (assuming two bytes per constant) nearly 61 megabytes of calibration constants for the AMU alone. Since the goal of SLD is for the total data written to tape to be approximately 200 kilobytes per event, it is obvious that a significant amount of online processing is necessary. Therefore, the SLD data acquisition system includes a large number of embedded processors, and is designed to allow a high degree of parallel processing. In such a system, the processing software must be thoroughly debugged and understood, since there can be no reprocessing of data if a mistake in the software is discovered.

1.4.1 WSM

The Waveform Sampling Modules (WSMs) are the lowest level processors, and are responsible for correcting for the bucket-by-bucket characteristics of the AMU, zero-suppressing the data, and executing the pulse-finding algorithm. This algorithm is described in detail in Chapter 3. Once the WSM is finished processing an event, the data are formatted and passed on to the AEB upon request. In the CRID, each processor in a WSM is responsible for the data from 2/3 of a drift box. Thus, the 40 CRID drift boxes are serviced by 60 WSM processors. These are contained on 16 WSM boards (8 boards for each half of the barrel, with two unused processors per side).

The hardware of each of the four independent sections in a WSM consists of a custom chip, called the Digital Correction Unit (DCU), and a programmable processor. In addition, fiber optic receivers are located on the WSM board. The DCU has the responsibility for performing the bucket-by-bucket AMU corrections and zero-suppressing the data.

Each bucket in the AMU is calibrated by measuring the output *vs.* input response using DC voltages. An eight-segment piecewise-linear fit is made to the

the CRID, this means that three spatial co-ordinates must be determined for each pulse. In addition, a quality word is produced, indicating whether the pulse is a minimum ionizing pulse and whether it occurred shortly after an earlier pulse. One co-ordinate is given directly by the wire number on which the pulse occurred. The second co-ordinate is determined from the start time (*i.e.* sample number) of the pulse. The third co-ordinate is determined by the relative pulse height at the two ends of the wire. The algorithm for determining these numbers from the raw data is described in detail in Chapter 3.

After the WSM has analyzed all of the data in an event, it notifies its AEB that the data are ready for readout. The original design of the data acquisition system implied that, under normal operation, no raw data would be sent up the analysis chain from the WSM; only pulse locations and amplitudes would available for recording and subsequent analysis. However, as of the middle of the 1993 SLD Physics Run, the CRID was sending the zero-suppressed raw data to be logged to tape, and performing the analysis off-line.

1.4.2 AEB

The Aleph Event Builder (AEB), another programmable processor, was designed for the ALEPH experiment at LEP.[18] Like the WSM, the AEB also uses a 16 MHz Motorola 68020 processor. The SLD system uses one AEB per subsystem. Thus, the CRID has only one AEB. The purpose of the AEB is to collect data from its subsystem, format the data for tape, notify the VAX when it has assembled the data from an event, and upon request, transfer the data to the VAX. In addition, the AEB controls the WSMs for its subsystem.

1.4.3 SLD VAX

SLD currently uses a DEC VAX 8800 as its main online computer. The primary purpose of this computer in data acquisition is to collect events from the AEBs and log the event data to tape. In addition, the VAX passes commands to the AEBs, and through the AEBs to the WSMs in each subsystem. The

VAX can also run a number of user processes for monitor and control of the experiment. In addition to the 8800, SLD uses a number of VAXStation 2000's as graphics workstations and several MicroVAXes for hardware monitoring. All of the VAXStations are configured into a VAXcluster with the 8800. The VAXStations are used for developing software, and for running control, monitoring, and analysis programs. The MicroVAXes are used for CAMAC-based slow monitoring and control functions. For example, a stand-alone MicroVAX on uninterruptible power is used for temperature and gas monitoring and control for the CRID.

1.5 VAX Software

The software used to monitor and control SLD is called the Solo Control Program (SCP), and is based on a program of the same name used for monitor and control of the SLC accelerator. The program can be run on X-Window consoles (*e.g.* VAXStations); 48 line, VT100-type terminals; and Commodore Amiga computers. The user interface is based on a matrix of virtual push-buttons, a number of display areas, and a message area. The user initiates actions by "pressing" various virtual pushbuttons on the screen. Software routines are attached to various buttons, and can cause displays to be generated, options to be selected, or controls to be changed.

From a programmer's point of view, the SLD data acquisition software is organized into a number of co-operating processes, running on one or more machines. SCPs obtain data from the main data stream by making a request to the data logging program. Other processes monitor and control the high voltage for the experiment, act as print servers and database servers, and allow CAMAC commands to be carried out, either on the local machine, or transparently to another machine. Additional processes run on the AEBs and WSMs for transmission and low-level analysis of the data stream.

The online code for SLD is written as a number of packages, implemented primarily as sharable images. These are used by all subsystems in SLD for such things as database management, user interface support, interprocess communication, CAMAC, and display functions. Each subsystem in SLD also has its own programs built on top of these packages. The use of sharable images reduces the size and link time of programs and enforces some degree of encapsulation of packages.

A number of DEC's software engineering tools are extensively used for development and maintenance of the SLD code. The Code Management System (CMS) software is used to co-ordinate development among multiple programmers, and provides an archive of all versions of a file, allowing changes to be backed out if needed. The Module Management System (MMS), a port of the UNIX *make* utility, allows the dependencies of a particular package to be specified; MMS "knows" how to update a package based on these dependencies, built-in rules, and user-specified rules. Other tools that are used are the Source Code Analyser (SCA), which analyses the static structure of programs, and, of course, the VMS Debugger.

1.6 Monitoring

There are two kinds of monitoring in SLD; monitoring based on the normal data stream from the detector, and monitoring obtained from other sources (*e.g.* CAMAC). The former will be called data monitoring, and the latter called slow monitoring. Slow monitoring for the CRID has been quite well thought out, while data monitoring will undergo major development as operating experience is gained with the CRID.

For the CRID, the slow monitor quantities include such quantities as temperature, heater ON/OFF, gas mixture, oxygen concentration, water vapor concentration, pressures, flow rates, UV transparency, electron lifetimes, and high voltage.[19] Control is provided for valve positions, UV monochromator, electron lifetime monitor, heaters, and high voltage. All critical controls, *e.g.* valve positions, do not rely on software to provide protection from illegal states. Instead, hardware has been built to ensure the safety of critical control items, using Alterra EP1800 programmable logic array chips.

Data monitoring includes drift velocity measurement and electrostatic distortion measurement. Both of these are accomplished using 19 UV fibers attached to each drift box. The fibers can be pulsed, using flashlamps, to provide fiducial markings in the data. Additional quantities, such as pulse height distributions, can also be determined from the data.

Data from the slow monitor system, along with monitor system control and configuration data, reside in databases. The database used by SLD, a four-level, hierarchical database, is a modified version of the SLC database. The database structure allows monitor processes to run as batch jobs, operating regardless of whether or not anyone is logged on looking at the data. A set of core routines is provided for all of SLD; these perform such functions as readout of typical monitor devices, limit checking and alarms, and time-history recording. More complicated readout and control are for the individual subsystems to implement. Each database has a database server process associated with it. The database server allows access to a database from multiple machines.

Chapter 2

CRID Detectors

This chapter discusses the construction and testing of the multi-wire proportional chambers used by CRID to detect single electrons produced by photon conversion. The design and construction details were very stringently controlled in order to meet the measurement accuracy goals.

2.1 Design Requirements

The design goals of the CRID electron detectors are to have a high efficiency for detecting single electrons and to measure all three co-ordinates of the photon-to-electron conversion position to 1 mm accuracy. The z co-ordinate, along the drift box or SLC beam direction, is found by measuring the drift time of the electron, the radial co-ordinate is measured by performing charge division on each anode wire, and the azimuthal co-ordinate corresponds to the wire address. Measuring the radial co-ordinate is essential in order to reduce the parallax broadening of the Cherenkov ring image.

The 1 mm accuracy criterion was adopted because this is the level of irreducible error in the CRID.[1] Diffusion in the drift box, chromatic aberrations due to the materials used, and momentum smearing due to track curvature in the magnetic field contribute around 1 mm of uncertainty to the photon conversion position.

Therefore, there is little to be gained by pushing the detector accuracy below this value.

The use of TMAE as a photo-cathode greatly influences the design of the detectors. At the design operating temperature of $\sim 28°C$, TMAE vapor has an absorption length of about 16 mm. Thus, the UV photons created in the avalanche at the anode wire can travel back into the gas volume and convert, resulting in feedback of secondary electrons (so-called afterpulses). This feedback is suppressed by using a blind structure (Figure 2.1), which limits the angle over which photons from the avalanche can reach the gas volume to about 6.6°, and by using a scallop-shaped cathode to eliminate direct "communication" between wires.

To achieve the desired 1 mm position resolution in the charge division co-ordinate, the Johnson noise from the anode wire must be kept low. The noise on the charge division co-ordinate is shown in Equation 2.5. Given the parameters of the CRID amplifiers, the Johnson thermal noise from the anode wire is the dominant contribution. Therefore, it is important to use a wire with as high a resistance as possible to lower the Johnson noise. For the CRID, $7\,\mu$m diameter carbon fibers were used, and these have a typical resistance of $40\,\mathrm{k}\Omega$ over their 10 cm length. One detector was built using $33\,\mu$m diameter carbon wires, and this is discussed in Section 2.6.

2.2 Anode Wires

The anode wires used in the CRID detectors were 7μm diameter carbon filaments.* The fibers came from the manufacturer in a bundle and had to be separated by hand into individual strands of useful length. Each end was taped to a small piece of cardboard and the fibers were laid on trays for later use.

Figure 2.2 shows a microscope picture of the cross-section of some of the carbon fibers. It shows that the wire diameters are not uniform. The pictures and later experience seem to indicate that there were two groups of fibers, one with a $7\,\mu$m diameter and one with a significantly small diameter. The small diameter

*ST–3 fibers, Toho Rayon Co., Tokyo, Japan.

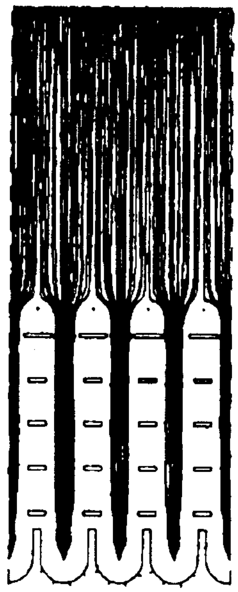

Figure 2.1: An electrostatic simulation of 4 cells of a CRID single-electron detector.

fibers have high resistance, and so would be good for charge division, but have significantly lower strength. Even if they survived the construction phase of the detector, they would threaten its long-term integrity. Therefore, it was necessary to weed out the weak fibers by measuring their resistance and strength.

In order to determine the physical attributes of the fibers, about 60 fibers were strained and measured until they broke. One end of each fiber was attached to a free-sliding table which was in turn attached to a load cell in order to measure the tension, which is quoted in gram weight equivalent. The other end of the fiber was attached to a table which was moved by a micrometer. The fiber was drawn over two small copper tubes separated by 10 cm; the tubes were connected to an ohmmeter to measure the resistance of the fiber. As the micrometer was turned to strain the fiber, the stretch, tension and resistance were recorded. As the tension increased, the tension was watched closely to try to catch the point at which the fiber broke.

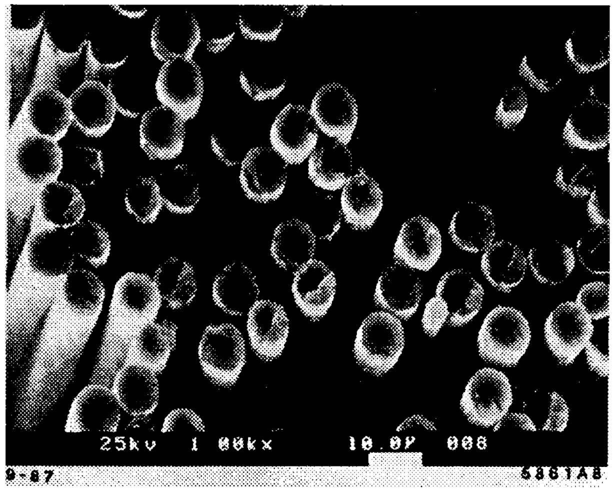

Figure 2.2: A microscope picture of some 7 μm carbon fibers used for the CRID anodes.

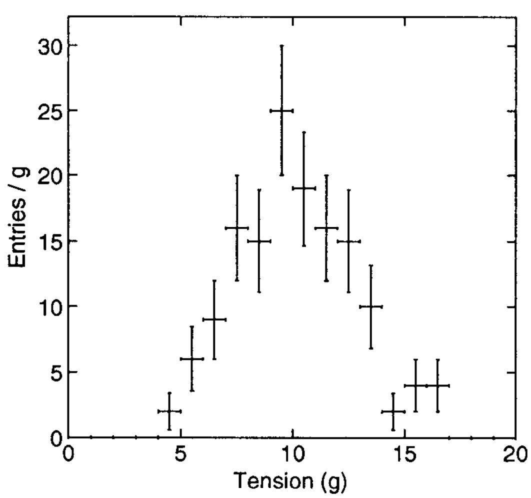

Figure 2.3: Distribution of the breaking tension of carbon fibers.

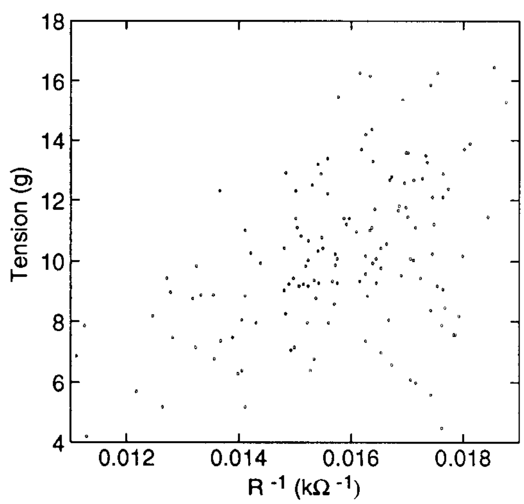

Figure 2.4: The breaking tension of carbon fibers versus the inverse of their resistance.

Figure 2.3 shows the distribution of breaking tension for the carbon fibers. The average is 10.1 g with a standard deviation of 2.1 g. Figure 2.4 shows the correlation between breaking tension and inverse resistance, which is proportional to the cross-sectional area of the fiber (see Section 2.3.1). The plot shows that the resistance can be used to give an upper limit for the breaking tension of a wire, but that other factors, such as the wire's handling history, reduce its strength.

2.3 Measurement of Tension

It is necessary to measure the tension of the anode wires in order to check the performance of the electronic load cell used to measure tension while stringing, to evaluate the consistency of the wire stretching operator, and to see if the wires creep, *i.e.* lose tension over time. There are a number of methods available to measure tension. For the CRID, however, there are special problems because the wires are highly resistive ($\sim 40\,\mathrm{k}\Omega$ for a 10 cm length) and quite brittle. In addition, it is necessary to perform the measurement on a finished cathode without endangering the wires.

A successful method was developed. A permanent magnet is placed under the wire frame. Vibrations are induced by a gentle stream of gas (air or N_2), thus producing periodic voltages across the wire. The signal is measured by a frequency spectrum analyser, from which the frequency of the fundamental vibration harmonic is obtained.

2.3.1 Theory

The normal mode vibration frequency of a uniform wire is given by

$$\nu_n = \frac{n}{2l}\sqrt{\frac{\tau}{\sigma}}, \tag{2.1}$$

where τ is the wire tension, σ the linear mass density of the wire, l the wire length, and n the mode index. The even harmonics will not be seen when the wire is in a uniform field, however the fundamental harmonic will be preferentially excited because the excitation source is generally low frequency in nature.

The carbon wires used to build the CRID proportional wire chambers are nominally 7 μm in diameter, but there is variation about this value. This leads to a variation in the linear mass density from wire to wire, and hence to a spread in the measured vibration frequency. This effect can be reduced by measuring the electrical resistance, R, of each wire and using the standard formula

$$R = \rho \frac{l}{A}, \tag{2.2}$$

where ρ is the volume resistivity (nominally $1.5 \times 10^{-3}\,\Omega \cdot \mathrm{cm}$) and A the cross-sectional area of the wire. From A and the nominal density ($1.77\,\mathrm{g/cm^3}$), a more accurate linear mass density can be found for each wire. It is assumed that the resistivity and mass density are constant along each wire and throughout the wire sample.

2.3.2 CRID Technique

Each wire is excited by a gentle, steady stream of N_2 gas which is directed along the wire from above.† The cathode should not be inside a cavity, since harmonics which are close to the cavity's resonance frequency may be preferentially excited. The wire is connected to a single-stage, non-inverting amplifier whose output goes to a frequency analyser (HP–3582A). A permanent magnet rests about 2–3 inches below the wire. The analyser can be programmed to average a reasonable number of spectra (4 or 8 is sufficient and takes little time), thereby smoothing the curve. The frequency is indicated on the screen once the analyser's cursor has been moved manually to the peak. The resistance of the wire is measured using a digital ohmmeter.

Figure 2.5a shows the tension for each wire of the second cathode strung, where the cross-sectional area was assumed to be constant; Figure 2.5b shows the same data, but the cross-sectional area was calculated from the resistance of each wire. The dashed lines indicate the average tension, and the dotted lines ± 1 standard deviation. Clearly, using the resistance to calculate the area reduces the spread

†It has recently been shown that the vibration can be induced by gently tapping the wire with a small hammer.

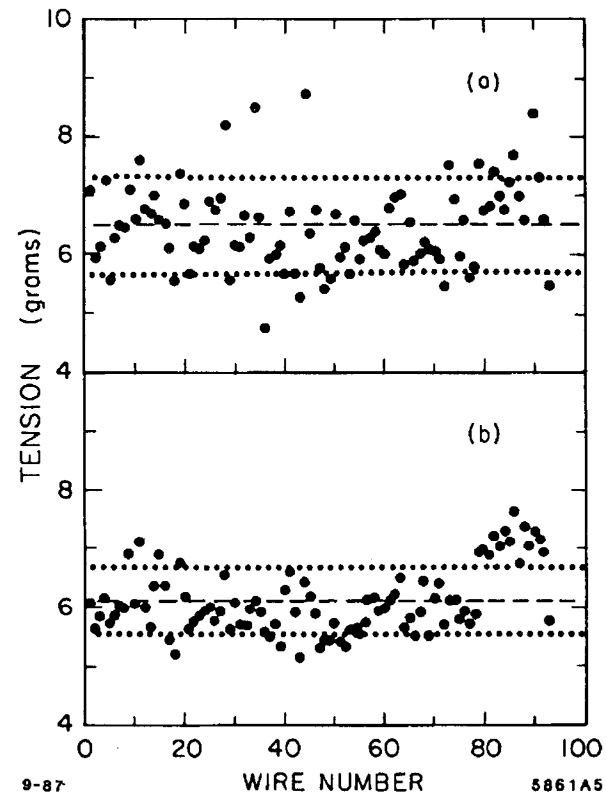

Figure 2.5: The tension of each wire for the second cathode strung. (a) shows the tension calculated with constant cross-sectional area. (b) shows the tension with the area calculated from the resistance. The final 15 wires were all strung on the final day of stringing.

of tensions, especially for those which are far from the mean because they have a different cross-sectional area. The last 15 wires of the cathode shown in Figure 2.5 were all strung on the final day of construction of this cathode, and obviously were unknowingly strung to a different tension.

This technique was used to measure the tension of all the anode wires of the CRID detectors after all wires were strung and electrical contact was made, but before the final gluing step (see section 2.4). This allowed any badly tensioned wires to be removed and replaced, though this did not need to be done often. (The cathode shown in Figure 2.5 was constructed before the tension measurement technique was used.)

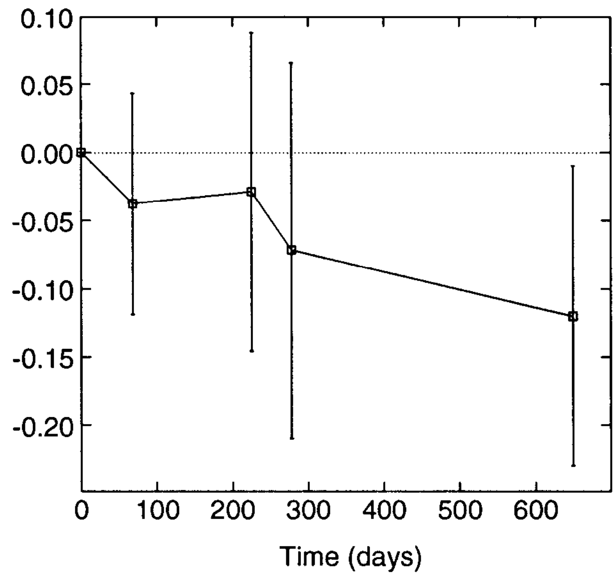

Figure 2.6: The tension creep for one cathode over time.

The tensions of the second cathode were measured at various times over a long period. Figure 2.6 shows the average change in tension over about a year and a half. The data indicate a creep of about 0.07 g per year, which is acceptable for the estimated 5–10 year lifetime of a detector.

2.3.3 Alternate Methods

"The Twanger"

This technique, which has been used frequently in the past, subjects each wire to a large, fast voltage pulse. The force between the large induced current and the surrounding magnetic field sets the wire in motion. The major drawback of this technique for the CRID setup is the large voltage ($> 3\,\mathrm{kV}$) and current required to excite the wire. The needed instantaneous current is six times the maximum carrying capability of the wires ($< 10\,\mathrm{mA}$ in air), and would place them in great danger. In addition, the large voltage step creates transients, resulting in a poor signal to noise ratio. The method was tried nonetheless, but results were not reproducible.

Audio Resonance

Each wire could be excited by an audio speaker; a standard speaker taped to the bottom of the wire frame, and a piezo-electric oscillator which could be placed within a millimeter of the wire were tried. If the amplified signal from the wire is observed while the source frequency is tuned, a resonance should be observed when the audio frequency matches the fundamental vibration frequency. The technique was tried without success.

Current Resonance

Similarly, vibrations can be excited by an oscillating current. In the past, this has been a traditional method for measuring wire tension. A current of $\sim 4\,\mathrm{mA}$ was run through each wire and an attempt was made, both visually and electrically, to observe resonant behaviour. The technique worked well for tungsten wires, but no signal was found for $7\,\mu\mathrm{m}$ carbon wires.

2.4 Construction of Detectors

The full construction of one detector for the CRID was a long process, stretching over about 2 months, but many detectors were built in parallel.

The first step was to build the cathode plane. The cathode is a "U"-shaped structure machined from aluminum and plated with nickel, repeated every 3.175mm (Figure 2.1). Along the long edge were glued two printed circuit boards with electrical pads and feed-through holes for connection to the anode wires. There is a common ground trace running between each anode pad for shielding. To string the anode wires, a fixture, shown in Figure 2.7, was built which held the cathode on alignment pins and had two movable arms for stringing fibers. On one end of each arm was a "frictionless" table attached to a load cell[‡] for measuring tension. The other end of the arm consisted of a table which could be moved with a micrometer. Both tables could be moved perpendicular to the cathode major axis in order to

[‡]Sensotec, Inc., 1200 Chesapeake Ave., Columbus, OH 43212.

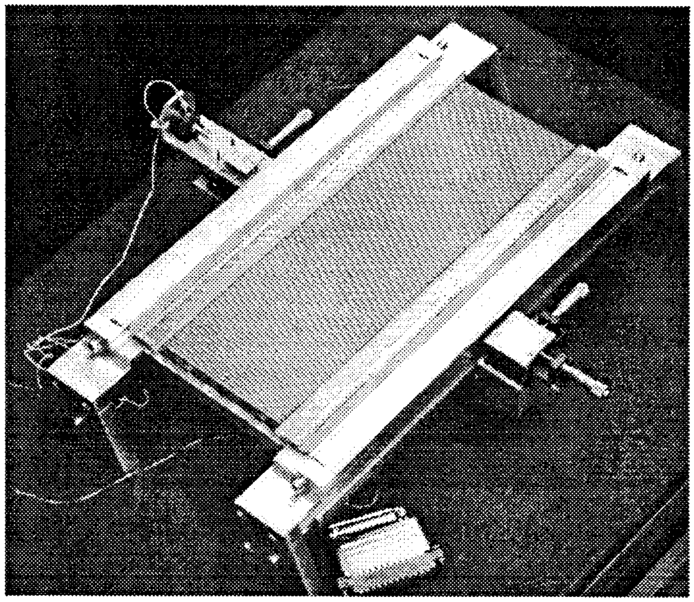

Figure 2.7: The wire stretching fixture for CRID cathodes with a cathode in place. The fixture used during main production actually had two stretching arms.

align the wires. The alignment was determined by two bars with precisely spaced V-grooves cut in them. The bars were gold-plated on top to provide electrical contact for a resistance measurement of the wires as they were strung.

The procedure followed in stringing a wire was as follows. The prepared wire, with a piece of stiff paper glued to each end, was laid across the fixture and attached to the tables with cellophane tape. The tables were adjusted so that the wire was correctly aligned on the appropriate V-grooves. The fiber was then lightly tensioned and the resistance was checked; wires with a resistance greater than 45 kΩ were not used. The tension was increased to 8 grams so that weak wires would break and then was reduced to the final value of 6 grams. Approximately 10% of the fibers did not survive the over-tensioning. The fiber was attached to the PC board in four places using fast-setting ("5 minute") epoxy,[§] which was allowed to dry for 15 minutes before the excess wire was cut away. Using the two stretching arms in parallel, our technician, Dana Millican, was able to string the 93 wires of a single cathode in about 3 days.

[§]EPOWELD # 8173, Hardman Co. Belleville, NJ 07109

When all the anode wires were strung, conducting silver epoxy, H20–E from Epotek, was used to establish electrical connection between each fiber and the contact pad; the glue was allowed to cure at 60°C for 12 hours. The tension and resistance of all the wires were then measured using the technique discussed previously. At this point, any wires which seemed to have a problem (*e.g.* low tension or poor contact) could be fixed or replaced (there actually were few problems). A final layer of epoxy, Shell Epon 826 + Versamid 140, cured at 40°C for 12 hours, was used to cover completely the previous epoxies and the PC boards in order to hold the wires securely in place and to protect against corrosion by TMAE.

The blind structure was constructed as a package. Each layer was made from 254 μm thick copper–beryllium sheets. Each sheet was etched to have 93 2 mm wide openings, but with a 305 μm wide connecting strip across the center of each opening. The sheets were heat-treated before etching to ensure flatness, and were electropolished after to remove sharp edges. All five planes were glued together along with G-10 spacers to form an easily removable, 15 mm thick package. 100 μm diameter Cu–Be wires were soldered on the top of the package, centered on the Cu–Be strips; these guide the electrons into the openings in the blinds. In addition, by biasing odd and even wires by $+350\,V$ and $-350\,V$, respectively, this wire plane can be used as a gate to prevent positive ions created in the avalanche at the anode wires, from reaching the drift volume.

A completed CRID detector is shown in Figure 2.8. The backplane is made of G-10 with printed circuit feedthrough boards going through it to bring the anode signals outside the drift box. There is a machined O-ring surface along the outer edge of the backplane to provide a gas-tight seal to the drift box. The cathode was mounted on the feedthroughs and solder connections were made between the traces and pins soldered in the anode wire feedthrough holes. All solder flux was carefully removed with alcohol, since flux combined with TMAE can adversely affect the electron lifetime. The blind plane assembly was aligned with respect to the cathode by means of registration pins and glued in place (the glue can be removed if repairs are necessary). The blind planes, gating wires, and cathode were connected to a set of feedthrough pins in the backplane. When operating,

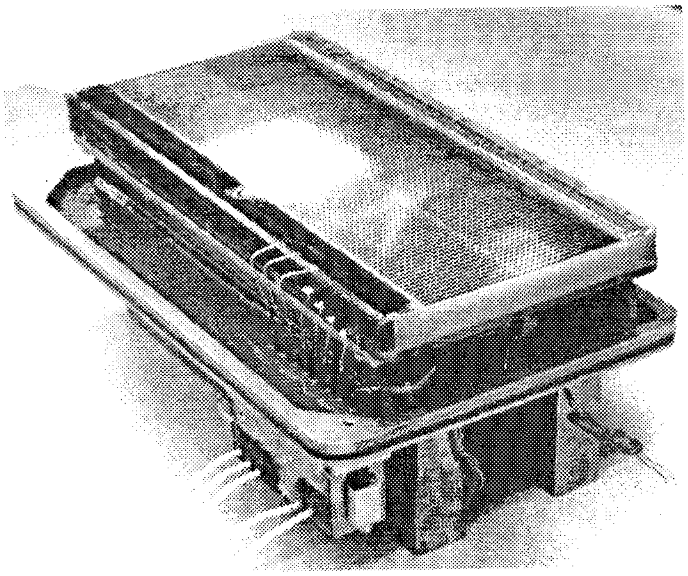

Figure 2.8: A completed CRID single electron detector.

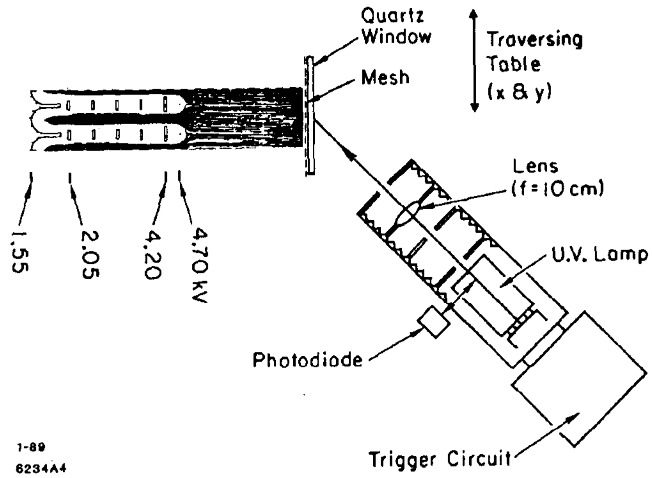

Figure 2.9: The detector test setup. The UV lamp is triggerable and can be moved in two dimensions. Electrons are emitted from a dense steel mesh.

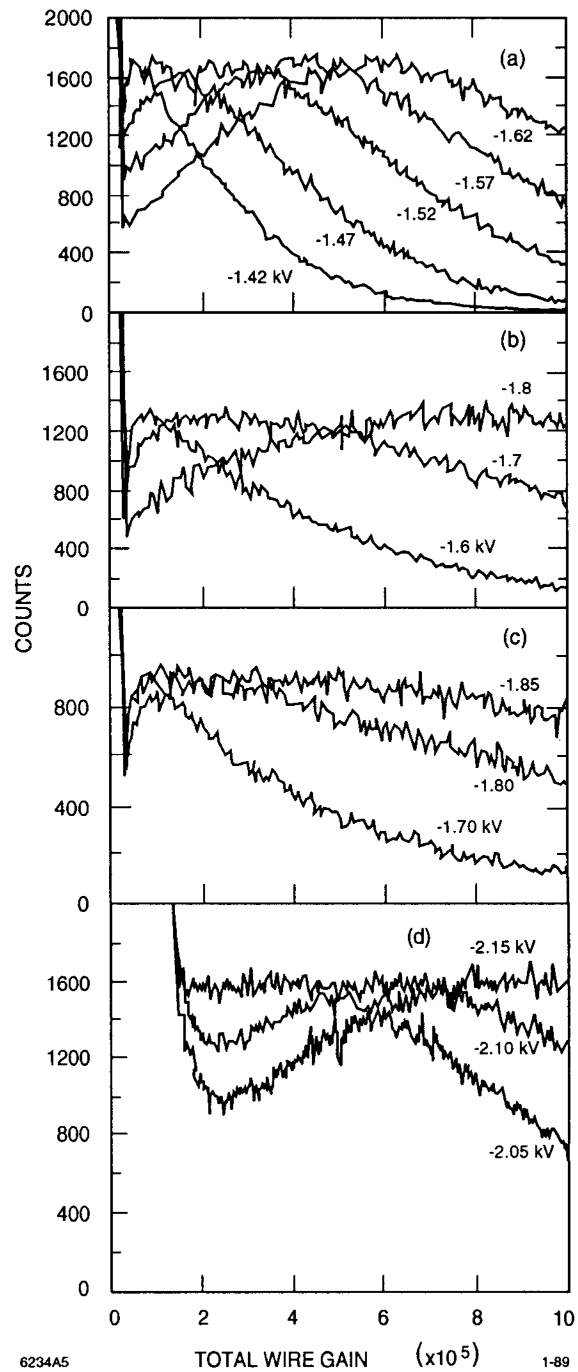

Figure 2.10: The single electron spectra measured with 7 μm wires in (a) C_2H_6, (b) 80% CH_4 + 20% C_2H_6 and (c) CH_4 gases as a function of total wire gain Q^{tot}_{L+R}; (d) the spectra for 33 μm wire in C_2H_6 gas.

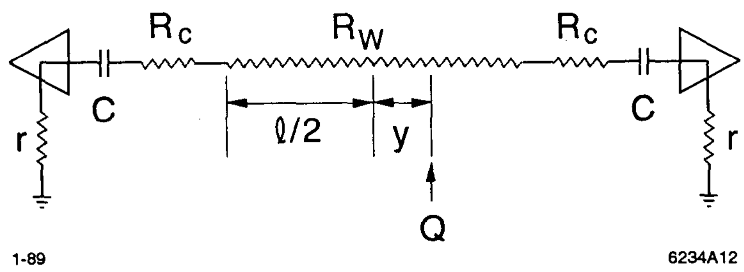

Figure 2.11: Equivalent model of the charge division.

the outer sides of these pins are connected to a fully-potted, high voltage filterbox which, among other things, defines the voltages of the intermediate blind planes via a resistor chain between the top and bottom blinds.

2.5 Detector Performance

To test the detectors, the test setup shown schematically in Figure 2.9 was built. The light from a UV lamp is collimated and focussed on a dense stainless steel cloth, causing electrons to be knocked out. The electrons then drift into the detector to produce an avalanche. The lamp is triggerable and can be moved on an x–y stage. The probability of producing one electron per UV flash is 1–5 %, depending on the aperture.

Figure 2.10 shows the single electron pulse spectra measured in C_2H_6, CH_4, and 80% CH_4 + 20% C_2H_6 for two wire diameters and for different cathode voltages. The present nominal operating choice is C_2H_6 gas with TMAE from a 26°C bubbler, and a cathode voltage of -1.50 kV.

The most important measurement of the detector performance is the charge division resolution. An electrical model of the CRID anode system is shown in Figure 2.11. The position, y, is calculated by

$$y = \frac{l}{2}\frac{Q_O - Q_I}{Q_O + Q_I}\frac{R_{ch}}{FR_w} \tag{2.3}$$

where Q_O and Q_I are the outer and inner measured charge, respectively,

Amp. Resistance r	$500\,\Omega$
Amp. Equiv. Noise Res. R_{eq}	$50\,\Omega$
Amp. Decoupling Cap. C	10 nF
Amp. Input Cap. C_{in}	10 pF
Detector Cap. C_{ch}	15 pF
Integration time T_G	200 ns
Ave. visible charge Q_{vis}	(2-3)$\times 10^5$ el.

Table 2.1: Parameters used in the noise model of charge division. See also Table 2.2.

Parameter	7 μm wire	33 μm wire
Wire length l	10.35 cm	
Wire resistance R_w	$40\,\mathrm{k}\Omega$	$5.2\,\mathrm{k}\Omega$
Wire-breaking tension	10.1 ± 2.1 g	60–70 g
Wire tension	6 g	12 g
Energy needed to break wire by spark	0.8 ± 0.3 mJ	> 300 mJ
Max decoupling capacitor (cathode to ground)	< 0.3 nF	> 5 nF
Contact resistance (ave.) R_c	$150\,\Omega$	$30\,\Omega$
Cathode voltage V_c	-1.55 kV	-2.05 kV
Average total gain Q^{tot}	$\sim (5-6) \times 10^5$	$\sim 6 \times 10^5$
Cathode surface gradient	1.8 kV/cm	3.3 kV/cm
Thermal noise σ_J	960 elec.	2480 elec.
Amplifier noise σ_{amp}	530 elec.	
Total noise (calculated)	1100 elec.	2540 elec.
Total noise (measured)	1150 elec.	2180 elec.
Distant-wire cross-talk	0.2 – 0.3 %	-
C_2H_6 charge div. σ_y/l	0.7 %	1.2 %
C.D. slope dy(meas.)/dy(true)	0.98	0.86

Table 2.2: Parameters for wire electrical model and results.

$R_{ch} \equiv R_w + 2R_c + 2r$ is the total resistance, and

$$F = \exp\left(-\frac{2T_G}{R_{ch}C}\right) \approx 1.0. \tag{2.4}$$

The factor F represents the affect of the R–C filtering of the circuit. Most of the parameters, along with typical values, are listed in Tables 2.1 and 2.2. The noise of a measured charge is made of two pieces: thermal Johnson noise, ΔQ_J, which is anti-correlated on the two ends of the wire; and amplifier noise ΔQ, which is independent for the two ends. Differentiating Equation 2.3 and using standard error propagation gives an RMS error[20]

$$\left(\frac{\sigma_y}{l}\right)^2 = \left(\frac{\sigma_J}{Q_{vis}}\right)^2 + \frac{1}{2}\left(\frac{\sigma_{amp}}{Q_{vis}}\right)^2 \left[\left(\frac{R_{ch}}{FR_w}\right)^2 + \left(\frac{2y}{l}\right)^2\right]. \tag{2.5}$$

The Johnson noise σ_J is given by

$$\sigma_J = 2.718\sqrt{\frac{kT\tau}{2R_{ch}}}, \tag{2.6}$$

where k is the Boltzmann constant, T is the absolute temperature and τ is the amplifier shaping time (65 ns). The amplifier noise is approximated by the FET channel thermal noise[21]

$$\sigma_{amp} = 2.718\sqrt{\frac{kTR_{eq}(C_{in} + C_{ch})^2}{2\tau}}. \tag{2.7}$$

For the values of the constants given in Tables 2.1 and 2.2, the thermal noise is significantly greater than the amplifier noise (see Table 2.2), which justifies the design criterion of using highly resistive anode wires.

The charge division resolution was measured using the detector test setup with C_2H_6 gas. Figure 2.12a shows a scatterplot of the measured charge division co-ordinate versus the total pulse height, while Figure 2.12b shows the projection along the co-ordinate axis. The resolution as determined from the full width at half maximum (*i.e.* ignoring the non-Gaussian tails) is $\sigma_y/l = 0.7\%$. The charge division resolution does not change significantly with position along the wire, as predicted. Also, the charge division linearity, *i.e.* the linearity of the measured co-ordinate versus the true co-ordinate, was found to be good, indicating good

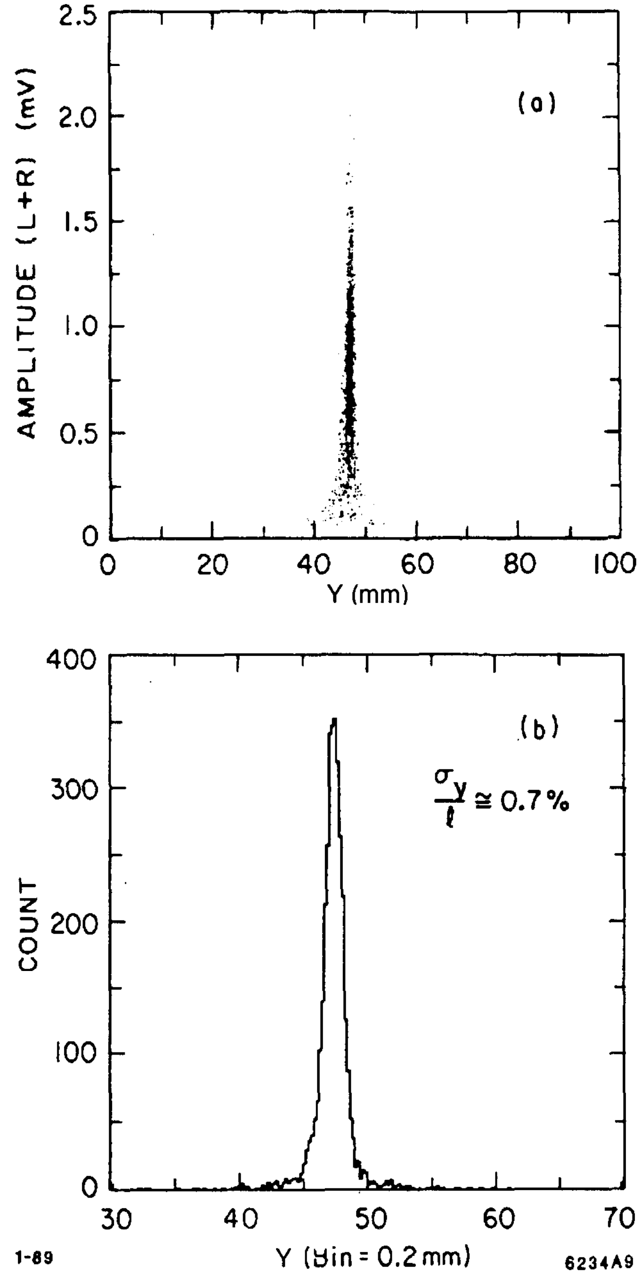

Figure 2.12: (a) The measured charge division resolution plotted against the total pulse height for C_2H_6 gas, $7\,\mu m$ wires, and nominal voltages ($V_c = -1.55\,kV$ and $V_1 = -2.1\,kV$). (b) Projection of (a) onto the y axis.

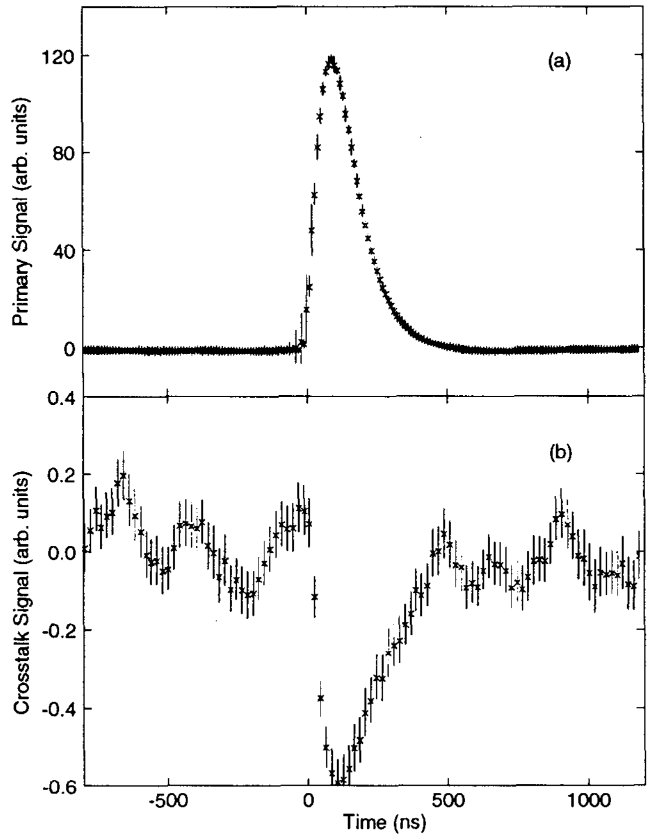

Figure 2.13: A measurement of the cross-talk with $7\,\mu m$ wires. (a) The primary signal. (b) The cross-talk on a distant wire.

resistance uniformity along the wire. During running in SLD, the noise is about $\sigma_y/l = 2.1\%$. The increase is due to increased noise in the final hybrid amplifiers, and a lower detector gain due to lower operating voltages ($V_c = -1.5\,kV$ and $V_1 = -1.75\,kV$, instead of $V_c = -1.55\,kV$ and $V_1 = -2.1\,kV$).

The detectors and amplifiers are optimized for single electron signals; however, the detectors will also see very large signals, consisting of about 1000 electrons, from minimum ionizing particles. Care was taken during the design of the amplifiers to ensure good recovery after very large pulses. To minimize cross-talk, shielded traces have been incorporated between the wire and amplifier inputs, and the largest cathode-to-ground capacitor possible, consistent with the prevention of wire breakage by a spark, has been used. The cross-talk was measured using two methods. Method one[22] used an Fe^{55} source to produce the pulses and an oscilloscope to superimpose many traces. The second method used single electron pulses from the detector test setup. Figure 2.13 shows the average of many superimposed signals for the primary channel and a distant wire. The cross-talk was of similar shape to the primary with an amplitude of 0.2–0.3% and opposite polarity; the shape and size do not change significantly with the distance between the two wires. Early measurements of the cross-talk found that, on an immediately neighbouring wire, the cross-talk also had a prompt, fast component of $\sim$ 1.3% of the main amplitude; this was somewhat reduced in the final electronics by careful shielding.

2.6 33 μm Wire Detector

As an option to using the 7 μm carbon wires, the use of 33 μm carbon fibers[¶] as anodes was investigated. These big wires are much less fragile, so that a much more robust detector can be built. Unfortunately, the lower wire resistance significantly increases the thermal noise, thus decreasing the charge division performance. However, their use would allow a larger cathode-to-ground decoupling capacitor, lowering the cross-talk.

The fiber characteristics were measured by stretching and breaking about 60 wires. The average breaking tension was 60–70 grams[‖] while the average resistance was 5.2 kΩ; also, the 33 μm wires are much more uniform than the 7 μm ones, and were much easier to handle.

One detector was built using these wires to test its performance. The anode wires were tensioned to 12 grams. The detector was tested in the detector test setup described previously. The results are listed in Table 2.2. The total noise was 2180 electrons, about double the noise for the 7 μm wires. The charge division resolution was 1.2%, $\sim$ 70% worse.It should be noted that the charge division slope, $dy(\text{meas.})/dy(\text{true})$, was 0.86, which is significantly different from the optimal value

[¶]Textron Specialty Material Co., Lowell, MA 01851, U.S.A.

[‖]Recent experience indicates that these wires are quite sensitive to the exact mechanical environment and should not be tensioned over about 30 grams.

of 1; however, this was mostly the result of not including the effect of the (relatively large) preamplifier input resistance, which is about 20% of the wire resistance for the two amplifiers.

In retrospect, the 33 μm wire was an valid option. The higher noise in the final CRID system means that the increased Johnson noise would not greatly harm the performance. Wire aging in a thick wire detector is more than a factor of 5 better than with the 7 μm anodes.[23] One of the most persistent problems for the CRID pulse finding algorithm has been dealing with heavily saturated signals from minimum ionizing particles (see Section 3.3) and the resulting cross-talk signals; if not properly treated, these signals can result in backgrounds which can confuse the pattern recognition algorithm. Using thicker wires for the anodes would allow the use of a significantly larger cathode-to-ground decoupling capacitor, greatly reducing the cross-talk. This would also provide greater protection for the anodes from sparks. At the time of writing, 5 detectors in the CRID were unable to hold voltage, probably due to a broken wire. However, this must be put in perspective; in three years of operation, only 8 out of a total of 3720 wires have broken, only 0.2%.

There were a number of reasons why the 33 μm wires were not used in the CRID. The system noise was planned to be lower due to lower electronics noise and higher detector gain, making the increased thermal noise significant. At the time, it was felt that the 7 μm detectors had a greater margin of safety with respect to operating voltages and high-voltage breakdown, although this is less true once the detectors have been exposed to TMAE. Also, the low resistance of the 33 μm fibers was a poor match to the $\sim 500\,\Omega$ input impedance of the preamplifiers; the conversion between measured charge division co-ordinate and real y co-ordinate would have had to been carefully calibrated, possibly on a wire-by-wire basis. Finally, by the time the 33 μm wires has been tested, the decision to use the 7 μm was essentially irreversible because of the amount of experience accrued with the thin wire detectors and because of some of the design decision already made.

In hindsight, the best scenario might have been that a medium thickness wire, maybe $\sim 20\,\mu$m, was tested early and used. This diameter would have provided a good compromise between noise level and wire strength.

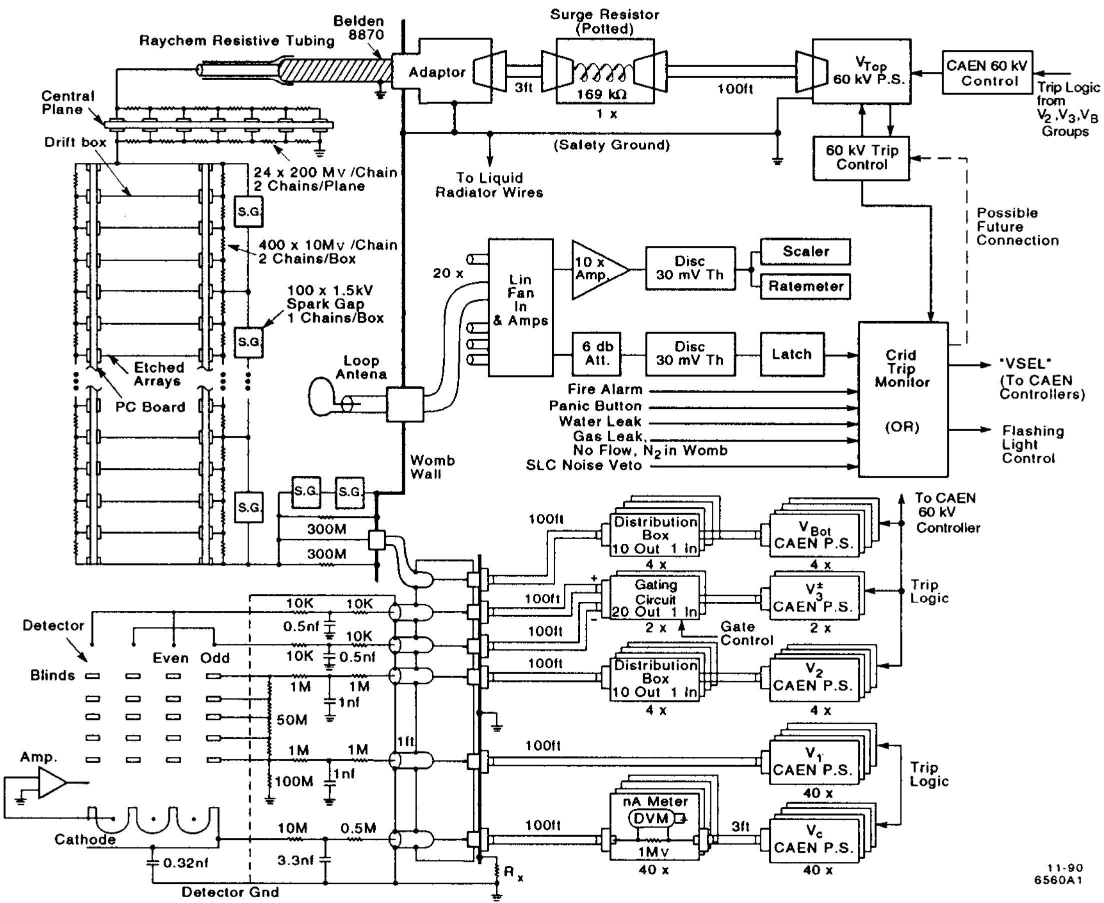

Figure 2.14: Overall CRID high voltage system. The nano-ammeters are shown in the lower right corner.

2.7 Cathode Current Monitoring

This section describes the methods used for the CRID to measure and monitor the currents drawn by the cathodes of the single-electron detectors. The main reason for developing this system was that the CAEN power supplies do not have sufficient current sensitivity to monitor the nanoamp currents seen by the cathodes.[24] The least significant bit of the CAEN current measurement corresponds to 100 nA, which means that the current can only be measured to a precision of about 200 nA. Figure 2.14 shows the overall CRID high voltage system, including the nano-ammeters.

It is necessary to measure cathode currents down to 1 nA for several reasons:

- The wire aging in TMAE laden gases is especially fast.[23,25] For instance, if a detector continuously draws 5 nA, it will lose half of its gain in about 2 years of operation. Thus, it is important to monitor the integrated charge dose of the CRID detectors at these very low currents. The detectors are protected by a trip level of 6 nA on a computer monitored ammeter, described below. When the current exceeds 6 nA, the voltage on the cathode is automatically ramped down to 80 % of nominal, essentially turning off the gain of the detectors.

- The cathode current correlates with SLD event size. Running at a current of about 5 nA corresponds to large event sizes due to excessively high backgrounds, making the analysis of such events more difficult. In a quiet environment, a CRID cathode draws about 2–3 nA, which is about twice the current from cosmic rays.

- A frequent cause of death for wire chambers is the Malter effect.[26] This is caused by the cathode being coated by an insulator due to faulty construction or wire aging. At high backgrounds, this insulator can be charged up by positive ions. Large fields develop across the thin layer of insulator causing an emission of electrons. These electrons will amplify and generate more positive ions. This positive feedback will lead to large standing currents, typically several hundred nanoamps. If a power supply has a high current trip setting (for the CRID, the CAEN power supplies are set to trip at 700 nA), these large currents may not cause a trip, and the chamber will deteriorate rapidly. This is probably the most common cause of wire chamber problems in high energy physics, and it is exacerbated by poor diagnostic capability.

- The low current diagnostic capability means that problems such as tiny current leaks or the initial onset of breakdown can be detected much sooner than would otherwise be possible.

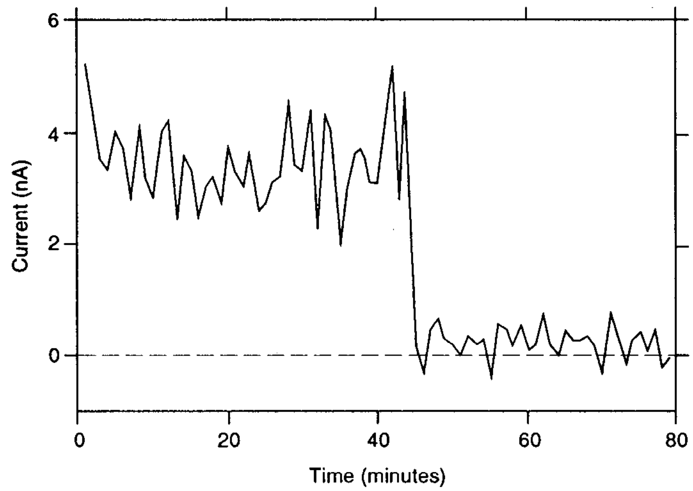

Figure 2.15: Effect of the cathode gating circuit on the current arising from cosmic rays in the prototype. Note that the cosmic ray current in the SLD is about half the value shown here. The gating circuit was turned on at about 45 minutes.

- The precise current monitoring capability of the CRID system has made possible such measurements as the spatial distortion in the TPC for very small currents.[27] The few nanoamp current drawn by a CRID cathode corresponds to spatial distortion at the millimeter level due to the field distortions caused by positive ions. This is another reason why not to run with the current higher than 5 nA, and why the detectors should be operated with the detector gating circuit running. Figure 2.15 shows the effect of using the gating circuit on the cathode current arising from cosmic rays; the gating circuit reduces the cosmic ray current from 3–4 nA to about 0.5 nA.

There are two basic problems to be overcome when building a system to measure the cathode currents. First, since the ammeter is connected to the detector cathode, it must float at the cathode voltage, which is approximately 1.5 kV. This means that the meter and, more problematically its power supply, must be carefully isolated from ground. The second problem is that leakage currents must be kept very small.

The following sections describe the two systems used to measure the cathode currents for the CRID. The basic method used is to measure the voltage across

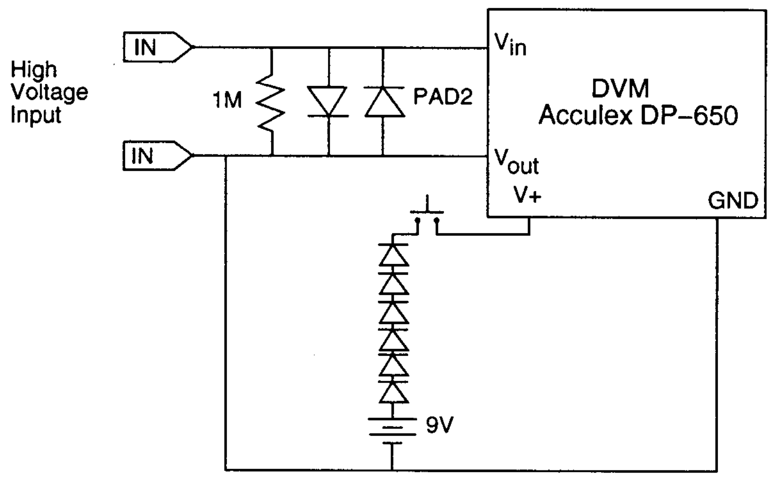

Figure 2.16: The circuit diagram for the basic nano-ammeter.

a precision 1 MΩ resistor in series with the cathode. The added resistance is not an issue because of the large resistance between the cathode and ground. By measuring the voltage to 0.1 mV, the current is measured to 0.1 nA. The first system is battery powered and relatively compact, and was used to instrument every detector in the barrel CRID for occasional diagnostic use. Unfortunately, this system cannot be used continuously because of power constraints and cannot be read into a computer. Thus, a second system was built to provide continuous monitoring of a few cathodes into the CRID monitor and control computer. An alternative circuit for computer monitoring has also been tried and will be discussed briefly.

2.7.1 Basic Nano-Ammeter

The circuit for the basic nano-ammeter, shown in Figure 2.16, is very straightforward. A miniature digital voltmeter is used to measure the voltage across a precision 1 MΩ resistor. The DVM is powered by a 9 V alkaline battery with 6 diodes in series to drop the voltage to roughly 5 V. In order to protect the DVM from burning out due to overvoltage, there are two low-leakage pico-amp diodes (Siliconix PAD2) across the 1 MΩ resistor. If these diodes blow, the DVM will read 0, since the resistor will be shorted by the diodes.

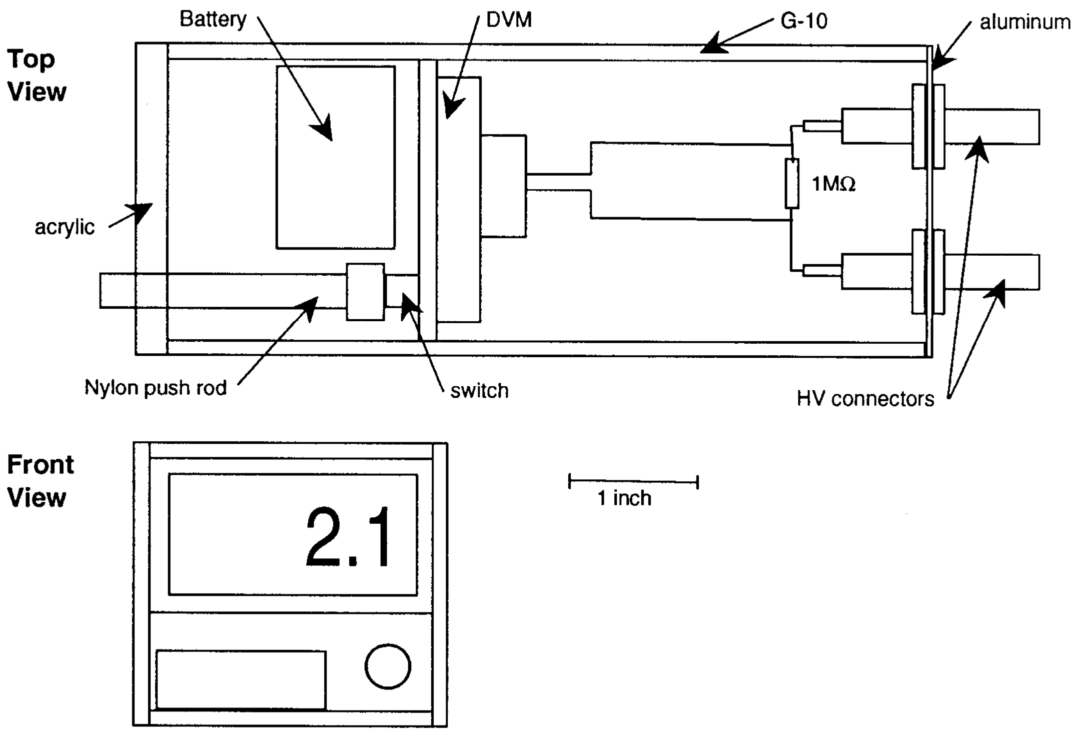

Figure 2.17: The layout of the basic CRID nano-ammeter.

The layout of the nano-ammeter is shown in Figure 2.17. The overall dimensions are 2.4 × 2.125 × 6 inches, excluding the high voltage connectors, so that 42 modules can be mounted in 14 inches of standard rack space. The box is constructed from G–10, a fiberglass/resin material. The front panel is clear acrylic and the back panel is aluminum. The G–10 pieces were assembled with DP–190 epoxy. The inside of the box is lined with a sheet of Kapton foil, which has a very large surface resistivity, and helps to cut down on leakage currents. All parts were cleaned with alcohol in an ultrasonic cleaner and the units were assembled with gloves to eliminate grease.

The units are turned on by means of a plunger going through the front panel. The 9 V battery is sufficient to operate the meter for roughly 8 hours, enough for months of operation, since it is only on for a few minutes at a time. The battery is in the front of the box, so it can be replaced easily when the high voltage is off.

To mount the meters and keep out noise, all units are inside an aluminum box in an equipment rack. The aluminum back of each meter, which holds the high voltage connectors, bolts against the back of the rack box, providing a solid conductor wall. The front of the rack box is accessed by a hinged lid which is normally kept closed. The front of the meters sits back a few inches from the front of the rack box to protect against noise while the door is open.

2.7.2 Computer Monitored Nano-ammeter

The circuit for the computer monitored nano-ammeters, shown in Figure 2.18, is more complicated because both the power coming in and the signal going out must be isolated from the high-voltage. The power is supplied by a transformer which is rated at 3 kV isolation. It provides ±12 V AC which is then regulated to the desired ±6 V with two voltage regulator chips. The power is used by an OP-27 op-amp to measure the voltage across a 1 MΩ resistor. The output of the op-amp drives the input of a OPI-120 opto-isolator. The low-voltage side of the opto-isolator is powered by an additional supply and is read directly into an SLD SAM (smart analog module) unit connected to the computer. Capacitors were placed in the circuit to limit pickup of 60 Hz noise from the power supplies. In addition, a temperature monitor chip (AD590) was placed on the circuit board for calibration.

The opto-isolator is a coupled light-emitting diode and a photo-transistor, and is not linear. However, since the meter is designed only to be read into a computer, it is trivial to remove the non-linearity with software. A cubic polynomial is used, but the cubic term is small. Also, when the circuit was being tested, it was discovered that it had a significant temperature dependence, thus the inclusion of the temperature measuring chip. The output of this chip also is read into the computer; to the accuracy desired, the dependence is linear and easily removed.

Unfortunately, the space requirement for these units is large. The transformers are roughly 3–4 inches on a side. Because all the CRID detector cathodes are powered individually, one transformer is needed for each cathode monitored. The

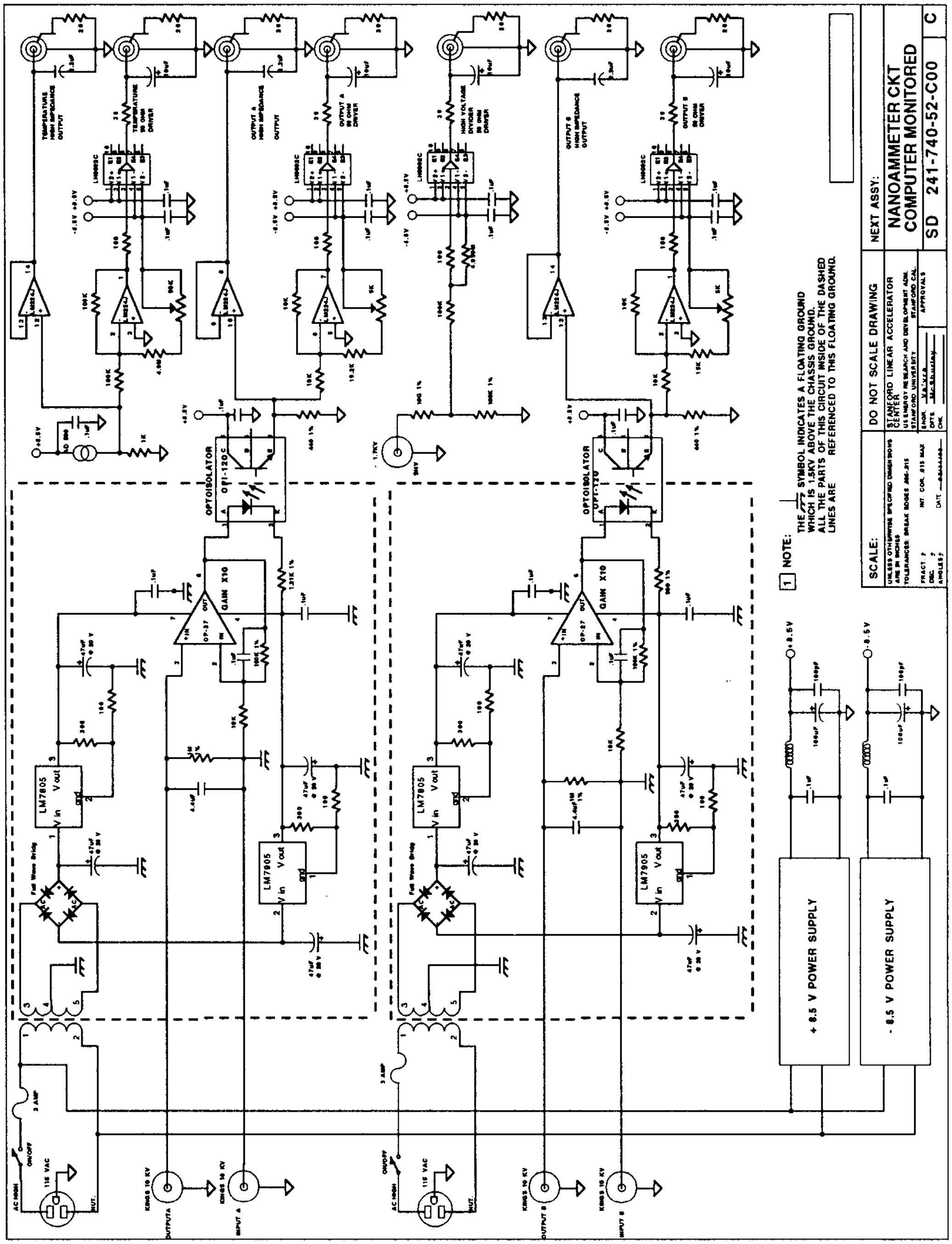

Figure 2.18: The computer monitored nano-ammeter circuit. Both high and low (50Ω) impedance outputs are provided. The 50Ω output was designed to feed a charge-sensitive FASTBUS ADC.

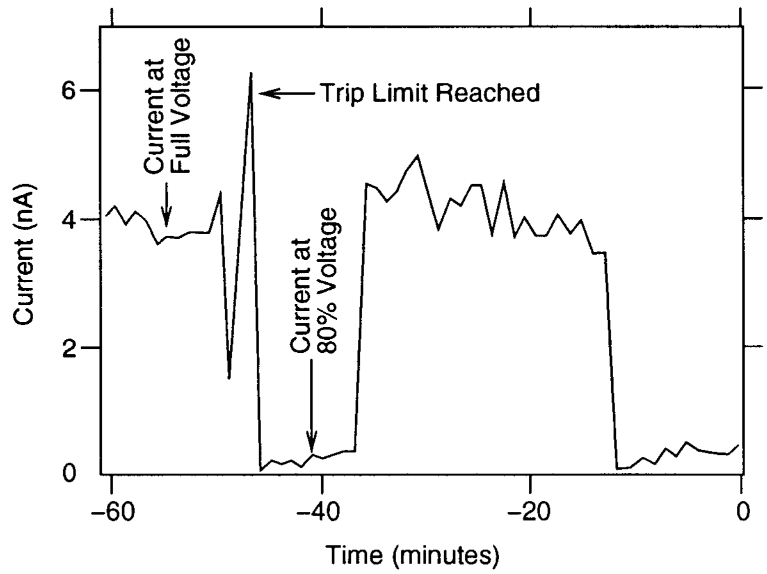

Figure 2.19: Time history of the cathode current during SLD running.

addition of the low-voltage power supply (which can be shared) means that only two meters could fit in 4 inches of standard rack space. It is possible that with careful layout, this could doubled to four ammeters.

Figure 2.19 shows a time history of the computer-monitored cathode current during SLD running. At the beginning, the current was steady at about 4 nA. When the current increased to 6 nA, the software tripped the CRID high voltage, bringing it down to 80 % of nominal. Once the operator decided that it was safe to run, the voltage was brought back up and the current resumed. At the end, the high voltage was taken down by the operator and the current went to near 0.

2.7.3 Alternate Circuit

An alternative computer-monitored circuit, shown in Figure 2.20, has been tested. The idea is to have the amplifier output drive a voltage controlled oscillator[♯] (MC 14046B). The AC output of the oscillator is sent through the opto-isolator and read into a scaler or possibly a frequency-to-voltage circuit. The output of a scaler

[♯]A similar circuit was suggested by H. J. Besh; the OPAL experiment is apparently using a similar circuit.

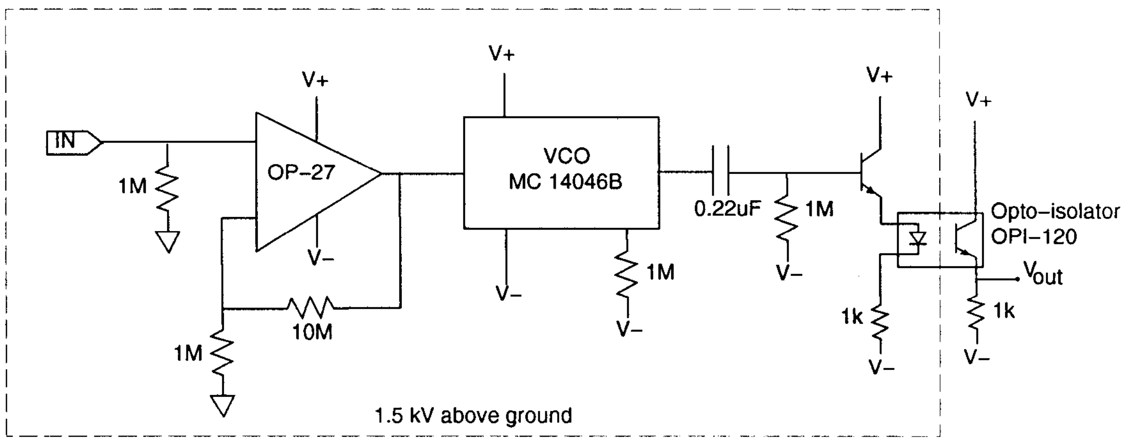

Figure 2.20: Rough circuit diagram for an alternate computer-monitored nano-ammeter.

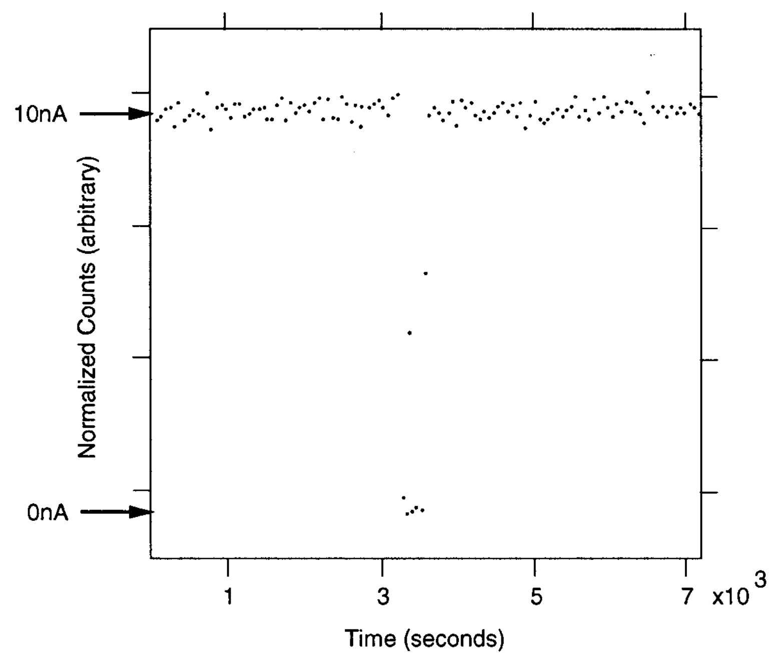

Figure 2.21: Output of a scaler measuring the frequency from the alternate circuit. The upper signal corresponds to 10 nA and the lower to 0 nA. The spread of the upper signal gives an uncertainty of about ±0.2 nA.

during a test run of this circuit is shown in Figure 2.21. The current was set at 10 nA except for a short time at 0 nA; the spread of the 10 nA measurements corresponds to an uncertainty of about ± 0.2 nA.

This design has a strong advantage in that it does not depend on the response of the opto-isolator; the frequency output should be linear with respect to voltage. The disadvantages are the increased complexity of the circuit and the complication of measuring the frequency.

Chapter 3

Deconvolution Pulse Finding

This chapter describes the algorithm used for the CRID to find pulses in the digitized data coming from the electronics. The algorithm must be fast because it is intended to be run in real-time in the WSMs. The algorithm is based on the fact that the specific pulse shape delivered by the CRID electronics can be deconvolved from the digitized data using a linear formula involving three data points. Complications arise from trying to distinguish very close pulses and from trying to deal with very large, saturating pulses and their tails. Tests were performed on the deconvolution pulse finding algorithm for charge division resolution, double pulse resolution, and small pulse efficiency using the prototype (non-hybrid) amplifiers and the detector test setup described in Chapter 2.

3.1 Amplifier Design

The photoelectron signal from the CRID detectors is very fast, with typical avalanche times less than 1 ns. However, this is much faster than the sampling rate of the data acquisition system (67.2 ns). Therefore, the CRID preamplifiers shape the signal to a much broader pulse. The impulse response of the preamplifiers is $t\exp(-t/\tau)$, with $\tau \simeq 65\,\mathrm{ns}$. This shape was chosen because it low noise characteristics but requires few components. The shaping time, τ, was chosen to match the sampling interval in order to minimize noise.[16]

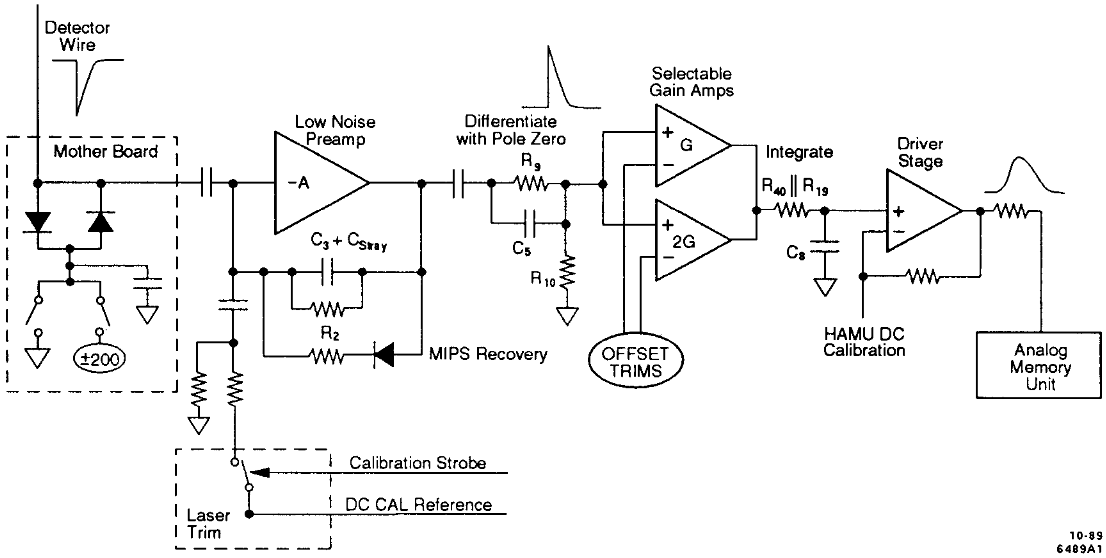

Figure 3.1: A block diagram of the CRID front-end amplifiers.

The amplifiers used for the CRID[14,15] consist of three stages (Figure 3.1): a low noise preamplifier; a video op-amp with two, digitally selectable gains; and driver video op-amp to drive the Hybrid Analog Memory Unit (HAMU) load. The preamp is implemented using a discrete JFET input. It has an input impedance of about 700 Ω and an RMS noise of about 500 electrons. After the preamp, the signal is processed to produce an RC–CR, or $t \exp(-t/\tau)$, shape. The signal is first differentiated with pole-zero cancellation. It is then buffered by the selectable-gain amplifier and put through an integrator.

A number of additional features were added to the amplifiers. At the input of the amplifier, there is a circuit which can isolate the anode wire from the amplifier and put ± 200 V on either end to heat the wire. This can be used to burn off polymerized deposits on the wires if the overall gain decreases significantly. There are also facilities to strobe the input of the preamp and to drive the output at a DC voltage. These are used separately to calibrate the amplifier and the HAMU.

The amplifier package was implemented using a semi-custom approach, with discrete capacitors and resistors when needed to provide precision shaping. Each channel is on its own board which plugs into a motherboard. The single channel approach eliminates on-board cross-talk and allows the amplifiers to be separated by grounded metallic screens which reduce the radiative cross-talk.

3.2 Deconvolution and Pulse Shape

The pulses due to single electrons are quite uniform in shape, varying only in amplitude and start time. This suggests that a deconvolution algorithm would be well-suited to the CRID. Such an algorithm relies on knowledge of a fixed pulse shape to extract information from a minimum of samples. The goal is to digitally remove the known broadening applied by the preamplifiers. It would sharpen the pulses, providing better time resolution and excellent separation of close pulses, even when one of the pulses is small with respect to the other. This technique has also been investigated for use at colliders with very fast crossing times, such as the SSC and LHC.[28]

When dealing with a fixed pulse shape, a deconvolution algorithm has two major advantages over a derivative algorithm. The deconvolution requires only a few samples to determine the parameters of the pulse. In the case of the CRID, there are only 512 samples to cover the maximum drift time, resulting in a sample interval of 67.2 ns. This means that a given pulse is only sample 4–5 times, not enough for a derivative calculation to accurately measure the start time. Also, the derivative of a pulse is negative in the tail region, whereas the deconvolved data is the zero (ignoring a constant pedestal). This means that a pulse closely following another pulse would be much easier to find in the deconvolved data since it would not be affected by the earlier pulse. This is illustrated by Figure 3.2, where the signal from a small pulse following a large one is fully below 0 in the pulse derivative; however, in the deconvolved signal, the second pulse is unaffected by and clearly separated from the first pulse.

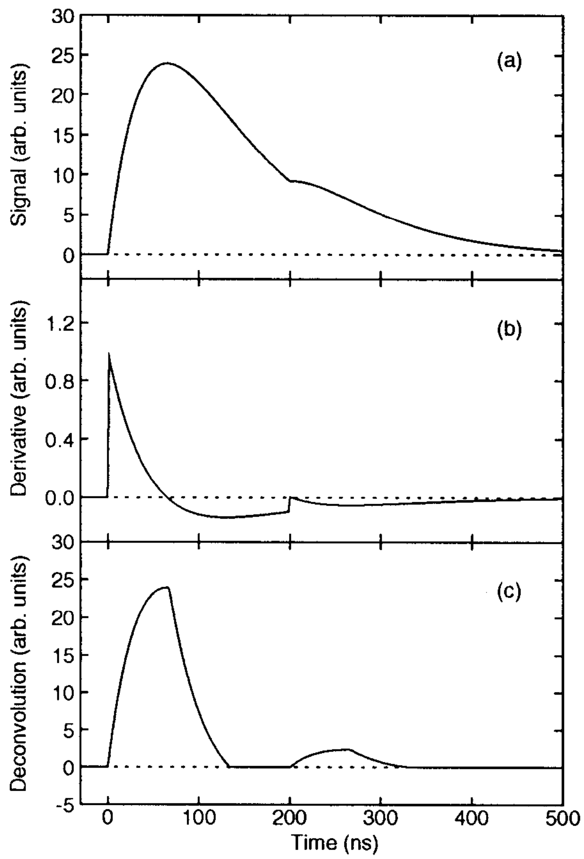

Figure 3.2: A comparison of deconvolution and derivative pulse finding. (a) Two $t\exp(-t/\tau)$ pulses, with $\tau = 65\,\mathrm{ns}$, separated by $200\,\mathrm{ns}$. The second pulse is 0.1 as large as the first. (b) The analytic derivative of (a). (c) The "continuous" deconvolved signal, as defined by Equation 3.7 with $T = 67.2\,\mathrm{ns}$ and perfect deconvolution constants.

The $t\exp(-t/\tau)$ shape is very conducive to deconvolution. The deconvolution equation is

$$d_i = r_i - 2\mathrm{e}^{-T/\tau} r_{i-1} + \mathrm{e}^{-2T/\tau} r_{i-2} \tag{3.1}$$

where T is the data sampling interval ($67.2\,\mathrm{ns}$), r_i is the i^{th} preamplifier output sample, and d_i is the i^{th} deconvolved sample. This equation was originally derived using a Z-transform,[16] which is the discrete version of a Laplace transform, but it is much easier to understand after the fact. First, it should be noted that, since the equation is linear, a constant pedestal in the input signal (even under a pulse) will translate to a constant pedestal in the deconvolved signal; therefore, it will assumed that the pedestal is 0 for the present discussion.

Again, if all three samples are ahead of a pulse, the deconvolution produces zero. If all three samples are fully on the pulse, we get

$$\begin{aligned} d_i &= t\mathrm{e}^{-t/\tau} - 2\mathrm{e}^{-T/\tau}(t-T)\mathrm{e}^{-(t-T)/\tau} + \mathrm{e}^{-2T/\tau}(t-2T)\mathrm{e}^{-(t-2T)/\tau} \\ &= \mathrm{e}^{-t/\tau}\left[t - 2\mathrm{e}^{-T/\tau}(t-T)\mathrm{e}^{T/\tau} + \mathrm{e}^{-2T/\tau}(t-2T)\mathrm{e}^{2T/\tau}\right] \\ &= \mathrm{e}^{-t/\tau}\left[t - 2(t-T) + (t-2T)\right] \\ &= 0 \end{aligned} \tag{3.2}$$

Therefore, the only points which produce a signal in the deconvolved data are those where the later one or two samples are on the pulse and the earlier two or one samples are on the pedestal.

Thus, the deconvolution removes the preamplifier broadening by reducing all single electron pulses to one or two samples (the one sample pulses are from the rare case where a sample falls directly at the start of the pulse). Two pulses which occur within 2 sample intervals, *i.e.* 140 ns, of each other can therefore be resolved. Also, the efficiency for finding a small pulse on the tail of a bigger pulse is greatly improved since the tails of pulses are effectively removed.

The pulse shape seen in the CRID is actually not exactly that of the amplifiers. There are two components to the charge avalanche in the detector, the electrons and the positive ions. While electrons are produced in great quantity, the majority of them only drift for approximately 10 μm right near the anode. The positive ions drift slowly away from the anode and travel a minimum distance of about 1 mm to the cathode surface (some drift all the way into the TPC volume). Since the signal in the detector is due to the induced current, the majority of the signal is due to the positive ions. The expected detector pulse shape, $C(t)$, is assumed to be the convolution of the amplifier response with the positive ion response. The positive ion response is determined by the current flow from point ionization entering the region of a cylindrical wire chamber[29]

$$i(t) \sim \frac{1}{t+t_0}. \tag{3.3}$$

Therefore, ignoring the electron contribution,

$$\begin{aligned} C(t) &= \int_0^t \left[t' \mathrm{e}^{-t'/\tau}\right] \left(\frac{1}{t-t'+t_0}\right) \mathrm{d}t' \\ &= \mathrm{e}^{-(t+t_0)/\tau}(t+t_0) \left\{ \ln\left(1+\frac{t}{t_0}\right) + \sum_{n=1}^{\infty} \left(\frac{t_0}{\tau}\right)^n \frac{1}{n \cdot n!} \left[\left(1+\frac{t}{t_0}\right)^n - 1\right] \right\} \\ &\quad -\tau \left[1-\mathrm{e}^{-t/\tau}\right]. \end{aligned} \tag{3.4}$$

The avalanche characteristic time t_0 was calculated to be 0.1 ns for CH_4 gas.[22] This calculation neglects effects such as signal propagation along the wire according to the Telegraph equations, and the propagation through the chamber's strip-line feedthrough.

Simulations and measurements (see Section 3.4.4) indicate that the major effect of the positive ions is to produce a slower pulse with respect to a delta function response. Also, since the positive ion response has a significant tail, the tail of produced pulse is higher than $t\exp(-t/\tau)$. Therefore, the CRID preamplifiers were tuned to have a small undershoot in the tail of their response, bringing down the tail of the overall shape. Therefore, the shape coming from the CRID preamplifiers for single electron events still is described well by $t\exp(-t/\tau)$, although the τ is not directly that of the preamplifiers.

3.3 Deconvolution Algorithm

The basic algorithm is as follows. The signals from the inner and outer channels of a particular wire are deconvolved separately, using possibly different time constants. Then, pulses are found using a simple threshold search on the sum of the deconvolved signals. Finding pulses by using the sum of the data from the two ends of the wire, instead of using each end separately, removes the systematic affect on efficiency due the location of the avalanche along the wire; that is, the efficiency will depend on the total amplitude of the pulse instead of the amplitude of the larger of the two signals. Once found, a hit is classified by how many samples are over threshold, and each case (up to 6) is treated separately. If the hit has 1, 2, or 3 samples high, it is considered to be a single pulse; 4, two pulses of 2 samples each; 5, two pulses of 3 each, where there is some overlap; and 6, two pulses of 3 each. For each pulse, the ratio of two consecutive deconvolved samples is compared to a pre-generated look-up table in order to interpolate the pulse's start time and to correct the amplitude for start-time dependent effects. Empirically, it was found that hits with greater than 6 samples over threshold were very rarely due to real pulses (they are generally due to cross-talk effects) and therefore the algorithm ignores these and continues looking at the data as if it had not found anything.

The algorithm must deal properly with the true pulse shape coming from detectors and amplifiers. The amplifiers have a finite frequency response which smears the leading edge of the pulse. Also, the positive ion response discussed in Section 2.5 alters the shape; however, the shape is still well approximated by $t\exp(-t/\tau)$, especially with the introduction of a small undershoot in the tail of the amplifier response. These effects are the reason that a hit with 3 samples above threshold is considered a single pulse. (There are certainly cases where two pulses overlap very closely and produce 3 samples above threshold, but, mathematically, these cannot be dis-entangled.)

The look-up table, which tabulates the relationship between sample ratio and start time, is used to correct for known deviations in pulse shape. The table is calculated by generating pulses using the best information about their shape and deconvolving them to find bucket ratios and amplitude correction factors. When pulses deconvolve to 3 samples, both pairs of ratios are tabulated to provide redundant information. In principle, each amplifier should have its own table, but memory constraints mean that each amplifier is classified as one of a small set (10-20) of representative cases.

Another method for dealing with a pulse shape different from $t\exp(-t/\tau)$ is to tune the constants used to deconvolve the data. The deconvolution Equation (3.1) can written in a general form as

$$d_i = r_i - C_1 r_{i-1} + C_2 r_{i-2} \tag{3.5}$$

where, nominally, the deconvolution constants, C_1 and C_2, are given by

$$C_1 = 2\mathrm{e}^{-T/\tau} \quad \text{and} \quad C_2 = \mathrm{e}^{-2T/\tau}. \tag{3.6}$$

In practice, however, C_1 and C_2 can be varied independently to maximize the performance of the algorithm when the pulse shape is slightly different from nominal. The measure of the "performance" used to find these constants is the amount of deviation from zero in the tail of a deconvolved pulse. For an analytic model for the true pulse shape, the deconvolution of that shape can be defined to be

$$d(t) = r(t) - C_1 r(t-T) + C_2 r(t-2T). \tag{3.7}$$

If the error, E, in the tail is defined as

$$E = \int_{3T}^{\infty} |d(t)| \mathrm{d}t, \tag{3.8}$$

then the deconvolution constants are found by minimizing E with respect to C_1 and C_2. The integral is started three sample intervals from the start of the pulse because it may not be possible to deconvolve the pulse into only two non-zero buckets and, if so, it is preferable to minimize any oscillations away from the main body of the pulse.

The biggest complication for the pulse finding algorithm is minimum ionizing particles (MIPs) which pass through the drift boxes. MIPs can leave many hundreds of electrons in the box which then drift into the detector over tens of nanoseconds. This leads to extremely large, long pulses which saturate the electronics (see Figure 3.3). The pulse finding algorithm recognizes MIP hits by the saturation. About the only thing it can do with them is to record the approximate start time and wire number, since it generally only sees one non-saturated sample. A (very) rough charge division calculation can be performed by using the length of time each amplifier saturates as a relative estimate of the amplitude.

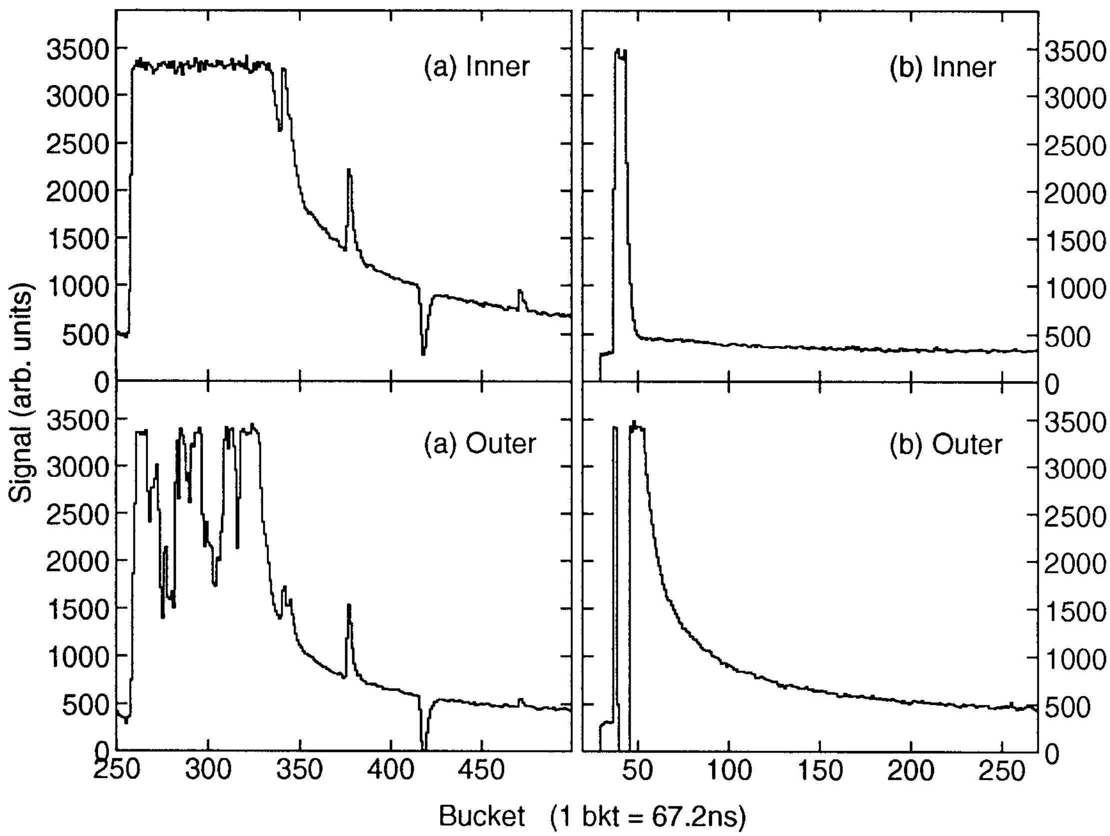

Figure 3.3: Two typical MIP signals in CRID data. The signals from both ends (inner and outer) of the wire are shown.

Since the CRID is not directly interested in MIP hits, the important issue is the recovery of the amplifiers and pulse finding afterward. The tail of a MIP hit can be very long; some last for 200 samples, equivalent to half a drift box. Also, while many decrease smoothly from saturation, others come out of saturation, go quickly negative, rebound positive and then decrease slowly to zero. Because of the length of the tails, it is important that the algorithm try to find any pulses there. It first finds the last saturated sample and continues work 3 samples later. From that point until the end of the snip (*i.e.* a section of data after zero suppression), it maintains pedestals which try to follow the tail. This works fairly well, although there are cases where it finds extra, generally small, pulses after a MIP hit.

Another effect of minimum ionizing particles is cross-talk. The extremely large pulses coming from MIPs lead to negative cross-talk signals in all other wires of a detector. This is very difficult to deal with because, to properly correct it, one needs knowledge of the source pulse amplitude and time. Since the algorithm is designed to work on only a single wire at a time, with no knowledge of other wires, cross-talk effects are not corrected by the deconvolution algorithm. One important effect which the algorithm attempts to deal with is the effect of the negative cross-talk pulses on pedestals. When the algorithm is maintaining pedestals, it can be fooled by cross-talk into producing an incorrectly low pedestal, resulting in fake pulses being found when the cross-talk recovers. Code was added to the algorithm to reduce the probability of calculating pedestals in the region of cross-talk pulses.

3.4 Tests of Pulse Finding

The following sections describe tests that were performed on the deconvolution pulse finding algorithm. They were done using the detector test setup described in the Section 2.5 and with early, prototype hybrid electronics. The signals were digitized using a LeCroy ICA with a sampling time of 20 ns and every third sample was used, resulting in a sampling interval of 60 ns. It needs to be stressed that these results were obtained before the final amplifiers were built and that, at the time, the deconvolution algorithm was in its infancy.

3.4.1 Charge Division

The charge division resolution was tested using the standard detector test setup and voltages (*e.g.* ethane gas and $V_c = -1.55kV$). Previous to the test, the resolution had been measured at

$$\frac{\sigma_y}{l} = 0.72\,\% \qquad \text{Amplitude Algorithm}$$

where l is the length of the wire (10.0 cm), with a pulse finding algorithm which summed 10 raw data samples to get an amplitude. Note that the routine included amplifier calibrations which were not used for the deconvolution test (the constants were different). With the deconvolution algorithm, the resolution was measured as

$$\frac{\sigma_y}{l} = 0.80\,\% \qquad \text{Deconvolution Algorithm}$$

In addition, the lamp source was moved by 22.5 mm, as measured by the stage micrometer. The charge division measurement indicated that the beam had been moved by 22.7 mm, well within errors caused by the impedance of the amplifiers.

3.4.2 Double Pulse Resolution

The deconvolution algorithm allows pulses right next to each other in the data to be found. Theoretically, pulses can be resolved when they are separated by just over one sample interval (for these tests, 60 ns) when the start times are aligned most favourably with the samples, and just under two sample intervals in the least favourable alignment. Therefore, we expect to be able to resolve two pulses separated by 1.5 sample intervals about 50% of the time. The situation is complicated by the fact that the real pulses have a tendency to appear as three high buckets in the deconvolved data, but hopefully this is a small effect.

Two types of tests were performed to measure the double pulse resolution: a set of tests where the "pulses" were provided by edges of known amplitude and separation from two pulsers, and one test with pulses from the detector test setup running with the UV lamp aperture opened up.

The test using the pulsers provided information about the resolution at known time separations and pulse amplitudes, but one thing must be kept in mind; the pulser edges were sent into the input stage of the amplifiers and therefore the pulse shape was not the true chamber shape (no positive ion effect). The pulsers were set up such that one pulser fired the other after some variable time delay (measured on a scope). The amplitudes were initially set equal at a value which produced a "typical" pulse height. Then, either the first or the second pulse was attenuated to investigate the effect of different pulse heights.

The results are shown in Figure 3.4. Figure 3.4a plots the efficiency to find the second pulse versus the time separation between the two for equal amplitudes,

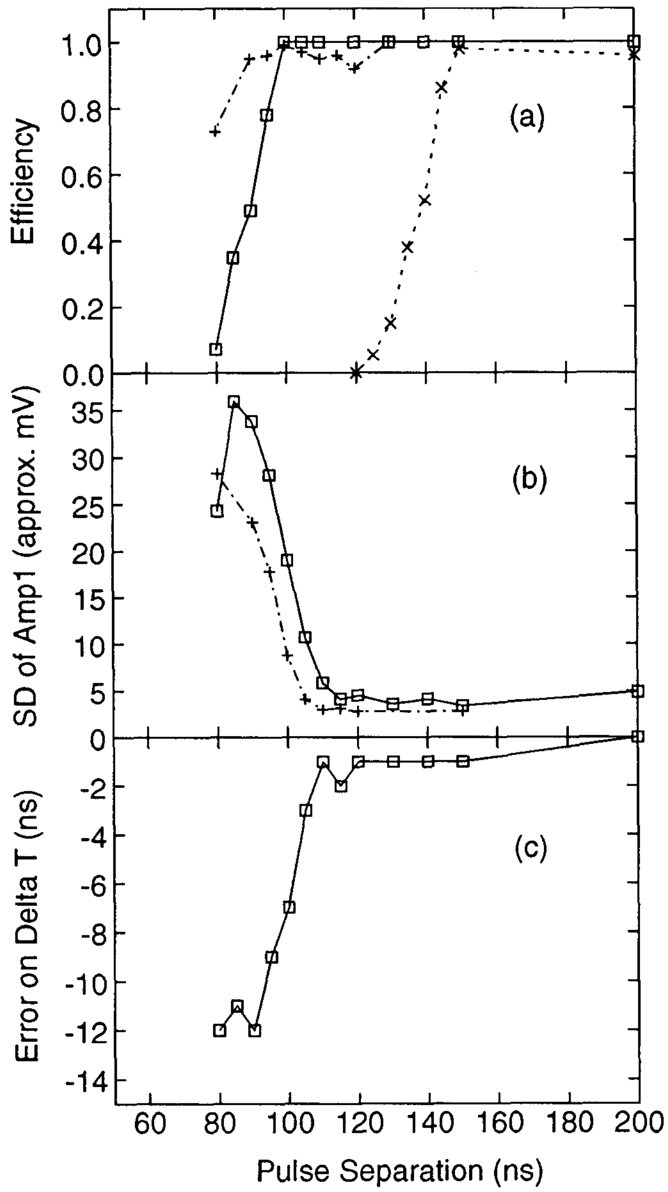

Figure 3.4: Results of the double pulse tests on the deconvolution algorithm: (a) the double pulse efficiency, (b) the spread of the measured amplitude of the first pulse, and (c) the error on the measured time separation for $Ampl = Amp2$ (solid line and $\square$), $Ampl = 10 \times Amp2$ (dots and $\times$), and $Ampl = 0.1 \times Amp2$ (dot–dash and $+$).

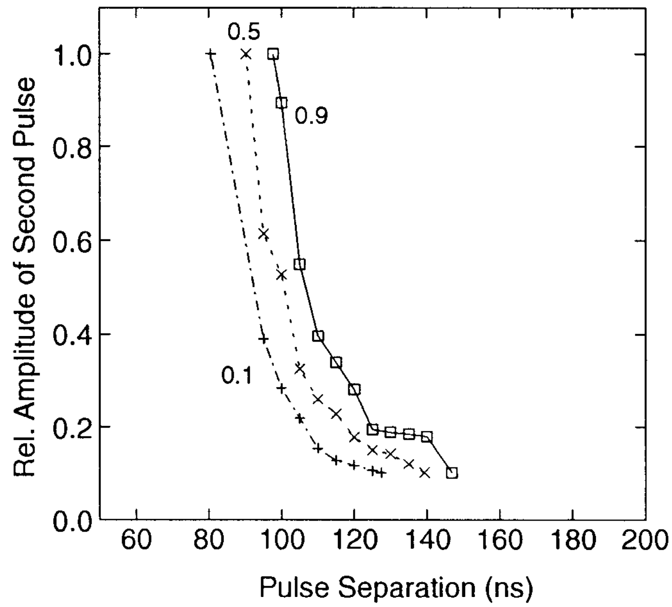

Figure 3.5: Contours of double pulse finding efficiency versus log amplitude ratio and pulse separation.

$Amp1 = 10 \times Amp2$, and $Amp2 = 10 \times Amp1$. It shows that apart from cases where the second pulse is much smaller than the first pulse, we do not lose a significant number of double pulses until they are closer than 100 ns. The efficiency for finding a small pulse following a big one may be better than that shown because the amplifier pulse undershoots in the tail, decreasing the amplitude of any trailing pulse. Figure 3.4b shows the spread of the measured amplitude for the first pulse for equal pulses and for a small initial pulse. This plot shows that even though we may not be losing pulses until 100 ns, the accuracy of the pulse amplitude starts to decrease at about 110 ns separation. Figure 3.4c shows the error in the measured pulse separation for equal amplitude pulses, and it indicates a similar degradation in accuracy.

The test using real pulses from a detector was accomplished by opening all the apertures in the UV lamp all the way. Events in which two pulses were found were accumulated in a plot of log amplitude ratio versus time separation; Figure 3.5 plots contours of efficiency versus log amplitude ratio and pulse separation. On

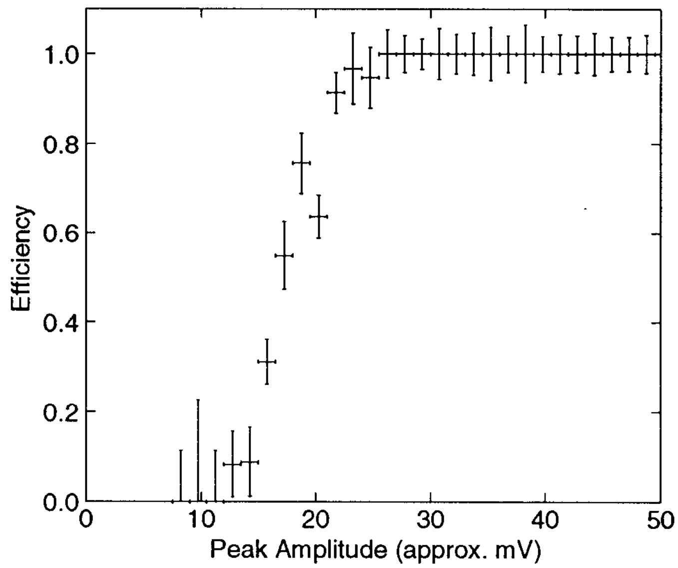

Figure 3.6: The efficiency for finding single pulses versus pulse size. The errors are the 90 % confidence limits.

average, the efficiency falls to 50% at 80 ns separation. If the time error measured in the test using the pulsers applies to these pulses, this should be increased to about 90 ns.

The results of both these tests indicate that the deconvolution algorithm performs as expected. In general, double pulses are not lost until about 100 ns separation, but errors start to increase below about 110 ns. The situation is worse if the second pulse is small, but little can be done about this.

3.4.3 Small Pulse Efficiency

The efficiency for detecting small pulses was measured by moving the UV lamp in the detector test setup as far toward one end of the wire as possible. Then, pulse finding was done independently on the sum on the two ends and and on the small amplitude end only. The two rates were compared as a function of pulse amplitude. Figure 3.6 plots the efficiency for finding the small pulse versus pulse amplitude. The results show that small pulses are found down to 20 mV.

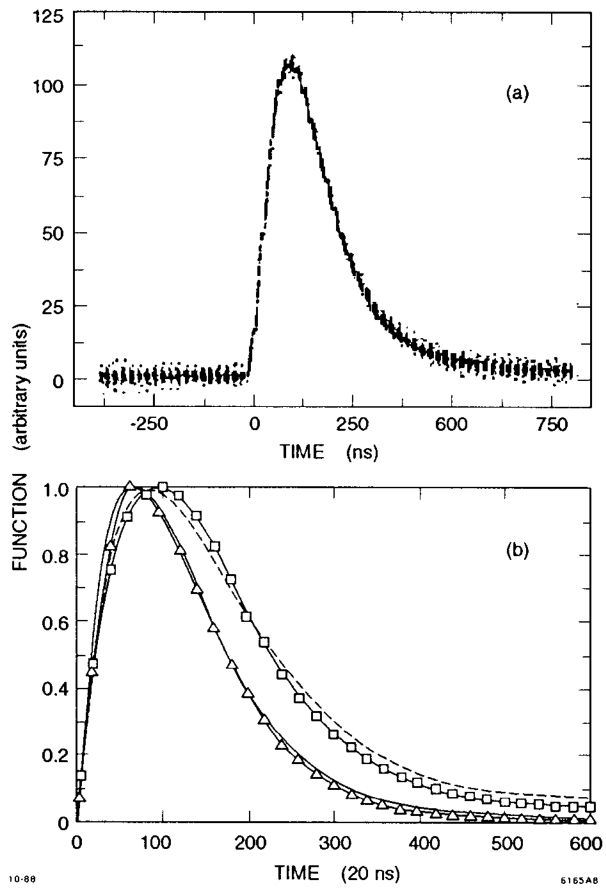

Figure 3.7: (a) The average single electron pulse shape from the prototype amplifier. (b) Comparison of the amplifier shape (△) with the calculated amplifier response $t\exp(-t/\tau)$, $\tau = 65\,\mathrm{ns}$ (solid line), and the single electron shape (□) with its calculated shape using Equation 3.4 (dashed line).

In interpreting this result, it should be pointed out that the deconvolution algorithm has a threshold which was set at approximately this level during the test. A deconvolved bucket must be above a certain cutoff (which was set to 10 amplitude units $\simeq 10\,\mathrm{mV}$) to be found as a pulse. The pulse amplitude is generally found by adding two buckets which are above the threshold and multiplying by a correction factor which is close to 1. Therefore, the software pulse threshold was approximately $20\,\mathrm{mV}$ for this test.

3.4.4 Pulse Shape

Figure 3.7 shows two measurements of the pulse shape from the prototype amplifiers using the detector test setup. Figure 3.7a shows many superimposed pulses which come from single electrons which were drifted into the detector. Figure 3.7b shows the amplifier and the detector pulse shapes and fits to these shapes. The amplifier response was measured by injecting charge into the front end of the amplifier via a 1 pF capacitor. The amplifier response is fit with the expected $t\exp(-t/\tau)$, yielding a time constant $\tau = 65\,\mathrm{ns}$. The single electron shape was fit with Equation 3.4. The figure shows that the agreement with the measured pulse shape is quite good, except in the tail region. This may be due to a slight undershoot in the amplifier response. The shape can also be fit fairly well by a simple $t\exp(-t/\tau)$, where $\tau \simeq 80\,\mathrm{ns}$.

3.5 Pulse Shape Calibration

The goal of the pulse finding algorithm is to deconvolve the pulse shape from the data, producing a delta function-like signal. This permits easy determination of the pulse's parameters (amplitude and start time), and allows for good separation between close pulses. In order to accomplish this, it is crucial that the true pulse shape be known. This is not straightforward for the CRID because of the positive ion effect. As mentioned earlier, the bare amplifier pulse shape is modified by the slow drift of positive ions in the chamber. Therefore, it is important to use pulses which come from real photo-electrons to determine the pulse shape.

From the early tests described in the previous section, it was known that, even with the positive ion effect, the CRID pulse shape is approximated very well by $t\exp(-t/\tau)$. The biggest deviation from this shape is in the tail of the pulse. The positive ions produce a significantly higher signal in the tail than can be fit while still fitting the leading edge. To help this situation, the electronics were tuned to add a small amount of undershoot to the amplifier shape to bring down the tail faster. Since this may not necessarily completely correct the shape, a second

$t\exp(-t/\tau_s)$ shape is added to the shape model, where τ_s is long, approximately 150–200 ns, with a small amplitude relative to the major shape.

Another deviation of the true pulse shape from nominal is due the maximum frequency response of the amplifiers. In order to follow the turn-on of a $t\exp(-t/\tau)$ shape, the amplifiers need a flat frequency response up to around 1 GHz. This would have been prohibitive for the CRID due to cost and space. To take into account the limited frequency response of the amplifiers, the pulse shape is smeared by averaging the nominal shape over a time interval, t_{sm}, which reflects the overall response time of the amplifier.

An analytic formula for this pulse model can easily be found. Smearing one $t\exp(-t/\tau)$ gives

$$p(t,\tau,t_{sm}) = \frac{1}{t_{sm}} \int_{t-t_{sm}/2}^{t+t_{sm}/2} \mathrm{d}t' \begin{cases} 0 & t' \leq 0 \\ (t'/\tau)\exp\left(-t'/\tau\right) & t' > 0 \end{cases} \tag{3.9}$$

The result of carrying out the integral is

$$p(t,\tau,t_{sm}) = \begin{cases} 0 & t \leq -t_{sm}/2 \\ \frac{\tau}{t_{sm}} - \left(\frac{t+\tau}{t_{sm}} + \frac{1}{2}\right)\exp\left[-\frac{t+t_{sm}/2}{\tau}\right] & -t_{sm}/2 < t \leq t_{sm}/2 \\ \left(\frac{t+\tau}{t_{sm}} - \frac{1}{2}\right)\exp\left[-\frac{t-t_{sm}/2}{\tau}\right] - & \\ \left(\frac{t+\tau}{t_{sm}} + \frac{1}{2}\right)\exp\left[-\frac{t+t_{sm}/2}{\tau}\right] & t_{sm}/2 < t \end{cases} \tag{3.10}$$

The model used to fit the CRID pulses is therefore,

$$S(t) = p(t,\tau,t_{sm}) + a_s p(t,\tau_s,t_{sm}), \tag{3.11}$$

where a_s is of the order of a few percent and τ_s is about 150 ns.

To fit the CRID pulses, it is necessary to deal with more than one pulse at a time. Since the pulses from photo-electrons come at an arbitrary start time with an arbitrary amplitude, there are 6 parameters needed to fit a single pulse; however, because the sampling interval is about the same as the pulse τ, there are only about 4 or 5 samples above noise on a single pulse. Therefore, the method chosen was to

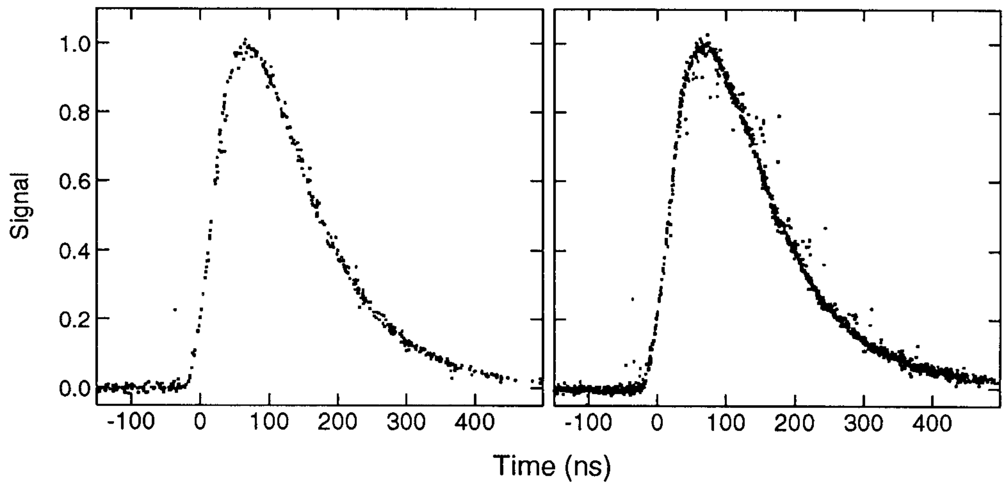

Figure 3.8: Two typical CRID single electron pulse shapes. The plots are produced by overlaying several, large amplitude pulses produced by photo-electrons.

fit sets of 5 pulses at once. For five pulses, there are 14 parameters and around 30 data points, leaving about 15 degrees of freedom. Cuts are made on the amplitude of pulses used in order to reduce the effect of noise. The correlation between the amplitudes and start times of each pulse found by the shape calibration and by the pulse finding algorithm can be used to check that the calibration is correct.

Figure 3.8 shows two typical pulse shapes produced by overlaying many pulses; large amplitude pulses were used to provide a clean shape. The shapes are fit quite well by the pulse shape model.

Figures 3.9 and 3.10 show the distributions of t_{sm} and τ_s, respectively, from one TPC. One problem experienced while performing the shape calibration is that both t_{sm} and τ_s are not well determined. t_{sm} is mostly determined by data points which fall very near the start of the pulse, and these points are generally small and affected by noise. The secondary $t\exp(-t/\tau_s)$ is only a few percent as big as the primary and is relatively very broad. Therefore, t_{sm} and τ_s were fixed at their approximate average values, 65 ns and 170 ns, respectively, before performing the calibration on the whole CRID.

Figure 3.11 shows the distribution of the primary pulse time constant, τ, versus the amplitude of the secondary shape, a_s, for the CRID amplifiers. The plot clearly

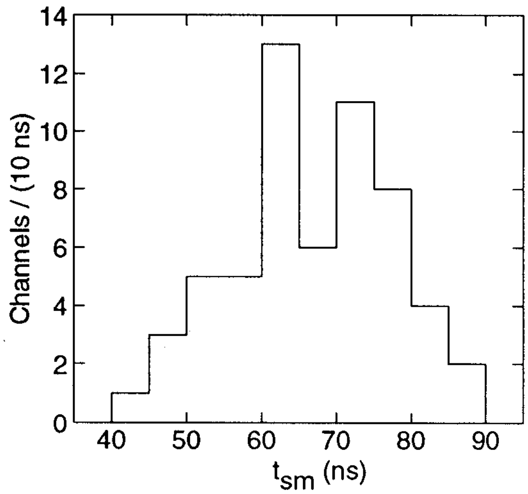

Figure 3.9: The distribution of pulse smoothing times, t_{sm}, from the shape calibration routine.

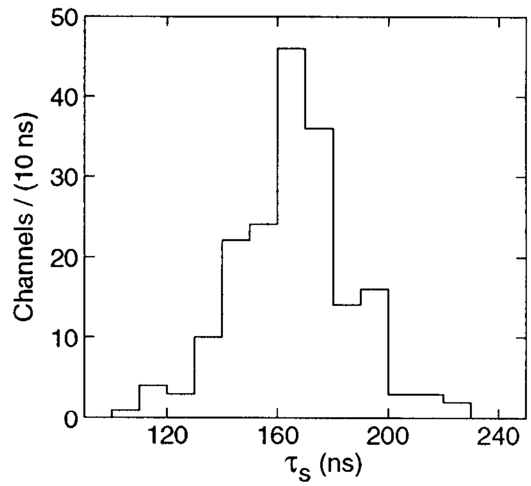

Figure 3.10: The distribution of pulse secondary time constants, τ_s, from the shape calibration routine.

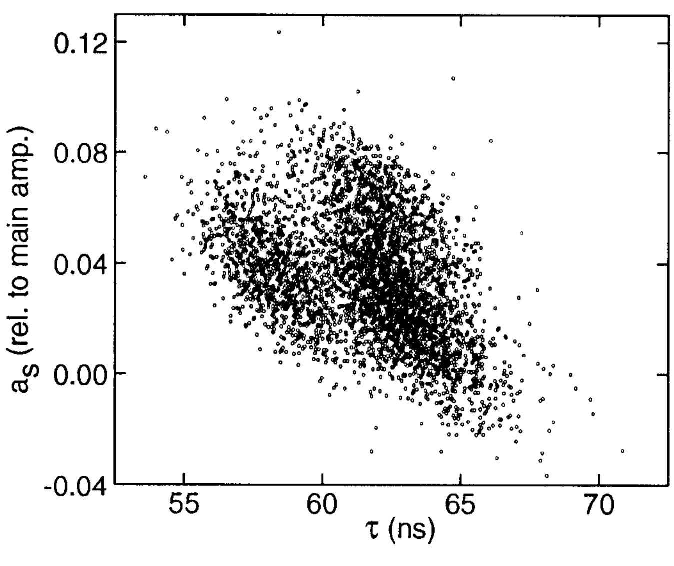

Figure 3.11: The distribution of pulse time constant, τ, against the amplitude of the secondary shape, a_s.

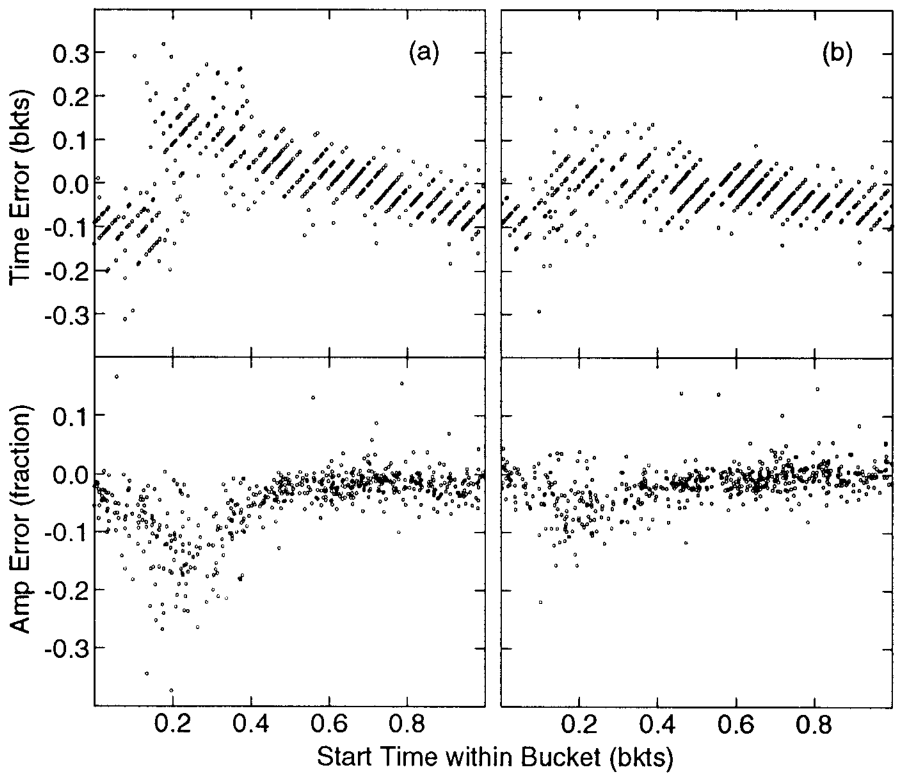

Figure 3.12: The result of the pulse shape calibration. Figure (a) shows the error in pulse start time and amplitude as a function of start time within 1 bucket before calibration. Figure (b) shows the same data with the calibration applied for the same amplifier.

shows three groups of points. If the co-ordinates are rotated by approximately $-0.5°$, the clusters become round, with dimensions approximately the same as the uncertainties of the co-ordinates. Therefore, the amplifiers were classified as belonging to one of the clusters. All amplifiers were assigned the τ and a_s of the center of the cluster.

Figure 3.12 shows the effect of the calibration on the results of the pulse finding. Figure 3.12a shows the error in the measured start time and amplitude as a function of the start time within one bucket for one amplifier before the calibration. Here, "error" is defined as the difference between the calibration fit number and the pulse finding number. The striping in the time error plot is due to the granularity of the start time from the pulse finding algorithm. Figure 3.12b shows the same data with the calibration applied in the pulse finding. The plot clearly shows that the errors have decreased by a factor of about 2. There is still some error; however, it would be impossible to remove all errors on all amplifiers since the shapes are categorized into a small number of representative shapes.

3.6 Preliminary CRID Results

Cherenkov rings have been observed in the CRID in both cosmic ray events and events from SLC collisions. The trigger for the cosmic events was provided by the Warm Iron Calorimeter.

Figure 3.13 shows integrated "full" and "half" rings from the liquid radiators due to cosmic ray muons and hadronic Z^0 decays. "Full" and "half" rings are distinguished by the angle between the track and the normal to the liquid radiator, "half" rings having an angle greater than 11.5°. This angle is essentially the same as the angular limit for total internal reflection in the quartz window of the liquid radiator. A track is used if its momentum is greater than 2 GeV/c, there are associated dE/dx hits in the TPC, and, for the hadronic events, the track is linked to data in the SLD Vertex Detector. To produce these plots, the positions of photons in the TPCs of interest are mapped into spherical co-ordinates using the measured track as the z axis. Signals are not used if they are believed to come from dE/dx hits or associated cross-talk, or if they are in the outer half of the TPC (the gas radiator side).

Figure 3.13 shows a clear signal from Cherenkov rings for both "full" and "half" rings. The additional background in hadronic events is due to the many other tracks and soft particles inside jets. The bands of hits to the right of the main ring in the "half" ring plots are due to Cherenkov photons emitted in the quartz window of the liquid radiator. The lack of hits near the centers of the plots is due to cuts against cross-talk signals.

The event and hit selection criteria described above, apart from the cut on track momentum, are also used to produce Figure 3.14. The photons remaining after the cuts are fit, in angle space, to a circle plus background, with the radius

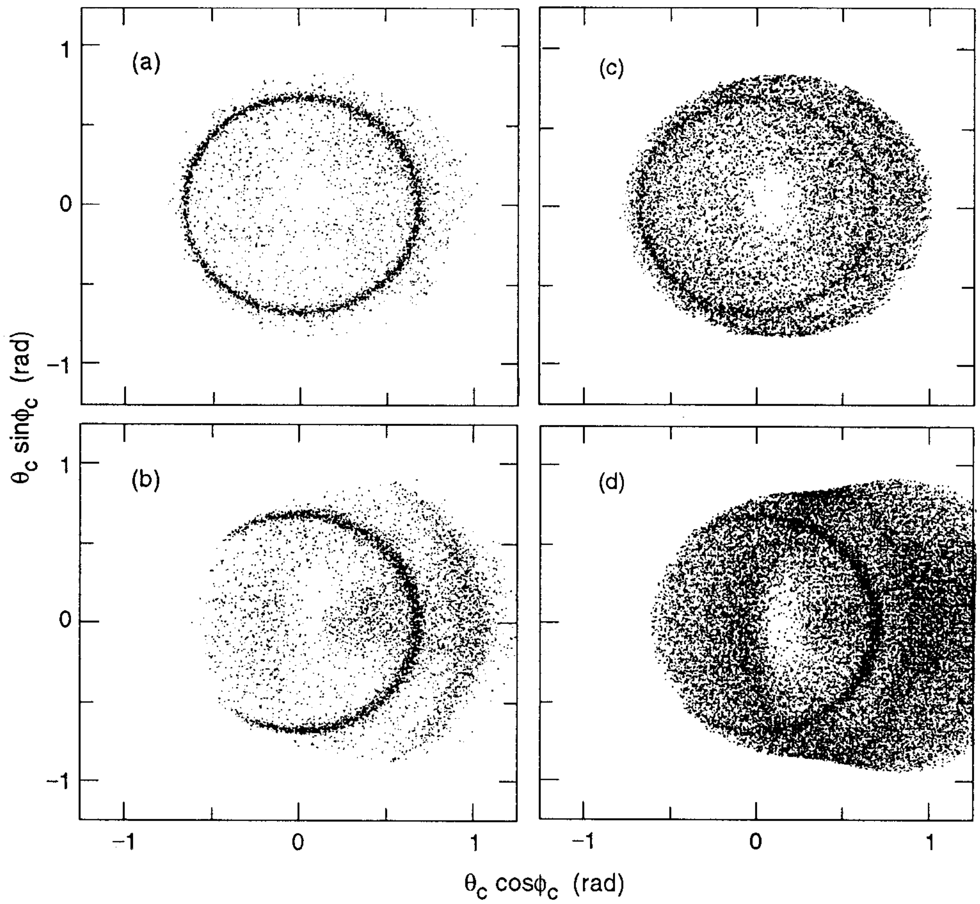

Figure 3.13: Preliminary integrated liquid rings in the CRID: (a) "full" and (b) "half" rings from cosmic ray muons, and (c) "full" and (d) "half" rings from hadronic Z^0 decays.

and center of the circle free. Figure 3.14a shows the fitted angular radius of the rings versus log momentum for tracks from hadronic decays. Clear bands due to pions, kaons and protons are visible. Figures 3.14b and 3.14c show the projections along radius for two different momentum ranges, giving some idea of the resolution and particle separation.

Figure 3.15 shows integrated Cherenkov rings from the gas radiator. A fit similar to that used for the liquid rings was performed to find the radius and center of the rings. Figure 3.15a shows the superimposed rings, 3.15b the radial projection of these hits, and 3.15c the distribution of number of hits per ring.

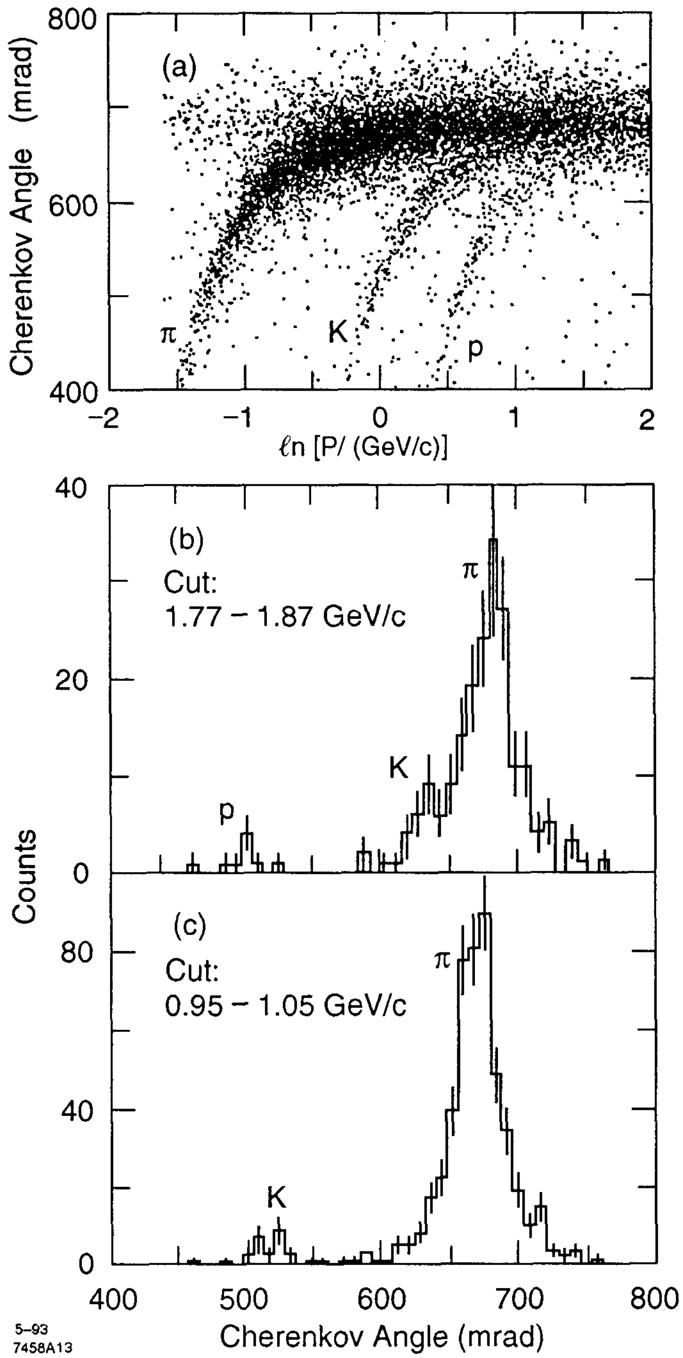

Figure 3.14: A preliminary demonstration of the particle ID ability of CRID. Data points are from fits to individual rings, which removes many systematic effects.

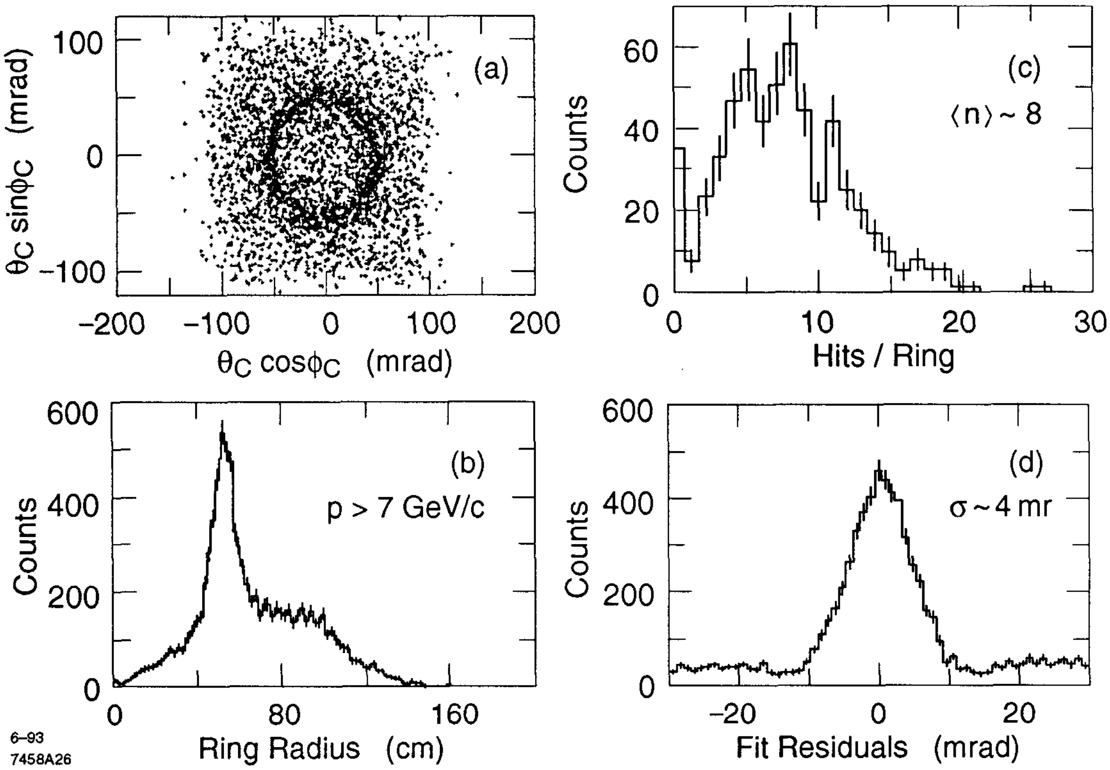

Figure 3.15: Preliminary results from CRID gas rings from Z^0 decays: (a) integrated rings, (b) angular radius of hits in (a), (c) number of photons per ring, and (d) local resolution of radius.

Figure 3.15d gives the local resolution of the radial co-ordinate; the plot shows the distribution of hit residuals from the fitted radius, accumulated over many rings.

The fits to the liquid and gas rings have shown that the CRID is performing up to design specifications in many respects. The resolution on a single ring is $\Delta\theta_C \sim 12$ mrad for the liquid rings and $\Delta\theta_C \sim 4$ mrad for the gas, quite close to the design parameters. The number of measured photons is about 16 for the liquid rings and 8–9 for the gas. However, the systematic errors are still large. The resolution measured over many tracks implies a systematic error of 10–15 mrad in the liquid rings and about 10 mrad in the gas rings. These errors are mostly likely caused by misalignments of the various components of the CRID, *i.e.* liquid radiators, TPCs, and mirrors.

Work on understanding the CRID is continuing. Efforts are continuing to try to understand and measure the alignment of all the elements of the CRID detector. Also, efforts are underway to understand and tune the maximum likelihood algorithm which is intended to produce the full particle ID information from the CRID.

Chapter 4

Light Quark Meson Spectroscopy

There are a number of reasons to study light quark meson spectroscopy, the study of mesons composed of u and d quarks. Table 4.1 shows a possible quark-model assignment for many of the well established resonances, as suggested by the Particle Data Group.[30] The light quark mesons have been studied for many years and the ground states are very well established, but many of the isovector excited states and their quark-model assignments are not well determined. While the known strange meson spectrum does not contain any extra states, the isovector sector has too many resonances to fit into the quark model. Also, higher mass states of the light quark system, such as the radial excitations, are quite poorly known when compared to the $c\bar{c}$ and $b\bar{b}$ systems.

The light quark meson spectrum is an important test of QCD potential models. While such relatively simple models like that of Godfrey and Isgur[31] work fairly well, they do not yet provide a complete picture of the meson spectrum. Mesons containing heavy c and b quarks involve short distances and low internal velocities, and therefore probe the interquark potential in the region where the Coulomb-like potential is most important. On the other hand, mesons composed of light quarks involve relatively large distances and high velocities. Thus, they probe the potential where QCD confinement is important. Also, relativistic effects on the motion of the quarks often have to be taken into account. Therefore, the

$N\,^{2S+1}L_J$	J^{PC}	$u\bar{d}$, $u\bar{u}$, $d\bar{d}$ $(I=1)$	$u\bar{s}$, $d\bar{s}$	$c\bar{c}$	$b\bar{b}$
$1\,^1S_0$	0^{-+}	π	K	η_c	
$1\,^3S_1$	1^{--}	ρ	$\mathrm{K}^*(892)$	$J/\psi(1S)$	$\Upsilon(1S)$
$1\,^1P_1$	1^{+-}	$b_1(1235)$	$\mathrm{K}_{1\mathrm{B}}$		
$1\,^3P_0$	0^{++}	$a_0(980)$	$\mathrm{K}_0^*(1430)$	$\chi_{c0}(1P)$	$\chi_{b0}(1P)$
$1\,^3P_1$	1^{++}	$a_1(1260)$	$\mathrm{K}_{1\mathrm{A}}$	$\chi_{c1}(1P)$	$\chi_{b1}(1P)$
$1\,^3P_2$	2^{++}	$a_2(1320)$	$\mathrm{K}_2^*(1430)$	$\chi_{c2}(1P)$	$\chi_{b2}(1P)$
$1\,^1D_2$	2^{-+}	$\pi_2(1670)$			
$1\,^3D_1$	1^{--}	$\rho(1700)$	$\mathrm{K}^*(1680)$	$\psi(3770)$	
$1\,^3D_2$	2^{--}		$\mathrm{K}_2(1770)$		
$1\,^3D_3$	3^{--}	$\rho_3(1690)$	$\mathrm{K}_3^*(1780)$		
$2\,^1S_0$	0^{-+}	$\pi(1300)$	$\mathrm{K}(1460)$	$\eta_c(2S)$	
$2\,^3S_1$	1^{--}	$\rho(1450)$	$\mathrm{K}^*(1410)$	$\psi(2S)$	$\Upsilon(2S)$
$2\,^3P_2$	2^{++}		$\mathrm{K}_2^*(1980)$		$\chi_{b2}(2P)$
$3\,^1S_0$	0^{-+}	$\pi(1770)$	$\mathrm{K}(1830)$		
$3\,^3S_1$	1^{--}			$\psi(4040)$	$\Upsilon(3S)$
$4\,^3S_1$	1^{--}				$\Upsilon(4S)$

Table 4.1: A summary of some of the quark-model assignments for known mesons as suggested by the Particle Data Group.[30] Some of the assignments, particularly in the isovector sector, are uncertain.

light meson spectrum is a strong test of a potential model's treatment of QCD confinement and long distance effects.

Finally, knowing the complete meson spectrum is important when searching for new physics. Any search for exotic states, such as glueballs, hybrids, and four quark states, requires extensive knowledge of the non-exotic states. This is due to the nature of such a search, where the regular mesons are background, possibly having the same quantum numbers as the exotic.

Light quark spectroscopy studies have significantly different challenges when compared with those involving c or b quarks. While experiments studying charmed or bottom mesons frequently find only 10's of events from a particular meson, light quark mesons are generally produced copiously. However, heavy quark mesons mostly have very narrow decay widths (less than 100 MeV/c^2 and typically a few MeV/c^2) and are reasonably well separated in mass. Light quark mesons, on the other hand, are mostly quite broad (150–500 MeV/c^2) and generally overlap each other significantly. Therefore, it is very important to analyse the events in a manner which separates different spin components, such as by performing a Partial Wave Analysis (PWA). This provides definite identification of a particular resonance and allows the extraction of small cross section components in the region of dominant resonances.

Chapter 5

The LASS Facility

The Large Aperture Superconducting Solenoid (LASS) spectrometer was built and operated at SLAC through 1982. An overview of the detector is shown in Figure 5.1 and a complete description has been published elsewhere.[32] The spectrometer consisted of two main sections, the solenoid spectrometer and the dipole spectrometer, which in combination, provided almost complete coverage of the full 4π solid angle in the laboratory frame. Slow moving particles were well reconstructed in the solenoid section, while fast, small angle particles were measured by the dipole spectrometer.

The solenoid spectrometer had a 22.4 kG magnetic field, produced by a four-coil superconducting magnet with an internal diameter of 1.9 m and length of 4.2 m. The dipole spectrometer used a conventional aluminum magnet which provided a maximum field of 18.0 kG and a field integral of 30.1 kG-meters through a 1 m tall gap. The pole pieces were 1.8 m wide and 1.1 m along the beam direction. The hydrogen target inside the solenoid measured 85.04 cm in length by 2.54 cm in radius when warm.

Charged particle tracks in LASS were measured using a combination of cylindrical proportional wire chambers (PWCs) and planar PWCs in the solenoid region, and magnetostrictive spark chambers and planar PWCs in the dipole region.

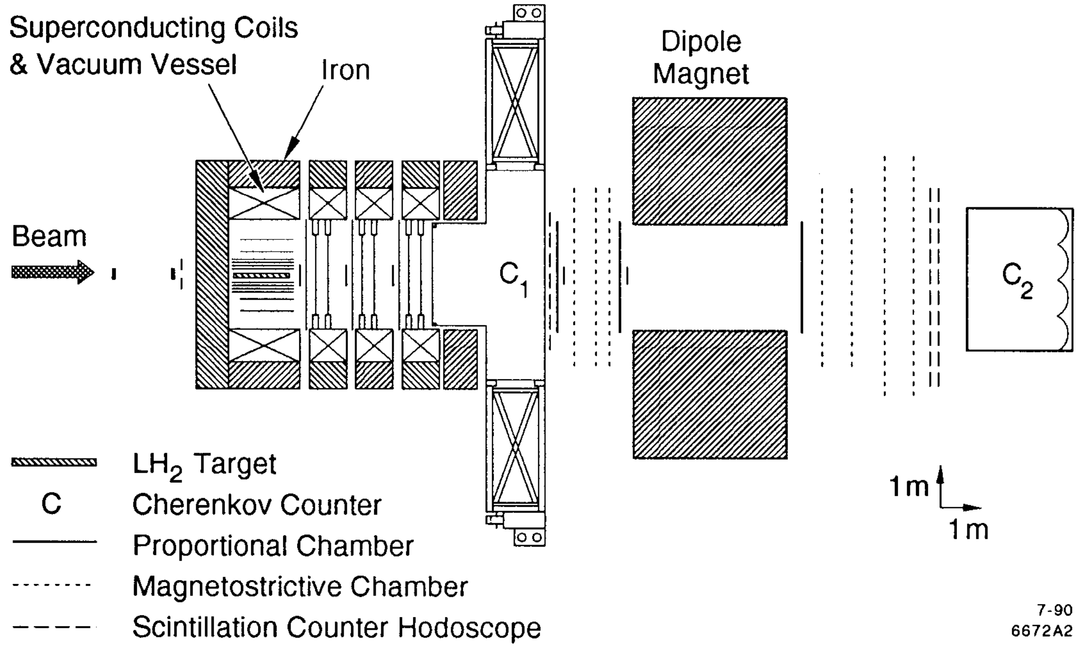

Figure 5.1: The LASS spectrometer. The incident beam direction, the solenoid with the target, the Cherenkov counters, and the dipole chambers are shown.

While the kinematics and topology of an event can strongly constrain the possible identity of the particles in that event, there are certain types of events, *e.g.* events with high momentum tracks, where specific particle identification is invaluable. Because of this, a great deal of particle identification hardware was built into the spectrometer. Particle identification was accomplished using two threshold Cherenkov counters, a time-of-flight (TOF) system, and dE/dx measurements in the cylindrical wire chambers.

The experiment described here, SLAC E-135, took data in several runs during 1981 and 1982 using both K^- and K^+ beams; however, only the K^- data were used in this analysis. There were 1.4×10^8 triggers recorded, with about 4 times as many K^- as K^+ events. The event reconstruction was performed at SLAC and Nagoya University in Japan. It was finished in 1985, requiring the equivalent of about two CPU years on SLAC's two-CPU IBM 3081K, and produced about 1,000 data summary tapes.

5.1 LASS Beamline

The 11 GeV/c kaon beam used in this experiment was produced by colliding 21 GeV/c electrons from the SLAC linear accelerator with a copper and beryllium production target. Electromagnetic showers in the target produced a host of secondaries, of which those within a 17.45 ± 3.85 mrad production angle were collected. The initial optics limited the particle momentum spread to 2.5%. Electrons were removed with 0.56 radiation lengths of lead absorber. Then, the beam passed through two radio frequency separators, where different particle species received different deflections because of their different arrival times. After the RF separators was a collimator which selected the desired particle species, namely kaons.

Following the separator section, the beam momentum was measured using six overlapping scintillator paddles positioned at a momentum-dispersed focus. The momentum was measured to within 0.5% full width. Further along the beamline, 13.1 m from the solenoid, the position of the beam was measured with another array of scintillators. The array was composed of 24 1/2" wide paddles, twelve oriented horizontally and twelve vertically.

Next in the beamline were two gas-filled, threshold Cherenkov counters. The C_π device was filled with 40 psia of hydrogen gas, in which only pions could radiate. The C_K counter was filled with carbon dioxide at 75 psia, and both pions and kaons produced light. It was found that the RF separation resulted in a kaon purity of $\sim 95\%$ for the 11 GeV/c K^- beam.

Just prior to the LASS solenoid was a set of proportional wire chambers to determine the beam position and direction. The package consisted of ten planes of PWCs, each built with sixty-four 20 μm diameter gold-tungsten sense wires spaced at 1.016 mm. The upstream set consisted of four planes, horizontal, vertical and at $\pm 45°$ to the vertical; while the downstream had six, two horizontal, two vertical and two again at $\pm 45°$. The second horizontal and vertical planes in the downstream set were offset by half the wire spacing from the first planes. The two sets were separated by 1 meter. This package measured the beam position to within 300 μm and direction to 0.3 mrad.

A set of three scintillators formed the last pre-target device. The first, SE, located 5 meters from the solenoid, served to count both beam particles and halo particles, where halo is any in-time, off-axis particle. It generated the start pulse for the time of flight system and other fast electronics, and was made especially thick (0.952 cm) to reduce time jitter in the output pulse. The SY and the R counter comprised the final beam tag. R had a 2.54 cm hole at its center to serve as a beam halo veto.

The beam in the target had an RMS size of 0.5 cm in each direction. The spills were 1.6 μsec long, and typically ran at a 90 Hz repetition rate. The yield was about 4–5 kaons per pulse, giving a trigger rate of approximately 16 per second, averaged over the entire experiment.

5.2 Liquid Hydrogen Target

The liquid hydrogen target cell provided the initial state protons for the experiment. At room temperature, the cell was 85.04 cm long and 2.54 cm in radius, and shrank to 84.06 cm when full of liquid H_2. The hydrogen was captured in a mylar bag, which was surrounded by mylar super-insulation inside of an 0.71mm thick aluminum vacuum jacket. It was supported by steel bracing to the upstream mirror plate of the solenoid. The liquid H_2 condition was monitored for temperature and pressure, as the target density was very important for determination of the experimental interaction cross section. The 2.54 cm radius of liquid H_2 implied that protons had to have at least 225 MeV/c to escape to the vacuum jacket, if they started on axis and propagated radially; this was a consequence of the $0.0716 \pm 0.0004\,\mathrm{gm/cm^3}$ mean liquid H_2 density measured over the course of the experiment.

5.3 Solenoid Spectrometer

The solenoid spectrometer is shown in Figure 5.2. The region was composed of the superconducting magnet, the cylindrical chambers, the gap, plug, bore and trigger

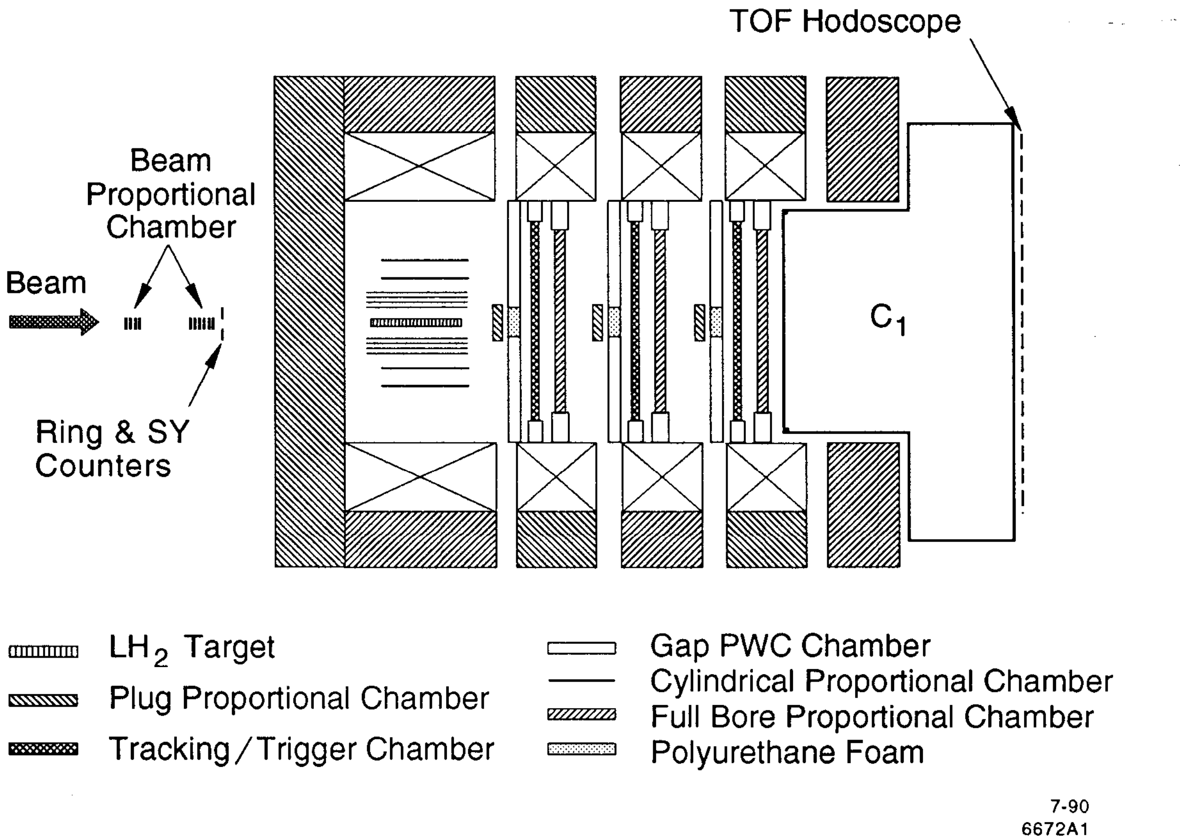

Figure 5.2: The solenoid magnet and interior components of LASS. The cross-hatched areas represent the solenoid itself, with the target and tracking chambers shown in appropriate relation. The kaon beam was incident from the left (upstream) end.

planar chambers, plus the Cherenkov counter C_1 and the time-of-flight hodoscope. Each is discussed below.

5.3.1 Solenoid Magnet

The magnet consisted of four separate superconducting coils, where the first segment held the cylinder package, and the three downstream pieces supported tracking chambers. The operating current of 1600 Amps generated an axial field of 22.4 kG, requiring 5000 liters of liquid helium from two local refrigeration units at 60 ℓ/hr in normal operation for cooling. The axial magnetic field component was measured to be uniform to 1% over the full inner diameter of 185 cm for the entire 465 cm length. The radial component was negligible on axis, becoming significant near 300 cm downstream, because of the downstream opening into C_1. A fiducial region was defined where the average field variation was less than 3.1%, with a radius of 75 cm and length of 320 cm.

5.3.2 Cylindrical Vertex Detector

There were six cylindrical proportional wire chambers, arranged to be coaxial with the target, with radii measuring 6.05, 9.55, 12.99, 16.55, 29.41, and 49.02 cm. The chambers consisted of a central anode wire plane of $20\,\mu$m diameter gold-plated tungsten wires, sandwiched between inner and outer layers of cathode strips. The anode wires were anchored to fiberglass circuit boards and had Lucite support rings halfway along their lengths. The cathode strips were made of an aluminum/mylar laminate and honeycomb paper core. They made $\pm 10°$ angles to the anode wires over 100 cm of active length in the inner four PWCs and $\pm 15°$ angles for 87 cm in the outer pair of chambers. The outer pair of chambers were recessed 7 cm from the upstream solenoid mirror.

Although it was not designed for it, the cylindrical detector was eventually used to measure dE/dx energy loss of slow-moving particles, providing an additional particle identification method. The signal strength from the cathode foils was used to measure energy loss for tracks of 600 MeV/c or less. There were noticeable effects from pulse saturation in the gas-filled chambers; nevertheless, correlating the measured ionization from several cylinder measurements per track provided useful particle identification information.

5.3.3 Planar Chambers

Each of the three downstream segments of the solenoid was instrumented with a gap, bore, plug, and trigger chamber ensemble. The gap chambers were single planes which cover the solenoid inner diameter. There were 758 anode wires strung 2.032 mm apart. The cathodes, made of aluminum-mylar laminate, were

6.86 mm wide strips 1.27 mm apart oriented at ±45°. The cathode-anode spacing was 0.508 cm. A central 16.51 cm diameter was covered with a Styrofoam backed mylar barrier, which prevented any signal generation in the region. This was essential in order to prevent the busy axial region from confusing the off-axis tracking in these chambers.

The plug chambers recorded tracks in the deadened region of the gap chambers. There were actually 5 plug chambers in the spectrometer. There were three in the solenoid and two additional ones downstream. The plugs measured 26 cm by 28 cm, and had 256 anodes at a 1.016 mm spacing. Each chamber had three anode planes, oriented horizontally, vertically and 35° to horizontal. These chambers worked well in the high-rate (5–10 MHz instantaneous) environment near the spectrometer axis.

The bore chambers provided track measurements inside, as opposed to between, magnet segments. There were three planes totalling 640 sense wires at a 2.032 mm pitch, with a 0.406 cm cathode–anode spacing. These chambers had octagonal frames, to maximize the tracking coverage inside the magnet sections.

The trigger chambers were originally intended to measure the track multiplicities for the event trigger; in the end, they primarily provided more redundancy in the tracking. Each chamber consisted of an anode and two segmented cathode planes. The anodes provided only the electric field, and as such were widely spaced at 4.064 mm. The upstream, or tracking, cathode, had two concentric rings of pads defined on it, 8 pads in the interior and 128 in the outer ring. The downstream, or trigger, cathode was more coarsely divided into 16 pads in the outer ring, with the same 8 inside. The trigger foil of the most downstream chamber was not read out.

5.3.4 C_1 Cherenkov Counter

The C_1 Cherenkov counter was inserted into the last of the four solenoid coils, filling the coil aperture, and extending downstream. The counter was a conventional gas threshold device using Freon 114 at atmospheric pressure. The threshold for pions was $\approx 2.6\,\mathrm{GeV/c}$, and for kaons $\approx 9.2\,\mathrm{GeV/c}$. The total path length in the counter was at least 180 cm, which implies that a fast pion could generate a cone of Cherenkov light of nearly 2 cm in radius at the end of the radiating volume. The volume was segmented into 38 cells, arranged into 2 small D-shaped cells on axis, and three concentric rings, each of 12 30° cells. The cells did not extend over the full length of C_1, but began 40cm from the upstream end. This design meant that a radiating particle could emit into more than one cell, even though the track passed through only one cell.

Each cell roughly focussed the incident light onto a mirror which reflected the light at right angles through a Fresnel lens, a collection horn, and onto a photomultiplier cathode. The phototubes were RCA 8850 Quantacons, magnetically shielded with μ-metal and iron jackets, plus a set of bucking coils, so as to correct for the strong fringe magnetic fields (about 2–4 kG) of the solenoid. Because of interference with the floor, the three bottom cells of the three rings had a different optical arrangement. Unfortunately, the horns for these cells proved to be somewhat inefficient at light collection, degrading the performance of these cells.

The performance of the counter was studied using pions from $\overline{K}^0$ decays. A particle trajectory was extrapolated through the Cherenkov counter in the presence of the solenoidal field. The expected pattern of Cherenkov emission for the track was calculated and then compared with what was actually observed. A careful study showed that the average efficiency of the device was 0.975 for particles above threshold, improving to 0.995 for tracks which radiated exclusively into a single cell.

5.3.5 TOF Hodoscope

The TOF hodoscope was used in conjunction with the SE upstream scintillator to determine the time a particle took to traverse the solenoid. The hodoscope consisted of 24 15° wedge paddles surrounding a set of four on-axis 90° scintillator segments. Each scintillator was 1 cm thick, and was optically connected to a Lucite light guide consisting of a light pipe, an elbow, and a Winston cone. The guide terminated at a photomultiplier tube, which was magnetically shielded similarly to the C_1 tubes. The tubes were read out by both an analog-to-digital converter (ADC) and a time-to-digital converter (TDC).

A signal from the SE counter started the TDCs. When the scintillation light from a passing particle was sensed in a phototube, the attached TDC was stopped and the pulse height recorded by the ADC. The pulse height information was used to correct the observed time for "time walk" in the readout electronics. The resulting resolution on the TOF measurement was $\approx 0.5\,\text{ns}$. The expected times for mass hypotheses of π, K, and p, as calculated based upon the track momentum and point-of-origin, was compared to the measured time in order to determine a probability for the hypothesis. Both times were corrected for transit time of the light in the scintillator and for dispersion. In this fashion, $\approx 3\sigma$ separation is found for π/K up to momenta of $\approx 1.1\,\text{GeV/c}$, and π/p to $\approx 2.5\,\text{GeV/c}$.

5.4 Dipole Region

The downstream half of LASS consisted of the 18 kG dipole magnet and sets of magnetostrictive and proportional chambers. This spectrometer measured the momentum of particles within 50-100 mrad of the beam axis which have $p > 1.5\,\text{GeV/c}$. The dipole region is shown in Figure 5.3.

Tracks in the dipole region were measured by a combination of magnetostrictive chambers and proportional counters located as shown in Figure 5.3. The magnetostrictive chambers generated the majority of the coordinates for the track finding in the LASS dipole region, and the technology provided a cost-effective means for obtaining good accuracy and high efficiency over a large area.

5.4.1 Dipole Magnet

The magnet was a water-cooled aluminum pancake, built of four stacked coils, which drew up to 7050 A at full field. At this excitation, an 11 GeV/c particle would develop about 900 MeV/c of transverse momentum, due to the 30.1 kG-m

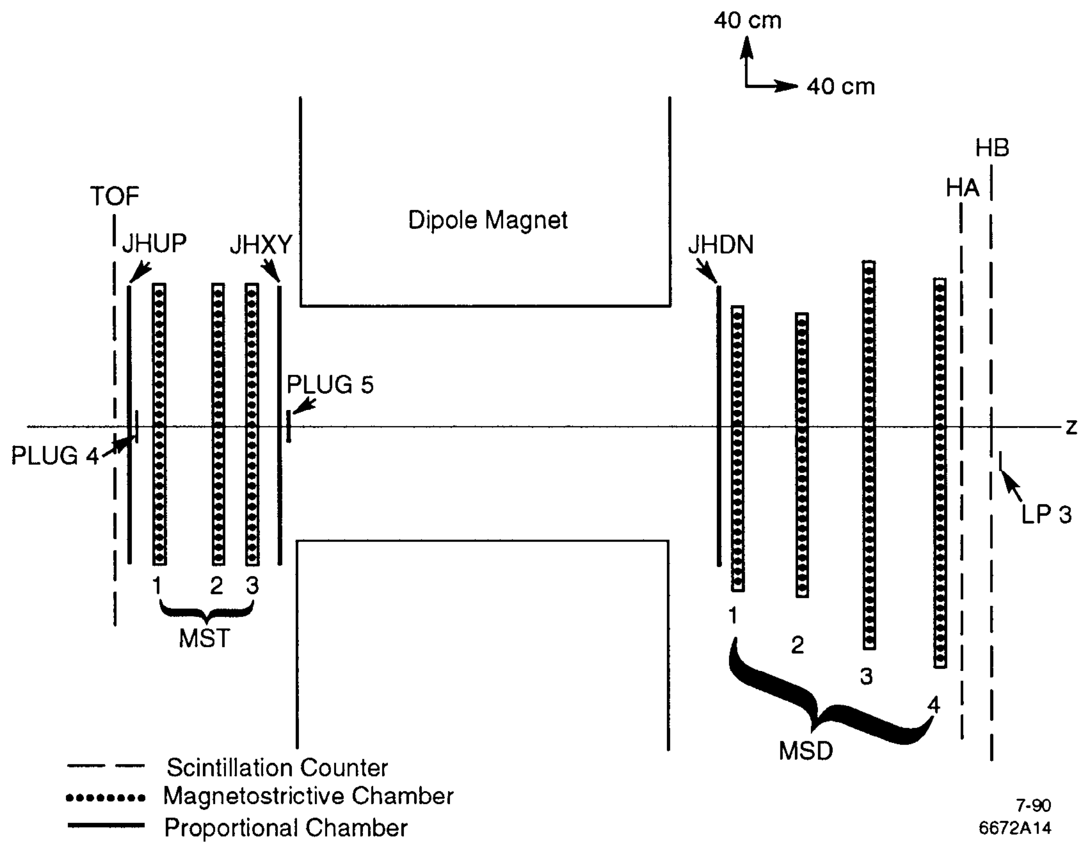

Figure 5.3: The dipole region of LASS. The magnet, chambers, and scintillation hodoscopes are shown.

field integral along the beam-axis. The magnet was operated at full field for better than half of the experiment, and about 2/3 strength for the remainder.

5.4.2 Dipole Chambers

A magnetostrictive chamber is a spark chamber read out with a special magnetostrictive wire which efficiently converts the electrical energy of a spark into a travelling acoustic pulse. The spark chamber consisted of two planes of woven wire cloth separated by 1 cm. One plane was kept at high voltage, the other at ground. When an event trigger was received, a high-voltage pulse was generated by a thyratron amplifier, so that a spark was created by any ionizing radiation in the gap. The induced current pulse on the wire cloth was transferred as an acoustical signal on a magnetostrictive wire wand. The wand was connected to a multi-hit TDC, which recorded the arrival times of the full set of sparks from the trigger and stored it for subsequent readout.

The first five chambers were 150 cm by 300 cm, and the most downstream pair of "super-chambers" were 200 cm by 400 cm. The upstream gap in each chamber determined the x and y coordinates, while the downstream gap was read out at $\pm 30°$ to the normal. There were polyurethane plugs installed on axis in order to deaden the spark gaps in the high flux region around the beam. The downstream chambers were displaced so that the dipole-bent beam would pass through the plugs.

There were two readout wands per chamber, reading out opposite sides of the chamber, except for MSD1 and MSD2 (see Figure 5.3) which had only one wand each. Also, each wire plane had two fiducial wires placed along the side of the plane. The fiducial wires were pulsed by the trigger and used to calibrate the time scale for each event. The full pulse train for the event was digitized, stored and read out via CAMAC. The digitization was performed with a 20 MHz clock, translating into roughly 0.27 mm spatial resolution for the x and y planes.

The magnetostrictive readout scheme had to be compensated for stray magnetic fields, which could have been large. It was necessary to magnetically bias the wands of the upstream magnetostrictive chambers. A separate coil of wire was wrapped around each wand to help alleviate the problem. However, it was still observed that the upstream chambers were less efficient than the downstream ones.

5.4.3 Johns Hopkins Proportional Wire Chambers

The proportional chambers shown in Figure 5.3 were built at Johns Hopkins University, and consisted of a single plane of 512 vertical wires with a 4.23mm wire spacing. The aluminum and polyester mesh cathodes of JHUP and JHDN were built with a 1.27 mm gap width, while the JHXY segmented aluminum-mylar foil cathode was made of 128 2.62 cm wide horizontal strips at a 0.16 cm gap width. These counters provided in-time corroboration and position information for dipole tracks, though the JHXY cathode efficiency was only about 50% and of limited use.

5.4.4 Scintillator Hodoscopes

The HA and HB scintillator arrays were immediately downstream of the last magnetostrictive chamber. Each counter consisted of two rows of scintillator paddles, with 21 paddles per row in HA and 38 per row in HB. The center paddles in each array were vertically displaced so that non-interacting beam particles did not generate signals. Each paddle was 83.82 cm long. These counters triggered the spectrometer electronics on events with dipole particles and provided in-time corroboration of tracks for track reconstruction. A small circular counter, the LP3 counter, of 9.84 cm radius situated over the central hole in the hodoscope array, functioned as an anti-coincidence counter, helping to ensure that there were no downstream beam tracks in a real event.

5.4.5 C_2 Cherenkov Counter

The final apparatus in the LASS spectrometer was the venerable C_2 threshold Cherenkov counter. It was used to aid in π/K separation for fast dipole tracks. The counter was divided into 8 segments, and filled with 1 atmosphere of Freon 12 (CCl_2F_2). Particles traversed a 2 mm thick aluminum sheet and at least 175 cm of gas. Two rows of four mirrors tilted at 10° from the vertical were used to reflect radiated photons through light pipes into XP2041 photomultipliers. There were four phototubes at the top of the counter and four at the bottom.

The threshold for pions in the counter was 2.9 GeV/c and for kaons 10.3 GeV/c. However, the geometry and magnetic environment of the unprotected photomultipliers moved the thresholds up, on the order of 10% for the π's.

5.5 E-135 Trigger

In order to be able to study the widest variety of physics in the experiment, the event trigger requirements were kept quite minimal. The basic requirement was that a beam particle interact in the target and produce at least two charged secondaries, thus effectively triggering on the full K^-p cross section into charged particles. In addition, a few special purpose triggers were used to monitor the spectrometer. The trigger can be broken into two pieces, the beam trigger and the cluster logic, described below.

5.5.1 Beam Trigger Logic

An acceptable beam particle was identified whenever the beam trigger logic determined that an incident beam particle was a kaon, that the particle entered the target, and that there was no other beam particle within ± 16 ns. A beam kaon must be identified as such by the beamline Cherenkov counters C_K and C_π (see Section 5.1). A candidate particle entered the target when signals from the SE and SY paddles were coincident and were anti-coincident with the halo veto counter R. The Θ–Φ hodoscope signals were used as fast timing signals to maintain a 16 ns trigger window.

In Boolean shorthand, the trigger logic definition was

$$BT = \Theta\Phi \geq 1 \textit{ and } \overline{\Theta\Phi \geq 2} \textit{ and } SE \textit{ and } SY \textit{ and } \overline{R} \textit{ and } C_K \textit{ and } \overline{C_\pi}. \tag{5.1}$$

5.5.2 Cluster Logic

The cluster logic determines when a viable target interaction was detected. By counting the number of hits on the anode wires in the innermost two cylindrical PWCs and the first two plug chambers, an event was recorded or discarded. The cluster count from each anode plane formed the logic signals of Table 5.1. All but the 32 central wires of plug 1 were ORed to generate the cluster multiplicities of Table 5.1, where the central wires are ignored as an additional safety against

Signal	Definition
$\mathrm{PLG}_1 \geq 1$	at least 2 of ($\mathrm{PLG}_1\ x \geq 1$, $\mathrm{PLG}_1\ y \geq 1$, $\mathrm{PLG}_1\ e \geq 1$)
$\mathrm{PLG}_1 \geq 2$	at least 1 of ($\mathrm{PLG}_1\ x \geq 2$, $\mathrm{PLG}_1\ y \geq 2$, $\mathrm{PLG}_1\ e \geq 2$)
$\mathrm{PLG}_2 \geq 1$	at least 2 of ($\mathrm{PLG}_2\ x \geq 1$, $\mathrm{PLG}_2\ y \geq 1$, $\mathrm{PLG}_2\ e \geq 1$)
$\mathrm{PLGS} \geq 1$	$\mathrm{PLG}_1 \geq 1$ *or* $\mathrm{PLG}_2 \geq 1$
$\mathrm{CYL} \geq 2$	$\mathrm{CYL}_2 \geq 1$ *and* ($\mathrm{CYL}_1 \geq 2$ *or* $\mathrm{CYL}_2 \geq 2$)
$\mathrm{CYL} \geq 3$	$\mathrm{CYL}_2 \geq 1$ *and* ($\mathrm{CYL}_1 \geq 3$ *or* $\mathrm{CYL}_2 \geq 3$)
$\overline{\mathrm{CYL} \geq 3}$	$\overline{\mathrm{CYL}_1 \geq 3 \textit{ and } \mathrm{CYL}_2 \geq 3}$
$\mathrm{CYL} = 2$	$\mathrm{CYL}_2 \geq 2$ *and* $\overline{\mathrm{CYL} \geq 3}$
$\mathrm{CYL} = 1$ or 2	$\mathrm{CYL}_2 \geq 1$ *and* $\overline{\mathrm{CYL} \geq 3}$

Table 5.1: The cluster logic signal definition. PLG and CYL denote plug and cylinder chambers, respectively. Counts are the number of hits in a chamber.

multiple beam triggers. Conversely, only the central wires of plug 2 were included. This allows for events with a single very forward track to be counted. Every signal as given in the table includes the requirement that cylinder 2 have at least 1 hit, because cylinder 1 had a large accidental rate. Finally, the $\mathrm{PLG}_1 \geq 2$ signal was relaxed after about 25% of the data were taken in order to improve the efficiency. Prior to the change, the requirement was that at least two (as opposed to one) of the planes had at least two hits.

5.5.3 Complete Event Trigger

The experiment used four physics triggers, $\mathrm{T0}_1$, $\mathrm{T0}_2$, $\mathrm{T0}_3$, and $\mathrm{T0}_4$, and four additional scaled triggers, T1, T2, T3, and T4, used for calibration and diagnostics. The trigger definition logic is shown in Figure 5.4.

Briefly, the separate trigger signals are:

- $\mathrm{T0}_1$ — ≥ 3 secondaries and 2 cylinder tracks.
- $\mathrm{T0}_2$ — 2 cylinder and 0 dipole tracks.
- $\mathrm{T0}_3$ — ≥ 1 forward and 1 or 2 transverse tracks.

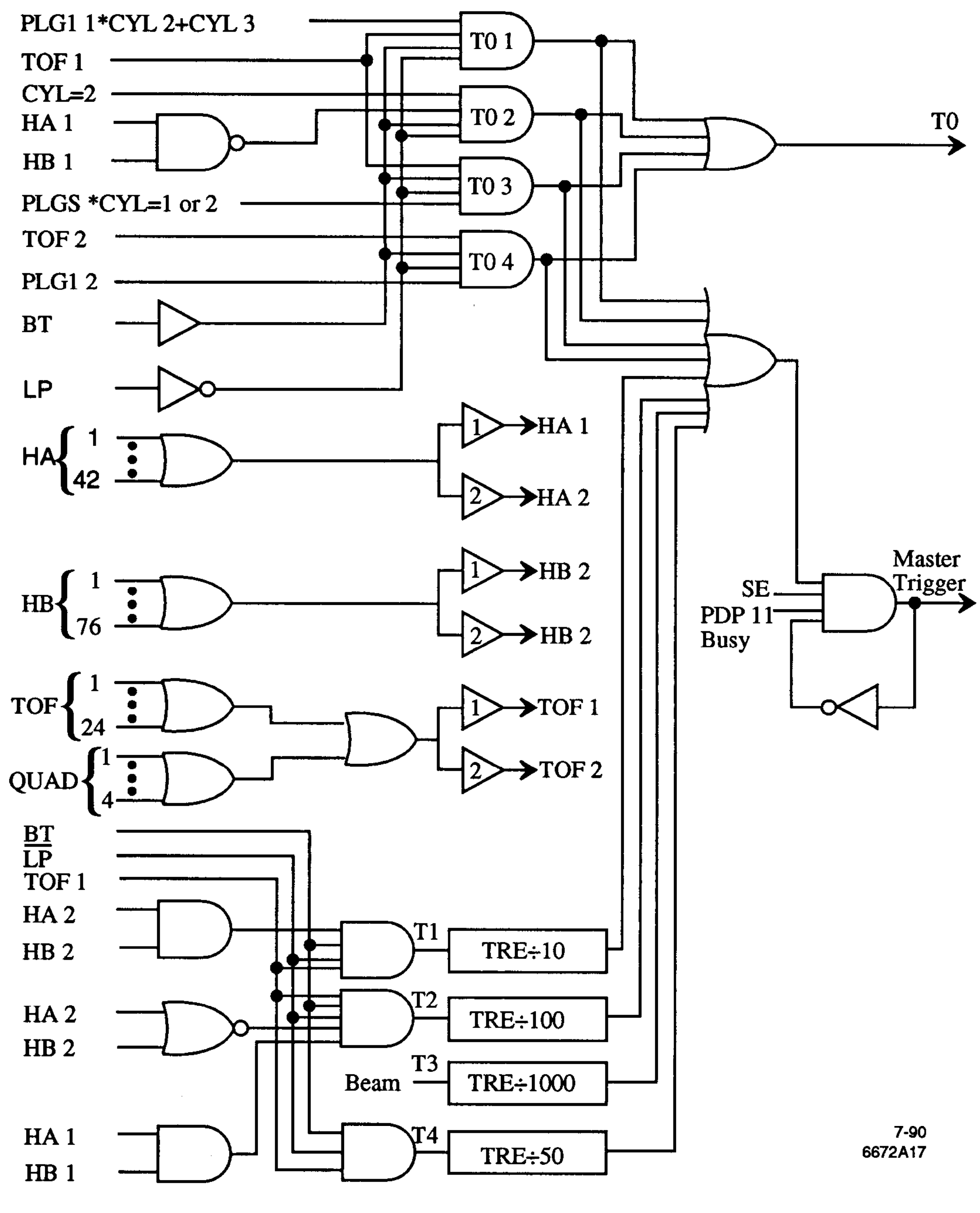

Figure 5.4: The complete trigger logic for experiment E-135.

- $T0_4$ — ≥ 2 forward tracks.
- T1 — beam decay trigger. The 3-prong decays of the beam kaons, known as "τ" decays, served as calibration monitors for the dipole magnet and the P-hodoscope, which measures beam momentum. Only 1 in 10 was recorded.
- T2 — elastic trigger. K^-p elastic scattering events were used for momentum calibration and studying track finding. Only 1 in 100 was recorded.
- T3 — random beam trigger. Only 1 in 1000 was recorded.
- T4 — random interaction trigger. Only 1 in 50 was recorded.

All trigger except T3 required an interacting beam track (BT and $\overline{LP}$). The random triggers, T3 and T4, were used to provide an unbiased event sample for Monte Carlo efficiency studies.

The trigger deadtime was driven by the time needed to clear the track ionization from the spark chamber gaps, about 15 ms, but could be larger for very high multiplicity events. On average, the detector was taking data 60% of the time that the beam was being delivered.

5.6 Data Acquisition

The data from the LASS electronics were read out through five CAMAC branches into a DEC PDP–11/04 minicomputer. From there, they were shipped via an IBM System 7 computer to the SLAC central computer center, where they were written to tape using one IBM 370 in the SLAC TRIPLEX computer system.* The data acquisition system was designed to handle about 50 events per second.

Although there were five CAMAC branches, only four were used at once. Data from the detector electronics were read into the device controllers for temporary storage until they were shipped to the PDP–11 using direct memory access (DMA). One CAMAC branch was dedicated to the hodoscope, TOF, Cherenkov

*The TRIPLEX consisted of a 2MB IBM 360/91, 2 3MB IBM 370/168s, 10 6250bpi tape drives, 4 IBM 5098 control units, and numerous disk drives and I/O devices.

counter and beamline electronics. Another handled the signals from the PWC anodes. A third controlled the cathode foil strip signals, and the fourth served the magnetostrictive chambers. The fifth branch served to monitor the voltage settings of some counters and to record the contents of some beam counting scalers.

On each event trigger, the PDP–11 read out the device controllers in parallel through the DMA branch drivers. When all the data had been transferred, the PDP formatted the new data for transfer to the System 7 computer. The System 7 computer sent the data to the TRIPLEX system over a 0.5 km coaxial cable.

The actual tape logging and the online monitoring of the spectrometer were performed on the TRIPLEX system. The tape logging procedure had the highest priority of any task. A background analysis program sampled the incoming event stream to provide single event plots and histograms of quantities such as multiplicity, chamber efficiencies, and missing mass.

5.7 Spectrometer Alignment

The measurement frame chosen for LASS was defined by the gap chambers, since they could be surveyed in situ most easily. The z positions were surveyed, and the anode wire locations were already known from precise bench measurements.

The other solenoid and dipole chambers are "found" relative to the measurement frame using straight line fits to tracks with the magnets turned off. The cylindrical chambers are located next by fitting tracks obtained with the magnets on. Tracks found in the planar chambers were projected back as helices, making allowances for the fact that chambers were not exactly round.

The beam chambers were aligned using T3 trigger events. The tracks in the plug and full-bore chambers were extrapolated into the beam chambers, and the beam chamber positions are adjusted until the residuals were acceptable.

The alignment of the magnetostrictive chambers unfortunately was found to vary on the scale of hours. The affect was traced to instabilities in the wands, and so the wand variations were carefully watched with a re-calibration made whenever the degradation was too severe, about once a week.

5.8 Spectrometer Calibration

The ADC electronics used throughout the experiment was subject to run–to–run variations over the length of data taking. These problems were due to pedestal fluctuations in the Cherenkov and TOF systems, and to both pedestal and gain changes in the cathode readouts. In the first case, 100 events at the beginning of each run were used to define the pedestals for the run. In the latter case, special calibration electronics was built into the channel amplifiers which permitted a set of calibration constants to be calculated at a greater frequency during runs.

The momentum calibration of the spectrometer was also monitored on a run-by-run basis. An absolute calibration was determined for the dipole, and the solenoid and P-hodoscope were calibrated relative to the dipole. The dipole calibration was obtained by reconstructing $K^0_S \to \pi^+\pi^-$ decays where at least one of the daughter π's went through the dipole magnet. The reconstructed $\pi^+\pi^-$ mass was compared to the real K^0_S mass, and the difference was converted to a dipole field scale factor, which was 1.007 for full field and 1.004 for half field. Also, elastic and "τ" triggers were independent sources of good dipole tracks. The elastic events, where the scattered K^- was dipole measured, provided a relative calibration between the P-hodoscope and the dipole at 11 GeV/c. The momentum dependence of the dipole calibration was checked using the slower π's from the "τ" decays.

A good measure of the run–to–run variations was found by summing the observed longitudinal momentum in a event and comparing it to the known beam momentum. Small shifts were observed and generally correlated to times were the downstream dipole chambers were moved to accommodate a change in the beam polarity.

5.8.1 dE/dx Calibration

To extract dE/dx information from the cylinder chambers, the pulse height information from the cylinder cathodes had to be understood. The seen pulse height, PH, is related to the ionization left by a track by

$$I = f_\theta \, PH \tag{5.2}$$

where θ is the angle defined by the track's momentum vector and the normal to the cylinder surface, and f_θ is the path length correction. If the cylinder package were homogeneous, f_θ would vary as $\cos\theta$, but there was an excess of signal as the tracks were more and more forward. There were saturation effects in the chamber which probably account for some of the increase, but the exact source of the effect is not known. Empirically, a quadratic polynomial in $\cos\theta$ was used to correct the pulse height.

The gas gain also affected the expected pulse height. An offline calibration for each cylinder was performed on a run-by-run basis using fast negative tracks. The velocity, β, dependence was measured using the protons from elastic events. The quantity $(f_\theta \, PH)^{0.3}$ was found to be approximately Gaussian. The β dependence of this quantity was parametrized with a quadratic. Using these parametrizations, a likelihood function for π/p was constructed. The overall likelihood was the product of the individual cylinder likelihoods.

5.9 Event Reconstruction

The event reconstruction code for the experiment consisted of three different stages: track finding, vertexing, and topology recognition. Each is discussed below.

5.9.1 Track Finding

The beam particles were measured by the beam chamber package. Often, there were several candidate beam tracks per trigger, and care had to be taken to insure that only the correct track was found. First, anode clusters were formed in the chambers and converted to spatial coordinates. Then, lists of possible matchpoints were formed for the upstream and downstream beam chambers, requiring that the time slot information for associated clusters be consistent. A beam track candidate was defined when a pair of consistent matchpoints from the upstream and downstream chambers was found. Candidates with the best timing consistency, a satisfactory number of coordinates along the track, and good agreement with the allowed beam phase space were kept. Finally, in-time corroboration with the $\Theta\Phi$ hodoscope and SY was required. Typically, there were 1.5 beam tracks per event in the data. Other found beam tracks in an event were usually due to non-interacting beam kaons which could also be found in the downstream dipole chambers. In that case, the relevant matchpoints were not used for any subsequent track finding.

Track finding in the solenoid region began by defining precise matchpoints in the gap chambers. Acceptable track candidates should trace out well-defined helices in the uniform magnetic field. Therefore, three matchpoints, each from a separate chamber, were chosen such that they were consistent with a helical trajectory. This track was used to look for corroborating matchpoints in the other solenoid chambers, where the search was done over areas defined by the estimated errors on the original matchpoints. Based on the total number of corroborating points found, a χ^2 fit to a helix was performed on the coordinates. The track was included in the list of solenoid tracks if the fit was acceptable (confidence level greater than 10^{-4}). The fit allowed for multiple scattering, assuming that the track is a π and that the scattering errors are uncorrelated. If the fit was poor, coordinates which contribute more than 12 to the χ^2 were be dropped and the track re-fit. This process was iterated until either too many track points were dropped or the fit succeeded. The procedure was repeated using all combinations of planar chambers, and then a similar procedure was carried out for the cylindrical package. The track finding efficiency is better than 99% in the solenoid region, as determined from Monte Carlo studies.

Tracks in the dipole region were found by first finding line segments in the region downstream of the magnet. Pairs of x-coordinates from two similar coordinate planes were found, and the segment was considered a candidate if it was corroborated by the associated spark gaps. The line segment was extrapolated into the other chambers, and if the number of found hits was acceptable, a least-squares fit to a common line was calculated. The fit was kept if the confidence level was $> 10^{-4}$. Line segments in the chambers upstream of the dipole were found by the same process. The full set of line segments from each side of the dipole was then crossed through the center of the dipole magnet. The upstream-downstream pair which was the best match for any track was selected, a first order estimate for the track momentum based upon the angle between the segments was made, and the estimate used to swim the downstream segment back through the dipole to the upstream piece. The process was iterated until the best angle through the field, *i.e.*, the most likely track momentum, was obtained. The momentum errors were based upon the chamber errors and the multiple scattering contribution.

Finally, the dipole and solenoid tracks were joined by finding a solenoid track which matched a dipole track and refitting the solenoid helix so that its momentum agreed with the dipole measurement. If the fit was successful, the original helix fit results were replaced with the new one. About 95% of the refits were successful, the failures arising primarily from "kinks" due to particle decay or large angle scatters.

5.9.2 Vertex Finding

An initial estimate of the primary vertex position in an event was made by taking the mean of the z co-ordinates of the points of closest approach of the tracks to the beam. Only tracks which passed within 1.5 cm of the beam and were in the vicinity of the target were included. The result was kept as the vertex position if the fit was reasonable ($\sum d^2$/degrees of freedom $< 1\,\mathrm{cm}^2$, where d is the distance of closest approach to the vertex). If not, the worst track was thrown out and a new vertex location calculated. This procedure rarely failed, except when there were two interactions in the target. To handle these cases, the tracks were split into an upstream and a downstream group if the track dropping failed. The group with the higher number of tracks was kept.

Topology	Description
1	single n-prong primary vertex
2	n-prong primary vertex and a V^0 consistent with a K_s
3	n-prong primary vertex and a V^0 consistent with a Λ or $\overline{\Lambda}$
4	n-prong primary vertex and a V^0 consistent with a γ
5	n-prong primary vertex and a $V^{\pm}$
6	n-prong primary vertex and 2 V^0s
7	n-prong primary vertex with a $V^{\pm}$ and a V^0
8	n-prong primary vertex with 3 V^0s

Table 5.2: The event topologies used in LASS.

Secondary vertices were found by making a list of all oppositely charged track pairs, including those associated with the primary vertex. Combinations were kept if they had a $\sum d^2 < 0.8\,\mathrm{cm}^2$ and a pair mass near the Λ, K^0 or γ mass when the appropriate track mass assignments were made. An additional list of charged vertex candidates was built by combining Λ and $\overline{\Lambda}$ candidates with π^- and π^+ tracks, respectively, and requiring the result to lie near the Ξ or Ω mass. $\Lambda\pi^-$ combinations were tried first and if a candidate was found, no attempt was made to find $\overline{\Lambda}\pi^+$ candidates. In order to reduce the combinatorial background, $V^{\pm}$ candidates were required to have a decay length of at least 1.0 cm.

5.9.3 Topology Recognition

After vertex finding, events were classified into various event topologies. The topology of an event refers to the configuration of vertices reconstructed by the tracking. Eight topologies, numbered 1 to 8, were used. They are described in Table 5.2. Each event was allowed to be interpreted as more than one topology, but a unique interpretation was assigned in each topology. Multiple interpretations in a given topology were resolved differently, depending on the topology.

For topology 1, one or two tracks were allowed to be dropped from the vertex if the original $\sum d^2$ per degree of freedom was poor. The track(s) which had the greatest impact on $\sum d^2$ per degree of freedom were dropped. For topologies 2, 3, and 4, one track was allowed to be dropped using the same criterion as for topology 1. Remaining ambiguities in topologies 2, 3, and 4 were resolved by additional criteria. First, if only one V^0 satisfied a tight mass cut, it was chosen. If not, the interpretation which used the most tracks was used, unless an interpretation using fewer tracks had a significantly better $\sum d^2$ per degree of freedom. In addition, for topology 3, the existence of a tight Λ interpretation automatically eliminated any $\overline{\Lambda}$ interpretation. Ambiguous interpretations in topologies 5, 6, 7, and 8 were resolved in a similar manner, and by maximizing the number of tight V^0s.

5.10 MVFIT

MVFIT is a multi-vertex fitting program that can enforce both geometric and kinematic constraints on the tracks present in an event. MVFIT uses the measured co-ordinates on the found tracks as the data to be fit. This distinction is important, because it is possible for a program which fits momenta to end up with a solution which seems good, but does not properly fit the co-ordinates.

MVFIT automatically applies a geometric constraint that forces all tracks in an event to emanate from the primary or secondary vertices present in the current interpretation of the event. In addition, MVFIT enforces three-momentum conservation at any secondary vertices. MVFIT can optionally enforce additional kinematic constraints on an event. In particular, MVFIT can enforce three-momentum conservation at the primary vertex, energy balance at the secondary vertices, and energy balance at the primary vertex. Momentum and energy balance at the primary vertex can be enforced with or without a missing neutral track.

MVFIT describes the data in terms of the following parameters:

- three-dimensional co-ordinates of the primary vertex.
- polar and azimuthal angle of each track helix, at the primary vertex.
- reciprocal of the momentum of each track, at the primary vertex.

- three-dimensional co-ordinates of each V^0 secondary vertex (the momentum of the V^0 is forced to be the sum of the momenta of the daughter tracks, and the V^0 momentum is forced to be in the direction of the line joining the primary and secondary vertices).
- path length of any $V^\pm$ track, along with the parameters of the $V^\pm$ track.

As a consequence of the parametrization, all tracks from the same vertex are forced to emanate from the same point.

The optional constraints are imposed through the method of Lagrange multipliers. Because of this, one additional parameter, the Lagrange multiplier, is added for each constraint. MVFIT uses χ^2 minimization, and employs a modified Newton–Raphson approach.[33] The equation to be minimized is

$$\mathcal{L} = \sum_i \left(\frac{x_i - x_{pred}}{\sigma_i}\right)^2 + 2\sum_j \lambda_j \mathcal{F}_j \tag{5.3}$$

where x_i and σ_i are the measured co-ordinates and uncertainties, x_{pred} the predicted co-ordinates, λ_j the Lagrange multipliers, and $\mathcal{F}_j$ the constraint equations. This function is expanded to second order about the point specified by the current values of the free parameters. The expansion is inverted to determine the point where the gradient of $\mathcal{L}$ is expected to vanish. The parameters are then assigned these new values, and the expansion is repeated. If the new parameters do not seem to have brought $\mathcal{L}$ closer to the minimum, the step size is decreased. The fit is said to have converged when $\mathcal{L}$ changes very little (typically less than 0.1), any energy balance constraint at a secondary vertex is fulfilled to a level of 0.1 MeV, and any energy–momentum constraints at the primary vertex are fulfilled to 20 MeV. The primary vertex constraint is imposed on the sum over all the constraint equations.

Fits usually converge in less than five iterations. Once the fit has converged, the χ^2 contribution from all co-ordinates is determined. If the point dropping option has been enabled, any co-ordinate with a χ^2 contribution greater than 12 is dropped and the fit is redone. This is repeated until no more points are dropped or more than 5 points have been dropped. In this latter case, the fit is considered to have failed. MVFIT also handles situations in which the function never reaches a minimum, but oscillates around it. This is handled by cutting the step size, as described above. Finally, MVFIT will not allow the position of the secondary vertex to move downstream of the measured co-ordinates of the decay daughters at that vertex. If the vertex position moves too far, the co-ordinates are dropped, regardless of whether point dropping is enabled.

Energy loss in the hydrogen target is modeled in the fit by using a Runge–Kutta stepping procedure[33] to track each particle inside the target. Once the particle has left the target, its path is parametrized as a helix. If the Runge–Kutta stepping significantly modifies the particle's track, the helical section of the track will no longer pass close to the measured co-ordinates. In this case, the parameters of the track are recomputed and the Runge–Kutta stepping is applied again. This procedure is iterated until the track, after accounting for energy loss, passes through the measured co-ordinates.

Multiple scattering is difficult to account for correctly, because it introduces correlations between the predicted co-ordinates for a track. In MVFIT, it is treated approximately by expanding the uncertainty of a track's position is it passes through the various components of the spectrometer. The error increase is determined using known distributions of the material in the detector. The increase in uncertainty is folded into the uncertainties of the co-ordinates. Tracks also experience continuous multiple scattering in the liquid hydrogen target, which is accounted for by an additional term to $\mathcal{L}$.

The fits used in the analyses described in this work require:

- geometric constraints only (GeoFit),
- an enforced mass constraint for each candidate V^0,
- an assigned mass for each track and the enforcement of energy-momentum balance at the primary vertex (4C Fit),
- the assumption of one missing neutral of an assumed mass at the primary vertex, and the enforcement of energy-momentum balance (1C Fit).

5.11 Monte Carlo Simulation

Although the precise manner in which a Monte Carlo event sample is generated depends on the channel being studied, there are a number of features independent of the channel. The thrown phase space of the beam follows from a study of T3 triggered events. The beam track is randomly interacted in the target, accounting for nuclear absorption effects in the liquid hydrogen. This first measured vector is then retracked back out of the target, corrected for energy loss and multiple scattering, and the found momentum smeared with the beam chamber errors. This method gives a good representation of the beam tracks. The other tracks from the T3 events are propagated through the spectrometer to create hits in the downstream chambers. Smeared by the respective chamber errors, these tracks then are used to simulate the effects of secondary beam particles, so that effects in the track finding due to these signals are properly accounted for.

Tracks produced by the interaction of the beam with a target proton are followed out of the target, correcting for multiple scattering, energy loss, absorption, weak decays, and non-uniformities in the magnetic fields. Multiple scattering effects are generated whenever material would be encountered in the real spectrometer. Nuclear absorption and weak decays are modeled simply as exponential effects with known characteristic absorption lengths, decay lifetimes, and decay branching ratios.

Every generated track is swum through the magnetic fields using a fourth order Runge–Kutta stepping algorithm to generate track coordinates in chambers until the track has interacted, decayed, ranged out, or exited the spectrometer. A polynomial approximation to the measured spectrometer magnetic field is used.

The responses of the chambers, scintillators, and Cherenkov counters are modeled as functions of the angle of incidence of the track and the measured device efficiencies. In the chambers, cathode simulation is more difficult than anode simulation, because the signal is more spread out and so the chance for overlap of two adjacent signals is greater. The cathode peak reconstruction takes account of this effect.

The performance of the Monte Carlo was studied using real data from n-prong, kaon "τ" decay, and elastic K^-p events. The elastic events serve as a check on the normalization of the experiment, because the cross section for elastic scattering is well known. Study of the "τ" decay events reproduced the known kaon mass very well.

Chapter 6

Analysis Techniques

6.1 Variables

The channels analysed in detail in this thesis can be described as one meson recoiling against a baryon, with the meson subsequently decaying to some number of pions. However, only the systems involving two pions were fully analyzed. For these systems, there are 9 parameters which describe the tracks, ignoring any decay of the baryon. However, since the center-of-mass energy and momentum are known, there are only 5 independent variables. In addition, since the initial system is azimuthally symmetric, the overall azimuthal angle of the final system is unimportant. Therefore, only 4 variables are needed to characterize the final system.

The variables used in the analyses are the mass of the meson system, the 4-momentum transfer, t, to the meson, and, for a dipion system, the two decay angles in the rest frame of the dipion. The definition of t used depends on whether the meson system of interest is traveling forward or backward in the center-of-mass frame. For example, for a forward dipion system, the momentum transfer of interest is

$$t(\mathrm{K}^- \to \pi\pi) = (p_{\pi\pi} - p_{beam})^2, \tag{6.1}$$

where p is a 4-vector. In many cases, however, a more interesting quantity is

$$t' \equiv -t - (-t)_{min} \tag{6.2}$$

where $(-t)_{min}$ is the minimum value of $-t$ allowed by the kinematics.*

The decay angles used are the Gottfried–Jackson angle, θ_{GJ}, and the Treiman–Yang angle, ϕ_{TY}, and are specified in the t-channel helicity frame. The Gottfried–Jackson angle is the angle, measured in the rest frame of the dipion, between one of the daughter pions and the z-axis, defined as the beam direction in the dipion rest frame. The Treiman–Yang angle is the azimuthal angle of one of the pions in this frame, with the y-axis along the normal to the plane containing the target and recoil momentum vectors, and the x-axis defined as $\hat{y} \times \hat{z}$. In the following analyses, the sign of θ_{GJ} is defined by the convention of "following the charge", *e.g.* for forward $\pi^+\pi^-$, the meson system is produced at a vertex with the beam K^- and therefore the angles are defined for the π^-.

6.2 Acceptance Correction

Since the true decay angular distribution of the meson system is of primary interest, the angular dependence of the acceptance function, as well as its dependence on mass and t', must be taken into account. The acceptance is calculated by generating a sample of Monte Carlo data which is approximately similar to the data, and processing it with the same programs used to select the data. Ignoring for the moment the mass and t' dependence, the acceptance is calculated as

$$a(\Omega) = \frac{dA_f/d\Omega}{dA_t/d\Omega} \tag{6.3}$$

where A_t is the angular distribution of generated events, and A_f is that of the accepted events.

*$(-t)_{min}$ is frequently referred to as t_{min}, with the negative sign implied. The Particle Data Group advocates the terminology "t_-" for this quantity.

The quantities of interest in the angular analysis are the moments of the spherical harmonics, $\langle Y_l^m(\theta,\phi)\rangle$, where

$$Y_l^m(\theta,\phi) = \sqrt{\frac{2l+1}{4\pi}\frac{(l-m)!}{(l+m)!}}P_l^m(\cos\theta)e^{im\phi} \tag{6.4}$$

and P_l^m are the associated Legendre polynomials. If the Monte Carlo sample is thrown flat in the angles, then

$$\frac{dA_t}{d\Omega} = \frac{N_t}{4\pi} \tag{6.5}$$

where N_t is the number of generated events. The distribution of accepted MC events can be written as

$$\frac{dA_f}{d\Omega} = N_f \sum_{l=0}^{l_{max}} \sum_{m=-l}^{l} \alpha_{lm} Y_l^m(\theta,\phi) \tag{6.6}$$

where N_f denotes the number of accepted events, the α_{lm} are the spherical harmonic moments (which will actually depend on mass and t'), and l_{max} is the maximum value of interest, as determined from the data.

A useful simplification of Equation 6.6 is found if one imposes parity invariance. In the t-channel helicity frame, the y-axis is defined by the cross-product of two particle momenta, and is therefore an axial vector. Therefore, under a parity transformation,

$$\hat{x} \xrightarrow{\text{P}} -\hat{x}, \quad \hat{y} \xrightarrow{\text{P}} \hat{y}, \quad \hat{z} \xrightarrow{\text{P}} -\hat{z}. \tag{6.7}$$

This means that under a parity transformation,

$$\theta_{GJ} \xrightarrow{\text{P}} \theta_{GJ}, \quad \phi_{TY} \xrightarrow{\text{P}} -\phi_{TY}, \tag{6.8}$$

and, therefore,

$$\begin{aligned} Y_l^m(\theta_{GJ},\phi_{TY}) \xrightarrow{\text{P}} Y_l^m(\theta_{GJ},-\phi_{TY}) &= Y_l^m(\theta_{GJ},\phi_{TY})^* \\ &= (-1)^m Y_l^{-m}(\theta_{GJ},\phi_{TY}). \end{aligned} \tag{6.9}$$

Thus, for the expansion of an arbitrary function

$$f(\theta_{GJ},\phi_{TY}) = \sum_{l=0}^{\text{inf}} \sum_{m=-l}^{l} C_{lm} Y_l^m(\theta_{GJ},\phi_{TY}), \tag{6.10}$$

we get the condition that

$$C_{lm} = (-1)^m C_{l,-m}. \tag{6.11}$$

If f is a physically measurable function, it must be real, and therefore

$$C_{lm} = (-1)^m C^*_{l,-m}. \tag{6.12}$$

The combination of the two restrictions implies that C_{lm} must be real.

Although parity is conserved in strong interactions, the detector is not necessarily parity invariant. Thus, it is not true that parity invariance can automatically be imposed on the acceptance. Dependence on parity would be manifest by non-zero imaginary components in the expansion of Equation 6.6. However, examination of the acceptance data shows that, within uncertainties, the detector is parity invariant. Using the previously derived restrictions, we get

$$\frac{dA_f}{d\Omega} = N_f \left\{ \sum_{l=0}^{l_{max}} \alpha_{l0} Y_l^0(\theta_{GJ}, \phi_{TY}) + \sum_{l=1}^{l_{max}} \sum_{m=1}^{l} \alpha_{lm} 2\mathrm{Re}\, Y_l^m(\theta_{GJ}, \phi_{TY}) \right\}. \tag{6.13}$$

The orthogonality of the spherical harmonics means that these constants are given by

$$\begin{aligned} \alpha_{lm} &= \langle \mathrm{Re} Y_l^m(\theta_{GJ}, \phi_{TY}) \rangle \\ &= \frac{1}{N_f} \sum_{events} \mathrm{Re} Y_l^m(\theta_{GJ}, \phi_{TY}), \end{aligned} \tag{6.14}$$

which is the average over the accepted Monte Carlo events. Substituting Equations 6.5 and 6.13 into 6.3, we get

$$a(\theta_{GJ}, \phi_{TY}) = 4\pi \frac{N_f}{N_t} \left\{ \sum_{l=0}^{l_{max}} \alpha_{l0} Y_l^0(\theta_{GJ}, \phi_{TY}) + \sum_{l=1}^{l_{max}} \sum_{m=1}^{l} \alpha_{lm} 2\mathrm{Re}\, Y_l^m(\theta_{GJ}, \phi_{TY}) \right\}. \tag{6.15}$$

The average acceptance is given by

$$\langle a(\theta_{GJ}, \phi_{TY}) \rangle = \frac{1}{4\pi} \int a(\theta_{GJ}, \phi_{TY}) d\Omega = \frac{N_f}{N_t}. \tag{6.16}$$

So far, the dependence of the acceptance on the mass of the meson system and on t' have been ignored. This is taken into account by allowing the moments, α_{lm}, and the average acceptance to vary with these parameters.

Because the Monte Carlo samples are thrown with different mass densities and t' slopes across the mass spectrum, there are discontinuities in event densities. At these discontinuities, reconstructed events would preferentially flow from regions of higher density to lower density, altering the calculated acceptance. In order to eliminate this, when calculating the acceptance, the events are re-weighted to be flat in mass and to have the same t' slope.

There are two common schemes for applying the acceptance correction to the data. One method is to give each event a weight equal to the inverse of the acceptance at the event's particular kinematic co-ordinates. Since the kinematic variables are continuous, this generally means that the average acceptance and any non-zero acceptance moments must be parametrized and fit for their dependence on mass and t'.

The other method involves correcting the data on a bin-by-bin basis. In a particular mass and t' bin, one can think of the true and measured moments as one-dimensional arrays, $[T]$ and $[M]$. One needs a square matrix, $[Y]$, to compute one from the other, *i.e.*

$$[M_{l'm'}] = [Y_{l'm'lm}][T_{lm}]. \tag{6.17}$$

If I_T is the true angular distribution and I_M the measured one, then

$$\begin{aligned} I_M(\Omega) &= a(\Omega) I_T(\Omega) \\ &= a(\Omega)\left[\sum_{l=0}^{l_{max}} T_{l0} Y_l^0 + \sum_{l=1}^{l_{max}} \sum_{m=1}^{l} T_{lm} 2\mathrm{Re} Y_l^m\right] \end{aligned} \tag{6.18}$$

Multiplying by a spherical harmonic and integrating, we get

$$\begin{aligned} M_{l'm'} &= \int \mathrm{Re}\, Y_{l'}^{m'} I_M d\Omega \\ &= \sum_{l=0}^{l_{max}} T_{l0} \int a(\Omega) \mathrm{Re}\, Y_{l'}^{m'} Y_l^0 d\Omega + \\ &\quad \sum_{l=1}^{l_{max}} \sum_{m=1}^{l} T_{lm} \int a(\Omega) \mathrm{Re} Y_{l'}^{m'} 2\mathrm{Re}\, Y_l^m d\Omega \end{aligned} \tag{6.19}$$

Spin L	$D_L(x)$
0	1
1	$1+x^2$
2	$9+3x^2+x^4$
3	$225+45x^2+6x^4+x^6$
4	$11025+1575x^2+135x^4+10x^6x^8$

Table 6.1: The Blatt–Weisskopf barrier factor polynomials.

The integrals are computed by calculating the average of the quantities over the accepted Monte Carlo events, and thus

$$Y_{l'm'lm} = \frac{4\pi}{N_t}\begin{cases} \sum_{events} \mathrm{Re} Y_{l'}^{m'} Y_l^0 & m=0 \\ \sum_{events} \mathrm{Re}\, Y_{l'}^{m'} 2\mathrm{Re}\, Y_l^m & m>0, \end{cases} \tag{6.20}$$

where the sums are over the accepted events.

The following analyses used the second method to correct for the acceptance because of the need to cut a large region of the $\Lambda\pi^+$ mass spectrum from the forward $\pi^+\pi^-$ sample in order to remove the effect of the Σ resonances on the $\pi^+\pi^-$ distributions.

6.3 Breit–Wigner Shapes

For a spin L resonance decaying into two spin 0 particles (*e.g.* pions), the resonance shape is described by

$$\frac{d\sigma}{dm} \propto \frac{m\Gamma(m)}{({m_R}^2 - m^2)^2 + {m_R}^2{\Gamma_T}^2(m)} \tag{6.21}$$

where m_R is the mass of the resonance, Γ the partial decay width to the channel analysed, Γ_T the total width, and m is the mass of the observed two-particle system. In this expression, only the propagation and decay of the resonance are described; no attempt has been made to represent the production characteristics of the state in question.

If the resonance width is large, it must be considered to depend on mass. The width is parametrized with the Blatt–Weisskopf formula[34]

$$\begin{aligned}\Gamma(m) &\propto \frac{q}{m}\frac{(qR)^{2L}}{D_l(qR)} \\ &= \left(\frac{q}{q_R}\right)^{2L+1}\frac{m_R}{m}\frac{D_L(q_R R)}{D_L(qR)}\Gamma_R \end{aligned} \tag{6.22}$$

where $D_L(x)$ are the polynomials given in Table 6.1, R is the barrier factor (typically of the order of $5\,\mathrm{GeV}^{-1} = 1\,\mathrm{fm}$), q is the magnitude of the 3-momentum of a decay daughter in the resonance rest frame, and Γ_R and q_R are Γ and q evaluated at $m = m_R$. If the partial and total widths have the same mass dependence, a resonance of a particular spin is completely characterized by M_R, Γ_R, and R.

6.4 Partial Wave Analysis

Partial Wave Analysis (PWA) is a powerful tool for the investigation of the spectroscopy of two- and three-body states. For example, resonant states which are approximately degenerate in mass may be separated by this technique, and, in particular, contributions due to small resonances may be extracted in a region dominated by a larger one. For dipion systems, such as those considered in this thesis, the differential cross section for a particular mass or t' interval is characterized by the spherical harmonic moments as described above. After acceptance correction. as described in Section 6.2, the relationships between these moments and the underlying amplitudes may be used to extract the relevant partial wave amplitudes.

The peripheral nature of the production of the dipion systems considered makes it natural to consider these processes as proceeding via one particle exchange in the t or u channels. In such a model, the naturality, η, of the exchange is defined as

$$\eta \equiv (-1)^J P, \tag{6.23}$$

where J and P are the spin and parity of the exchanged particle; $\eta = +1$ is referred to as natural parity exchange while $\eta = -1$ is called unnatural parity exchange.

The production amplitude, $L_{\lambda\eta}$, for a resonant system of spin L and t-channel helicity λ by natural ($\eta = +1$) or unnatural ($\eta = -1$) parity exchange is given by

$$L_{\lambda\eta} = c_\lambda \left(H^L_\lambda - \eta(-1)^\lambda H^L_{-\lambda}\right), \quad c_\lambda = \begin{cases} 1/2 & \lambda = 0 \\ 1/\sqrt{2} & \lambda \neq 0 \end{cases} \tag{6.24}$$

where H^L_λ is the helicity amplitude, and $\lambda = 0,\ 1$. In practice, it appears unnecessary to consider values of $\lambda > 1$, and so in the present analyses, λ is given only the values 0 and 1. The observed moments are expressed as sums of bilinear products of production amplitudes, the relationship being given by[35]

$$t_{lm} = \sum_{LL'\lambda\lambda'\eta} \left[\tfrac{(2L+1)(2L'+1)}{2l+1}\right]^{1/2} \langle LL'00|l0\rangle\,(-1)^{\lambda'}\,\langle LL'\lambda\lambda'|lm\rangle \frac{1}{4c_\lambda c_{\lambda'}} \mathrm{Re}(L_{\lambda\eta} L'^{*}_{\lambda'\eta}), \tag{6.25}$$

where $\langle|\rangle$ are Clebsch–Gordan coefficients. Baryon helicity is summed over and the property of spin coherence at the nucleon vertex is assumed. The relations between the moments and the spin amplitudes and their relative phases are tabulated in Appendix A. The notation used to indicate particular amplitudes is that the spin is indicated by the spectroscopic letter (*i.e.* S, P, D, *etc.*) while the subscript indicates the helicity and naturality of the exchange. A subscript of + or − indicates helicity 1, natural or unnatural parity exchange, respectively, while a subscript of 0 indicates helicity 0, unnatural parity exchange (the helicity 0, natural parity exchange amplitude is 0 by Equation 6.24).

The process of going from the moments to the amplitudes cannot be done analytically, since the moments are composed of bilinear combinations of the amplitudes plus phases. The calculation is done by minimizing the χ^2 between the measured moments and the moments calculated from the amplitudes. The full covariance matrix of the measured moments is used. Since experimental errors may make it impossible to find an exact match to the moments, the fit is performed many times, starting from randomly chosen initial conditions, and any solution which has a satisfactory χ^2 is accepted. A χ^2 of 3 per moment is considered acceptable.

Because a partial wave analysis involves much calculation and can result in multiple solutions, it is helpful to be able to calculate quantities which have a strong contribution from one wave, even if they may be slightly contaminated by other waves. The σ's defined in Appendix A are such quantities. For example, if one can neglect D and higher waves, σ_{+}^{P} projects the P_{+} amplitude with a small component of S-wave. A quantity of particular interest to the analysis of $K^{-}p \rightarrow \Lambda\pi^{+}\pi^{-}$ is σ_{+-}^{P}, defined as

$$\begin{aligned} \sigma_{+-}^{P} &\equiv \sqrt{\frac{5}{2}}t_{42} - \sqrt{\frac{10}{3}}t_{22} \\ &= |P_{+}|^{2} - |P_{-}|^{2} \qquad \text{(neglecting F-wave).} \end{aligned} \tag{6.26}$$

This combination can show the existence of P-wave even in the presence of a significant D-wave, provided that $|P_{+}|^{2}$ and $|P_{-}|^{2}$ are not the same size.

Chapter 7

$\Lambda\pi^+\pi^-$ Analysis

The simplest channel to examine a multi-pion spectrum is

$$K^-p \rightarrow \Lambda\pi^+\pi^-, \tag{7.1}$$

which occurs mainly via virtual K or K* exchange. This channel is very simple, having only 4 charged tracks and no neutral particles. Therefore, a 4C MVFIT to the tracks will provide a very powerful tool to select events and provide a very clean sample.

7.1 Event Selection

The starting point for the analysis was a set of tapes generated at Nagoya, Japan. The events were selected to contain a Λ and 2 oppositely charged tracks. The tracks were assumed to be either pions or kaons, in any combination, giving four hypotheses, $\pi^+\pi^-$, K^+K^-, $K^+\pi^-$, and π^+K^- (the πK hypotheses were used to fit $\Lambda K^0_L K\pi$ final states). Events were cut if the square of the missing mass was greater than $1\,(\mathrm{GeV}/c^2)^2$ in absolute value, for all hypotheses. At this stage, the events were fit with a GeoFit, which constrains the geometry of the tracks to be consistent, followed by a Λ mass constrained fit. Hypotheses which produced a low missing mass were fit with a four constraint MVFIT. In addition, events which were consistent with the hypothesis $\pi^+\pi^-\pi^0$, where the π^0 was not detected, were

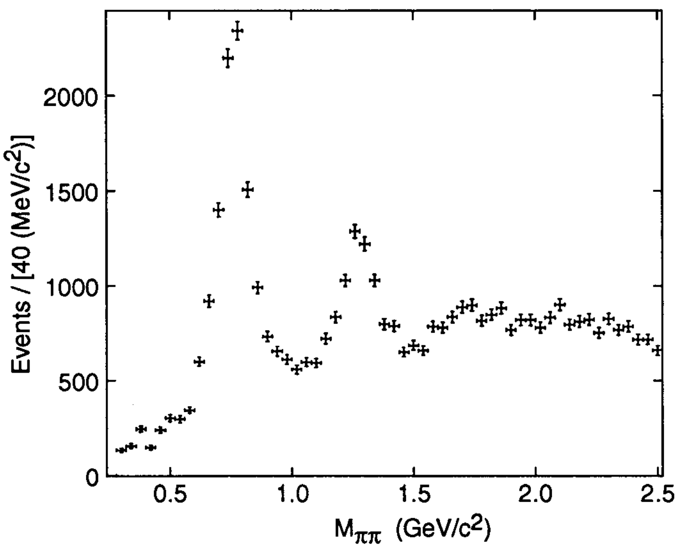

Figure 7.1: The $\pi^+\pi^-$ spectrum after requiring a 4C MVFIT with confidence level greater than 10^{-6}.

fit with a 1C MVFIT. The data set produced contained 1,461,824 events on 26 magnetic tapes.

The first step of this analysis was to require that events have a successful 4C 2 pion fit and that the confidence level from the fit be greater than 10^{-6}. This level provided a compromise between a clean sample of well-measured events and good statistics. The $\pi^+\pi^-$ spectrum at this stage is shown in Figure 7.1.

Figure 7.2 shows the Λ mass spectrum taken from the GeoFit quantities. It shows that the Λ is quite free of background. Figure 7.3 shows the decay distance of the Λ after the 4C Fit. The pile-up just above zero arises because the fit demands that the decay length be positive (as determined by the Λ momentum), whereas resolution effects can smear the quantity negative. The decay length was cut at 1 mm. A plot of decay helicity versus mass for the Λ did not show any bands which would indicate contamination from K^0s or photons.

The next step was to use the particle identification information from the cylinder dE/dx measurement, the time-of-flight system and the Cherenkov counters. The dE/dx measurement is expressed as a ratio of probabilities for two particle species, either π/K or π/p. The particle separation depends on the momentum;

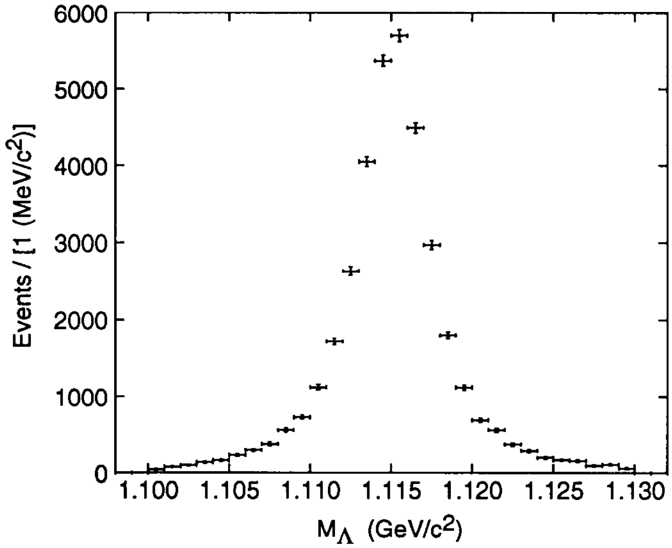

Figure 7.2: The Λ mass distribution.

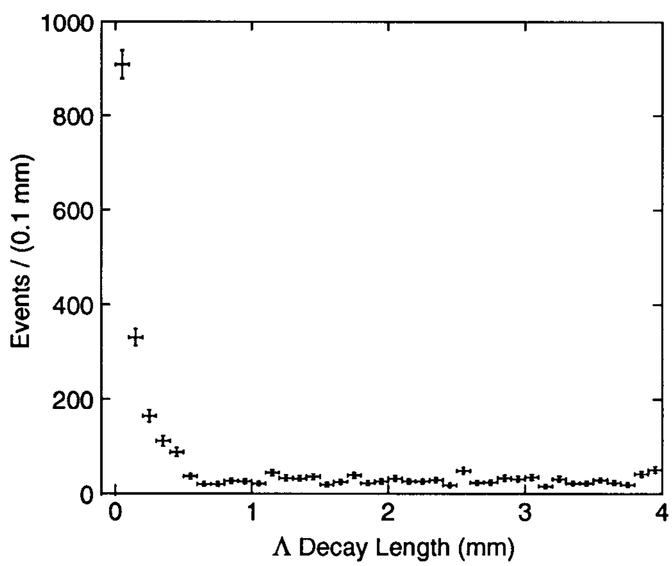

Figure 7.3: The Λ decay length distribution.

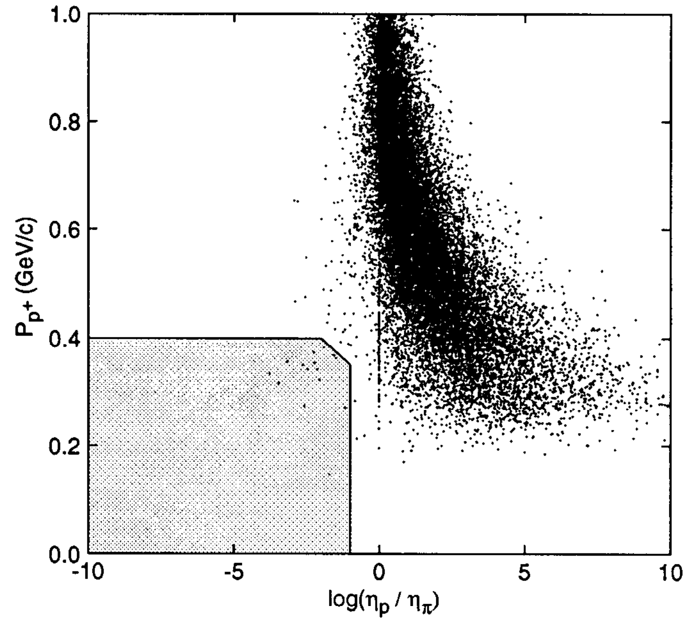

Figure 7.4: The dE/dx measurement for the p daughter of the Λ. The π/p probability ratio is plotted on the x axis. Events in the shaded region were removed.

dE/dx provides good separation up to about 0.6 GeV/c. The π/p ratio versus the track momentum for the proton daughter of the Λ is shown in Figure 7.4. One can see a small set of events forming a band moving to the left in the plot; these are kaons or pions and were remove by the cut shown in the plot. The other particles did not show any contamination in the dE/dx measurement.

The time-of-flight data (TOFDEV) is expressed as the number of standard deviations between the measured flight time and the expected time for a particular particle mass hypothesis. TOFDEV assuming a pion is plotted versus momentum for the proton daughter of the Λ in Figure 7.5. At very low momentum (less than about 0.4 GeV/c) the measurement is useless because the track can be affected greatly by energy losses in the material of the detector. One can see in the figure a strong band of events from protons going to the left and a faint one from pions in the center. The events in the shaded box in Figure 7.5 were cut, since only those could be positively identified as non-proton. The other particles appeared to be clean.

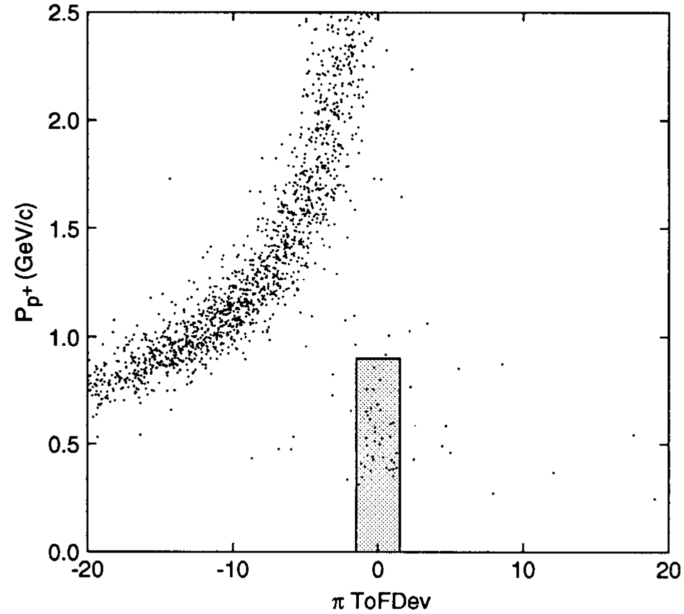

Figure 7.5: The time-of-flight measurement for the p daughter of the Λ. The x-axis shows the number of standard deviations between the measured and predicted flight time if the particle were a pion. Events in the shaded box were removed.

Using the Cherenkov counters for particle ID is generally more difficult because one must deal with thresholds and efficiencies. In principle, the signature of a pion is no Cherenkov light below the pion momentum threshold ($\sim 2.6\,\text{GeV/c}$) and light above the threshold. In practice, one must be careful because not all cells have good efficiency and the Cherenkov photons might not be detected. Also, threshold turn-on is not a step function and one must be careful about how many photons are expected. In this analysis, the Cherenkov information in the region of the pion threshold (2.5 to $3.0\,\text{GeV/c}$) was not used. Figure 7.6 shows momentum versus the Cherenkov ADC counts for the π^+. Only events where the counter efficiency was over 90% are shown. The events in the shaded box were designated as kaons. Since, if one primary track is a kaon, the other must also be one, it was required that if both primary "pions" had Cherenkov information, they must agree that an event contained kaons for the event to be cut. Otherwise, if only one track had Cherenkov information and it was identified as a kaon, the event was cut. The requirement of identifying both tracks as kaons if possible was made to reduce

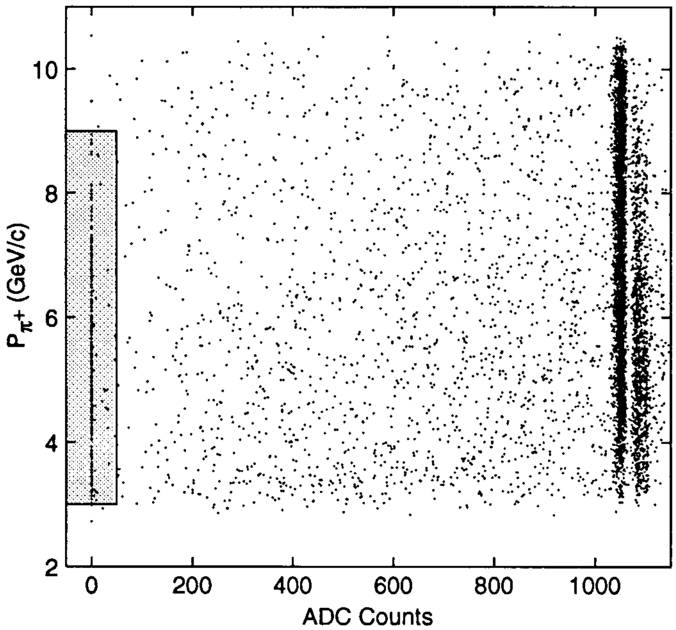

Figure 7.6: Momentum versus the ADC counts in C_1 for the π^+. Only those events where the Cherenkov photon detection efficiency was 90% or greater are shown. Events in the shaded region were removed.

the number of events wrongly cut, and seems to have been sufficient to clean the sample.

The final particle ID cut was to remove events where a photon converted to two electrons and the electrons were recorded but called pions. These can be recognized by looking at the invariant mass of the two tracks when they are called electrons and at the angle between the tracks. Pairs of tracks from photons will have a very low mass and a very low opening angle. All track pairs in the event were checked and events were cut when a pair involving a track used in the event had a mass less than $40\,\mathrm{MeV/c^2}$ and an opening angle less than $2°$.

The small bump around $0.380\,\mathrm{GeV/c^2}$ in the original $\pi^+\pi^-$ spectrum is actually from the decay $\phi \to \mathrm{K^+K^-}$, where the kaons were misidentified as pions. Figure 7.7a shows the pion decay helicity angle in this mass range before the particle ID cuts. The curved band is typical of a misidentified resonance. Figure 7.7b shows the same plot after the particle ID cuts; the ϕ contamination appears to be

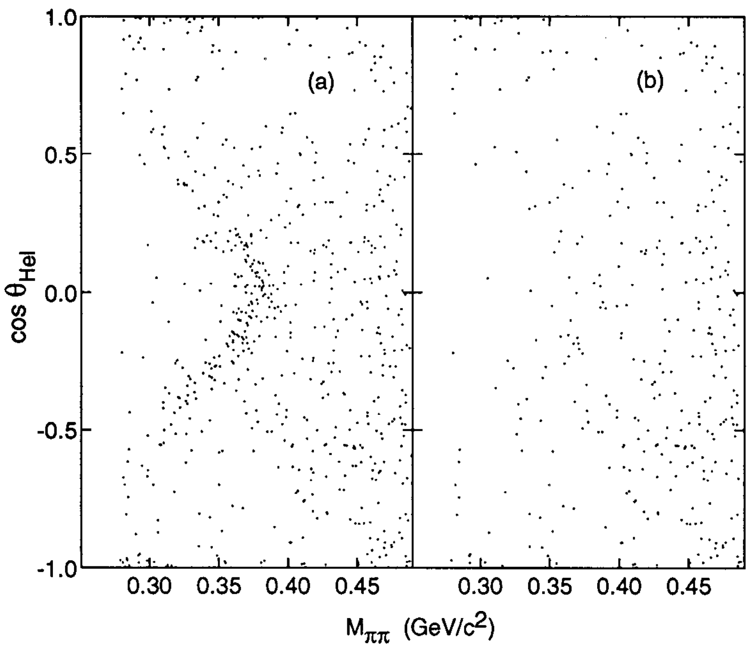

Figure 7.7: Contamination from $\phi \to K^+K^-$: (a) before particle ID cuts, (b) after cuts.

Description of Cut	# Events Cut	# Events Remaining
Input events	—	1,461,824
Unsuccessful 4C Fit	1,404,602	57,222
4-C Confidence Level $< 10^{-6}$	20,815	36,407
Lambda Decay Length < 0.1 cm	3024	33,383
TOF Particle ID	39	33,344
dE/dx Particle ID	15	33,329
Cherenkov Particle ID	841	32,488
Photon conversion	117	32,371
Output events	—	32,371

Table 7.1: Summary of cuts used in $\Lambda\pi^+\pi^-$ event selection.

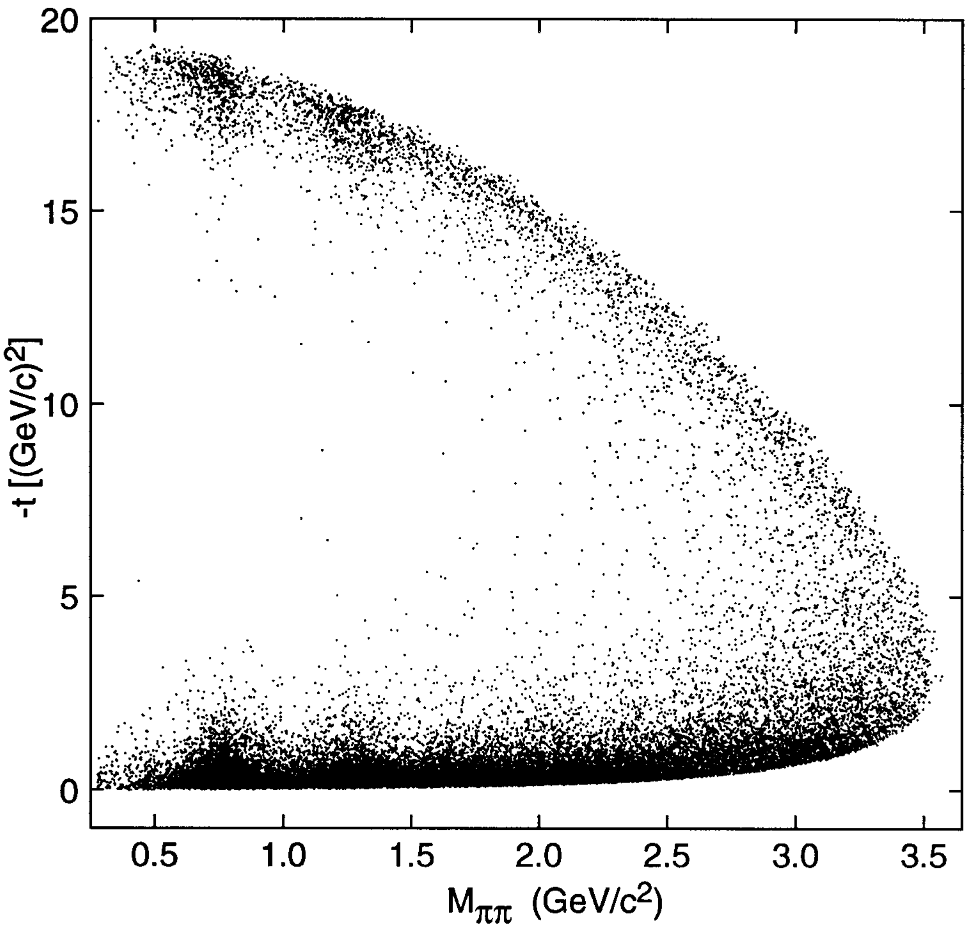

Figure 7.8: The Chew-Low plot for the $\pi^+\pi^-$ system. The y-axis shows the 4-momentum transfer between the beam and dipion system.

completely removed. However, due to poor statistics, the region below 0.4 GeV/c^2 in $\pi^+\pi^-$ mass was not used in the subsequent analysis.

Table 7.1 shows a summary of the cuts made and the number of events removed by each. The final event sample consists of 32,371 events. Figure 7.8 shows the Chew-Low plot, *i.e.* the 4-momentum transfer versus mass, for the $\pi^+\pi^-$ system. It clearly shows the separation between forward and backward production. The sample was split into backward Λ (*i.e.* forward $\pi^+\pi^-$) and forward Λ (backward $\pi^+\pi^-$) samples by cutting on the Feynman x of the Λ at 0. The backward Λ sample is discussed in the following sections and the forward sample is described in Section 7.8.

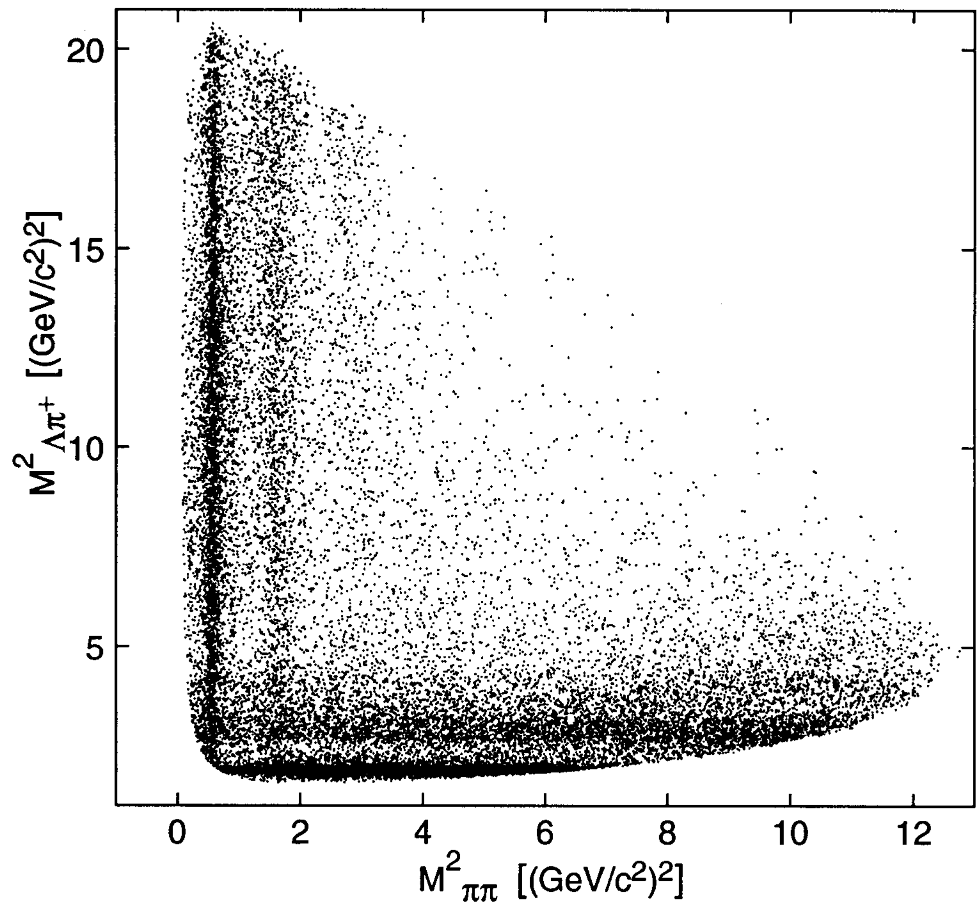

Figure 7.9: The Dalitz Plot for backward Λ events.

7.2 Backward Λ Sample

Figure 7.9 shows the Dalitz plot for events where the $\pi^+\pi^-$ system is peripherally produced with respect to the incident K^-, *i.e.* where the $\pi^+\pi^-$ system is moving forward in the center of mass frame. The sample consists of 28,343 events. Clear resonance bands are observed for the $\pi^+\pi^-$ system in the vicinity of the ρ and $f_2(1270)$, and there is also some indication of a faint band around 1.7 GeV/c^2, possibly due to the $\rho_3(1690)$. Figure 7.10 shows strong production of $\Sigma^+(1385)$ in the $\Lambda\pi^+$ system, as well as clear evidence of the production of several higher mass Σ states in the mass range 1.7–2.1 GeV/c^2. No production of low-mass $\Lambda\pi^-$ states can be seen in Figure 7.11; this is to be expected for slow Λs since the production

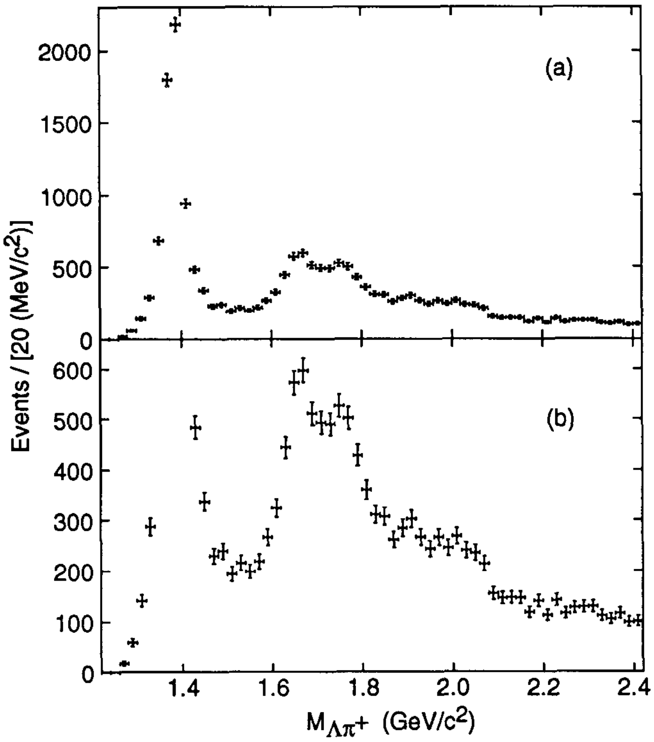

Figure 7.10: The observed $\Lambda\pi^+$ mass spectrum with a backward Λ (a) for all events, and (b) with the $\Sigma^+(1385)$ suppressed.

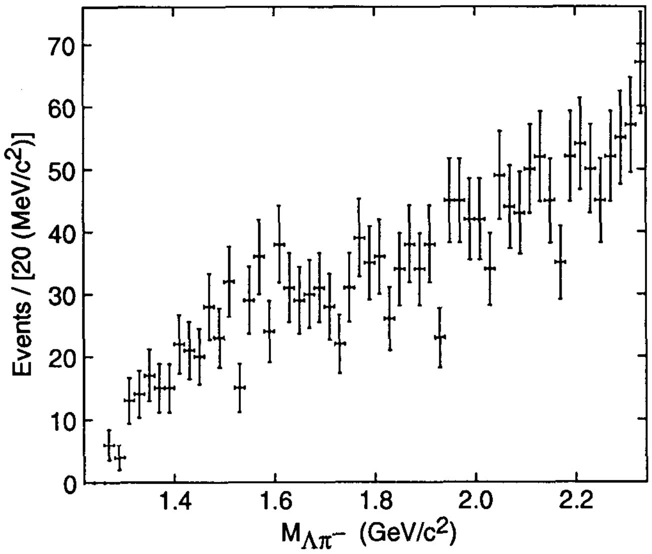

Figure 7.11: The observed $\Lambda\pi^-$ mass spectrum with a backward Λ.

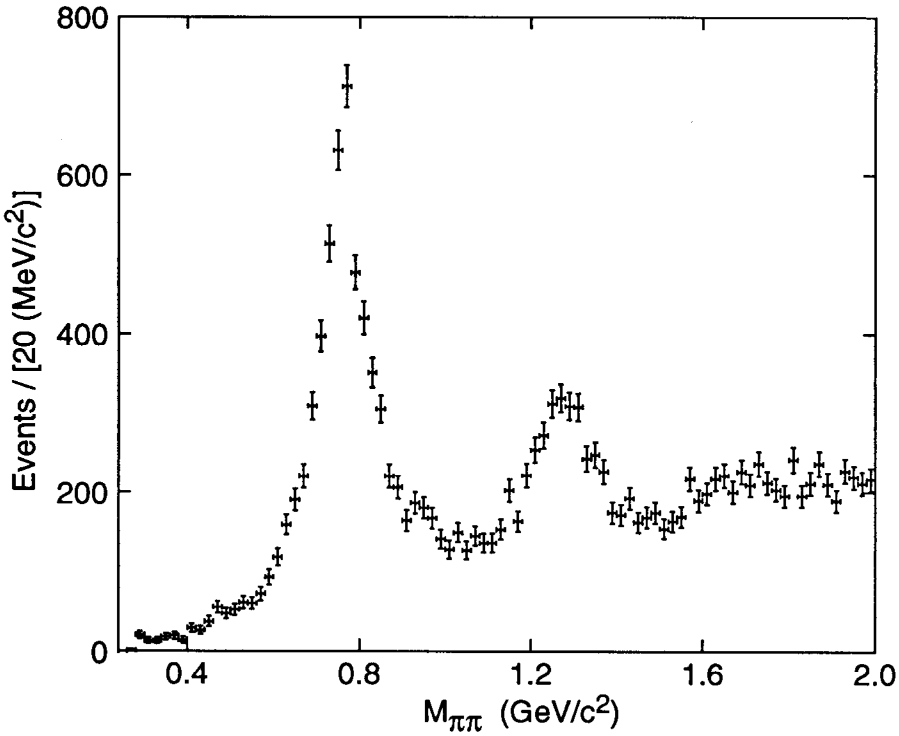

Figure 7.12: The observed forward $\pi^+\pi^-$ mass spectrum.

of such states would require the exchange of a doubly–charged meson system in the t-channel. The Dalitz plot of Figure 7.9 is very similar to those observed for Reaction (7.1) at lower energies,[36–39] and this clearly demonstrates the uniformity of acceptance of the LASS spectrometer, trigger and software.

The forward $\pi^+\pi^-$ mass spectrum is shown in Figure 7.12 for the mass region below $2\,\mathrm{GeV/c^2}$. The peak in the ρ region is severely distorted with respect to a simple Breit–Wigner line-shape. This is a consequence of ρ–ω interference, and will be discussed in Section 7.5. There is a second peak in the vicinity of the $f_2(1270)$; however, the analysis of Section 7.6 shows that this is not due entirely to the production of this resonance. Finally, there is perhaps a small, broad enhancement at $\sim 1.7\,\mathrm{GeV/c^2}$; this corresponds to the faint band observed in the Dalitz plot, but its presence is masked to a large extent by the reflections of Σ^* resonances into the $\pi^+\pi^-$ mass spectrum.

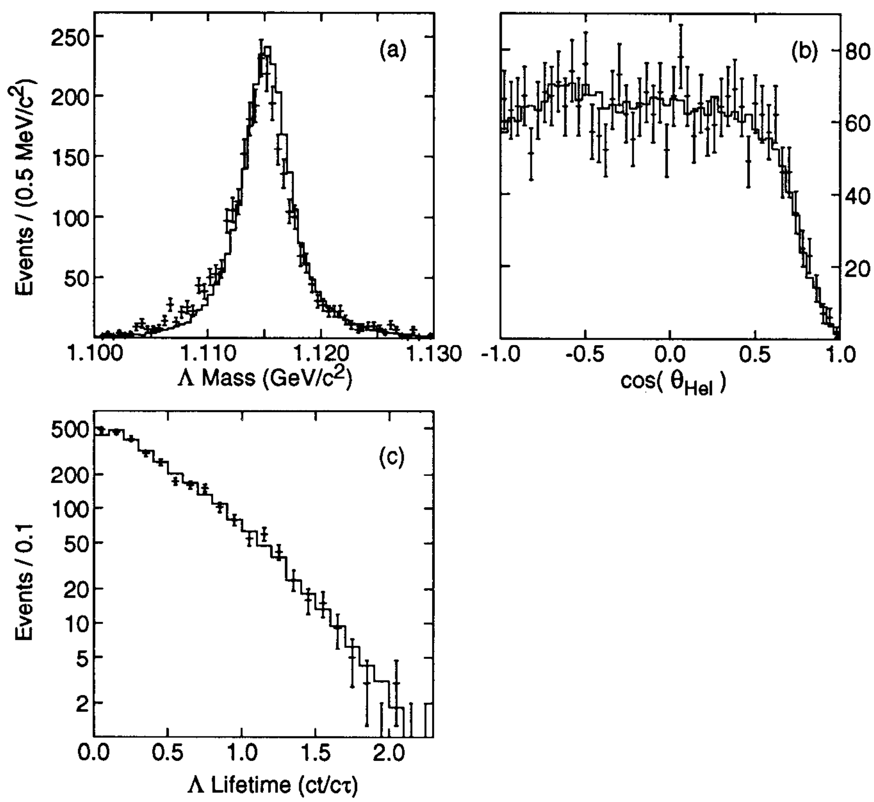

Figure 7.13: A comparison of the Monte Carlo Λ parameters with those from the data in the ρ mass region: (a) the mass (b) decay helicity and (c) proper decay time distributions. The MC is shown as the histogram and data as the points.

7.3 Monte Carlo Sample

Before the analysis can proceed, the data need to be corrected for the acceptance of the detector and sample selection cuts. This is done by using the Monte Carlo event generator to create an event sample which reasonably mimics the true data sample. Then, by comparing the generated and reconstructed quantities of the Monte Carlo sample, we can determine the acceptance and its dependence on various kinematic quantities.

When generating a Monte Carlo sample, the statistical uncertainties from the MC sample should be insignificant compared to those from the data sample. Therefore, the MC sample should be about 10 times bigger than the data set.

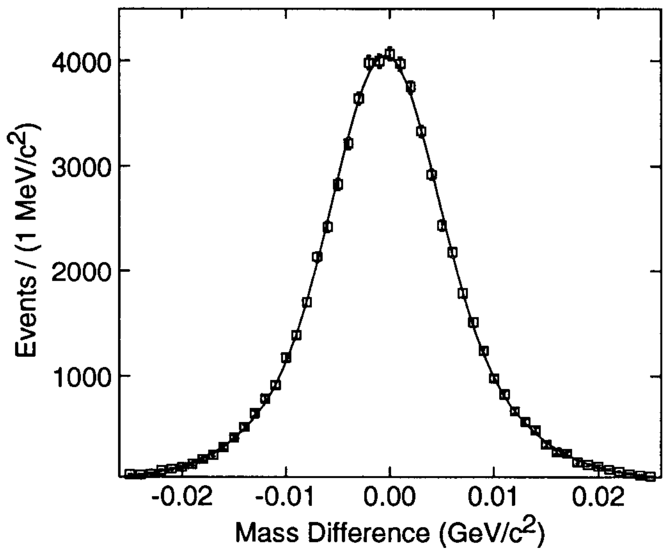

Figure 7.14: The mass resolution at the ρ mass, as measured from the Monte Carlo sample. The curve is the sum of two Gaussians.

The Monte Carlo sample was thrown flat in $\pi^+\pi^-$ mass with extra events around the ρ and $f_2(1270)$. The events were thrown uniformly in $\pi^+\pi^-$ decay angles and with a t' distribution similar to the data.

To check the performance of the Monte Carlo generator, we can look at the reconstructed parameters of the Λ. The mass, decay helicity, and proper decay time are shown in Figures 7.13a through 7.13c, respectively. The Λ mass comes from the GeoFit. The agreement can be seen to be quite good. The loss of events around $\cos(\theta_{Hel}) \sim 1$ is due to the low momentum of the daughter proton. In this region, the proton is moving backward relative to the direction of the Λ. This means that the proton is very slow in the lab frame and therefore cannot escape the target.

The Monte Carlo can be used to estimate the $\pi^+\pi^-$ mass resolution, which is needed when fitting resonance shapes. Figure 7.14 shows the difference between the generated and reconstructed masses for the two pion system in the region of the ρ. The distribution was fitted with two Gaussians whose means were constrained to be the same. The fit gives widths of 4.7 and 9.2 MeV/c^2, where the wider one has a amplitude of 1.02 relative to the narrower.

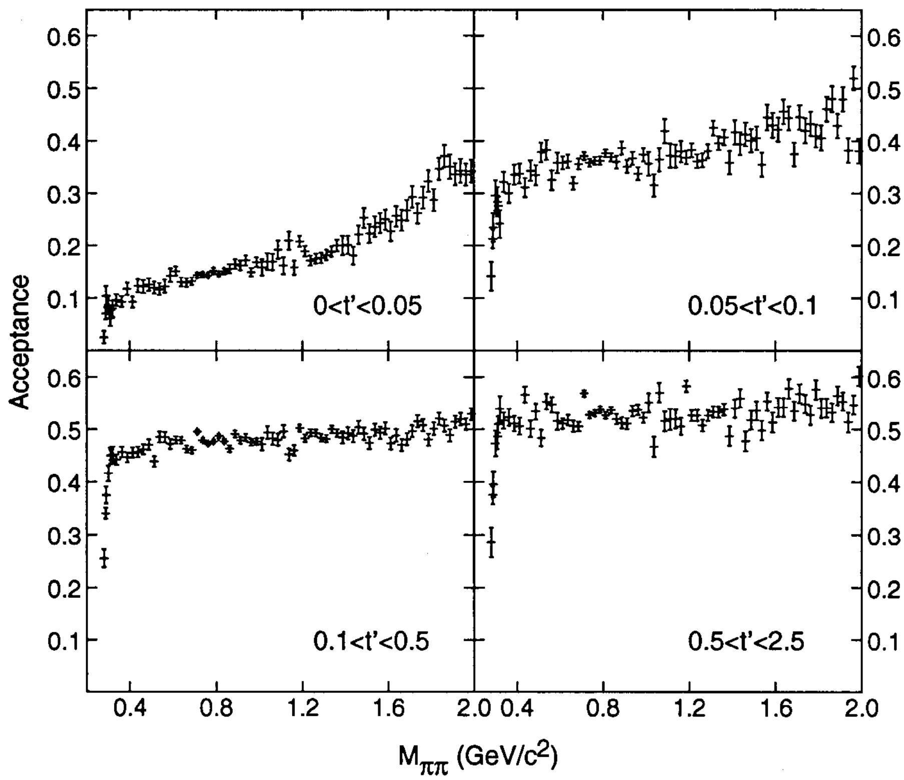

Figure 7.15: The acceptance for the forward $\pi^+\pi^-$ system in various t' bins.

7.4 Acceptance Corrected Moments

The average acceptance (before the cuts on $\Lambda\pi^+$ mass) as a function of $\pi^+\pi^-$ mass is plotted in Figure 7.15 for various t' bins. Except at low t', the acceptance is very good, near 50%, and is fairly uniform. The losses at low t' are generally due to absorption of slow protons from the Λ decay in the hydrogen target. Figure 7.16 shows the non-zero acceptance moments; the values are normalized to α_{00}. Their small sizes show that the detector is quite uniform over all 4π.

Figure 7.17 shows a few of the acceptance corrected moments for the forward $\pi^+\pi^-$ system. Many of the moments tend to drift away from zero as the mass increases. This is due to the overlap of resonances in the $\Lambda\pi^+$ system. Figure 7.18 shows the distribution of $\cos\theta_{GJ}$ versus mass while Figure 7.19 shows the distribution of ϕ_{TY}. The $\Lambda\pi^+$ resonances are evident as the dark bands near 1 in $\cos\theta_{GJ}$

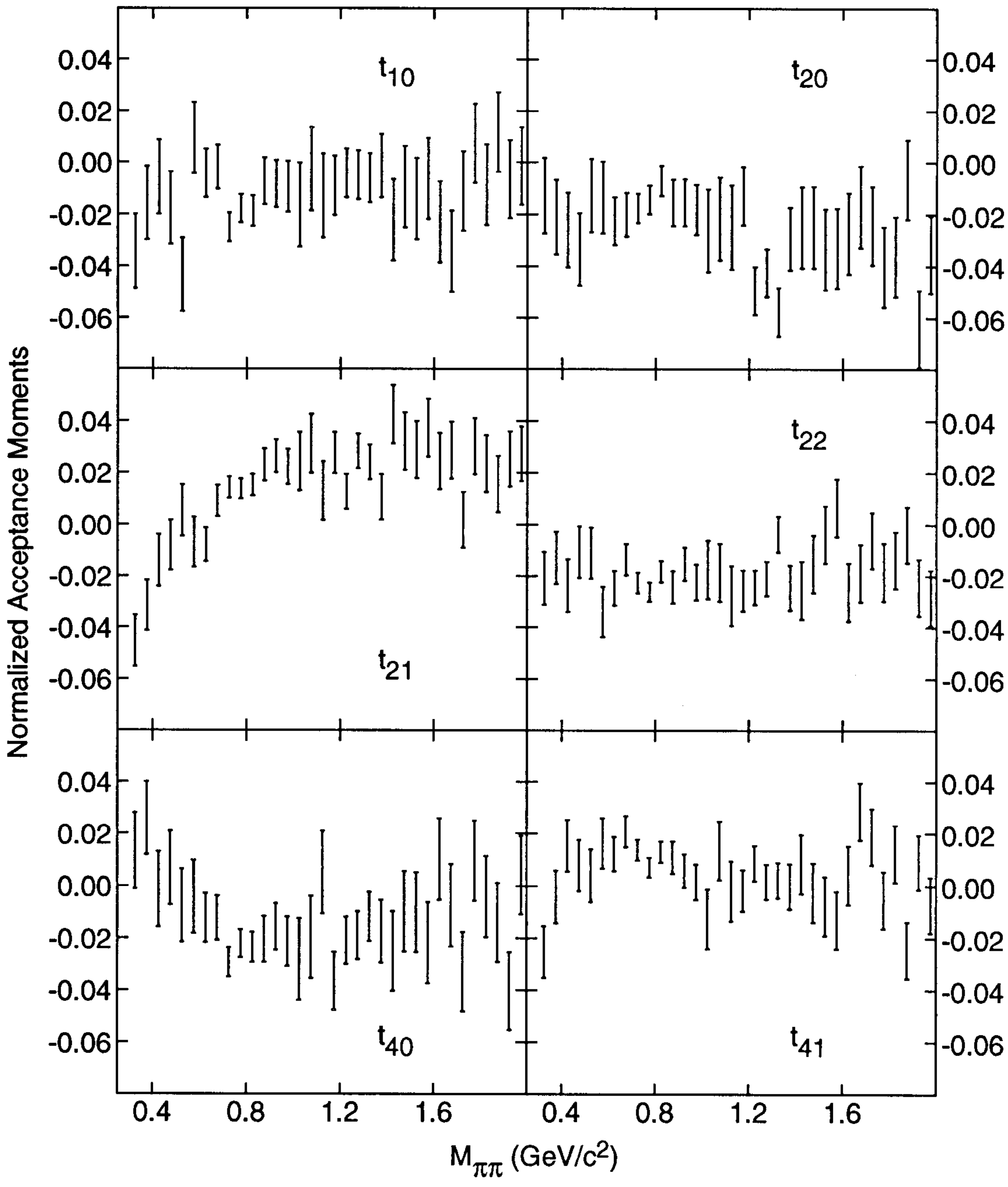

Figure 7.16: The non-zero acceptance moments for the forward $\pi^+\pi^-$ system.

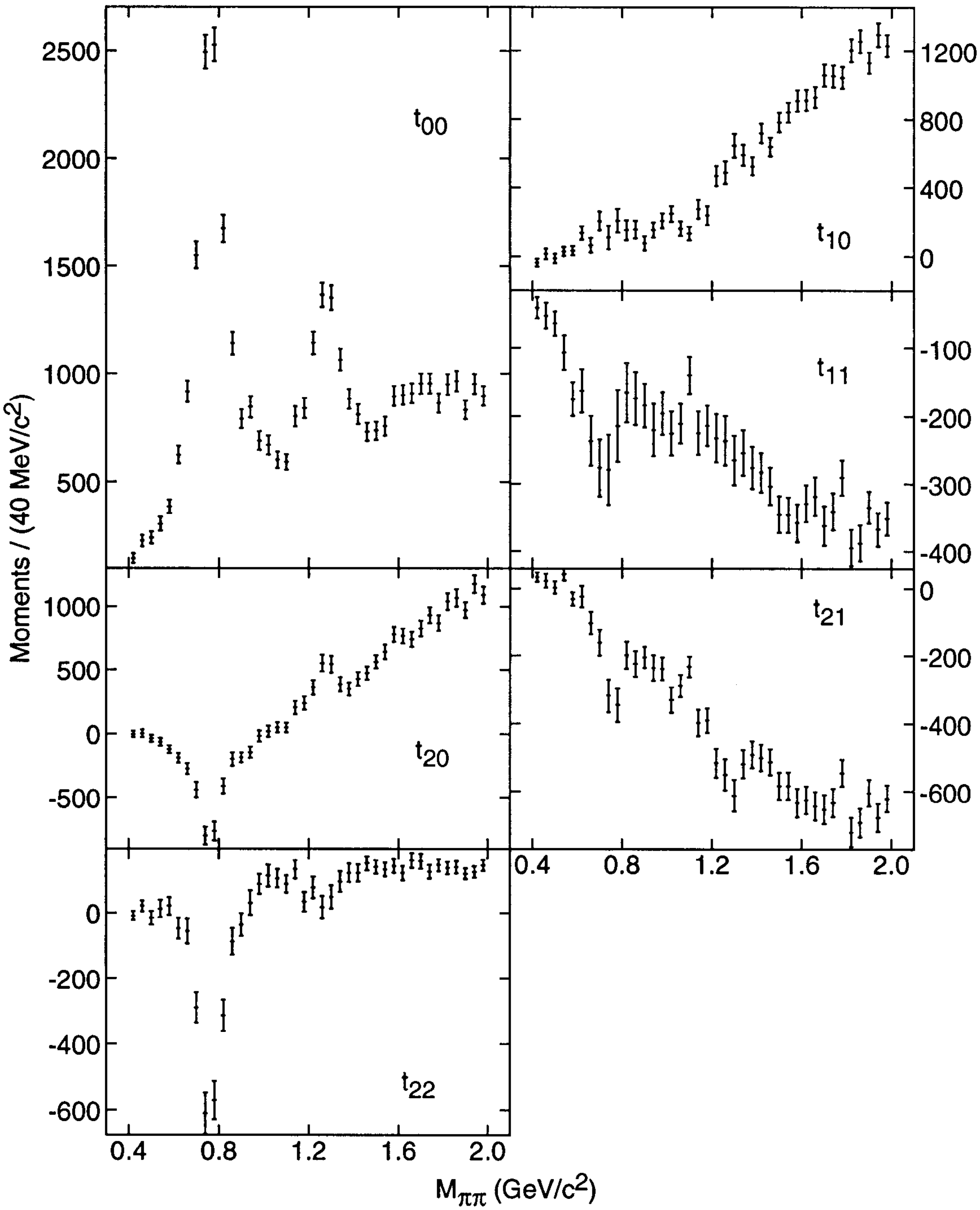

Figure 7.17: Some of the acceptance corrected moments without a cut on Σ^* resonances. The steady drift from zero in such moments as t_{11} is caused by overlap with these resonances.

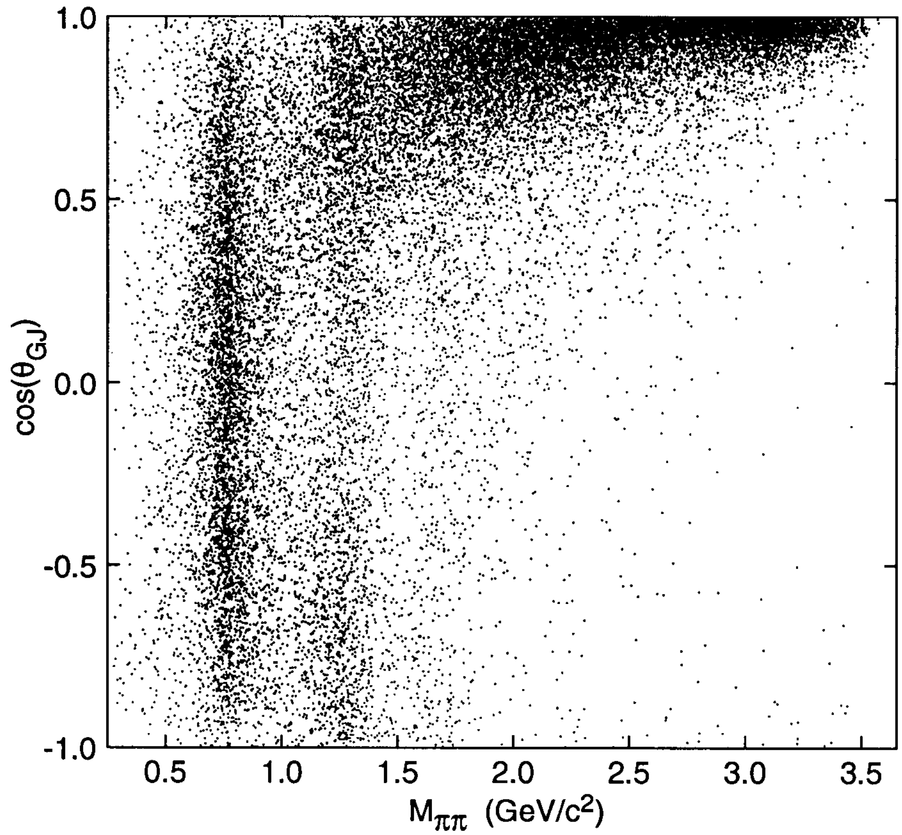

Figure 7.18: The mass dependence of $\cos\theta_{GJ}$. The overlap from the $\Lambda\pi^+$ resonances can be seen as the dark band at high $\cos\theta_{GJ}$.

and near zero in ϕ_{TY}. These overlaps must be removed before the $\pi^+\pi^-$ system can be properly analyzed.

There are two possible ways of removing the overlapping resonances. One is to make definite cuts in the $\cos\theta_{GJ}$–ϕ_{TY} plane. Then, the correction matrix for the moments can be calculated analytically.[40] The other method is to make cuts on the mass of the unwanted particle pair and use the Monte Carlo sample and the acceptance correction method to correct the moments. The former method has the advantage of not increasing the uncertainties during the correction process. However, it is more complicated in that the cuts must depend on mass and t' in order to follow the changing region of overlap. Also, the effective area in the $\cos\theta_{GJ}$–ϕ_{TY} plane removed by the cuts tends to be larger for

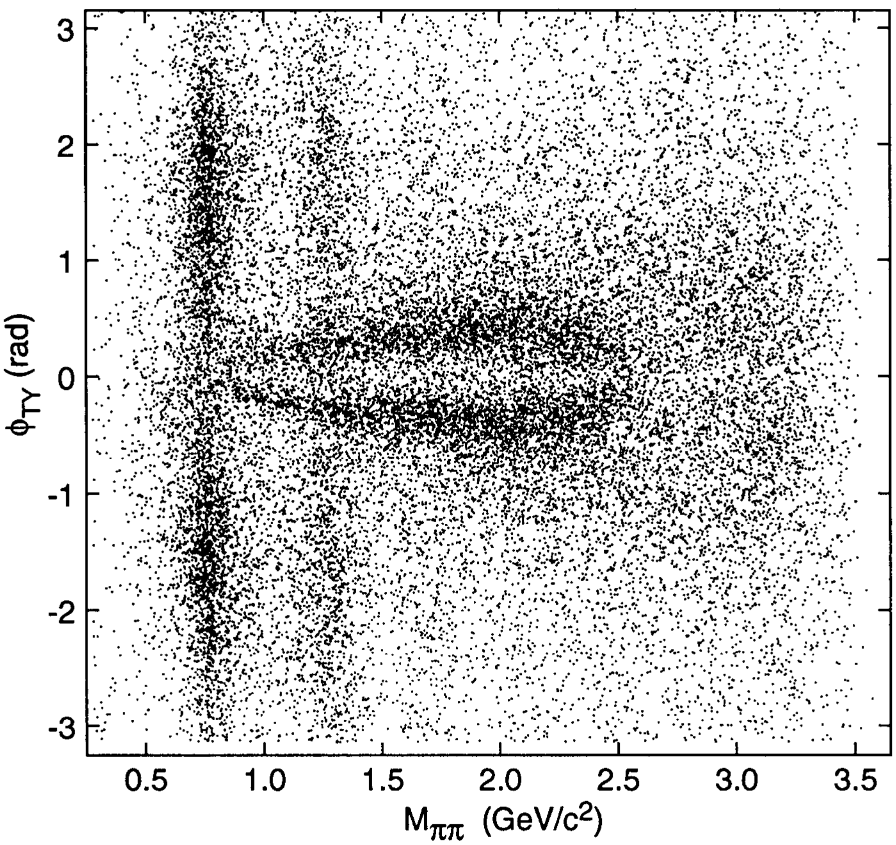

Figure 7.19: The mass dependence of ϕ_{TY}. The overlap from the $\Lambda\pi^+$ resonances can be seen as the dark bands near the center of the plot.

the former method, leading to more significant instabilities in the corrected moments.

Because of the large region of overlap from Σ^*s, it was necessary to make cuts in $\Lambda\pi^+$ mass. The shaded regions in Figure 7.20 indicate the event that were removed; the cuts extend from 1.3 to 1.52 GeV/c^2 and 1.6 to 2.15 GeV/c^2. The small region left in between the two cuts was needed to maintain the stability of the corrected moments at high $\pi^+\pi^-$ mass.

Figures 7.21, 7.22, and 7.23 show the acceptance corrected moments for the $\pi^+\pi^-$ system with the Σ resonances removed. The moments, t_{lm}, are related to

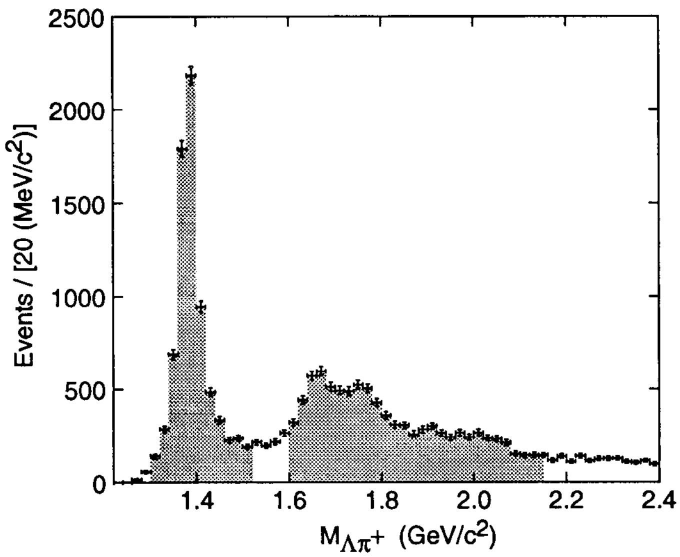

Figure 7.20: The regions removed from the $\Lambda\pi^+$ spectrum. The regions cut go from 1.3 to 1.52 GeV/c^2 and 1.6 to 2.15 GeV/c^2.

spherical harmonics by

$$t_{lm} = \sqrt{4\pi} \sum_{events} Y_l^m(\Omega) \tag{7.2}$$

and the covariance matrix is

$$E_{lml'm'} = 4\pi \sum_{events} Y_l^m(\Omega) Y_{l'}^{m'}(\Omega). \tag{7.3}$$

The measured covariance matrix is corrected by

$$[E_T] = [Y]^{-1}[E_M]([Y]^{-1})^T, \tag{7.4}$$

where $[Y]$ is the acceptance correction matrix, including the Σ cuts, mentioned in Section 6.2. The t_{00} moment is, in fact, the acceptance corrected number of events.

Comparison of Figure 7.17 with Figures 7.21 through 7.23 show that while the Σ cuts have removed a large part of the drift of the moments, some still remains, particularly in the $m = 0$ moments. This probably indicates that there still are problems with resonances in the $\Lambda\pi^+$ system. Unfortunately, no more of the $\cos\theta_{GJ}$–ϕ_{TY} plane can be removed without causing large, probably unphysical, fluctuations in the corrected moments at higher $\pi^+\pi^-$ masses.

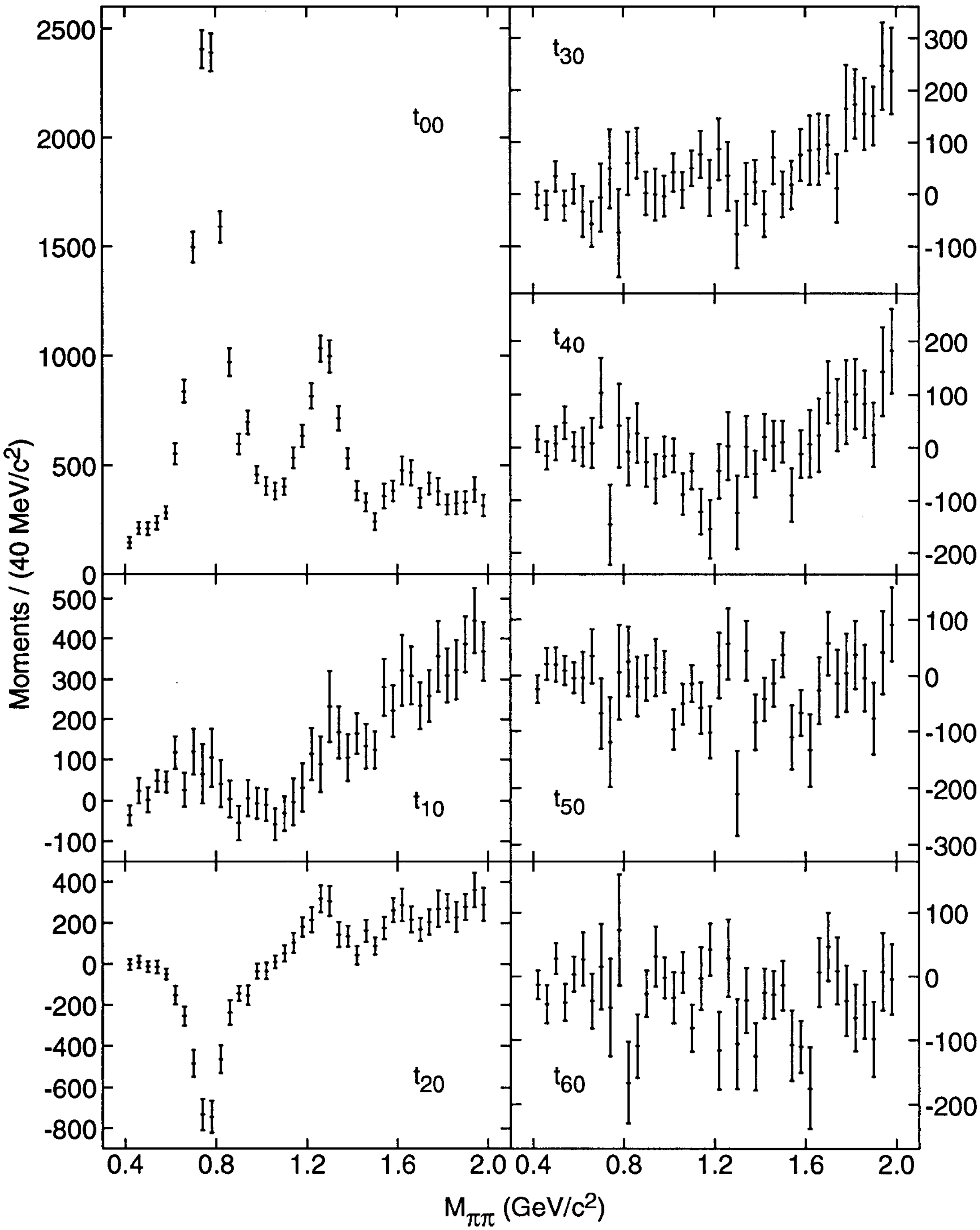

Figure 7.21: The $m = 0$ acceptance corrected moments for the forward $\pi^+\pi^-$ system.

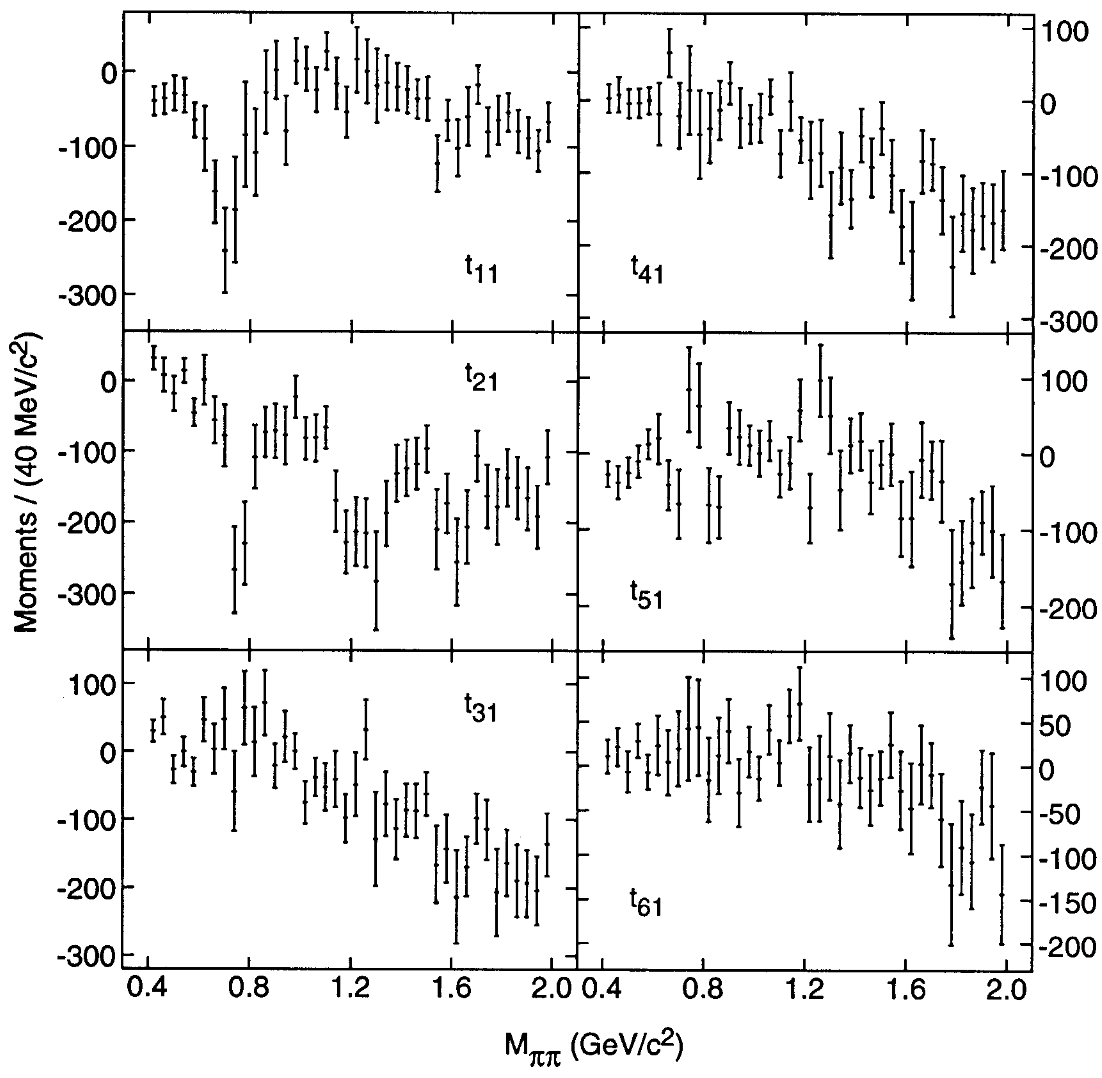

Figure 7.22: The $m = 1$ acceptance corrected moments for the forward $\pi^+\pi^-$ system.

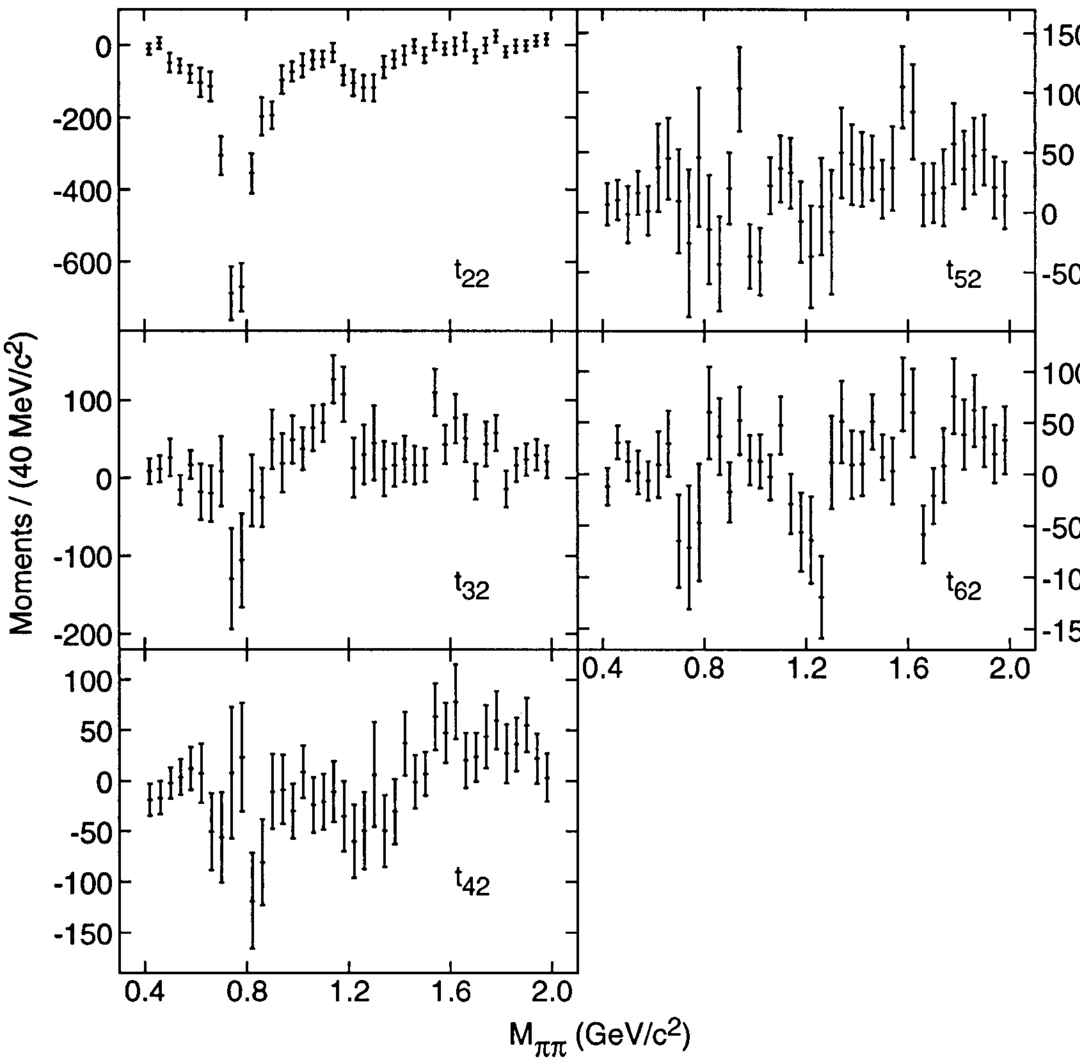

Figure 7.23: The $m = 2$ acceptance corrected moments for the forward $\pi^+\pi^-$ system.

7.5 Analysis of ρ Region

The primary feature of the $\pi^+\pi^-$ mass spectrum is the large ρ resonance at 770 MeV/c². The shape of the resonance, however, is distorted and cannot be described well by a Breit–Wigner line shape. This is due to interference between the ρ and the ω, caused by mass mixing of the two resonances.

The possibility of significant ρ–ω mass mixing has been recognized for many years,[41] and early estimates were that the resultant $\omega \rightarrow \pi^+\pi^-$ branching fraction might be $\sim$ 1–5%.[41–43] The ρ line shape with interference is derived as follows. The $\pi^+\pi^-$ production amplitude, S, near the ρ is given by[44]

$$S = [A(\rho)\ A(\omega)] \left\{[M] - m^2\,[I]\right\}^{-1} \begin{bmatrix} T(\rho \rightarrow \pi\pi) \\ T(\omega \rightarrow \pi\pi) \end{bmatrix}, \tag{7.5}$$

where $[I]$ is the unit matrix, A the production amplitude of the specified resonance, T the specified direct decay rate, and $[M]$ the mass matrix, given by

$$[M] = \begin{bmatrix} m_\rho^2 - i m_\rho \Gamma_\rho & -\delta(m_\rho + m_\omega) \\ -\delta(m_\rho + m_\omega) & m_\omega^2 - i m_\omega \Gamma_\omega \end{bmatrix}. \tag{7.6}$$

The parameter δ expresses the electromagnetic mixing of the ρ and ω, and is complex. The direct decay element $T(\omega \rightarrow \pi\pi)$ was calculated to be about 8 keV and therefore can be neglected.[45]

Defining

$$P_x \equiv m_x^2 - m^2 - i m_x \Gamma_x, \tag{7.7}$$

$$\Delta \equiv \delta(m_\rho + m_\omega), \tag{7.8}$$

and

$$D \equiv P_\rho P_\omega - \Delta^2, \tag{7.9}$$

S is

$$\begin{aligned} S &= [A(\rho)\ A(\omega)] \begin{bmatrix} P_\omega/D & \Delta/D \\ \Delta/D & P_\rho/D \end{bmatrix} \begin{bmatrix} T(\rho \rightarrow \pi\pi) \\ 0 \end{bmatrix} \\ &= \frac{A(\rho)T(\rho)P_\omega}{D} \left\{1 + \frac{A(\omega)}{A(\rho)}\frac{\Delta}{P_\omega}\right\} \\ &= \frac{A(\rho)T(\rho)}{P_\rho} \left\{1 + \frac{A(\omega)}{A(\rho)}\frac{\Delta}{P_\omega}\right\} \frac{1}{1 - \Delta^2/P_\rho P_\omega}. \end{aligned} \tag{7.10}$$

The first factor of Equation 7.10, when squared, is just the standard ρ Breit–Wigner line shape without interference effects. Therefore, the cross section is given by

$$\sigma(m) = BW_\rho(m)\left|1 + \frac{A(\omega)}{A(\rho)}\frac{\Delta}{P_\omega}\right|^2 \frac{1}{|1-\Delta^2/P_\rho P_\omega|^2}, \tag{7.11}$$

where $BW_\rho(m)$ means a ρ Breit–Wigner shape. The final factor is very near 1 for the predicted value of $|\delta| \sim 2.5\,\mathrm{MeV}$.[42]

In the ρ region, only S- and P-waves are required, and the combination of moments,

$$\sigma_+^P \equiv \frac{1}{3}t_{00} - \frac{\sqrt{5}}{6}t_{22} \tag{7.12}$$

$$= |P_+|^2 + |S|^2/3 \quad \text{(neglecting D-waves)} \tag{7.13}$$

which projects the P-wave natural parity exchange cross section yields the mass distribution shown in Figure 7.24. The S-wave contribution is negligible compared to that due to $|P_+|$, as will be seen in Section 7.6.

The distribution of Figure 7.24 was fit to Equation 7.11, smeared by the mass resolution measured in Section 7.3. The parameters of the ρ and ω were fixed to the Particle Data Group (PDG) values[30] of $m_\rho = 768\,\mathrm{MeV/c^2}$, $\Gamma_\rho = 151\,\mathrm{MeV/c^2}$, $m_\omega = 782\,\mathrm{MeV/c^2}$, and $\Gamma_\omega = 8.4\,\mathrm{MeV/c^2}$. Initially, a linear background was included, but was found to be unnecessary and was omitted in the final analysis. The fit yields the value $(2.15 \pm 0.35)\,\mathrm{MeV/c^2}$ for the magnitude of the mass-mixing term δ. This implies a branching fraction of $(1.5 \pm 0.5)\%$ for the decay $\omega \to \pi^+\pi^-$, in excellent agreement with the original estimates and with the present world average of $(2.21 \pm 0.30)\%$.[30] In order to obtain this result, complete coherence of the ρ and ω production amplitudes has been assumed; also, these production amplitudes have been assumed to be equal, as expected from SU(3). This is justified by the fact that the fitted value of the ρ–ω production phase is (-8 ± 10) degrees, consistent with the SU(3) prediction of 0, and by cross section data from other experiments.[46] The quality of the fit, as indicated by the solid dots in Figure 7.24, is excellent, and the underlying line shape, represented by the solid curve, exhibits a rather spectacular interference effect. The ρ Breit–Wigner line shape, shown as the dotted curve, clearly does not provide a good description of the data.

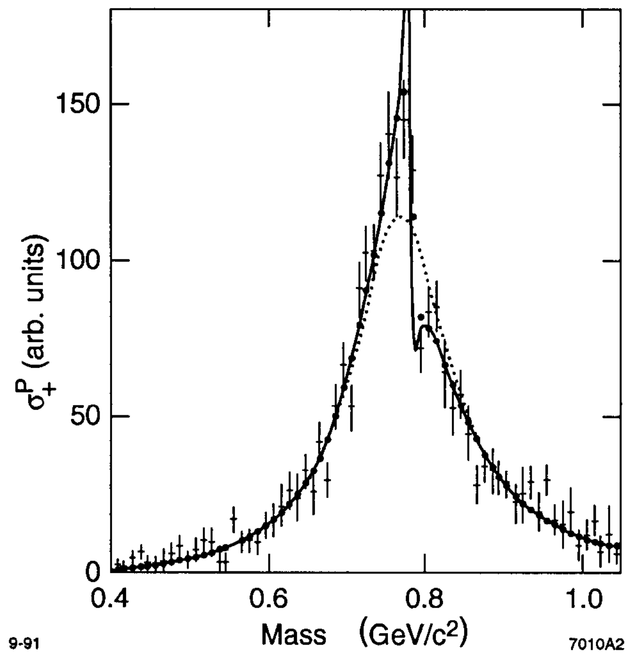

Figure 7.24: The σ^P_+ projection for the forward ρ. The data are shown as crosses, the solid curve represents the fit described in the text, and the dots correspond to the integral of this curve, after smearing for resolution, over each 10 MeV/c^2 bin. The dotted curve shows the contribution to the solid curve resulting from the ρ Breit–Wigner line-shape.

To measure the resonance parameters of the ρ, the distribution in Figure 7.24 was fit with the ρ parameters free. The result is $(766 \pm 3)\,\mathrm{MeV/c^2}$ for the mass, $(151 \pm 9)\,\mathrm{MeV/c^2}$ for the width, and $5^{+3}_{-2}\,\mathrm{GeV^{-1}}$ for the barrier factor. The uncertainties are statistical only. These results compare very well with the current world averages[30] of $(768.1 \pm 0.5)\,\mathrm{MeV/c^2}$, $(151.5 \pm 1.2)\,\mathrm{MeV/c^2}$, and $5.3^{+0.9}_{-0.7}\,\mathrm{GeV^{-1}}$.

The t' differential cross section for the moments combinations σ^P_+, σ^P_-, and σ^P_0 at the ρ are shown in Figure 7.25. These plots were made by computing the moments *without* removing the Σ resonances. The background was removed by subtracting sidebands on either side of the ρ and renormalizing the number of events to the total cross section (see Section 7.9). The lowest bin does not extend to $t' = 0$ because the acceptance is too small to properly determine the cross section. The

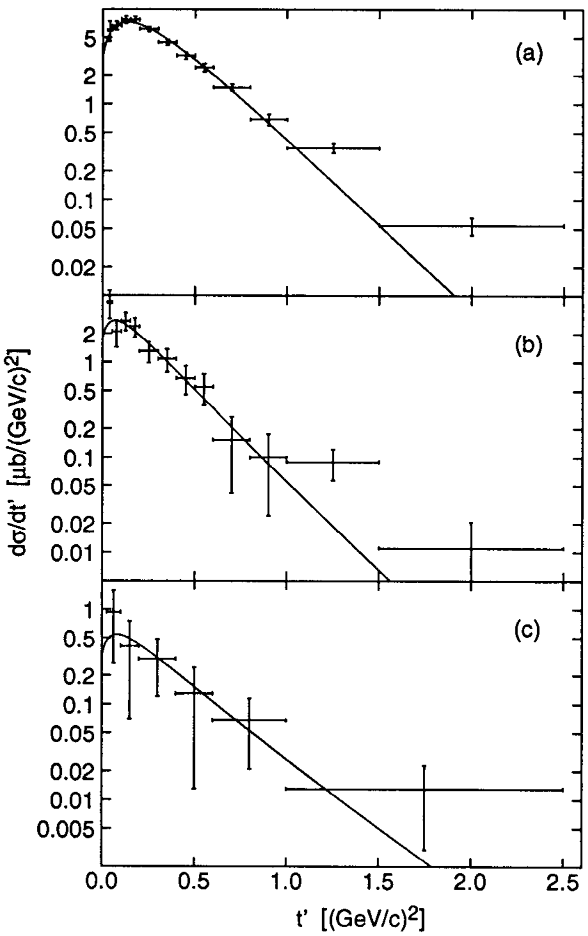

Figure 7.25: The differential cross section for (a) σ_+^P, (b) σ_-^P, and (c) σ_0^P at the ρ. The curves represent the fits described in the text; only the points below $t' < 1.0\,(\mathrm{GeV/c})^2$ were fit.

Quantity	Exchange Mass (MeV/c^2)	Slope α ((GeV/c)$^{-2}$)	χ^2/DoF
σ_+^P	660 ± 110	3.1 ± 0.5	2.3 / 7
	890	3.90 ± 0.14	4.3 / 8
σ_-^P	440 ± 170	3.3 ± 1.4	4.1 / 8
	493	3.7 ± 0.6	4.2 / 8
σ_0^P	493	2.8 ± 1.7	0.5 / 3

Table 7.2: The results of fits to the ρ differential cross sections. The fits with no uncertainty on the exchange mass were performed with the mass fixed.

distributions, up to $t' < 1.0\,(\mathrm{GeV/c})^2$, were fitted with the form

$$\frac{d\sigma}{dt'} \propto \frac{[t' + (m_\Lambda - m_\mathrm{p})^2]\mathrm{e}^{-\alpha t'}}{(t' + m_x^2)^2}, \tag{7.14}$$

where m_x is the mass of the exchange particle, namely the K* for natural parity exchange and the K for unnatural parity exchange. The results of the fit are given in Table 7.2. For σ_+^P and σ_-^P, two fits were performed, one where the exchange particle mass was allowed to vary and one with it fixed. The fitted exchange masses are roughly consistent with the expected values and all the fitted slopes are quite consistent with a single value of $\sim 3.9\,(\mathrm{GeV/c})^{-2}$.

7.5.1 Λ Polarization

The polarization of the Λ at the ρ was measured from its decay asymmetry. The decay distribution of the Λ is given by

$$f(\cos\theta) \propto \frac{1}{2}(1 + \alpha_\Lambda P \cos\theta), \tag{7.15}$$

where $\alpha_\Lambda = 0.642$ is the weak decay parameter,[30] and P is the polarization. The decay angle, θ, is the angle between the daughter proton and the decay plane normal, defined as $\hat{n} = \hat{\Lambda} \times \hat{K}$, where $\hat{K}$ is a unit vector along the incident beam momentum and $\hat{\Lambda}$ along the Λ momentum. The polarization was computed by

$$P = \frac{2}{\alpha_\Lambda}\frac{N_+ - N_-}{N_+ + N_-}, \tag{7.16}$$

where N_+ is the number of events in the forward hemisphere (*i.e.* $\cos\theta > 0$) and N_- the number in the backward hemisphere.

In order to measure N_+ and N_-, one needs the acceptance corrected number of events; however, there is an additional acceptance loss around $\cos\theta \sim 0$ which was not parametrized in the general acceptance calculation (this loss is part of the average acceptance when one is looking at mass or t' spectra). The loss is due to the fact that when $\cos\theta = 0$, the proton is travelling in the same plane as the Λ. When it is travelling backward in the Λ rest frame, it is moving slowly in the lab frame, thus significantly increasing the probability that it is absorbed in the

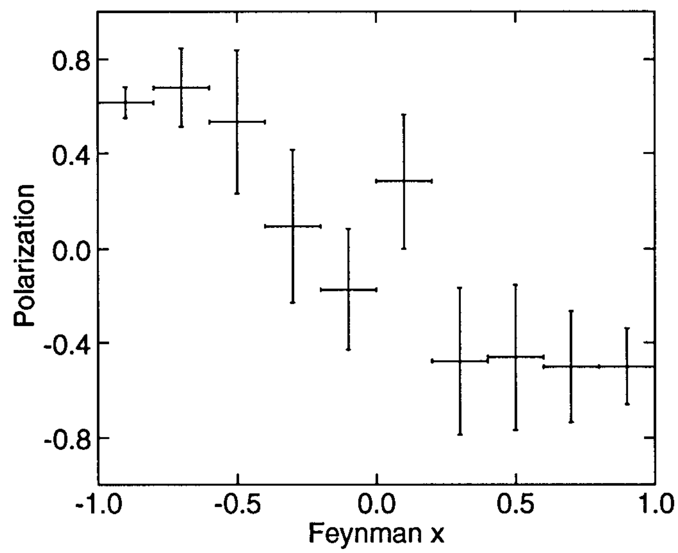

Figure 7.26: The polarization of the Λ at the ρ.

target. To correct for the loss, the data and the Monte Carlo were binned into 10 bins in $\cos\theta$ at each point where the polarization was measured. The data were corrected using the relative number of events in the corresponding MC bin, and summed to find N_+ and N_-.

Figure 7.26 shows the polarization versus Feynman x at the ρ. The $\Lambda\pi$ resonances have been removed as in the earlier analyses before computing the polarization. The polarization is obviously large and positive for backward Λ events ($x < 0$) and strongly negative in the forward direction. The distribution is very similar to the ones measured by the 4.2 GeV/c Bubble Chamber experiment[37] and in inclusive Λ studies.[47]

7.6 Amplitude Analysis of $f_2(1270)$ Region

A partial wave amplitude analysis of the $\pi^+\pi^-$ system was carried out using S- and P-waves (*i.e.* 6 parameters) in the mass region up to 1.0 GeV/c^2 and using S-, P- and D-waves (12 parameters) from 1.0 GeV/c^2 to 1.5 GeV/c^2. The resulting S and P amplitudes and phases are shown in Figure 7.27 and the D amplitudes

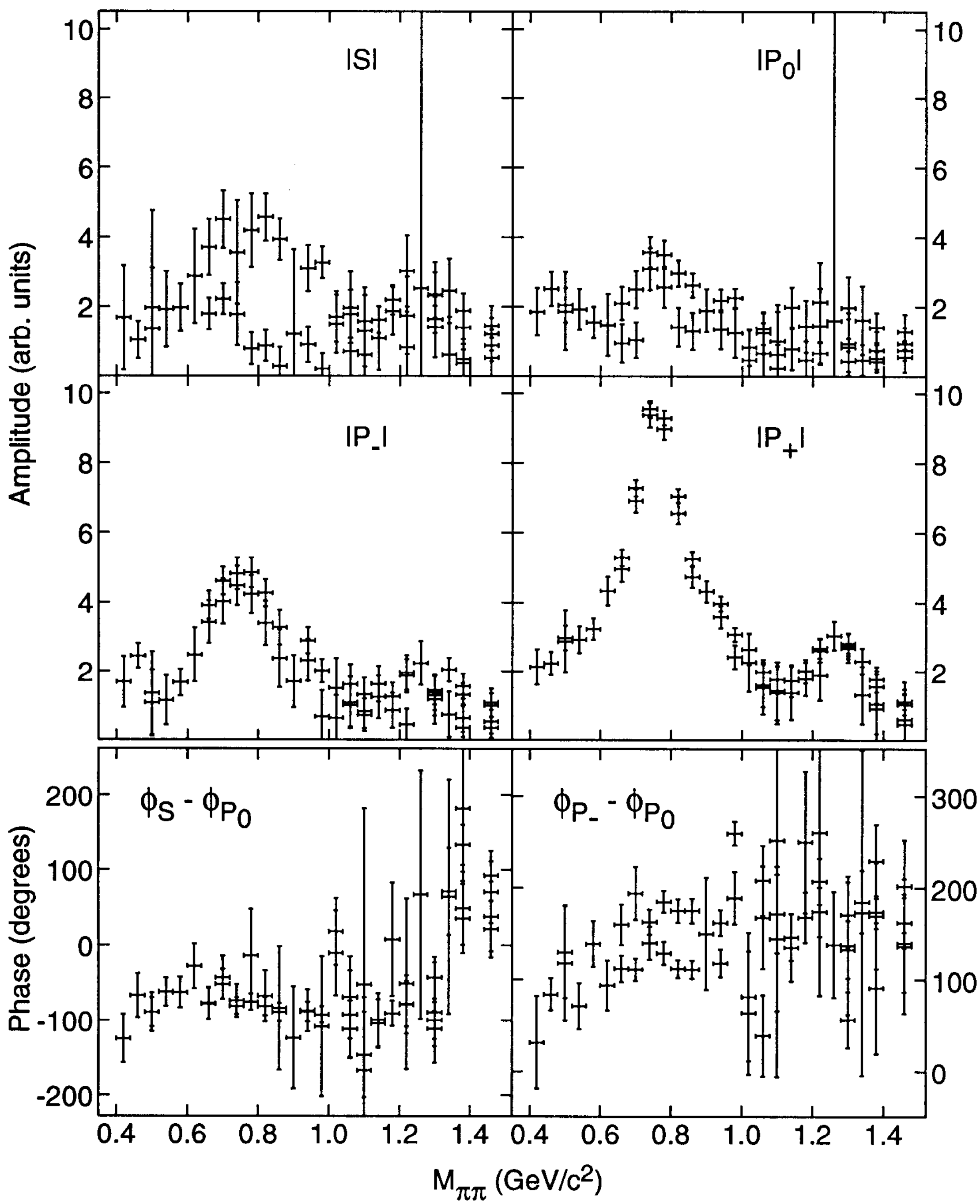

Figure 7.27: The S- and P-wave amplitudes and relative phases for the forward $\pi^+\pi^-$ system. Above $1\,\mathrm{GeV/c^2}$, the results are from a PWA including D-waves.

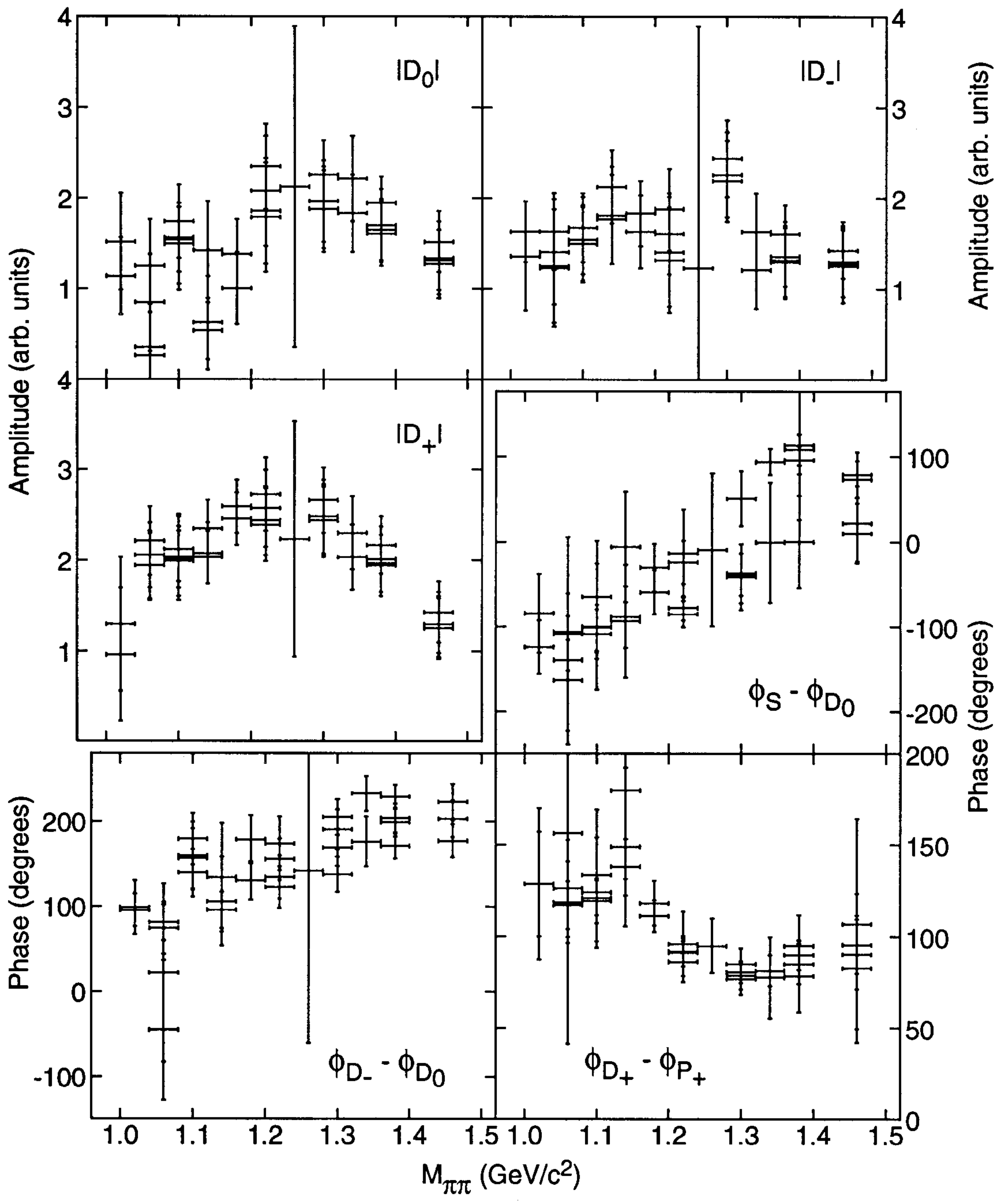

Figure 7.28: The D-wave amplitudes and relative phases for the forward $\pi^+\pi^-$ system.

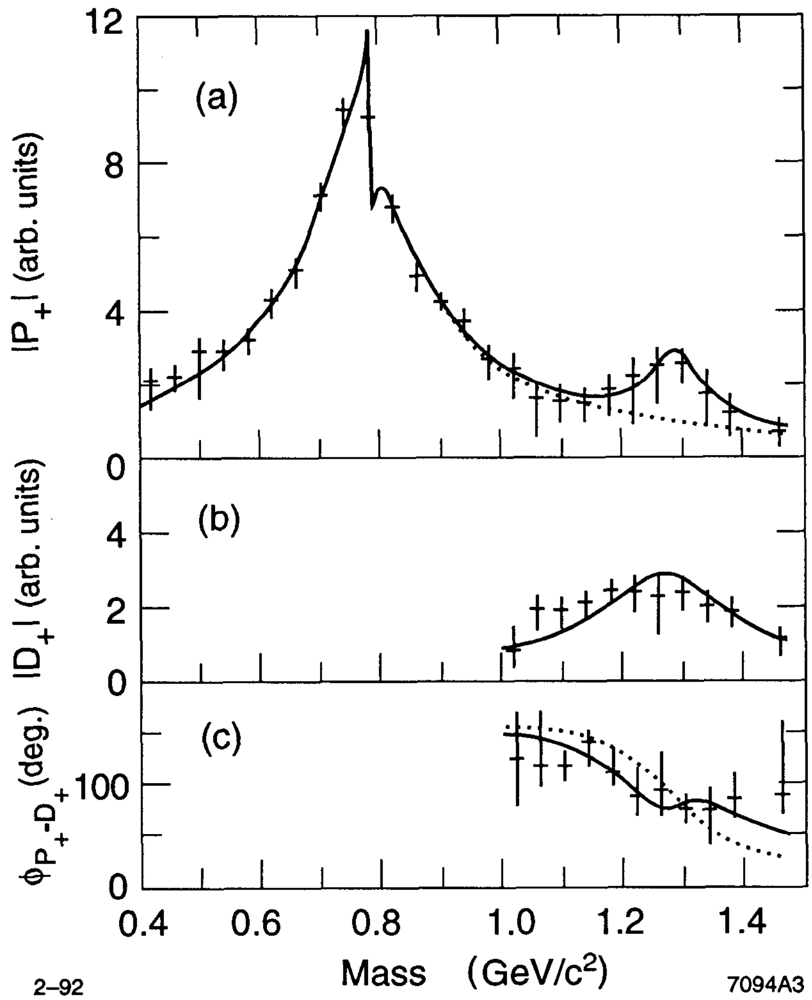

Figure 7.29: The fits to the (a) P_+ amplitude, (b) D_+ amplitude, and (c) P_+–D_+ relative phase. The dotted curves correspond to the solid curves with the additional P-wave Breit–Wigner set to zero.

and phases are show in Figure 7.28. The resulting S-wave is small and subject to large uncertainties. The ρ region is dominated by the P_+ amplitude, but P_- is also significant; P_0 is smaller than P_- and not very well defined. The D_+ and D_- waves show bumps at the $f_2(1270)$, but D_0 is essentially flat. An unexpected feature is that P_+, and to a lesser extent P_-, also exhibit structure in this mass range.

Parameter	Fit A	Fit B
$\rho(1300)$ Mass (MeV/c^2)	1290 ± 30	1290^{+20}_{-30}
$\rho(1300)$ Width (MeV/c^2)	90^{+40}_{-30}	120^{+60}_{-50}
$\rho(1300)$ Phase (degrees)	80 ± 20	90 ± 30
$\rho(1300)$ Amplitude (rel. to ρ)	0.28 ± 0.04	0.26 ± 0.05
ρ–$f_2(1270)$ Phase (degrees)	12 ± 10	6 ± 11
χ^2/DoF	23/41	9/33

Table 7.3: Results of fits to P_+ and D_+ magnitudes and relative phase. Errors are statistical only. Fit B comes from the PWA with $|D_+|$ fixed.

To determine the parameters of the higher P-wave resonance, the P_+ and D_+ amplitudes and their relative phase were fit. The points used in the fit must incorporate multiple solutions from the partial wave analysis. The data points themselves are the average of any multiple solutions. The errors are found by determining the points where the χ^2 function of the PWA increases from its minimum by 4 (*i.e.* a two standard deviation interval) and dividing by 2. If a 2σ point could not be found in the physical region, the 1σ point was used. The data are shown in Figure 7.29.

The P-wave was described by the sum of the ρ–ω mixing shape found earlier and a Breit–Wigner describing the 1.27 GeV/c^2 region, while the D_+ wave was represented by an $f_2(1270)$ Breit–Wigner. The fit is shown in Figure 7.29 as the solid curves. The fit results are shown in Table 7.3 as "Fit A". A fit to the data excluding the second P-wave resonance, shown as the dotted curves in Figure 7.29, yields a χ^2 of 46 for 45 degrees of freedom. While this is an acceptable χ^2, the dotted curves do not provide a good description of the P_+ amplitude or the relative phase in the region 1.1–1.4 GeV/c^2.

In order to better define the P-wave amplitudes, the D_+ amplitude in the PWA was fixed to the $f_2(1270)$ Breit–Wigner shape with the amplitude set to that found in the previous fit, and the PWA was redone. The P_+ amplitude and the P_+–D_+ relative phase were fitted as before; the results are shown in Table 7.3, "Fit B", and in Figure 7.30. This fit yields a mass and width for the new resonance, the $\rho(1300)$,

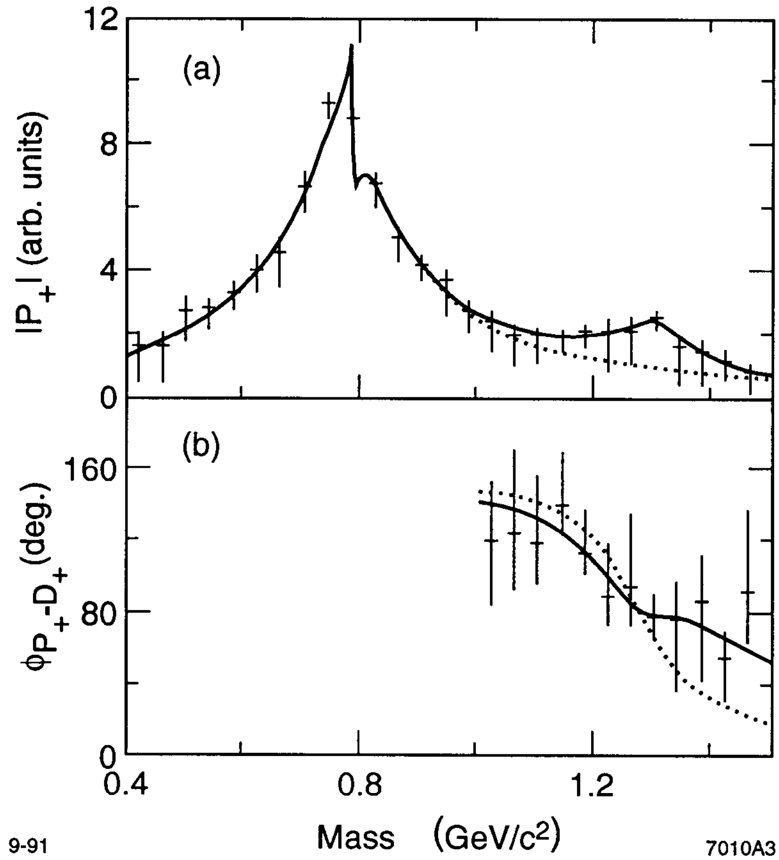

Figure 7.30: The mass dependence of (a) the P_+ amplitude and (b) the P_+–D_+ relative phase resulting from the fits to the spherical harmonic moments with the D_+ amplitude fixed. The curves are the same as for Figure 7.29.

of $(1290^{+20}_{-30})\text{MeV/c}^2$ and $(120^{+60}_{-50})\text{MeV/c}^2$, respectively. The resulting description of the data of Figures 7.30a and 7.30b is clearly very good. The dotted curves of Figure 7.30 again correspond to no $\rho(1300)$ contribution, and do not provide a good description of the data. Finally, the size of the $\rho(1300)$ amplitude relative to that of the ρ indicates an elasticity $\sim 5\%$ for this state.

As further evidence for the $\rho(1300)$, Figure 7.31 shows the progression of the quantity σ^P_{+-} through the different stages of the analysis, where

$$\begin{aligned} \sigma^P_{+-} &\equiv \sqrt{\frac{5}{2}}t_{42} - \sqrt{\frac{10}{3}}t_{22} \\ &= |P_+|^2 - |P_-|^2 \quad \text{(neglecting F-wave).} \end{aligned} \tag{7.17}$$

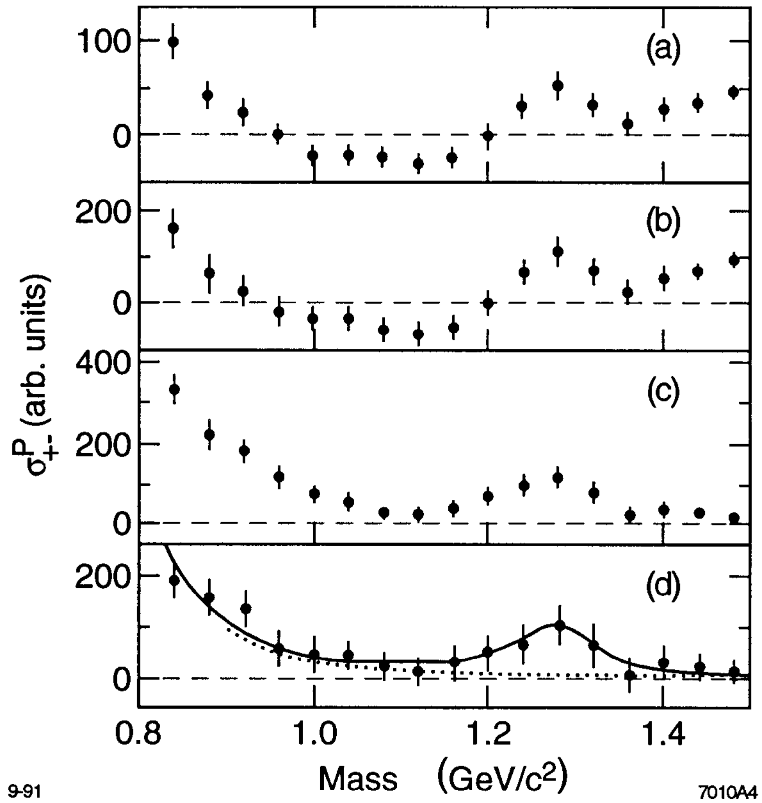

Figure 7.31: The σ^P_{+-} projection of the data at different stages of the analysis: (a) the raw data, (b) the acceptance corrected data, (c) the data with the Σ^* overlap removed, and (d) the data after correction for the overlap cuts. The curve in (d) is the same as for Figure 7.30a renormalized for this data.

Figure 7.31a shows σ^P_{+-} for the raw data sample; 7.31b for the acceptance corrected data; 7.31c for the data with the Σ^* overlap removed; and 7.31d for the data corrected for the Σ^* removal. The bump in the P-wave around 1.27 GeV/c^2 is clearly visible in all cases, indicating that it is very unlikely to be a figment of the analysis, instead of a feature of the data. A curve corresponding to "Fit B" of Table 7.30 is drawn on Figure 7.31d to show the agreement.

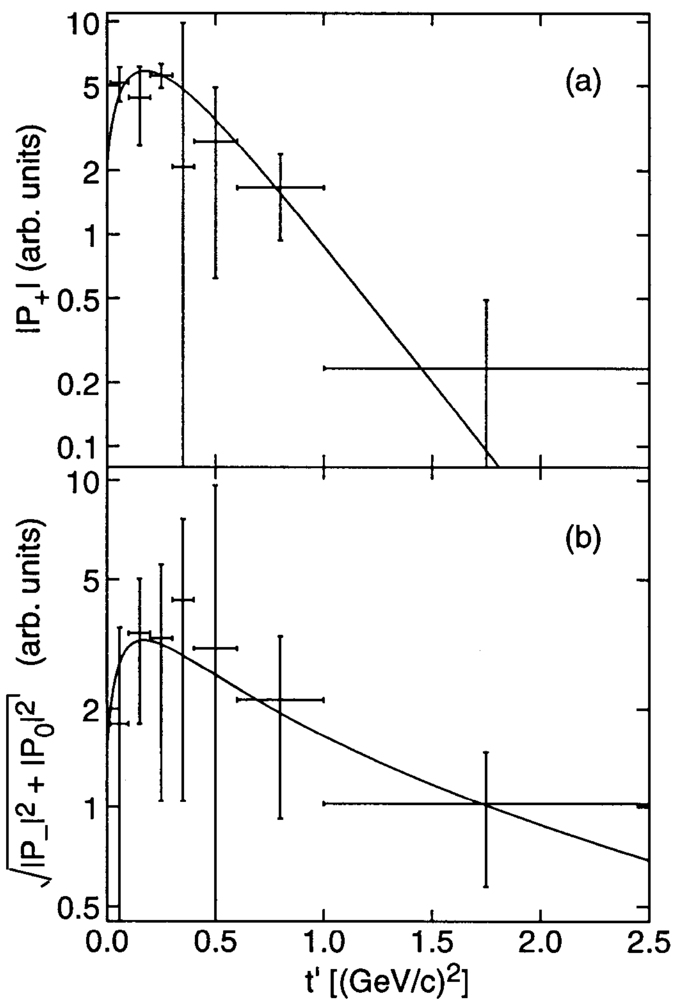

Figure 7.32: The (a) P_+ and (b) P-wave unnatural parity exchange amplitudes ($\sqrt{|P_-|^2 + |P_0|^2}$) for the region $1.2 < m_{\pi^+\pi^-} < 1.4\,\mathrm{GeV/c^2}$. The curves show the fits with the exchange mass fixed, as described in the text.

7.6.1 t' Spectra

The P- and D-wave t' spectra were determined by performing a partial wave analysis on the data with $1.2 < m_{\pi^+\pi^-} < 1.4\,\mathrm{GeV/c^2}$. The P_+ and P-wave unnatural parity exchange amplitudes (*i.e.* $\sqrt{|P_-|^2 + |P_0|^2}$) are shown in Figure 7.32, while the corresponding D-wave spectra are shown in Figure 7.33. No correction has been made for the effect of the ρ tail in this region.

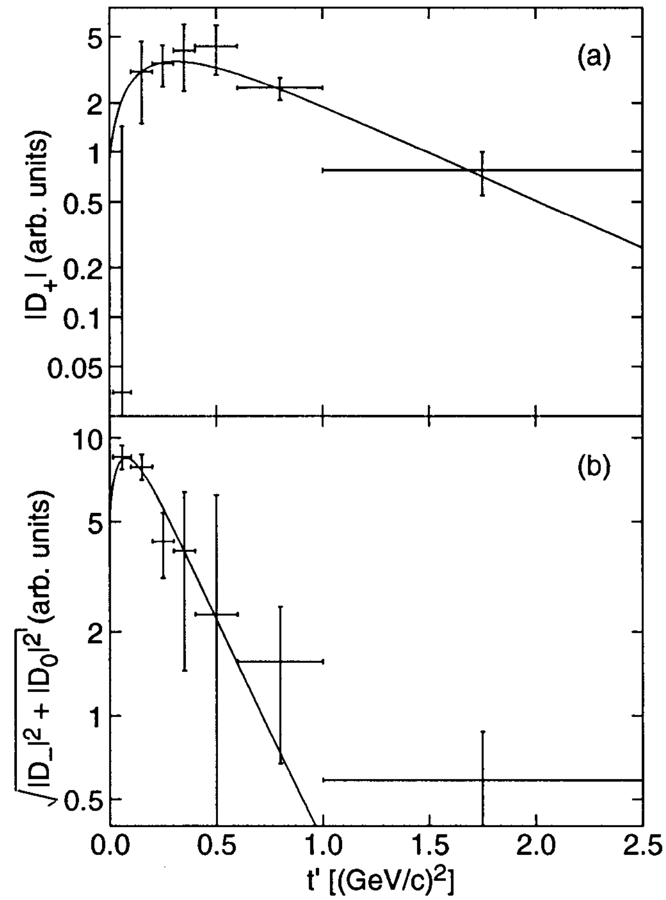

Figure 7.33: The (a) D_+ and (b) D-wave unnatural parity exchange amplitudes ($\sqrt{|D_-|^2 + |D_0|^2}$) for the region $1.2 < m_{\pi^+\pi^-} < 1.4\,\mathrm{GeV/c^2}$. The curves show the fits with the exchange mass fixed, as described in the text.

Similar to the ρ differential cross section, the shapes were fit with Equation 7.14, both with the exchange particle mass free and fixed. The results are shown in Table 7.4.

Quantity	Exchange Mass (MeV/c^2)	Slope α ((GeV/c)$^{-2}$)	χ^2/DoF
$\lvert P_+\rvert$	600 ± 200	1.7 ± 1.0	1.0 / 4
	890	2.8 ± 0.7	1.6 / 5
$\sqrt{\lvert P_-\rvert^2 + \lvert P_0\rvert^2}$	690 ± 520	0.6 ± 1.2	0.2 / 4
	493	0.1 ± 0.4	0.5 / 5
$\lvert D_+\rvert$	2130 ± 3610	2.0 ± 1.1	2.2 / 4
	890	1.1 ± 0.3	2.8 / 5
$\sqrt{\lvert P_-\rvert^2 + \lvert P_0\rvert^2}$	330 ± 50	0.7 ± 0.5	2.0 / 5
	493	3.0 ± 1.3	6.1 / 5

Table 7.4: The results of fits to the t' spectra for the region $1.2 < m_{\pi^+\pi^-} < 1.4\,\mathrm{GeV/c^2}$. The fits with no uncertainty on the exchange mass were performed with the mass fixed.

7.7 Amplitude Analysis of High Mass Region

In order to determine the wave content of the broad bump in the mass spectrum around $1.7\,\mathrm{GeV/c^2}$, an amplitude analysis allowing F-waves was performed in the region $1.5\,\mathrm{GeV/c^2}$ to $2.0\,\mathrm{GeV/c^2}$ using $80\,\mathrm{MeV/c^2}$ bins. All amplitudes are poorly defined, but there is some evidence for a spin 3 resonance around $1.7\,\mathrm{GeV/c^2}$. The amplitude analysis is hampered by residual backgrounds from the Σ^* overlap which cannot be removed without creating instabilities in the subsequent correction. Figure 7.34a shows the F_+ amplitude and Figure 7.34b the Y_6^2 moment, which is proportional to $(|F_+|^2 - |F_-|^2)$. The curves in Figure 7.34 are spin 3 Breit–Wigners with a mass of $1690\,\mathrm{MeV/c^2}$ and width of $215\,\mathrm{MeV/c^2}$, the PDG values[30] of the $\rho_3(1690)$. The Y_6^2 curve includes a constant background, shown as the dotted curve. The curves are in reasonable agreement with the data, but lack of data prevents a definite conclusion.

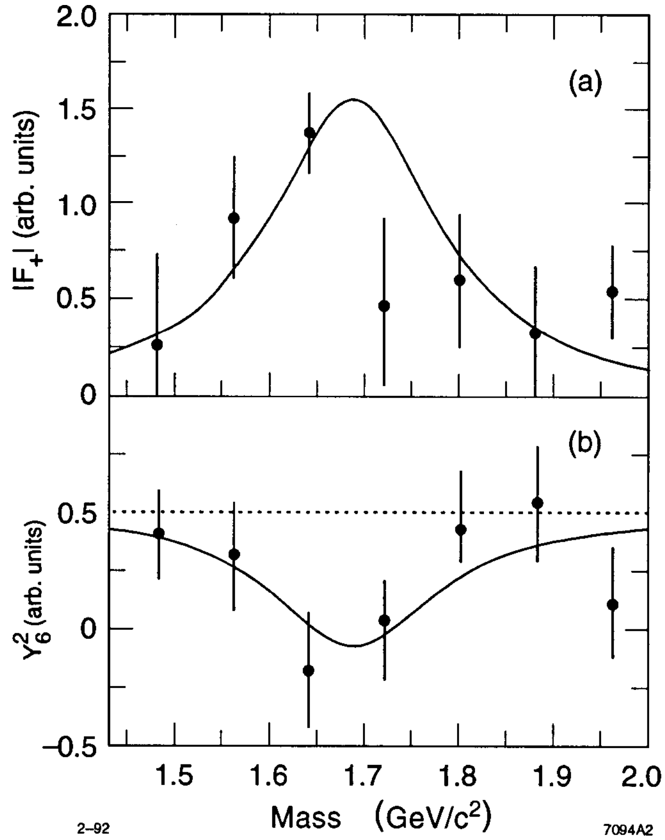

Figure 7.34: The mass dependence of (a) the F_+ amplitude and (b) the Y_6^2 moment from 1.5 GeV/c^2 to 2.0 GeV/c^2 in 80 MeV/c^2 bins. The curves represent the $\rho_3(1690)$. Figure (b) includes a constant background shown as the dotted curve.

7.8 Forward Λ Sample

Figure 7.35 shows the Dalitz plot for the sample of 4016 events which have a forward-going Λ. There are clear bands in the $\pi^+\pi^-$ system at the ρ and $f_2(1270)$. There is also evidence of $\Sigma^+(1385)$ and $\Sigma^-(1385)$ production, as well as the higher mass Σs seen in the backward data (see Figures 7.36 and 7.37). The $\pi^+\pi^-$ spectrum corresponding to Figure 7.35 is shown in Figure 7.38 in 40 MeV/c^2 bins. The mass bump around 1.27 GeV/c^2 is stronger relative to the ρ than in the forward $\pi^+\pi^-$ system. The relatively poor statistics make the ρ–ω interference much less obvious than in the forward sample, and the need for wide bins makes analysis difficult.

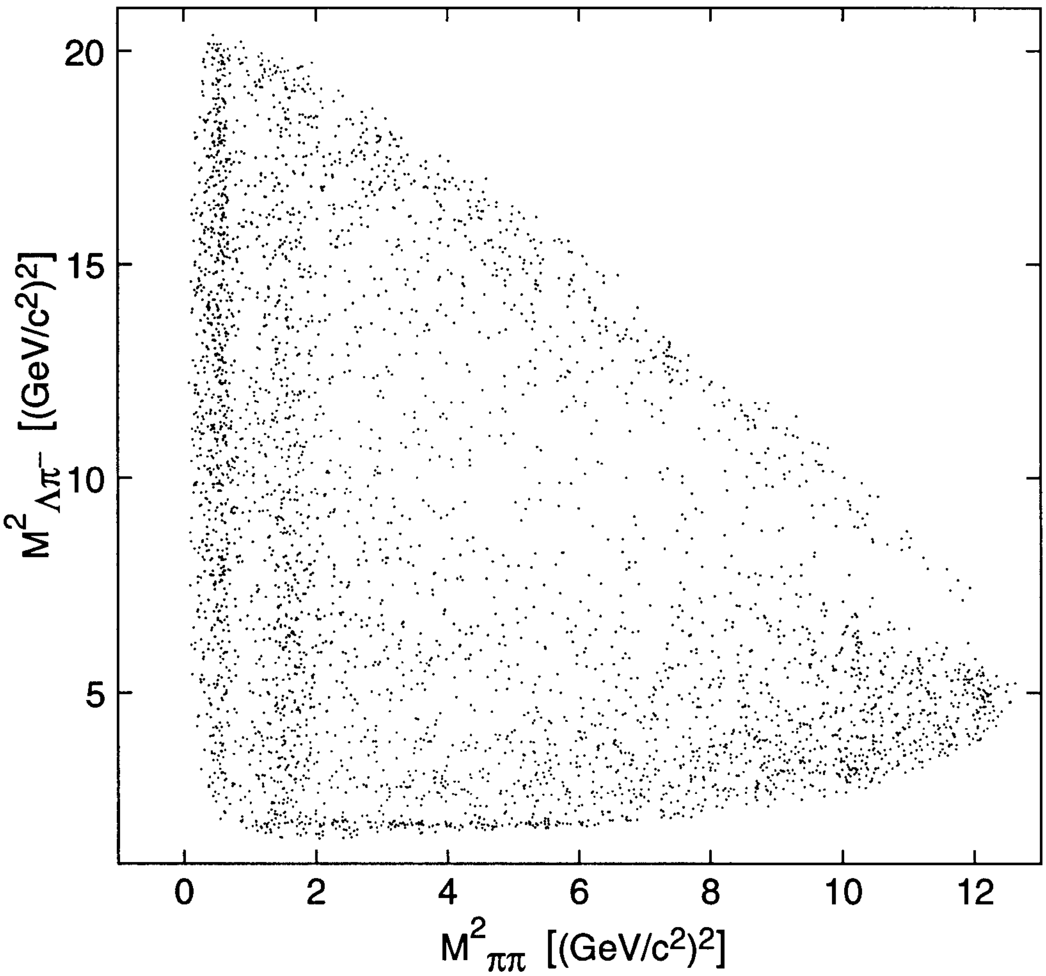

Figure 7.35: The Dalitz Plot for forward Λ events.

To find the moments, both $\Sigma^+(1385)$ and $\Sigma^-(1385)$ were removed by removing events with $m_{\Lambda\pi} < 1.48\,\mathrm{GeV/c^2}$. The higher mass Σ^+ states were not removed for lack of statistics. The moments were acceptance corrected, including the loss of events for the Σ^* cut. The acceptance corrected moments in $80\,\mathrm{MeV/c^2}$ bins are shown in Figures 7.39 through 7.41.

An amplitude analysis was performed including S- and P-waves below $1\,\mathrm{GeV/c^2}$ and up to D-waves from $1\,\mathrm{GeV/c^2}$ to $1.5\,\mathrm{GeV/c^2}$. The results are shown in Figures 7.42 and 7.43. ρ production is seen in all three amplitudes, but $|P_+|$ is somewhat larger and better defined. The shape of the ρ resonance is severely distorted

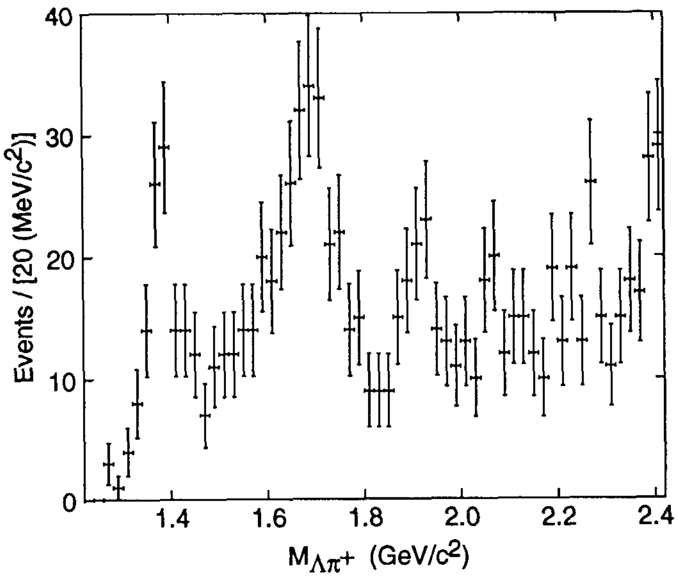

Figure 7.36: The observed $\Lambda\pi^+$ mass spectrum with a forward Λ.

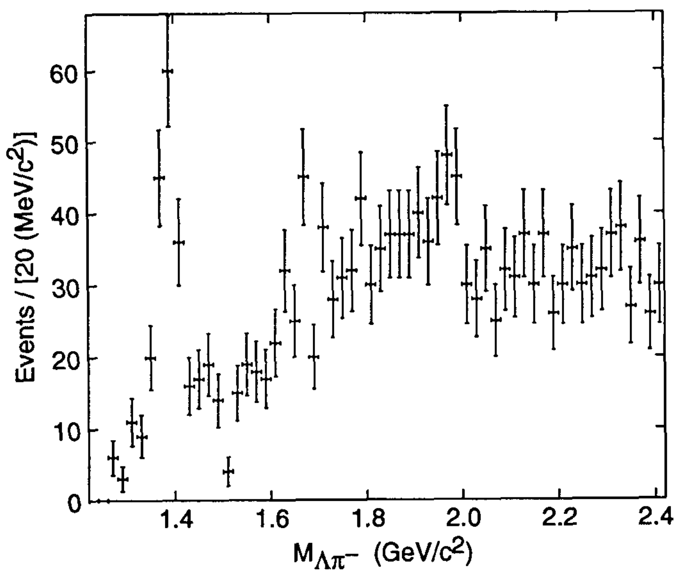

Figure 7.37: The observed $\Lambda\pi^-$ mass spectrum with a forward Λ.

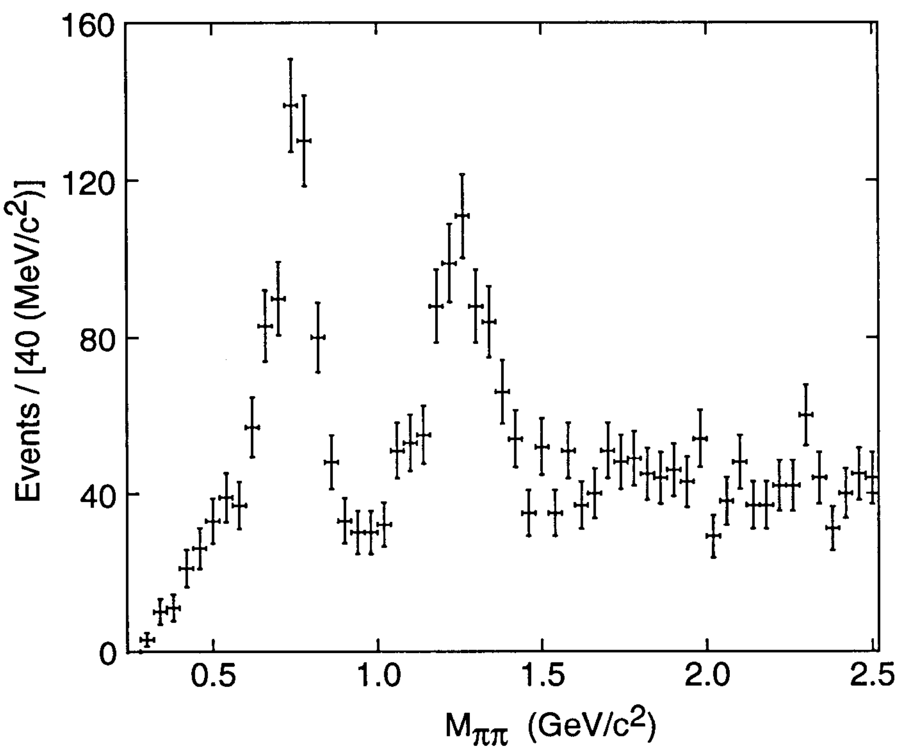

Figure 7.38: The observed mass spectrum for backward $\pi^+\pi^-$ events.

on the low side. The $f_2(1270)$ meson appears to be produced in roughly equal quantities in the three amplitudes, but $|D_-|$ is the best defined. As in the forward $\pi^+\pi^-$ system, there appears to be a second, spin 1 resonance in the data which is consistent with the $\rho(1300)$ found earlier, although multiple solutions make it less clearly defined.

The mass dependence of the P_+ and D_- amplitudes are shown in Figures 7.44a and 7.44b, respectively. The points and uncertainties were found to span the multiple solutions in each bin, as described in Section 7.6. The curves are Breit–Wigner fits to the amplitudes. The P_+ amplitude function included a factor of $m_{\pi\pi}^{-2}$, which was necessary to fit the low side of the ρ. This factor was determined empirically from the data, but could be attributed to the effect of an angular momentum barrier at the production vertex. The $\rho(1300)$ mass and width are fixed to the values from "Fit B" of Table 7.3, while the masses and widths of the

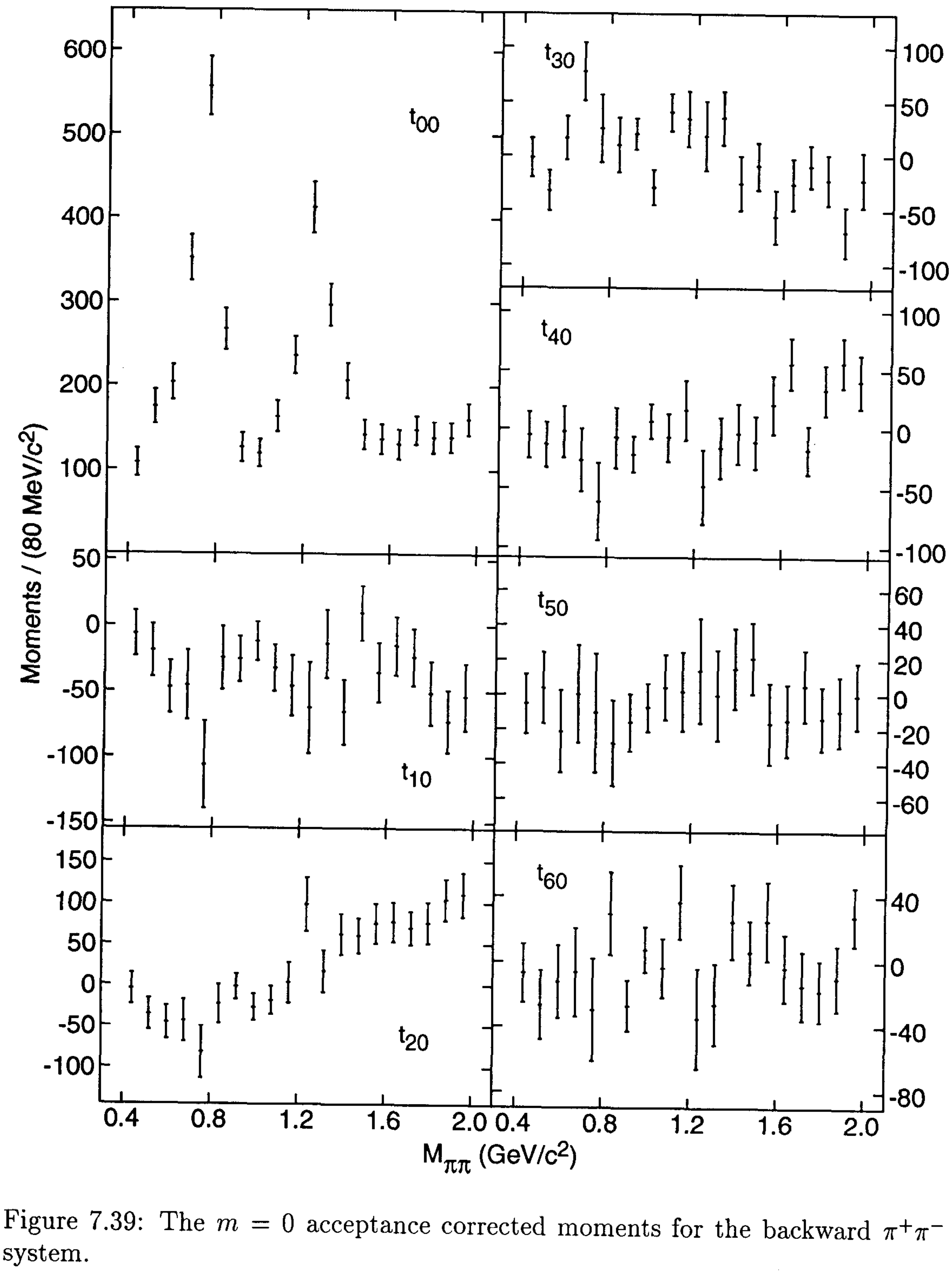

Figure 7.39: The $m = 0$ acceptance corrected moments for the backward $\pi^+\pi^-$ system.

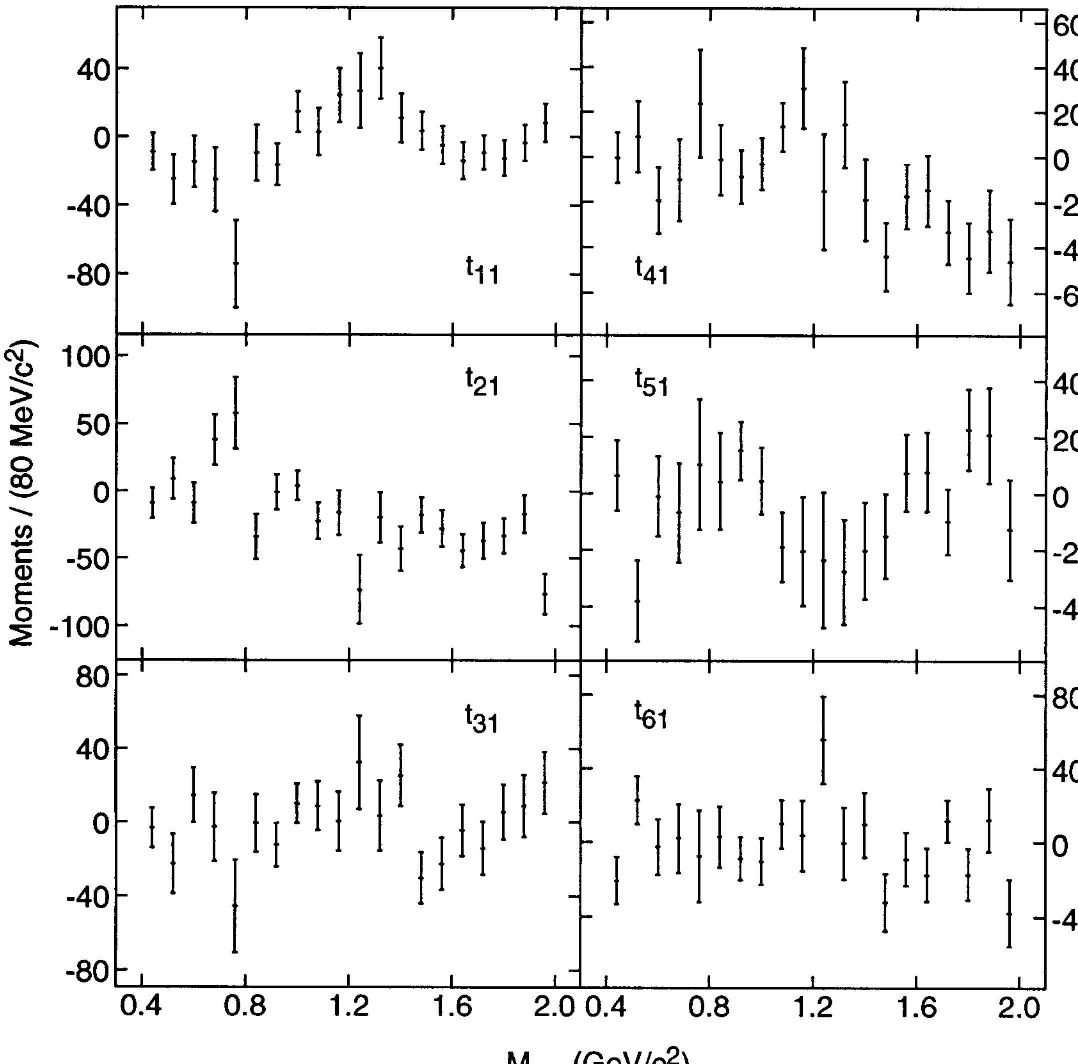

Figure 7.40: The $m = 1$ acceptance corrected moments for the backward $\pi^+\pi^-$ system.

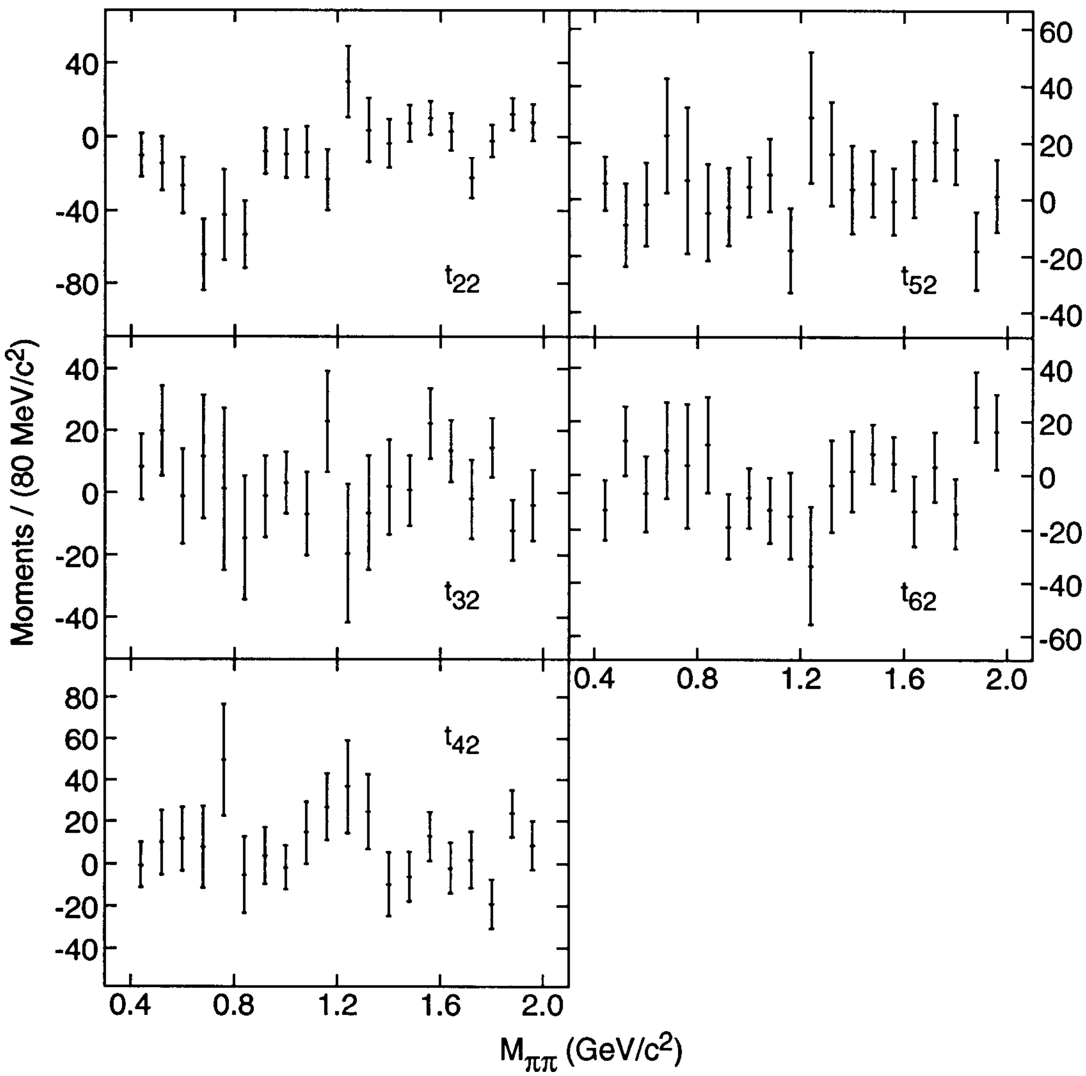

Figure 7.41: The $m = 2$ acceptance corrected moments for the backward $\pi^+\pi^-$ system.

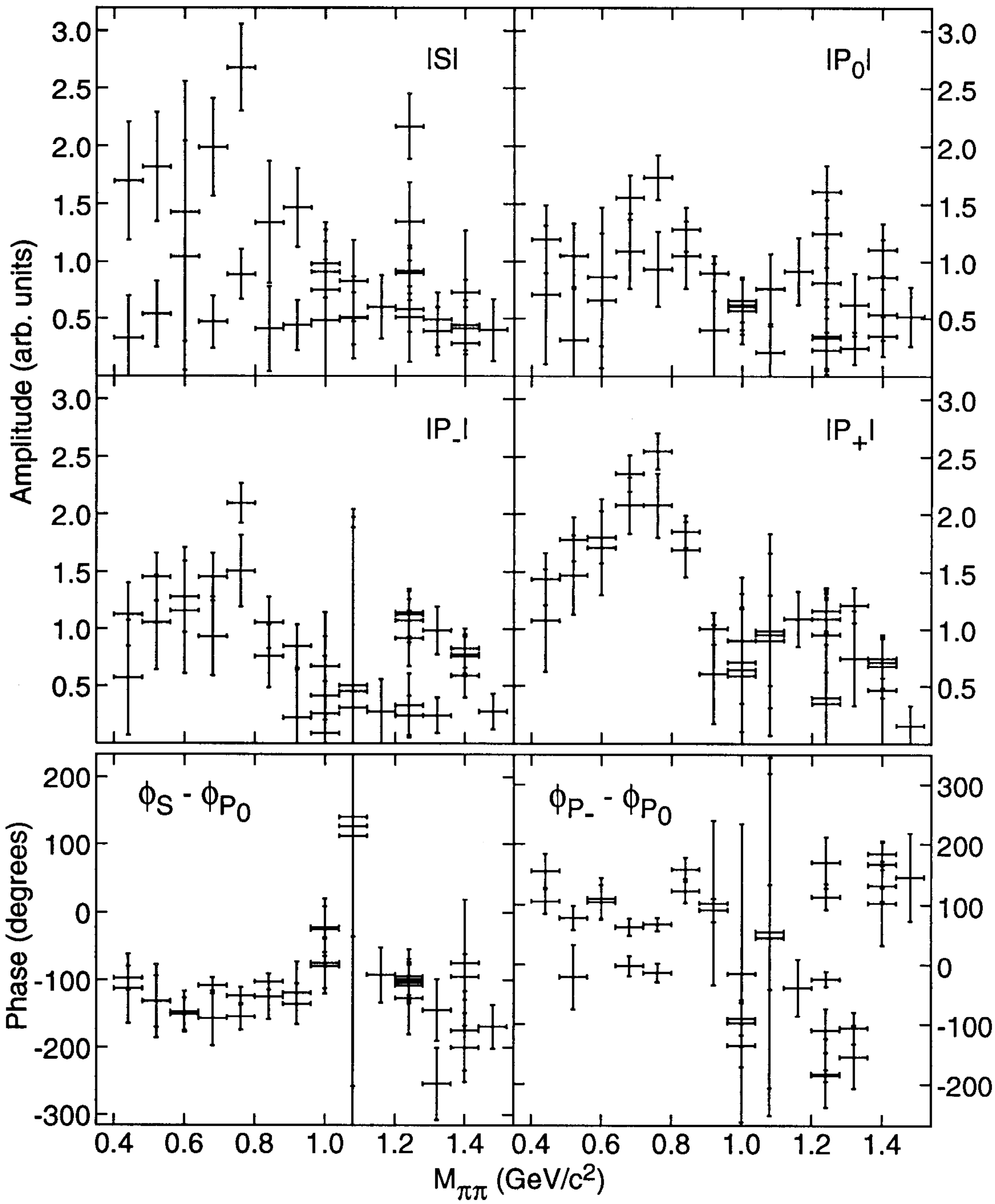

Figure 7.42: The S- and P-wave amplitudes and relative phases for the backward $\pi^+\pi^-$ system.

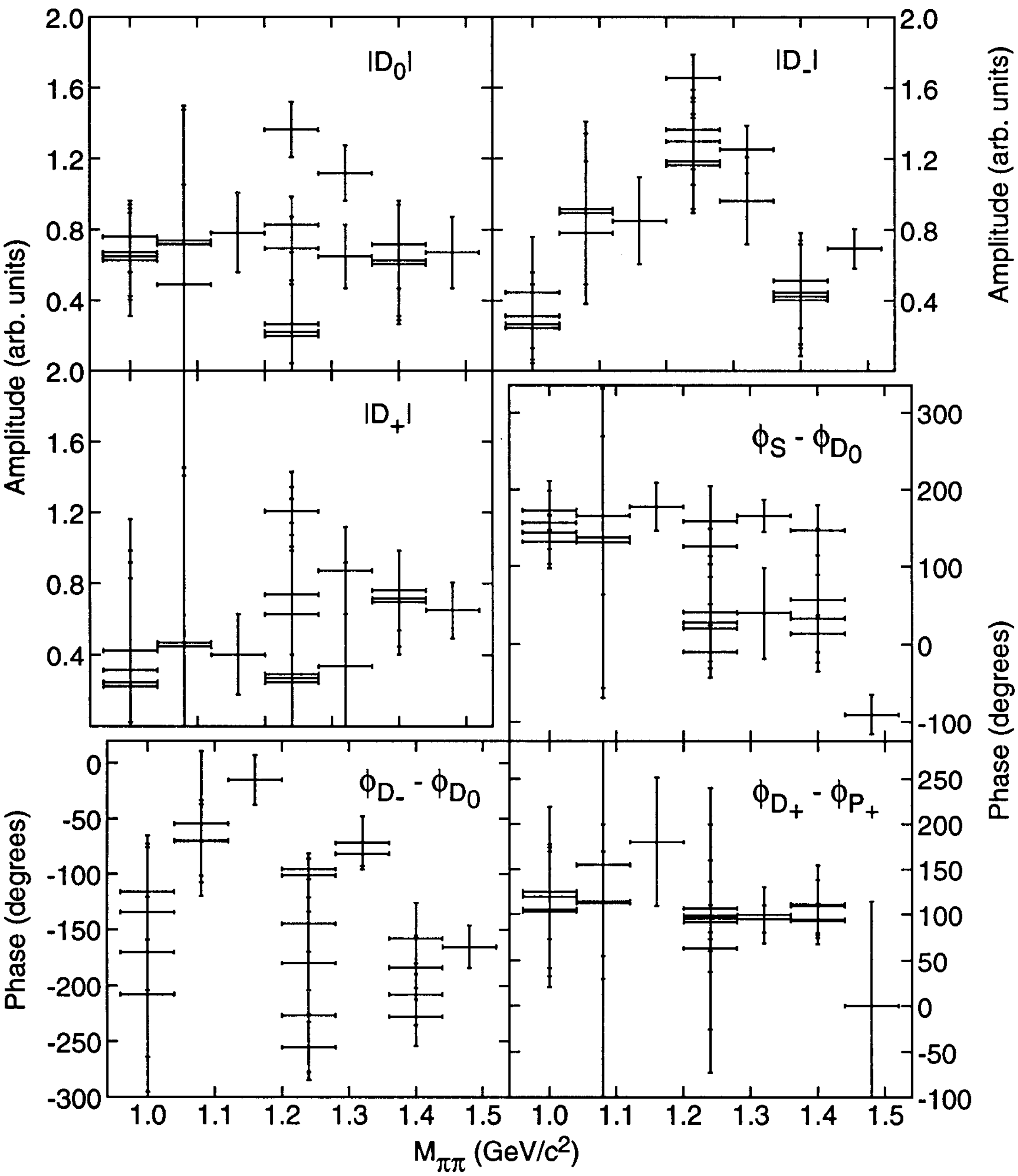

Figure 7.43: The D-wave amplitudes and relative phases for the backward $\pi^+\pi^-$ system.

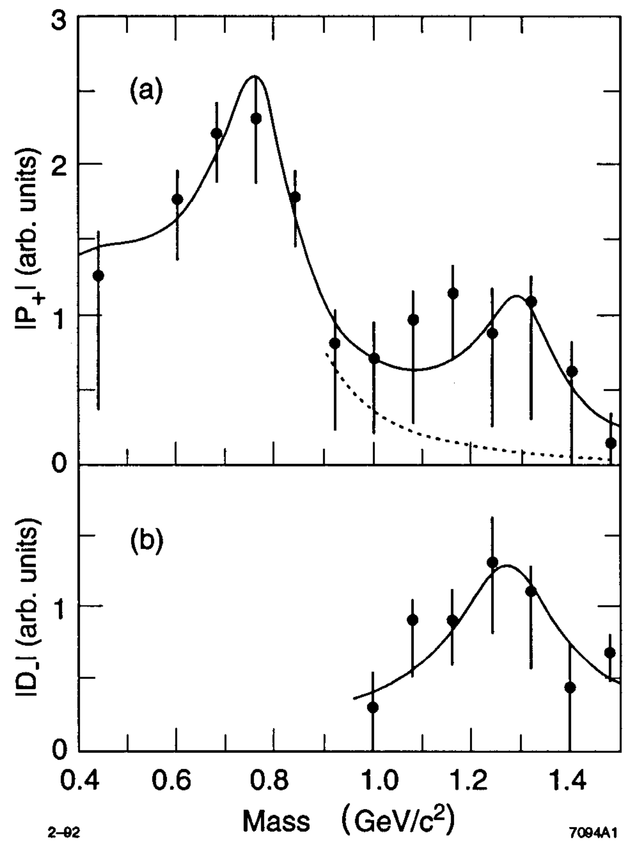

Figure 7.44: The fits to the (a) P_+ and (b) D_- amplitudes for backward $\pi^+\pi^-$. The curves represent a Breit–Wigner fit; the P_+ amplitude was multiplied by $m_{\pi\pi}^{-2}$. The resonance parameters of the $\rho(1300)$ were fixed to the values of "Fit B" in Table 7.3.

ρ and $f_2(1270)$ are fixed to the PDG values.[30] The dotted curve in Figure 7.44a is the fit with no $\rho(1300)$ contribution. The fit does support the presence of the $\rho(1300)$ with the same resonance parameters as found in the forward data, but the statistics are very poor.

Resonance	Cross Section (μb)
Forward ρ	4.74 ± 0.20
Natural parity	3.22 ± 0.12
Unnatural parity	1.57 ± 0.15
Backward ρ	0.21 ± 0.02
Natural parity	0.14 ± 0.01
Total ρ	4.95 ± 0.20
Forward $\rho(1300)$	$0.26 \pm 0.05 \pm 0.06$
Natural parity	0.14 ± 0.04
Forward $f_2(1270)$	1.50 ± 0.14
Natural parity	0.72 ± 0.10
Unnatural parity	0.85 ± 0.11

Table 7.5: Cross sections for resonances in Reaction 7.1 to decay to $\pi^+\pi^-$. Uncertainties are statistical only, except for on the forward $\rho(1300)$ cross section.

7.9 Cross Sections

The cross sections for the production of the meson resonances produced in Reaction 7.1 were calculated from the various fits to the Breit–Wigner shapes. The normalization was determined by integrating the shape for $\pm 5\Gamma_0$ about the resonance mass (the integral was cut off at threshold if necessary). For all resonances, the barrier factor, R, was fixed to $5\,\mathrm{GeV}^{-1}$.

Table 7.5 lists the various cross sections for decay to $\pi^+\pi^-$. The values have been corrected for the visibility of the Λ, using a branching fraction of $(64.1 \pm 0.5)\%$. The overall normalization of the experiment is $4.095(\mathrm{nb})^{-1} \pm 2.7\%$. Except for the forward total $\rho(1300)$ cross section, the uncertainties listed are statistical only, but include the normalization uncertainty. The ρ cross sections come from fits of the number of events and of the σ^P moments combinations (see appendix A). A linear background was included to allow for the S wave. The $\rho(1300)$ and $f_2(1270)$ cross sections were calculated from the PWA fits. The forward $\rho(1300)$ cross section comes from a fit of the total spin 1 intensity (*i.e.* $|P_+|^2 + |P_-|^2 + |P_0|^2$). However,

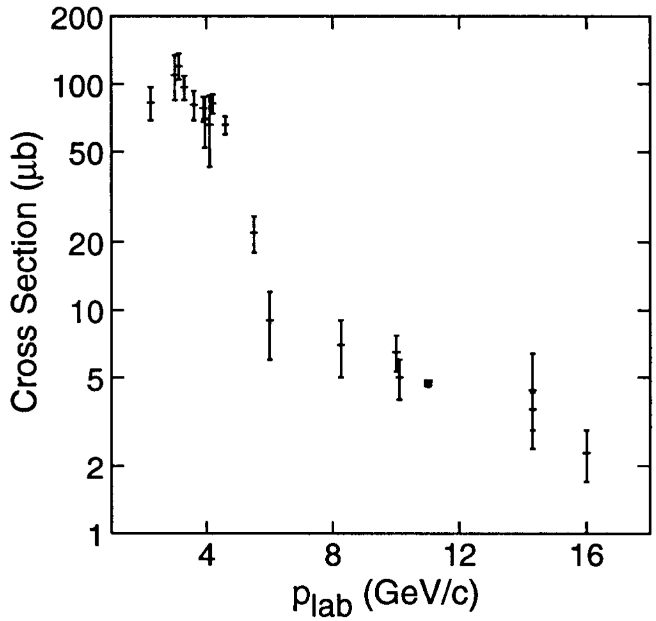

Figure 7.45: The total ρ cross section versus laboratory momentum. The current experiment is shown as the solid square; the uncertainty is smaller than the point.

because of multiple solutions from the PWA, the intensity is essentially double-valued; therefore, a systematic uncertainty of 0.06 μb has been added.

Figure 7.45 shows the total ρ cross section for many experiments at various laboratory momenta;[46] the current result agrees well with previous experiments. Using the accepted branching fraction[30] for $f_2(1270) \to \pi\pi$ of $0.849^{+0.025}_{-0.013}$ and a Clebsch–Gordan coefficient of 2/3 for the charged mode, we get a total cross section for forward $f_2(1270)$ of $(2.65 \pm 0.26)\mu$b.

7.10 Discussion

In the only other large statistics analysis of the $\pi^+\pi^-$ system in Reaction (7.1),[38] no amplitude analysis was attempted because of the much more severe kinematic overlap with Σ production at the 4.2 GeV/c incident K^- momentum; it was simply assumed that the bump at $\sim$ 1.27 GeV/c^2 was due to $f_2(1270)$ production. However, the P-wave amplitude structure obtained for $\pi^+\pi^-$ elastic scattering by

Hyams *et al.*[48] does show some intriguing irregularity in this mass range. The value of the absorption parameter, η, is systematically below 1 throughout this region by an amount which is quite consistent with the presence of a $\rho(1300)$ state of elasticity $\sim$ 5%. Indeed, the parametrization in Hyams *et al.* of the P-wave amplitude in terms of the ρ and the $\rho(1590)$ (elasticity $\sim$ 25%) provides a poor description of the mass dependence of η, and also of the Y_1^0 and Y_3^0 spherical harmonic moments, in this mass range; the addition of the $\rho(1300)$ with elasticity 5% greatly improves the fit to the η mass dependence.

In the context of the $q\bar{q}$ level scheme, the $\rho(1300)$ is most naturally interpreted as the first radial excitation of the ρ. Taken together with the $\rho(1590)$ of Hyams *et al.*, this results in a level structure for the isovector 1^- states in the isovector sector which is remarkably similar to that observed in the strange meson sector.[49] The mass splittings are almost identical, and the first radial excitation has elasticity $\sim$ 5–10% in both cases. In this regard, it should be noted that the rest frame decay momenta for the $\rho(1300)$ and the $K_1^*(1410)$ are almost the same, so that, if the small elasticity is related to the nodal structure of the final state radial wave function,[49] it would be expected that *both* states should be highly inelastic.

This picture of the isovector 1^- level structure agrees to some extent with that of Donnachie and Mirzaie,[50] in that there are indeed two excited ρ states, and each has width $\sim 200\,\mathrm{MeV/c^2}$. Furthermore, the elasticity of the lower mass state is $\sim$ 5%, while that of the higher mass state is $\sim$ 20% in each case. However, the mass values obtained by Hyams *et al.* and the present analysis are very different from those obtained by Donnachie and Mirzaie, namely $\sim 1.47\,\mathrm{GeV/c^2}$ and $\sim 1.7\,\mathrm{GeV/c^2}$. Part of the difference arises from the treatment of the phase of the lower mass excited ρ. This analysis allowed the phase to vary; Donnachie and Mirzaie fixed it at 180 degrees, which is in disagreement with the present analysis. Also, it should be pointed out that the model of Donnachie and Mirzaie does not reproduce the mass dependence of the P-wave η parameter in the $1300\,\mathrm{MeV/c^2}$ region as measured in Hyams *et al.*

More recently, Donnachie, Kalashnikova and Clegg[51,52] have suggested that the $\rho(1300)$ (referred to as the ρ_x by them) does not fit in the isovector multiplet, but rather, is a 4-quark $q\overline{q}q\overline{q}$ state. This would suggest that the differential cross section for the $\rho(1300)$ should be steeper than that of a $q\overline{q}$ state since a 4-quark state presumably is a more extended object. However, the exponential slope of the $\rho(1300)$ P_+ amplitude is flatter than that of the ρ, although the difference is only 1.5–2.0 standard deviations. The $\rho(1300)$ unnatural parity exchange amplitude is significantly flatter than corresponding ρ amplitudes, but the signal is very small, with large uncertainties. Also, while the $f_2(1270)$ is still considered a $q\overline{q}$ state, the slope of the D_+ amplitude is significantly flatter than that of the ρ P_+ amplitude. Therefore, while the present analysis cannot rule out the $\rho(1300)$ being a 4-quark state, the data tend to favor a flatter differential cross section, and therefore a normal $q\overline{q}$ state.

In summary, the $\pi^+\pi^-$ system in Reaction (7.1) has been analysed and has shown a rather striking corroboration of the phenomenon of ρ–ω interference. The measured resonance parameters of the ρ are consistent with the current Particle Data Group numbers,[30] while the differential cross section and Λ polarization are consistent with those measured at 4.2 GeV/c.[37] Partial wave amplitude analyses of the forward and backward $\pi^+\pi^-$ data have provided evidence for the existence of a new P-wave state, the $\rho(1300)$, and for the $\rho_3(1690)$. The $\rho(1300)$ is most readily understood as the first radial excitation of the ρ. Its mass and width were found to be $(1290^{+20}_{-30})\mathrm{MeV/c^2}$ and $(120^{+60}_{-50})\mathrm{MeV/c^2}$, respectively. The cross section for forward production was measured as $(0.26 \pm 0.05 \pm 0.06)\mu\mathrm{b}$, implying that the elasticity is $\sim$ 5%.

Chapter 8

$\Lambda\pi^+\pi^-\pi^0$ Analysis

The reaction

$$K^-p \rightarrow \Lambda\pi^+\pi^-\pi^0 \tag{8.1}$$

is somewhat more difficult to analyse than the two pion channel because of the π^0. Since LASS does not detect neutral particles, the π^0 must be reconstructed assuming that the missing momentum is taken up by the π^0. The resolution of the missing mass squared for LASS is about $0.15\,(\mathrm{GeV/c^2})^2$ full width at half maximum, which means that a missing π^0 cannot be resolved from a photon. One tool of differentiation is MVFIT; one can fit the events with only the total energy constrained (a 1C Fit). This provides some separation between pion and photon, but the amount cannot be determined since the neutral particle now looks like a pion. Previous LASS analyses which included a π^0 have been interested in a known resonance which involves the π^0, and therefore, a background subtraction on that resonance could be done. This is not possible in the present analysis since we are interested in unspecified resonances which might decay to one or two pions plus the π^0.

8.1 Event Selection

In order to get a reasonably clean sample for the Reaction (8.1), the cuts on the events must be quite stringent. First, all 4C events were removed. Any event

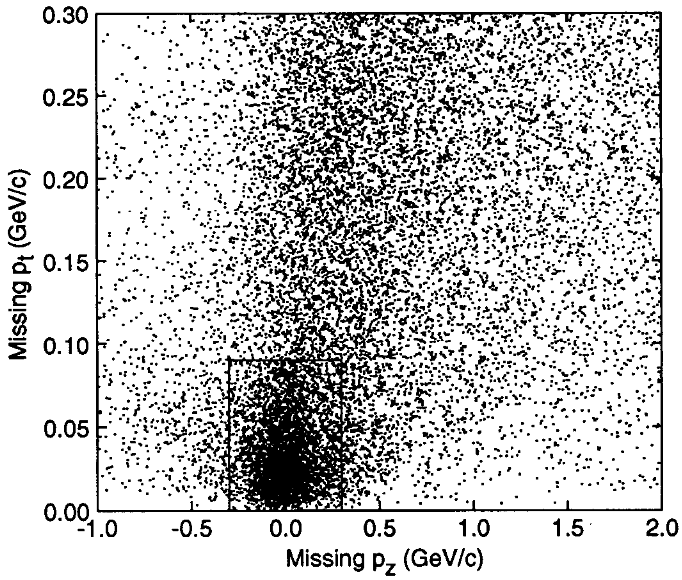

Figure 8.1: The distribution of missing p_t versus p_z for the 3 pion sample. The events inside the box were removed.

which successfully fitted as a $K^-p \to \Lambda\pi^+\pi^-$ or $K^-p \to \Lambda K^+K^-$ event, with any confidence level, was removed. Events were then required to have a successful GeoFit. Events with missing mass squared (MM^2) greater than $1\,(\mathrm{GeV/c^2})^2$ in absolute value were removed; this does not remove any reasonably well measured π^0 events, which should have $MM^2 = 0.0182\,(\mathrm{GeV/c^2})^2$. A cut on the confidence level of the 1C Fit was delayed until the end so that the missing mass distribution was unbiased and therefore could be used to monitor the sample.

Figure 8.1 shows the distribution of events in the missing p_t–p_z plane. The cluster of events around 0 is from events which are essentially 4C but, for some reason, do not pass the fit. There are also events in this region where the π^0 comes from the decay $\Sigma \to \Lambda\pi^0$, because these π^0s tend to be slow. The events were removed by cutting events with $|p_z| < 0.3\,\mathrm{GeV/c}$ and $p_t < 0.09\,\mathrm{GeV/c}$.

The next requirement was that the missing momentum be reasonably well measured. The most poorly measured tracks in LASS are fast, forward tracks which were not measured in the dipole region. For these tracks, the momentum uncertainty is dominated by the uncertainty of the sagitta of the track helix, and

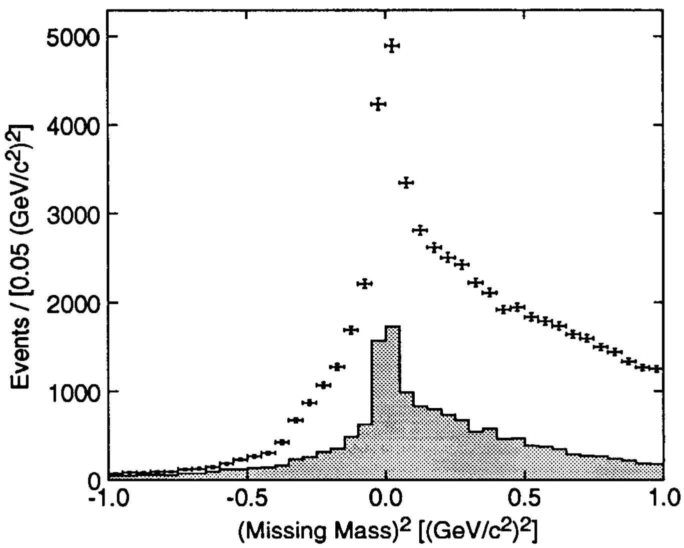

Figure 8.2: The early missing mass squared distribution. The shaded area indicates the events removed by the p_t–p_z and momentum resolution cuts.

is given by[53]

$$\sigma^p_{est} = 36\frac{pp_z}{(\Delta z)^2 \tan\theta}, \tag{8.2}$$

where p and p_z are the total and longitudinal momentum of the track, Δz is the z separation (*i.e.* along the beam direction) between the first and last measured co-ordinate on the track, and θ is the polar angle of the track. σ^p_{est}, p, and p_z are measured in GeV/c, while Δz is in cm. Events were cut if any track with $p > 3.0$ GeV/c was not dipole measured and had $\sigma^p_{est} > 0.360$ GeV/c. Figure 8.2 shows the missing mass squared distribution for the event sample before the p_t–p_z and σ^p_{est} cuts, along with the distribution of the events removed by these cuts.

The particle identification cuts are important in this channel because of the difficulty of reconstructing the missing π^0. The distributions, however, are essentially the same as for the two pion channel. Time of flight cuts were applied to all particles. The TOF ID was used for pions with momentum between 0.5 and 3.0 GeV/c. If the particle was cleanly measured by the TOF system and was slower than 3 standard deviations from the expected time (TOFDEV

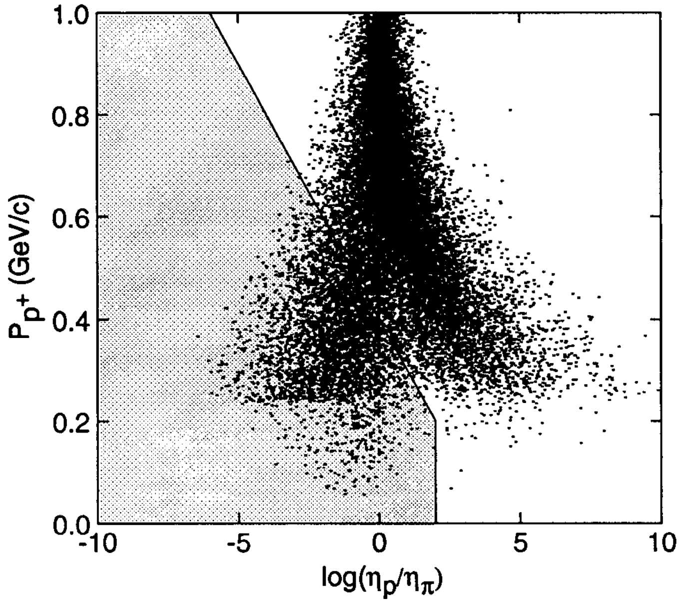

Figure 8.3: The distribution of the proton momentum versus the log ratio of pion over proton probability from the dE/dx measurement. The area removed is indicated by the shaded region.

< -3), the event was removed. For the proton from the Λ decay, events with $p_{\mathrm{p}} < 4\,\mathrm{GeV/c}$ and TOFDEV > 3 were removed. The cylinder dE/dx measurements showed contamination only for the proton. The distribution of ID probability and particle momentum is shown in Figure 8.3; protons should have positive values of the log probability ratio. The region cut is indicated by the shaded region. For the Cherenkov measurement of the proton, if the track was well isolated and it produced more than 1000 ADC counts, the event was cut, removing pions and kaons. For the pions, events were cut if the track was isolated, the momentum was less than 2.5 GeV/c and there were more than 1000 counts in the ADC. Events were also cut if they contained any pion with a momentum between 3 and 9 GeV/c which produced less than 50 ADC counts in a Cherenkov cell with an expected efficiency greater than 90%. The final particle ID cut was to removed events where a photon converted to two electrons which were then misidentified. This cut is the same as the one described in Section 7.1.

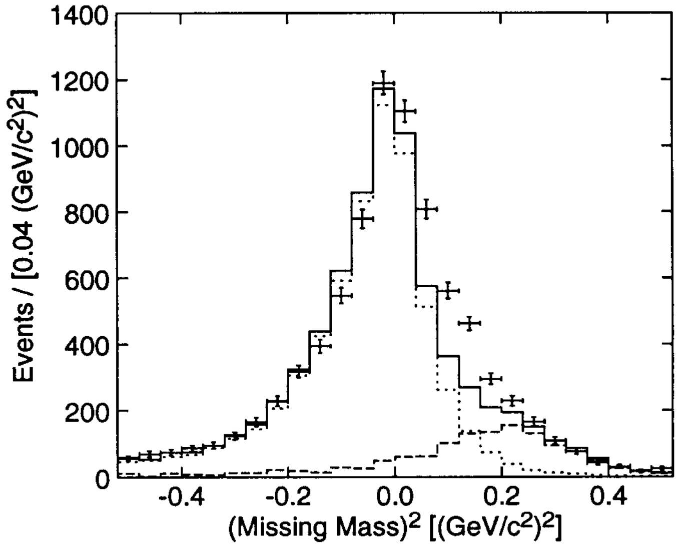

Figure 8.4: The missing mass squared distribution after the particle ID but with 1C Fit confidence level $> 10^{-2}$. The data is shown as the points while the distributions from π^0 and η Monte Carlos are shown as dotted and dashed histograms respectively. The solid histogram represents the sum of the two.

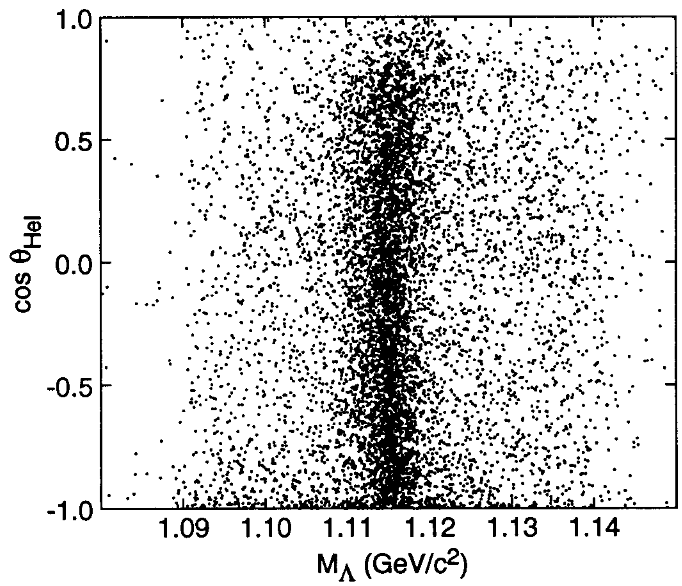

Figure 8.5: The distribution of the Λ helicity angle versus the Λ mass. The photon contamination is the band at $\cos\theta_{hel} \simeq -1$.

Description of Cut	Events Cut	Events Remaining
Input Events	—	1,461,824
4C Events	82,793	1,379,031
Unsuccessful GeoFit	174,016	1,205,015
$\lvert MM^2\rvert > 1.0\,(\mathrm{GeV/c^2})^2$	453,753	751,262
Missing P_t–P_z	65,617	685,645
ΔP_{est} cut	131,218	554,427
dE/dx Particle ID	39,193	515,234
ToF Particle ID	56,311	458,923
Cherenkov Particle ID	106,037	352,886
Photon conversion	5,991	346,895
$MM^2 > 0.08\,(\mathrm{GeV/c^2})^2$	226,869	120,026
Λ Helicity cut	6619	113,407
Unsuccessful 1C Fit	32,095	81,312
Lambda Decay length $< 0.1\,cm$	7344	73,968
1C Confidence Level $< 10^{-2}$	17,501	56,467
Final Sample	—	56,467

Table 8.1: Summary of cuts used in $\Lambda\pi^+\pi^-\pi^0$ event selection.

At this stage, the missing mass distribution was checked for contamination. If there were a significant number of events where the missing neutral was actually an η, there would be too many events at high MM^2. The MM^2 distribution for events with a 1C Fit confidence level greater than 10^{-2} is shown in Figure 8.4 along with distributions from π^0 and η Monte Carlo samples, normalized to match the data. There is clearly a significant contribution from missing η events. Also, there appears to be an excess of events in the data with $0 < MM^2 < 0.2\,(\mathrm{GeV/c^2})^2$, probably caused by events with two or three missing π^0s. Events with $MM^2 > 0.08\,(\mathrm{GeV/c^2})^2$ were removed from the sample. The Monte Carlo data indicates that this removes about 70% of the η events and retains 90% of the π^0 events.

Figure 8.5 shows the distribution of the Λ helicity angle versus mass for 1C confidence greater than 10^{-2}. There are no obvious bands which would indicate contamination except for excess events at $\cos\theta_{hel} \simeq -1$. These are from photons which pair create and the electrons are misidentified. Events with $\cos\theta_{hel} < -0.95$ were removed. The $\pi^+\pi^-$ mass spectrum (see Figure 8.6) indicates that there remains a small amount of contamination from K^0, which means that some of the Λ candidates are still mis-identified.

At this point, the 1C Fit results were examined. The Λ decay length distribution showed the same pile up at 0 that was in the two pion channel (see Figure 7.3). Events with decay length less than 0.1 cm were removed. Finally, the 1C Fit confidence level was cut at 10^{-2}; the high confidence level is needed to try to separate the π^0 from other neutral particles. The total list of cuts and the number of events removed is shown in Table 8.1. The final sample contains 56,467 events.

8.2 Backward Λ Sample

The sample is split into forward and backward Λ events by cutting on Feynman x of the Λ at 0. The various spectra involving the Λ and a pion for the backward Λ sample are shown in Figure 8.6. The chief feature is the strong production of $\Sigma(1385)$, particularly in the $\Lambda\pi^+$ channel. There is also evidence for production of higher mass Σs, but only in $\Lambda\pi^+$. The enhancement at threshold in the $\Lambda\pi^0$ spectrum is due to misidentified $\Sigma \to \Lambda\gamma$ decays.

The two pion spectra shown in Figure 8.7 show significant ρ production in all modes. There is also evidence of a resonance around 1250 MeV/c^2, but in the $\pi^+\pi^-$ channel only. This indicates that it is dominated by $f_2(1270)$, which is a neutral, $I = 0$, species. There is a small bump in the $\pi^+\pi^-$ spectrum around 500 MeV/c^2, indicating the presence of K^0. This indicates that there is still some background in the channel, with either the Λ or π^0 mis-identified.

The $\pi^+\pi^-\pi^0$ mass spectrum is shown in Figure 8.8. The plot shows three strong resonances, plus there is some indication of higher, weaker bands. The first resonance is the η, though we shall see that the events seen are actually a mixture of the 3π and $\pi^+\pi^-\gamma$ decay modes of the η. The strongest resonance is the ω at 780 MeV/c^2. The peak around 1 GeV/c^2 is in fact due to a mixture of η' and ϕ

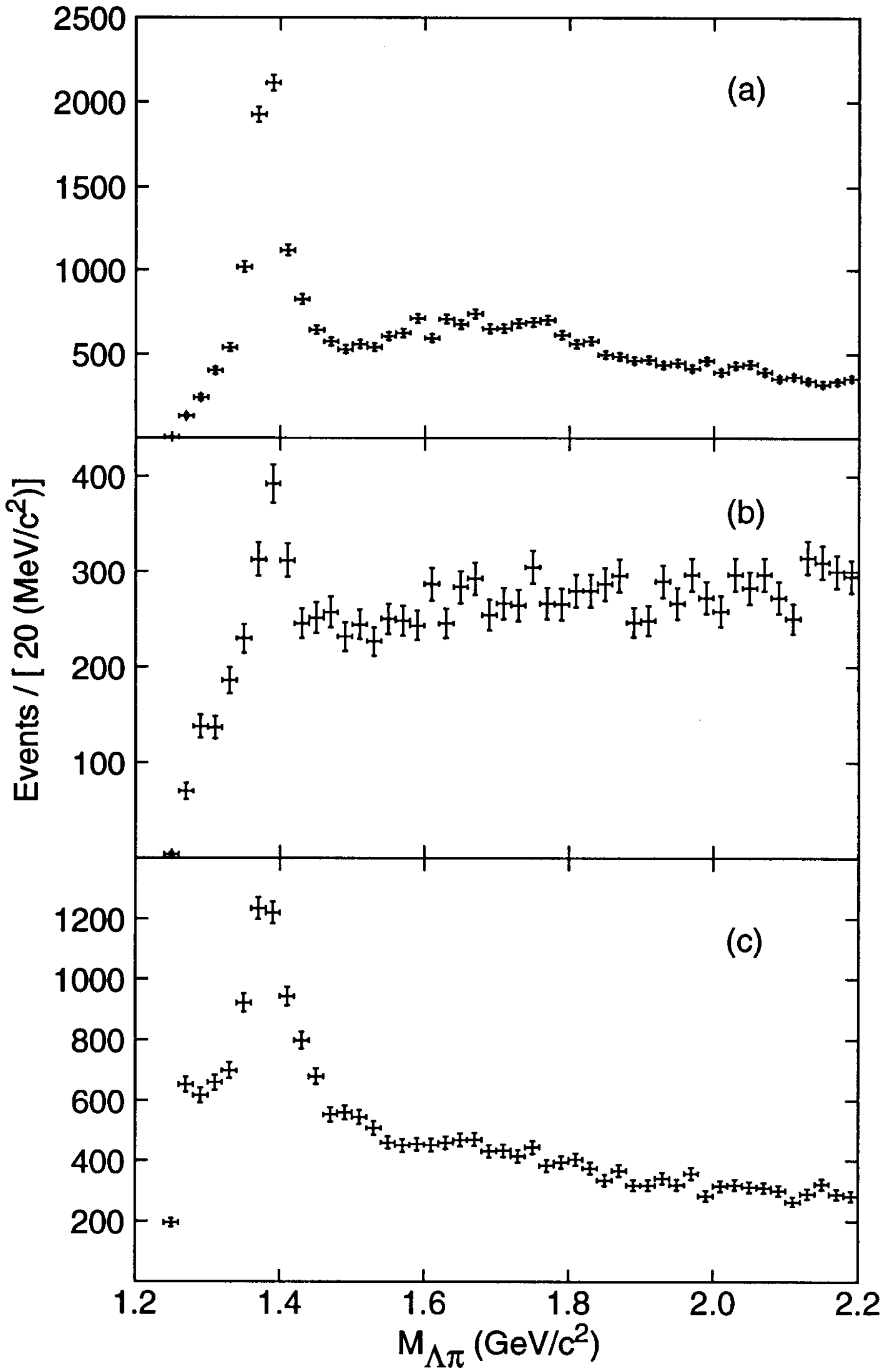

Figure 8.6: The raw $\Lambda\pi$ spectra for the backward Λ sample: (a) $\Lambda\pi^+$, (b) $\Lambda\pi^-$, and (c) $\Lambda\pi^0$.

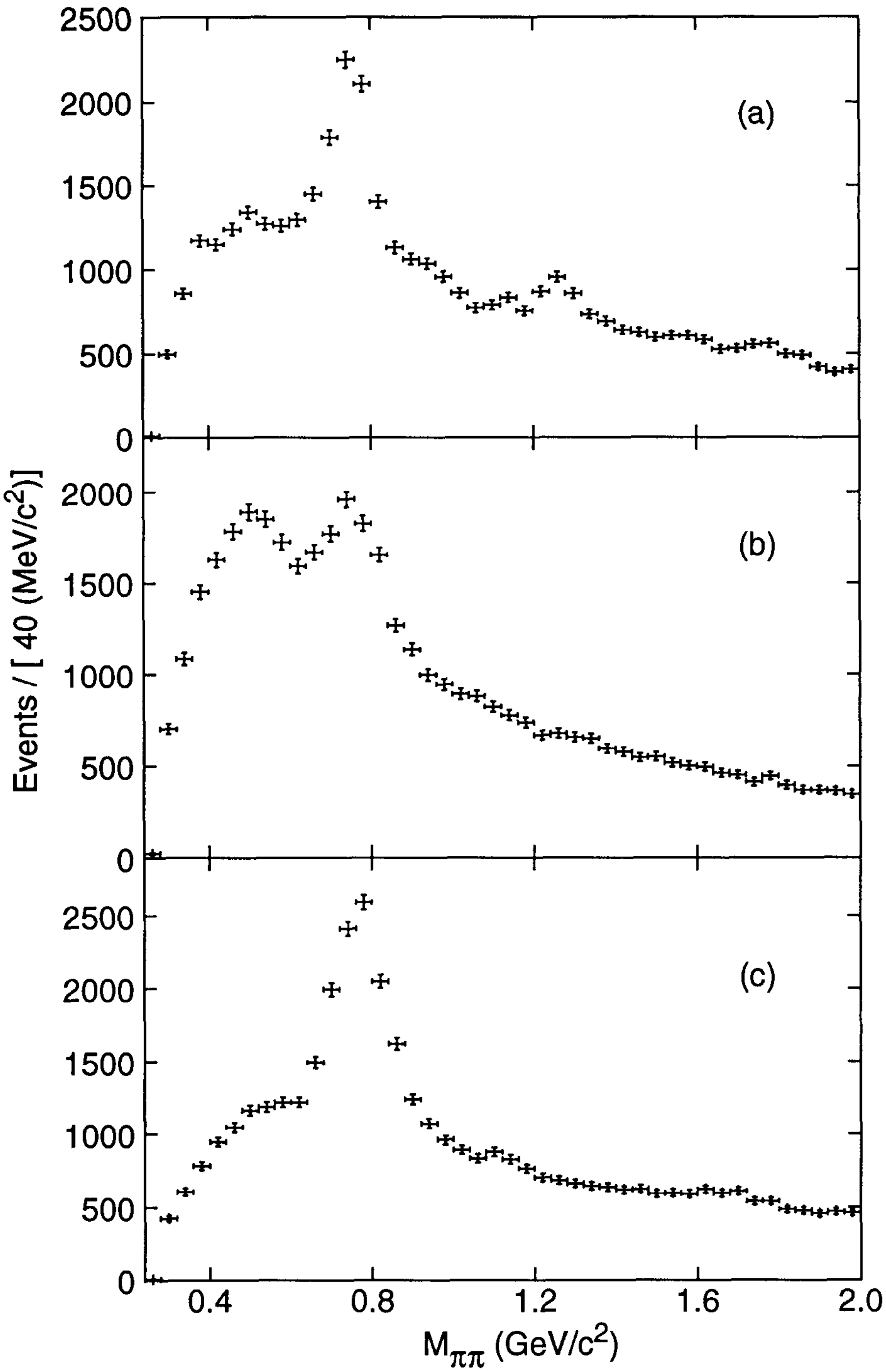

Figure 8.7: The raw $\pi\pi$ spectra for the backward Λ sample: (a) $\pi^+\pi^-$, (b) $\pi^+\pi^0$, and (c) $\pi^-\pi^0$.

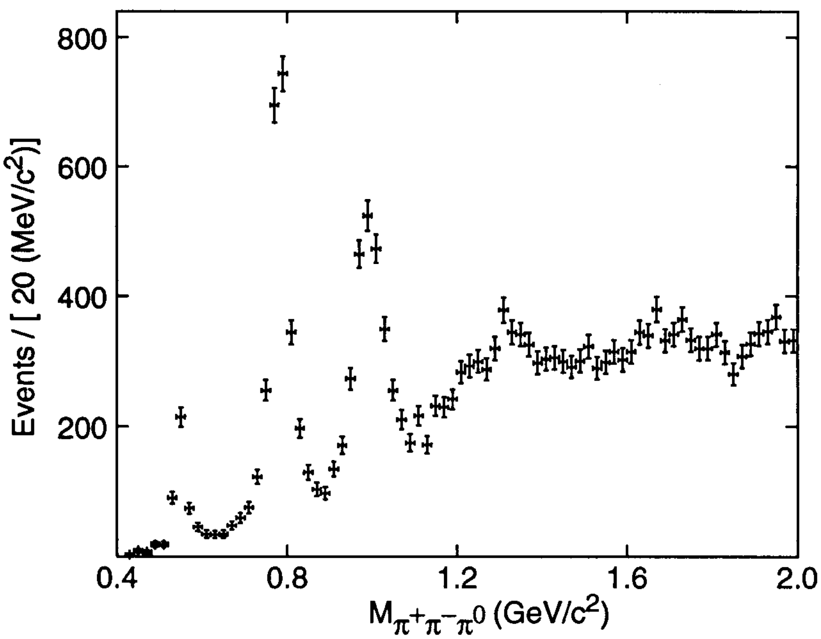

Figure 8.8: The raw $\pi^+\pi^-\pi^0$ spectrum for the backward Λ sample.

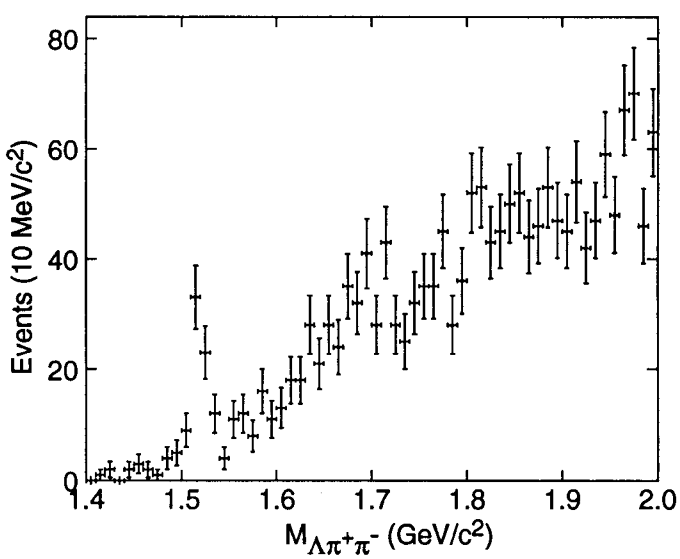

Figure 8.9: The $\Lambda\pi^+\pi^-$ spectrum for the backward Λ sample.

decays, specifically $\eta' \rightarrow \pi^+\pi^-\gamma$ and $\phi \rightarrow \pi^+\pi^-\pi^0$. Given its width, the small bump at about 1.3 GeV/c^2 may be due to the $a_2(1320)$.

The spectrum for $\Lambda\pi^+\pi^-$ for backward Λ is shown in Figure 8.9. The resonance just above 1.5 GeV/c^2 almost certainly results from the decay of the $\Lambda(1520)$ resonance.

8.3 Forward Λ Sample

The $\Lambda\pi$ spectra for the forward Λ sample are shown in Figure 8.10. The dominant feature is again the production of $\Sigma(1385)$, but it is much weaker than in the backward sample. The $\Lambda\pi^0$ spectrum shows significant contamination from $\Sigma \rightarrow \Lambda\gamma$ and almost no $\Sigma(1385)$.

The $\pi\pi$ spectra shown in Figure 8.11 have similar features to the backward Λ sample. The dominant feature is the ρ resonance, while the bump present only in the neutral spectrum indicates the presence of $f_2(1270)$.

The backward three pion mass spectrum (Figure 8.12) is significantly different from the forward sample. The η and η'/ϕ peaks are missing. The only significant feature is the presence of the ω. There is a broad feature around 1.3 GeV/c^2 which may again be due to $a_2(1320)$.

8.4 Analysis of $\Lambda\eta$

In order to measure the line-shape and cross section of the resonances in 3 pion system, we need to determine the acceptance and resolution. Monte Carlo events were thrown flat in mass and decay angles and with a t' slope similar to the data. The acceptance was measured in various mass–t' bins and then fit in order to fully parametrize it. The mass dependence of the average acceptance is shown in Figure 8.13. The t' dependence of the acceptance around the η is shown in Figure 8.14. The mass and t' dependences were parametrized as a line above a fixed point and a cubic polynomial below. At the meeting point, the two functions were forced to have the same value and slope. The meeting point was 0.6 GeV/c^2

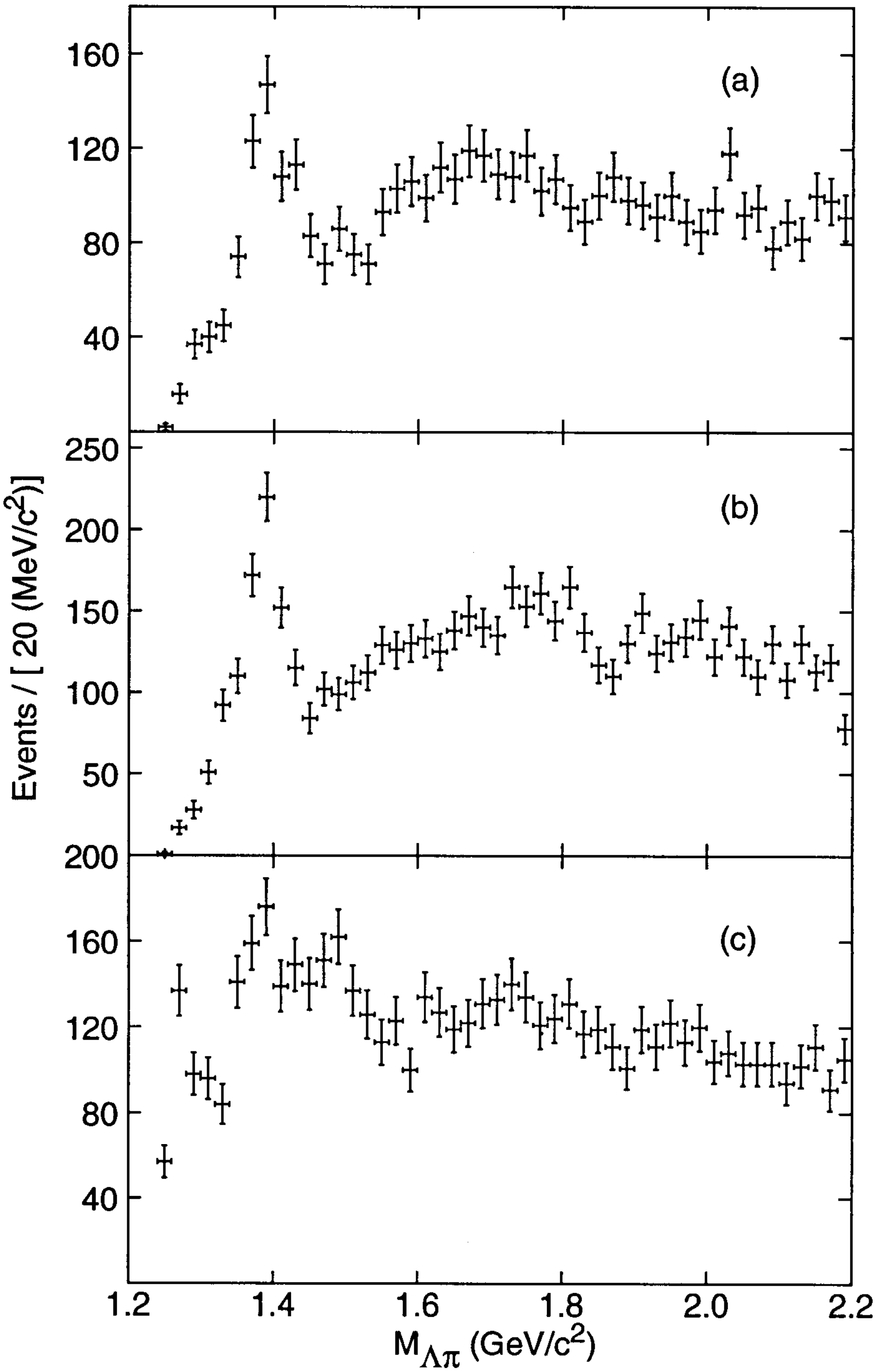

Figure 8.10: The raw $\Lambda\pi$ spectra for the forward Λ sample: (a) $\Lambda\pi^+$, (b) $\Lambda\pi^-$, and (c) $\Lambda\pi^0$.

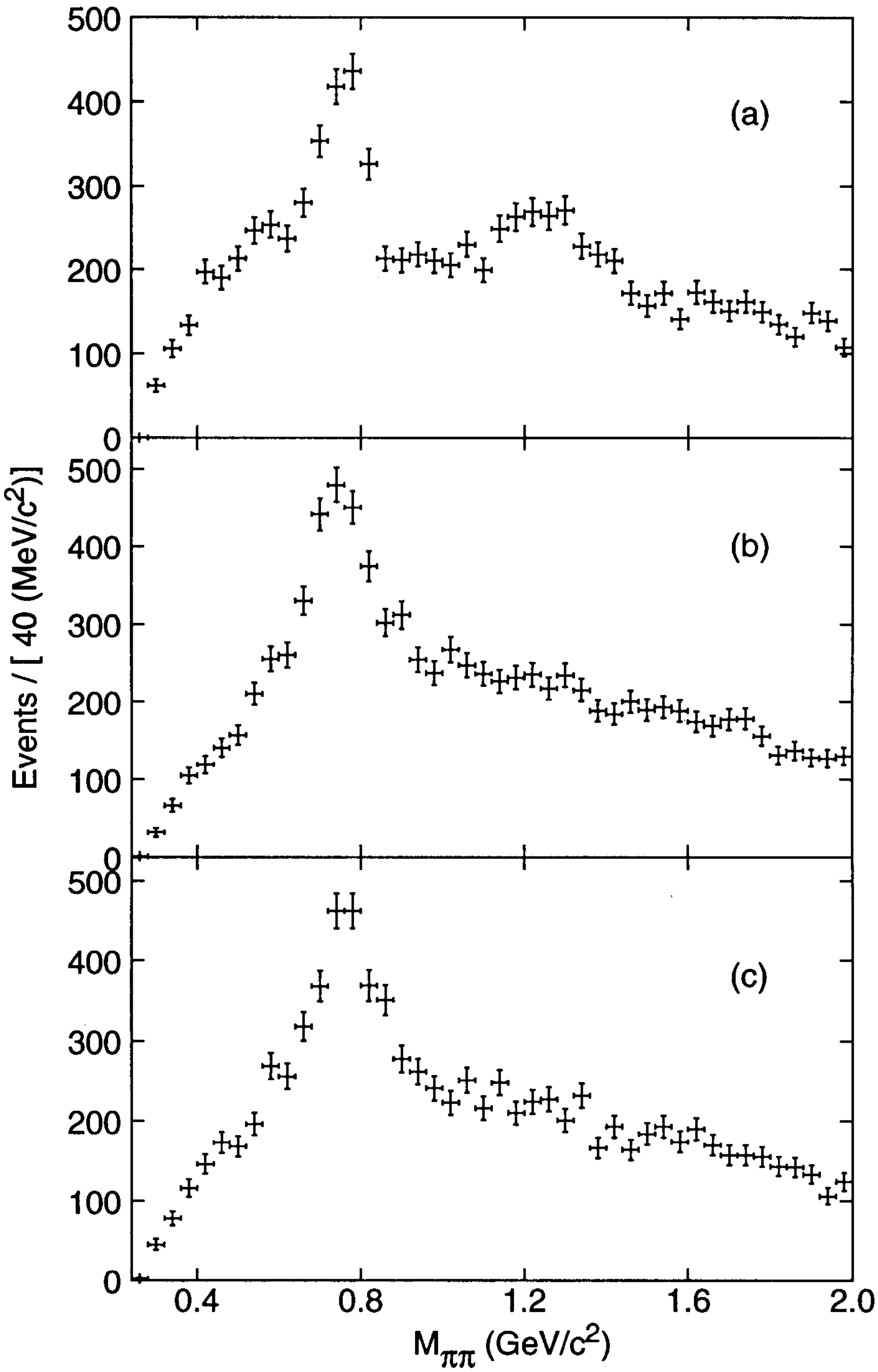

Figure 8.11: The raw $\pi\pi$ spectra for the forward Λ sample: (a) $\pi^+\pi^-$, (b) $\pi^+\pi^0$, and (c) $\pi^-\pi^0$.

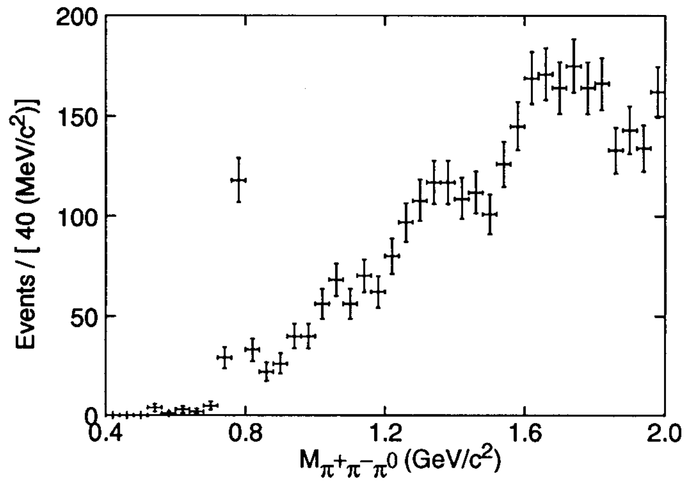

Figure 8.12: The raw $\pi^+\pi^-\pi^0$ spectrum for the forward Λ sample.

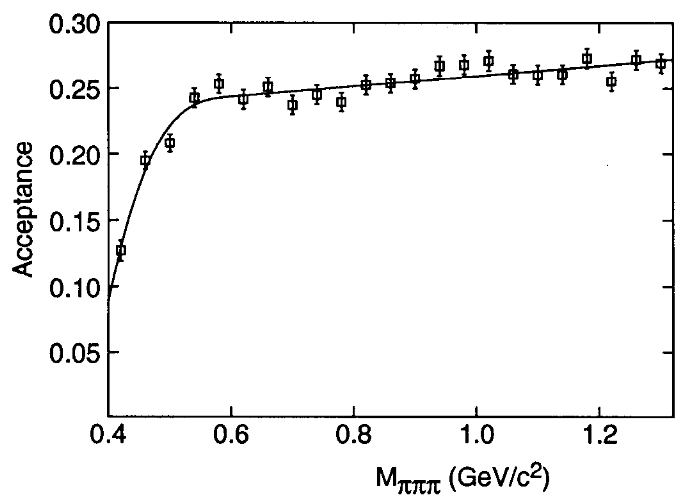

Figure 8.13: The mass dependence of the acceptance for the forward 3 pion system. The curve is the fit described in the text.

for the mass dependence and 0.2 $(\mathrm{GeV/c})^2$ for t'. The fits are shown as the curves in Figures 8.13 and 8.14. The decrease in acceptance at low t' is caused by absorption of the Λ's proton daughter in the target, while the fall off at higher t' is caused by the resolution cut on fast forward tracks (*i.e.* the cut on σ^p_{est}). The acceptance correction was performed by weighting each event by the inverse of its acceptance.

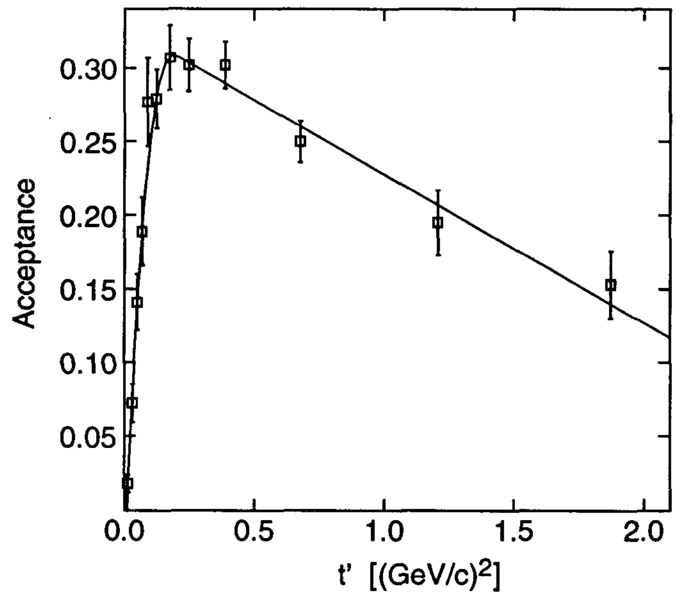

Figure 8.14: The t' dependence of the acceptance in the region of the η. The curve shows the fit described in the text.

The η mass spectrum, corrected for acceptance, is shown in Figure 8.15. Events in the t' range 0.025 to 2.5 (GeV/c)^2 were included; the t' distribution was cut off at low t' because of the poor acceptance. The η line shape is clearly distorted on the upper side due to $\eta \to \pi^+\pi^-\gamma$ events, where the photon is misidentified. In order to fit the line shape, 2,000 Monte Carlo events were thrown where the η was forced to decay to $\pi^+\pi^-\gamma$. These events were reconstructed assuming the missing neutral particle was really a pion and the resulting shape was subsequently used in the fit of the measured η line shape.

Because of the very narrow width of the η, the detector resolution defines the shape of the peak. The resolution was determined from the Monte Carlo by finding the difference between the thrown and reconstructed 3 pion masses. The resolution data were fit with two Gaussians constrained to have the same mean. The widths of the two were allowed to vary linearly with mass in order to fit the tails of the distribution; the widths were constrained to vary in the same manner. This form fit the resolution quite well. The fitted Gaussians had widths of 6.7 and 15.5 MeV/c^2 with equal amplitude and a slope on the widths of $-35\,\mathrm{MeV/c^2/(GeV/c^2)}$.

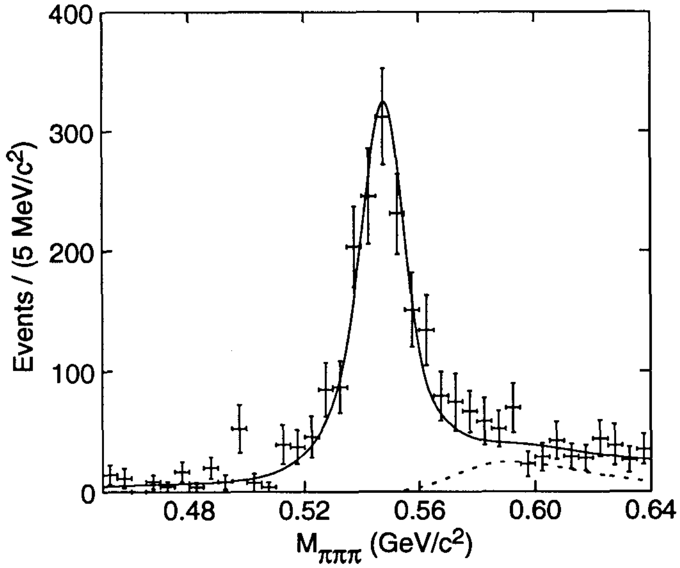

Figure 8.15: The acceptance corrected mass spectrum of the η. The solid curve is the fit to the line shape. The dashed curve shows the contribution from the $\pi^+\pi^-\gamma$ decay mode.

The η shape was fit with a resolution function plus the photon decay shape and a linear background. The ratio of the number of events in the 3π peak to that of the photon peak was fixed using the branching fractions from the Particle Data Booklet,[30] namely, 23.6% and 4.88%. The mass of the η was fixed to the PDG value of 547.5 MeV/c^2. The fitted shape is shown in Figure 8.15 as the solid line. The contribution from $\eta \rightarrow \pi^+\pi^-\gamma$ decays is shown as the dashed curve. The fitted amplitude gives a cross section of $(2.36 \pm 0.16)\mu$b. To correct for the loss due to the low t' cutoff, the fitted t' shape (see below) was extrapolated and used to find the average cross section in the missing region. This gives a correction of $(0.72 \pm 0.12)\mu$b resulting in a total forward cross section of $(3.1 \pm 0.2)\mu$b, where the uncertainty is statistical only. Since the backward cross section is too small to measure, this is also the total η cross section.

An interesting aspect of the η is the t' distribution, shown for this analysis as Figure 8.16e. This distribution was made by sideband subtracting the events in the η peak; however, because of the photon decay mode events on the high side of the peak, only one background region on the low side was used. The values in the plot were renormalized to the total measured cross section to account for the loss of real events. The dip in the cross section around $t' \sim 0.4\,(\mathrm{GeV/c})^2$ and the subsequent rebound of the cross section is qualitatively explained by Regge theory[54] if the coupling to the $\mathrm{K}_2^*(1430)$ trajectory is suppressed.

The differential amplitude for a single signature Regge trajectory is given by

$$\mathcal{M} \propto \frac{1 \pm \mathrm{e}^{-\imath\pi\alpha(t)}}{2} \mathrm{e}^{-bt/2} s^{\alpha(t)}, \tag{8.3}$$

where s is the center of mass energy squared. The initial fraction is known as the signature factor, the sign being the signature. The signature is positive for even spin resonances and negative for odd spin resonances. Generally, even and odd signature trajectories overlap and are strongly degenerate. When two trajectories of opposite signature are strongly exchange degenerate, they have the same $\alpha(t)$ function, the same slope b and add coherently, giving

$$\frac{d\sigma}{dt} \propto \mathrm{e}^{-bt} \frac{s^{2\alpha(t)}}{p_{lab}^2}, \tag{8.4}$$

where p_{lab} is the lab momentum of the beam, removing any dependence on the signature factors. If, however, the coupling to one of the trajectories is zero, the differential cross section of Equation 8.4 is modulated by $\sin^2(\pi\alpha(t)/2)$ or $\cos^2(\pi\alpha(t)/2)$, and will go to zero where this factor goes to zero.

The η and η' differential cross sections from the 4.2 GeV/c Bubble Chamber experiment,[55] the 8.25 GeV/c Bubble Chamber experiment,[56] and this experiment[16] are shown in Figure 8.16. The η data with $t' < 2.0\,(\mathrm{GeV/c})^2$ were fit with

$$\frac{d\sigma}{dt} = A \exp(-bt) \frac{s^{2\alpha(t)}}{p_{lab}^2} \sin^2(\pi\alpha(t)/2), \tag{8.5}$$

while the η' data with $t' < 1.0\,(\mathrm{GeV/c})^2$ were fit with

$$\frac{d\sigma}{dt} = A \exp(-bt) \frac{s^{2\alpha(t)}}{p_{lab}^2}. \tag{8.6}$$

$\alpha(t)$ was determined for the K^* trajectory*, giving

$$\alpha(t) = 0.25 + 0.884\,t, \tag{8.7}$$

*The t for a real resonance is simply its mass squared while α is equal to its spin.

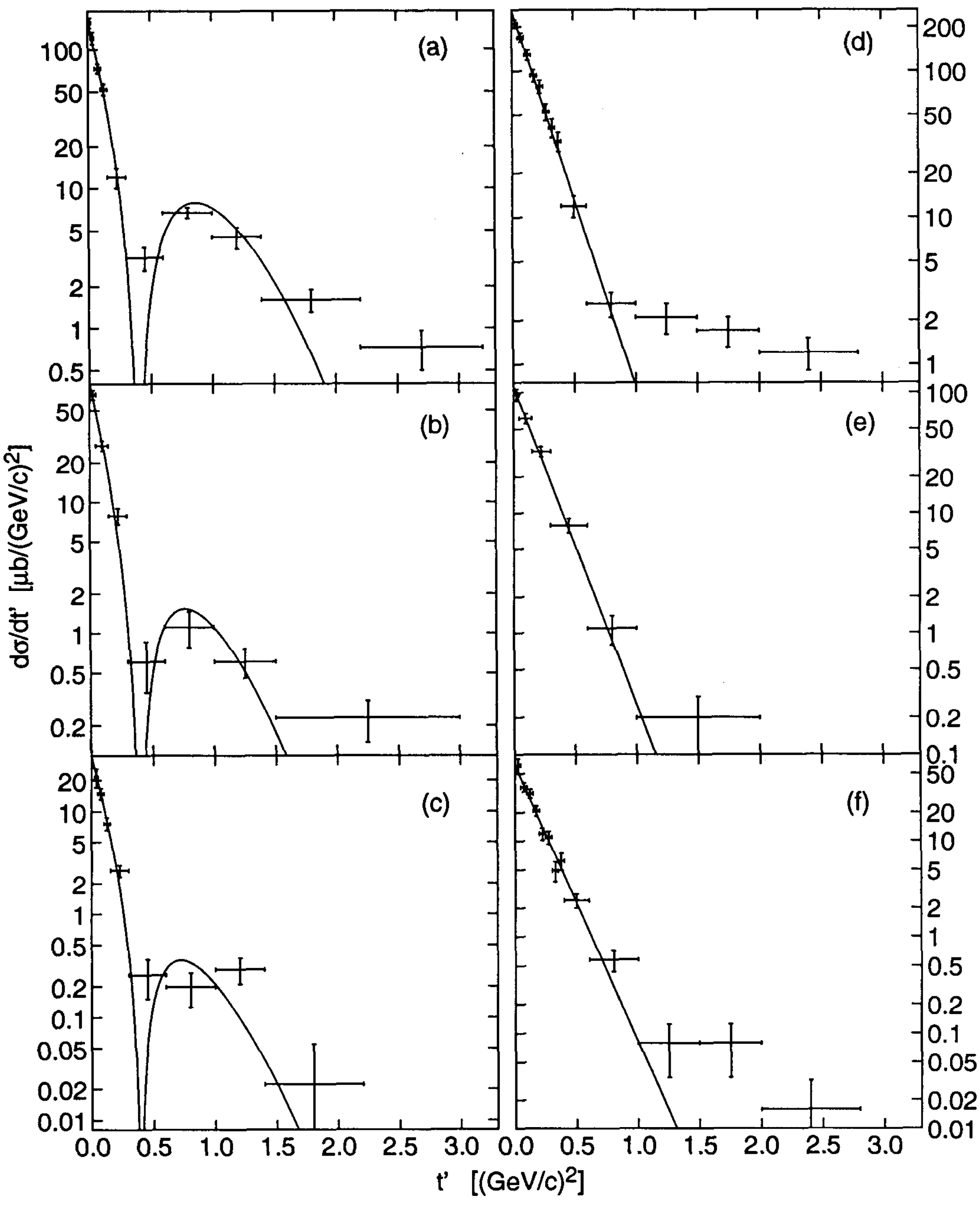

Figure 8.16: The t' distributions of the η and η' at different energies: (a), (b), and (c) show the η differential cross sections at 4.2 GeV/c [55], 8.25 GeV/c [56], and 11 GeV/c [this analysis]. (d), (e), and (f) show the η' differential cross sections at 4.2 GeV/c [55], 8.25 GeV/c [56], and 11 GeV/c [16]. The curves are the fits to the shapes given by Regge theory.

Resonance	p_{lab} [GeV/c]	Amplitude [μb/(GeV/c)^2]	Slope [(GeV/c)$^{-2}$]	χ^2 / DoF
η	4.2	2440 ± 120	-0.04 ± 0.10	21 / 7
	8.25	3300 ± 200	-0.25 ± 0.20	5 / 4
	11	2080 ± 190	-0.6 ± 0.3	11 / 7
η'	4.2	1500 ± 70	-2.0 ± 0.2	6 / 8
	8.25	1890 ± 150	-1.1 ± 0.3	1 / 3
	11	1620 ± 140	-1.2 ± 0.4	10 / 8

Table 8.2: The results of fits to the η and η' differential cross sections at 4.2 GeV/c, 8.25 GeV/c, and 11 GeV/c.

with t in (GeV/c)^2. The results are shown in Table 8.2. The uncertainties are statistical only. The expressions clearly represent the general shape of the data at lower t'. If Regge theory is correct, the amplitudes and slopes for the two resonances should be the same at different energies. While there are deviations, the data points do agree within a few sigma. However, one would also expect the η and η' slopes to agree because of the close kinship of the two states. Also, the high t' data clearly does not agree with the Regge form, particularly for the η'. It is possible to use a more complicated expression where the two different signature trajectories are added incoherently and have different slopes b. This does greatly improve the agreement at high t', but, given the uncertainties of the measurements, there is no way to determine if this is a reasonable representation.

8.5 Analysis of $\Lambda\omega$

The t' dependence of the acceptance for the ω region is shown in Figure 8.17. It was parametrized in the same manner as for the η. The acceptance corrected mass spectrum is shown in Figure 8.18. The shape was fit with a spin 1 Breit–Wigner, smeared by the detector resolution as discussed in the previous section, plus a linear background. The Gaussians in the resolution function had widths of 13.8 and 43.0 MeV/c^2; the wider had a relative amplitude of 0.32, and the widths changed

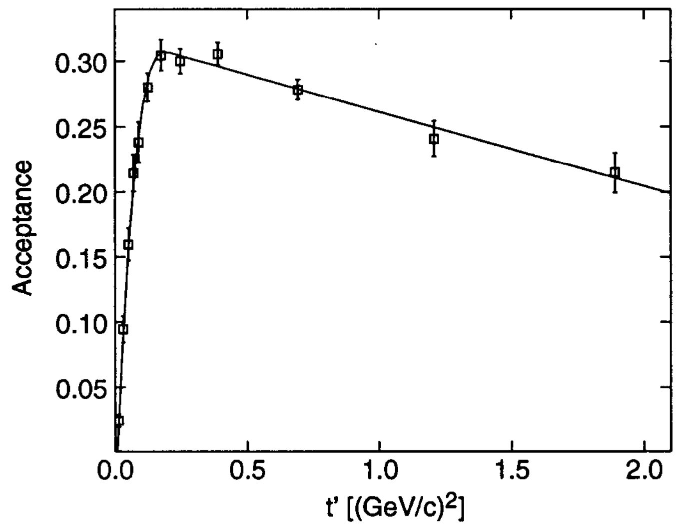

Figure 8.17: The t' dependence of the acceptance in the region of the ω. The curve is the result of the fit described in the text.

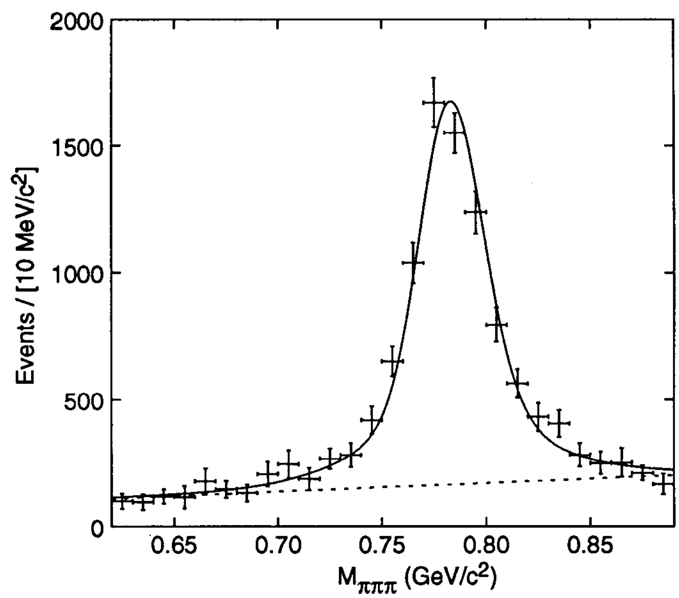

Figure 8.18: The acceptance corrected ω mass spectrum. The solid curve is the fit to the line shape, with the dotted curve showing the background.

with a slope of 33 MeV/c^2/(GeV/c^2). The mass and width of the ω were fixed to the Particle Data Group value[30] of 781.95 MeV/c^2 and 8.43 MeV/c^2. The fit gives a cross section of $(3.18 \pm 0.13)\,\mu$b, corrected for the Λ and ω visibility, for forward ω. This does not include the region $0 < t' < 0.025\,(\mathrm{GeV/c})^2$ where the acceptance is very low. It is estimated from the fit to the t' distribution (see Figure 8.19) that this region accounts for $(0.08 \pm 0.01)\,\mu$b. Therefore the forward cross section is $(3.26 \pm 0.14)\,\mu$b. A fit to the backward data gives a cross section of $(0.44 \pm 0.05)\,\mu$b, giving a total cross section of $(3.70 \pm 0.15)\,\mu$b. The uncertainties are statistical only.

The differential cross sections for the ω are shown in Figure 8.19. The three plots show the (a) σ^P_+, (b) σ^P_-, and (c) σ^P_0 contributions. This separation is made using the same σ combinations used in Chapter 7 and described in Appendix A, but using the angles of the decay plane normal for the three pion system.[57] The data are background subtracted (using two sidebands) and renormalized to the total measured cross section. The curves in Figure 8.19 are fits of the data points below $t' < 1.0\,(\mathrm{GeV/c})^2$ to Equation 7.14. The results are given in Table 8.3. The fitted slopes are all quite consistent with a single value of about $4\,(\mathrm{GeV/c})^{-2}$.

The data from two experiments at different energies can be used to calculate the parameters of the effective exchange trajectory in a Regge exchange model.[58,54] The high statistics results from the 4.2 GeV/c Bubble Chamber experiment[37] were used for this calculation. The differential cross section in the Regge exchange model is given by

$$\frac{d\sigma}{dt} \propto s^{2\alpha(t)}/p_{lab}^2 \tag{8.8}$$

where s is the center of mass energy squared, p_{lab} the lab momentum of the beam, and $\alpha(t)$ is the Regge trajectory. Taking a ratio of cross sections measured at different energies gives

$$\alpha(t) = \frac{1}{2}\frac{\log\left(p_1^2\sigma_1/p_2^2\sigma_2\right)}{\log\left(s_1/s_2\right)}. \tag{8.9}$$

The computed Regge trajectory is shown in Figure 8.20. Like the t' distributions, the data for this experiment were computed by sideband subtracting the ω spectrum and renormalizing the cross section to the total cross section found earlier. The two dashed lines in the plot represent the K and K* trajectories,

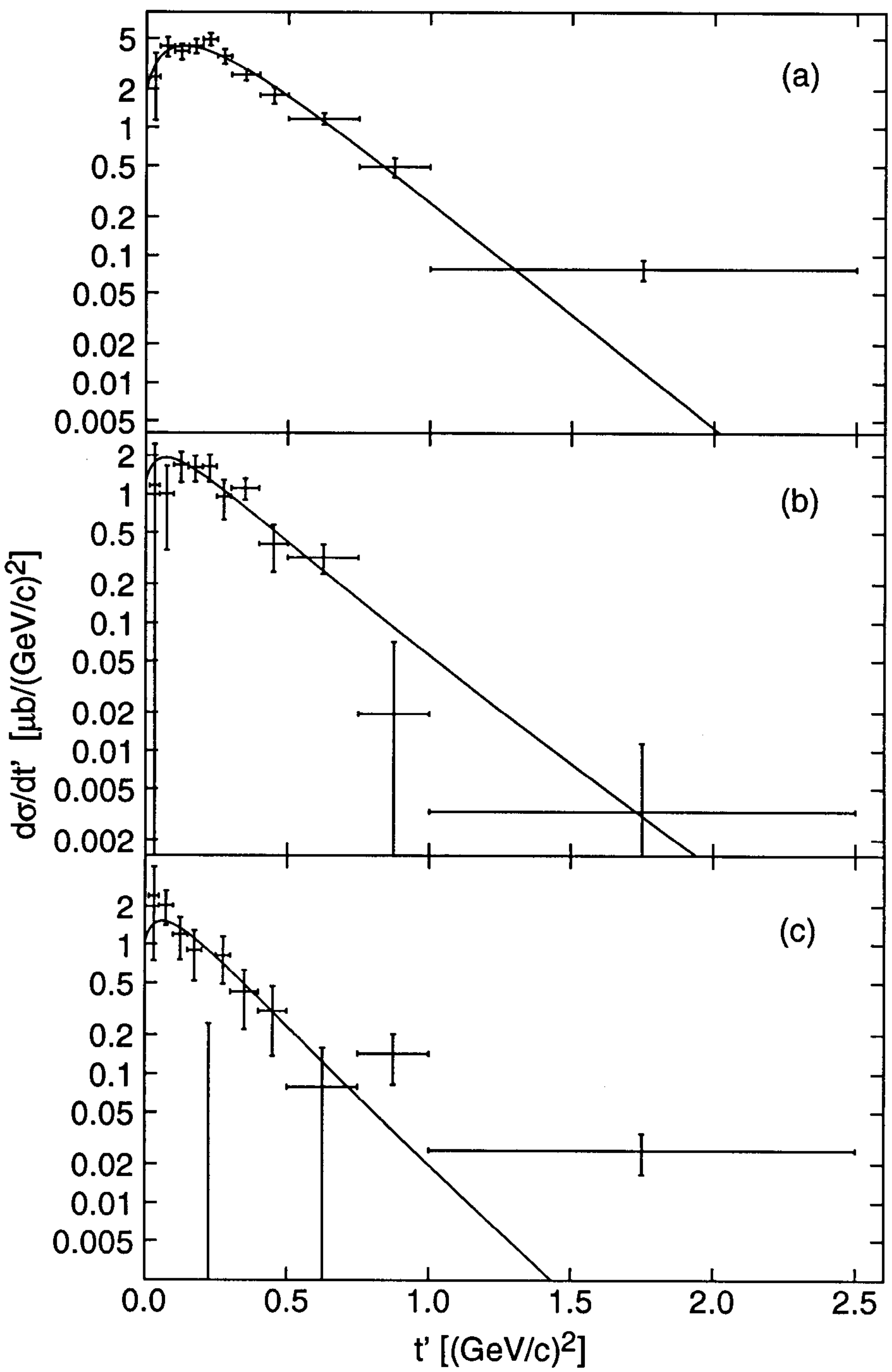

Figure 8.19: The acceptance corrected, sideband subtracted ω differential cross sections for (a) σ_+^P, (b) σ_-^P, and (c) σ_0^P. The curves show the fits described in the text.

Quantity	Exchange Mass (GeV/c^2)	Slope α ((GeV/c)$^{-2}$)	χ^2/DoF
σ_+^P	0.70 ± 0.20	3.3 ± 0.8	6.7 / 7
	0.890	3.9 ± 0.2	7.1 / 8
σ_-^P	0.493	3.3 ± 0.5	8.7 / 8
σ_0^P	0.493	4.2 ± 1.2	5.2 / 7

Table 8.3: The results of the fits to the ω differential cross sections.

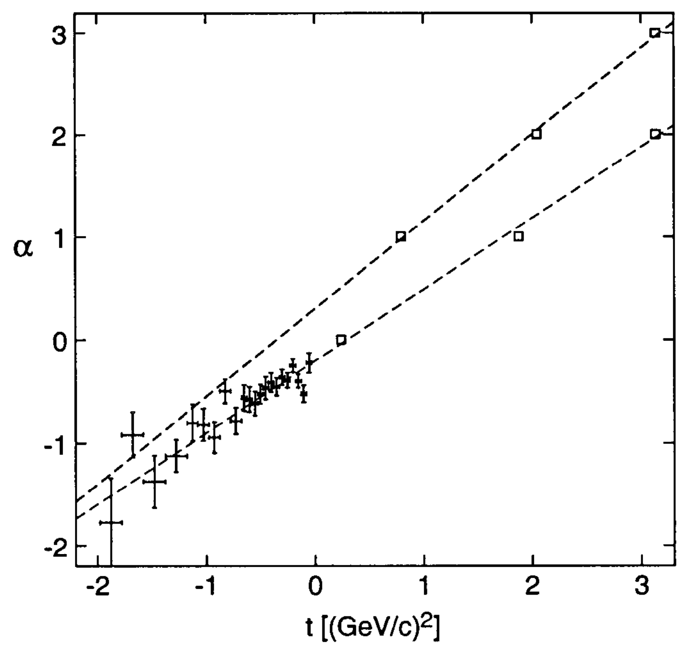

Figure 8.20: The Regge trajectory for the ω computed from the LASS and 4.2 GeV/c Bubble Chamber results.[37] The points with error bars are the data. The open squares show various K and K* resonances. The lower and upper dashed lines show the K and K* trajectories, respectively.

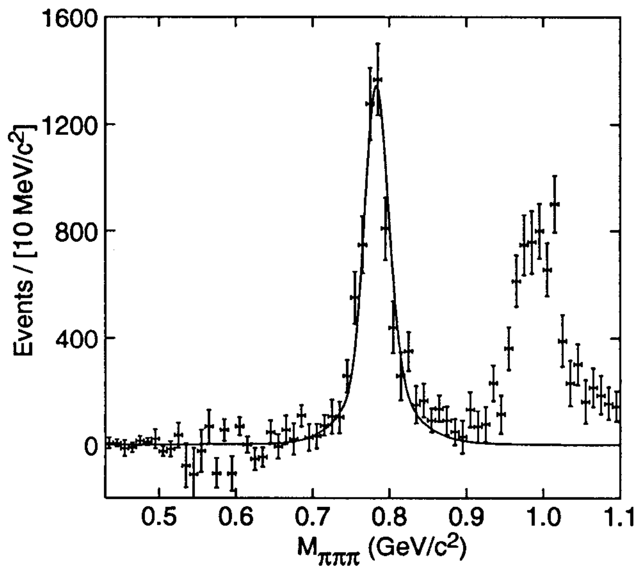

Figure 8.21: The acceptance corrected 3 pion mass spectrum weighted by Y_2^0. The curve is the fit to ω line shape without any background. Only the data below $0.9\,\mathrm{GeV/c^2}$ was fit.

the lower, flatter one being the K line. The K trajectory appears to fit the data well; however, this is in direct contradiction to the results of Figure 8.19, which clearly shows that ω production is dominated by natural parity exchange. This discrepancy is, in fact, not contentious because the ω is strongly affected by Regge absorption effects,[37] and therefore cannot be described by simple Regge poles.

The ω mass spectrum can be analysed in another manner. Since the ω is a 1^- resonance, conservation rules dictate that the $\pi^+\pi^-$ system will be produced in a relative P-wave. Therefore, the ω signal can be enhanced above the background by weighting events by the spherical harmonic Y_2^0, where the angles are the angles of the π^+ in the $\pi^+\pi^-$ rest frame with the z-axis defined by the π^0 direction. The acceptance corrected, Y_2^0 weighted spectrum for the 3π system is shown in Figure 8.21. The η and background under the ω are almost completely suppressed. The bump around $1\,\mathrm{GeV/c^2}$ is not suppressed because it is composed of higher spin objects. A fit of the ω line shape below $m < 0.9\,\mathrm{GeV/c^2}$ without background, is shown in the figure. The cross section obtained is consistent with the previous result.

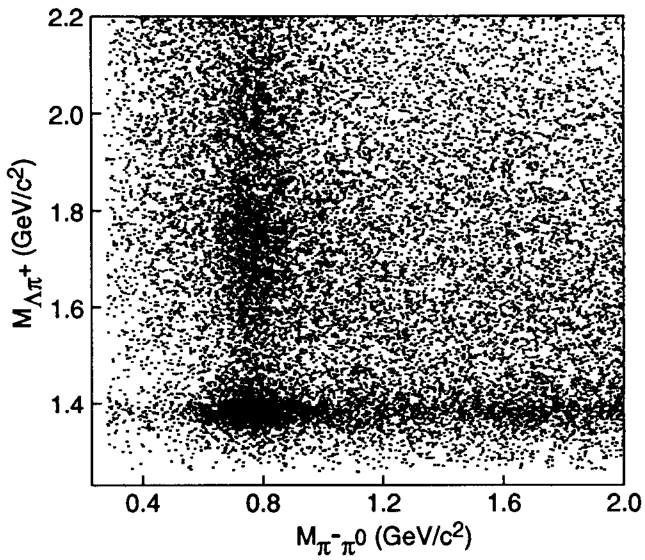

Figure 8.22: Backward $\Lambda\pi^+$ mass versus $\pi^-\pi^0$ mass. The plot clearly shows that correlation between the production of resonances in the two channels.

8.6 Analysis of $\Sigma^+(1385)\pi^-\pi^0$

The $\pi^-\pi^0$ channel is a particularly good place to look for more evidence of the $\rho(1300)$. Since this is a charged channel, the $f_2(1270)$ cannot be present. In addition, G-parity conservation implies that all even spin resonances are disallowed. For a fermion–anti-fermion system, the G-parity is given by $G = (-1)^{J+I}$. The G-parity of two pions is $+1$, and, therefore, J even implies that $I = 2$, which cannot exist in a meson system. ($I = 0$ is disallowed because this is a charged state.) In practice, however, the S-wave is needed in most partial wave analyses to compensate for background.

The correlation between the $\Lambda\pi^+$ and $\pi^-\pi^0$ systems is shown in Figure 8.22. The ρ^- is clearly correlated with the $\Sigma^+(1385)$, and therefore the $\pi^-\pi^0$ system can be analysed more cleanly if the $\Sigma^+(1385)$ is selected. A clean $\Sigma^+(1385)$ signal was found by the method of sideband subtraction, which implicitly assumes that the background is linear. Figure 8.23 shows the $\Lambda\pi^+$ spectrum for the forward $\pi^-\pi^0$ system, along with the signal and sideband regions. The signal region used was 1.340–1.430 GeV/c^2, and the sidebands were 1.265–1.310 and 1.460–1.505 GeV/c^2.

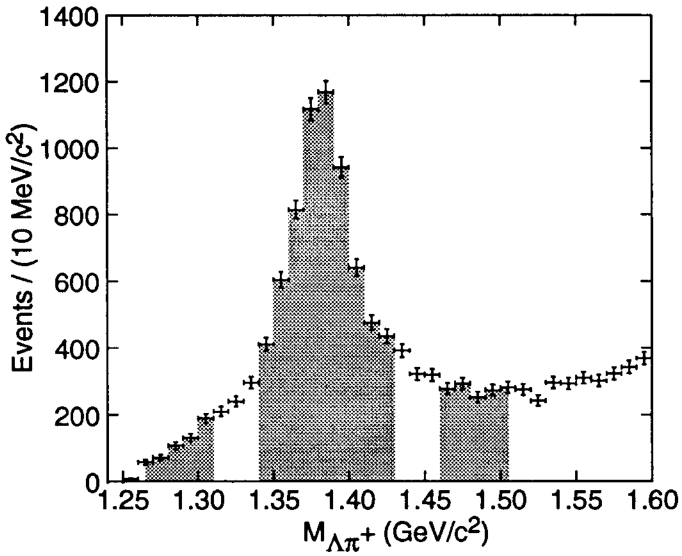

Figure 8.23: The backward $\Lambda\pi^+$ mass spectrum in the region of the $\Sigma^+(1385)$. The shaded regions indicate the signal and sideband regions used in the analysis.

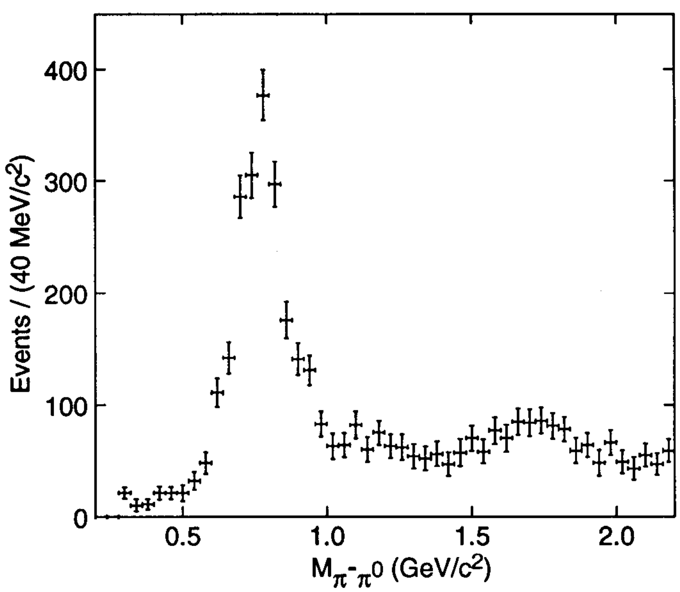

Figure 8.24: The raw forward $\pi^-\pi^0$ mass spectrum. The $\Sigma^+(1385)$ background has been subtracted.

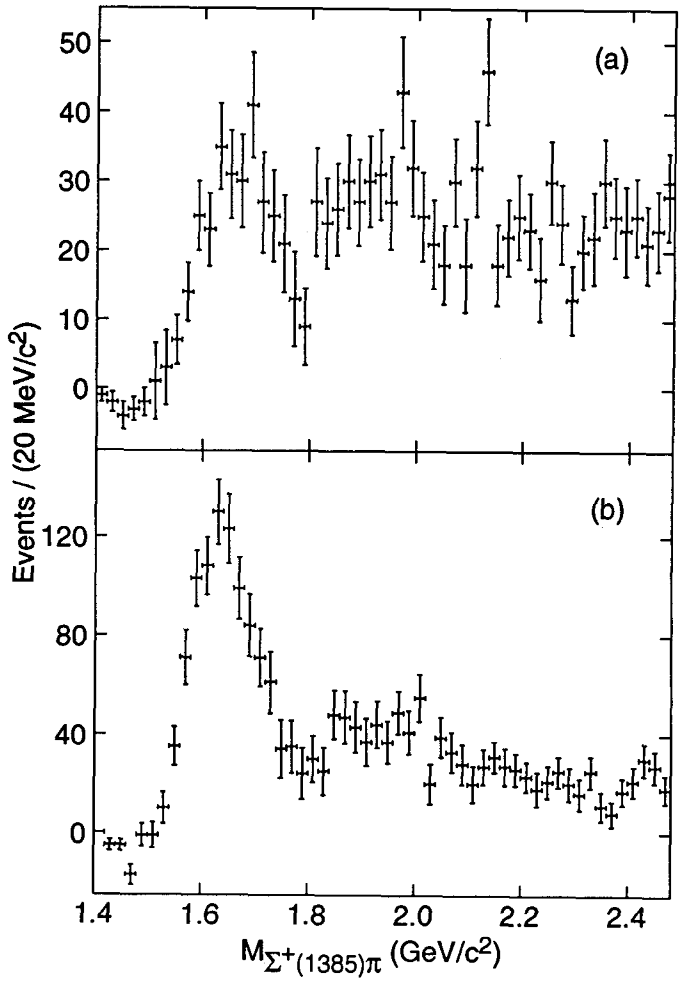

Figure 8.25: The background-subtracted mass spectra for (a) $\Sigma^+(1385)\pi^-$ and (b) $\Sigma^+(1385)\pi^0$ in the forward $\pi^-\pi^0$ sample.

The sideband subtracted, forward $\pi^-\pi^0$ spectrum (not acceptance corrected) is shown in Figure 8.24. The only significant feature is the large ρ peak. There does appear to be a bump around 1700 MeV/c^2, which could be the $\rho_3(1690)$, but it is not big enough over background to be properly analysed. Figure 8.25 shows the $\Sigma^+(1385)\pi^-$ and $\Sigma^+(1385)\pi^0$ sideband subtracted spectra for the forward $\pi^-\pi^0$ sample. There is clear contamination in both spectra from higher mass Λs and Σs. The bump in the $\Sigma^+(1385)\pi^-$ spectrum around 1.6 GeV/c^2 is enhanced for $\pi^-\pi^0$ mass above the ρ. These resonances were removed by cutting events with $m(\Sigma^+(1385)\pi^-) < 1.85$ GeV/c^2 or $m(\Sigma^+(1385)\pi^0) < 2.1$ GeV/c^2.

In order to find the acceptance, 140,000 Monte Carlo events were thrown with a $\Sigma^+(1385)$ Breit–Wigner shape for the $\Lambda\pi^+$ mass distribution. The $\pi^-\pi^0$ distribution was uniform in mass, except for extra events around the ρ mass. The Monte Carlo events were reconstructed and selected with the same program as the data. The data Y_l^m moments were corrected bin by bin using the Monte Carlo acceptance moments. The corrected $\pi^-\pi^0$ moments are shown in Figures 8.26 through 8.28. The width of bins varies over the mass range in order to keep the uncertainty in each bin low; the moments have been normalized for the bin width.

A partial wave analysis was performed up to 1.5 GeV/c^2 with S- and P-waves. From 1.5 GeV/c^2 and up, the χ^2 of the fit became unacceptable, and therefore F-waves were added to the analysis. The D-waves amplitudes were checked; they showed no significant structure and were therefore fixed to 0. The F-wave amplitudes had very large uncertainties, making drawing conclusions about the spin 3 content difficult. Figure 8.29 shows the S- and P-wave amplitudes from the PWA. Above 1.0 GeV/c^2, the data has been double-binned to provide better resolution. The S-wave amplitude shows little structure and is expected to have come from background.

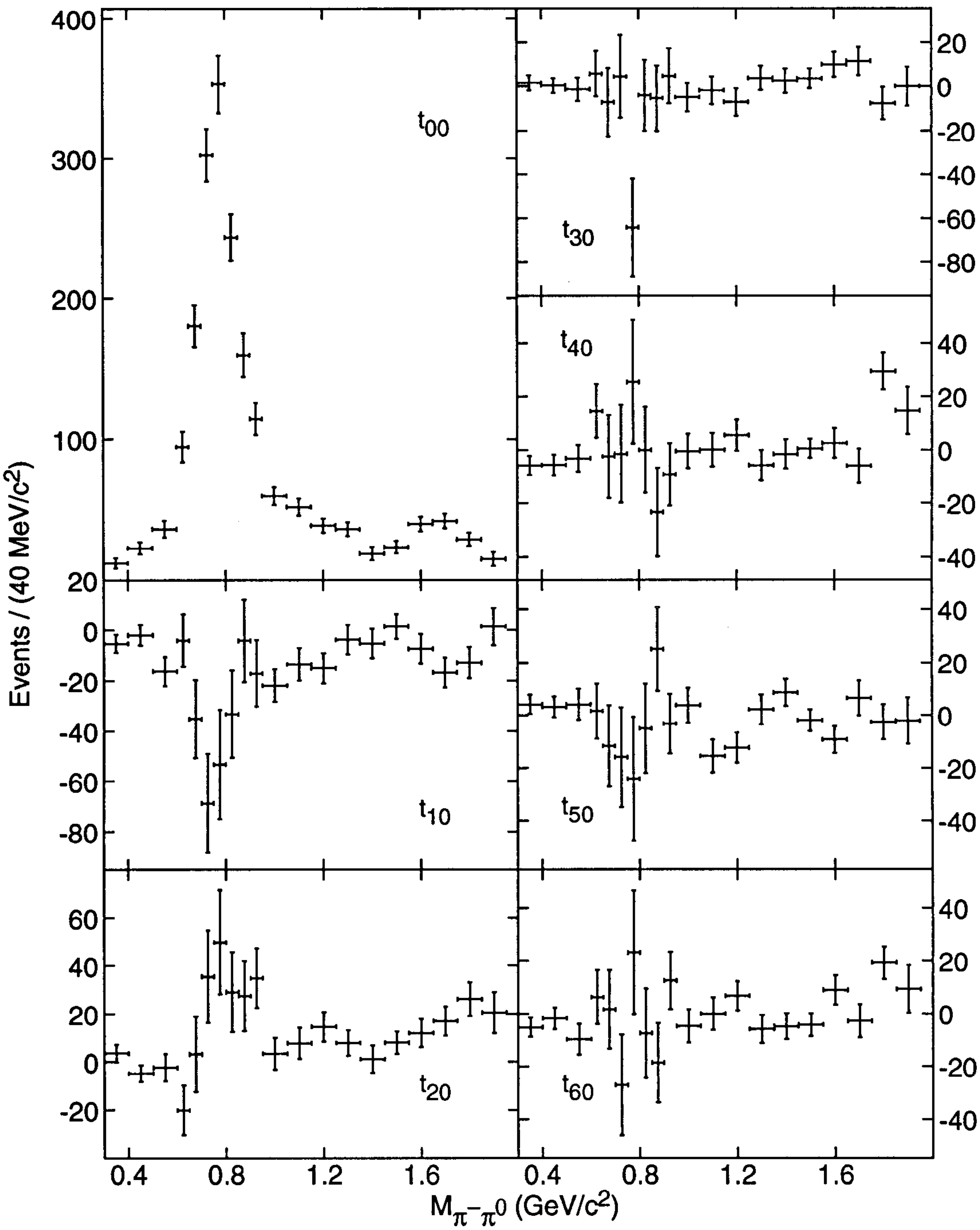

Figure 8.26: The $m = 0$ moments for the forward $\pi^-\pi^0$ system.

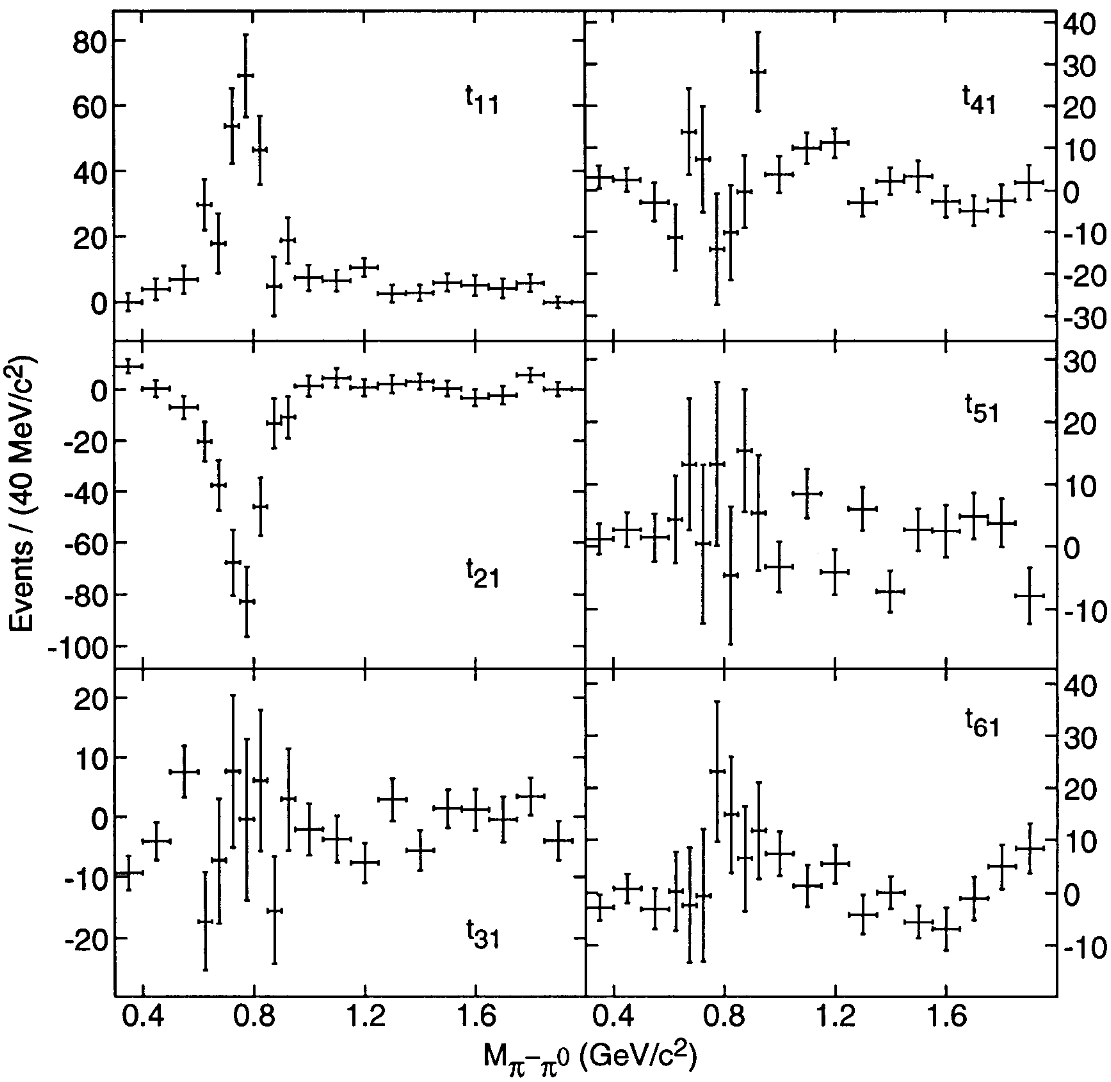

Figure 8.27: The $m = 1$ moments for the forward $\pi^-\pi^0$ system.

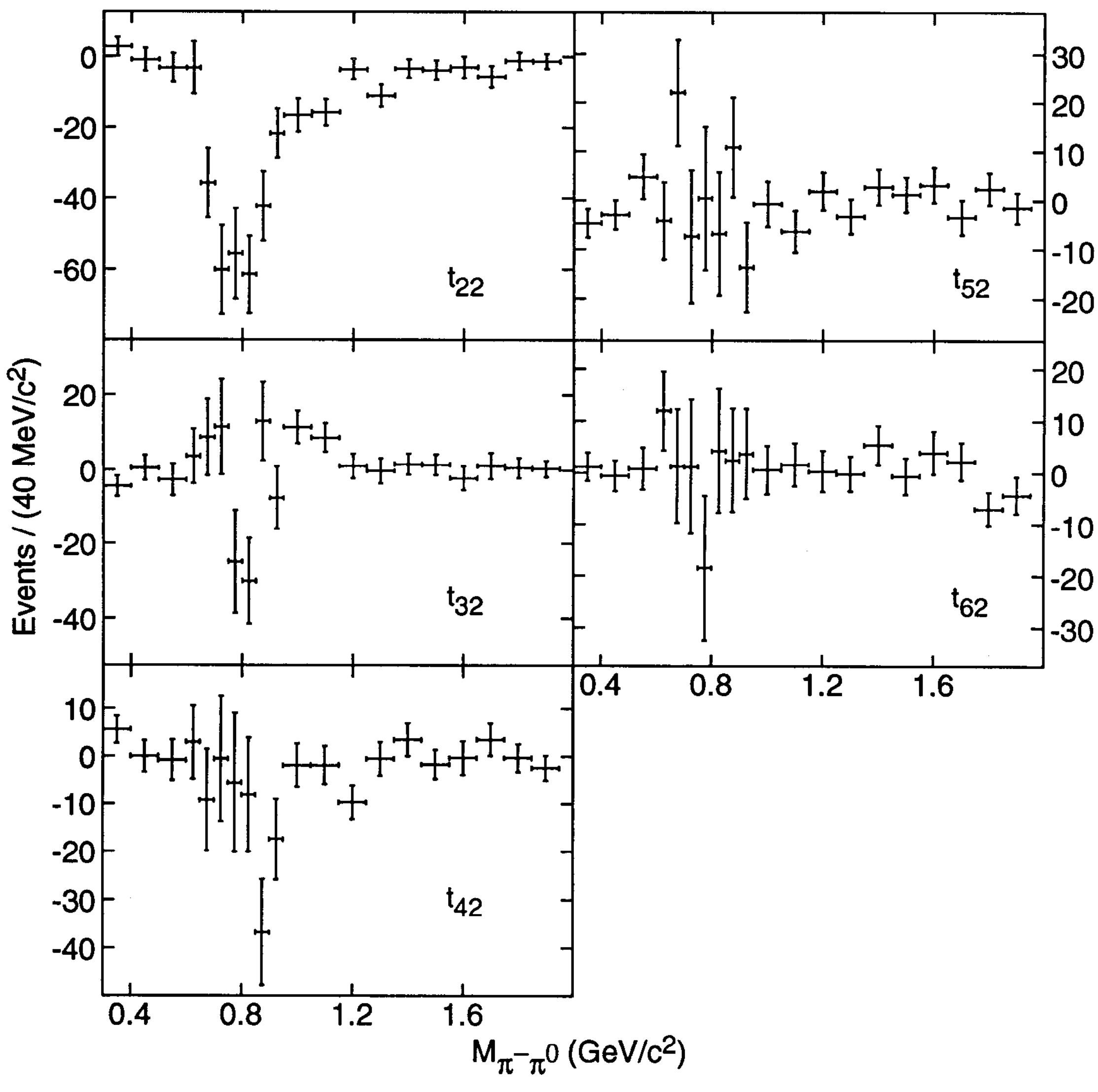

Figure 8.28: The $m = 2$ moments for the forward $\pi^-\pi^0$ system.

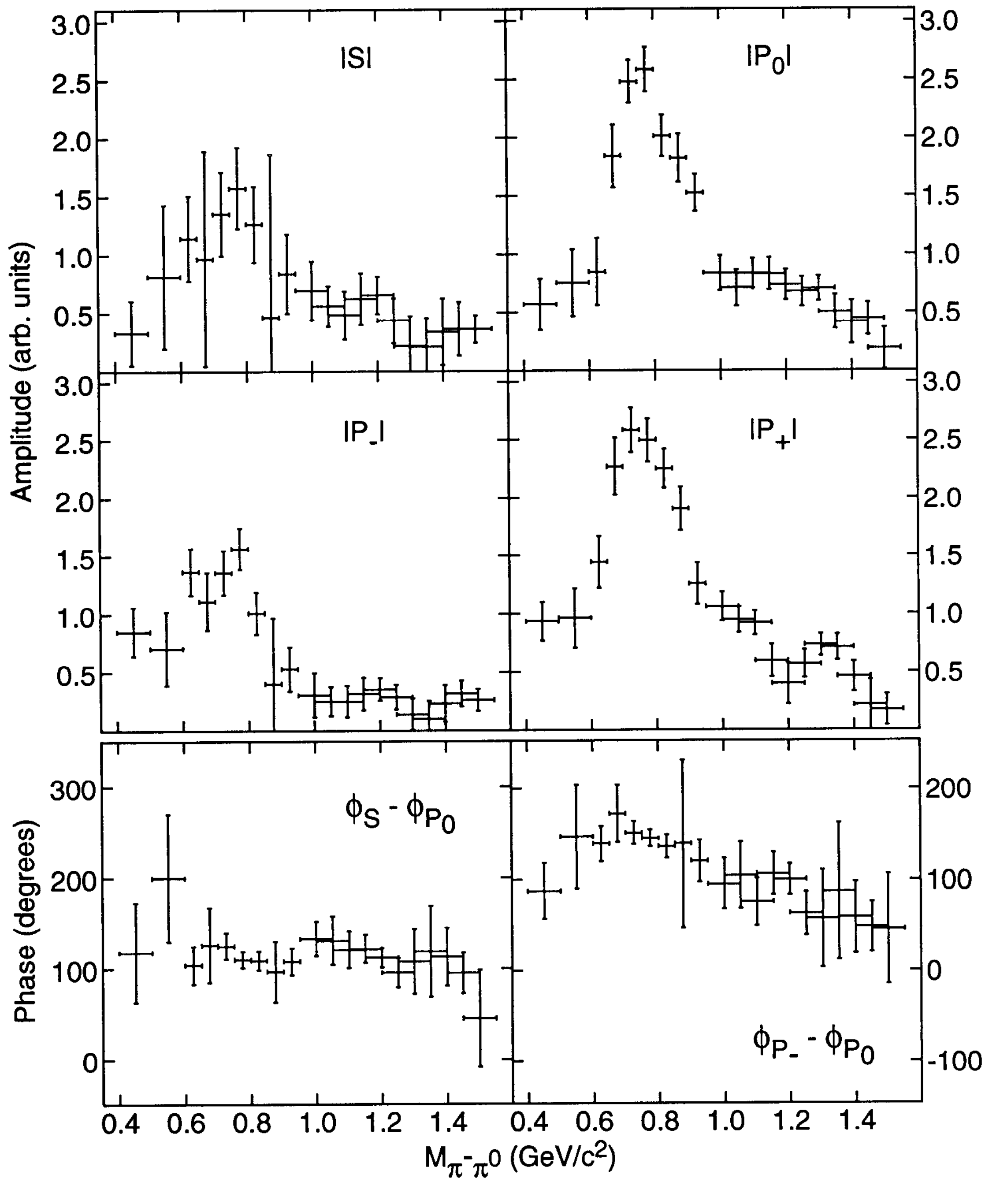

Figure 8.29: The results of a partial wave analysis of the forward $\pi^-\pi^0$ system. Below 1.5 GeV/c^2, only S- and P-waves were used. From 1.5 GeV/c^2 and up, F-waves were included in the fit, but are not shown.

Quantity	P_0	P_+	Total Amplitude
ρ x-sec. (μb)	0.33 ± 0.03	0.38 ± 0.03	0.75 ± 0.06
$\rho(1300)$ x-sec. (μb)	0.026 ± 0.014	0.017 ± 0.008	0.031 ± 0.011
Phase (degrees)	144 ± 31	118 ± 27	100 ± 22
χ^2 / DoF	10 / 13	16 / 13	6 / 13
χ^2 without $\rho(1300)$	31 / 15	37 / 15	35 / 15

Table 8.4: The results of independent fits to various P-wave amplitudes from the partial wave analysis. The cross sections are for the decay to $\pi^-\pi^0$ and are corrected for Λ and $\Sigma^+(1385)$ visibility.

The P-wave amplitudes in Figure 8.29 show an excess of events in the tail of the ρ around $1.2\,\text{GeV/c}^2$. The P_+ and P_0 amplitudes and spin 1 total amplitude (*i.e.* $\sqrt{|P_+|^2 + |P_-|^2 + |P_0|^2}$) were fit individually with two spin-1 Breit–Wigners without background. The extra set of bins above $1.0\,\text{GeV/c}^2$ were *not* used in the fit. The first Breit–Wigner's mass and width were fixed to the mass and width of the ρ, while the second's were fixed to the parameters of the $\rho(1300)$ found in Chapter 7, namely $1300\,\text{MeV/c}^2$ and $120\,\text{MeV/c}^2$. The free parameters of the fits were the amplitudes and the relative phase of the two resonances. The results are shown in Table 8.4 and Figure 8.30. The cross sections were calculated in the same way as was done in the previous chapter, and are corrected for the visibilities[30] of the Λ (64.1%) and $\Sigma^+(1385)$ ($88 \pm 2\%$).

The fits clearly corroborate the presence of the $\rho(1300)$ resonance; the region from 1 to $1.4\,\text{GeV/c}^2$ is not well described by the tail of the ρ, as indicated by the dotted curves in Figure 8.30. The phase and relative amplitude of the $\rho(1300)$ agree with the results of the 2 pion analysis, namely about $90°$ and 5%.

To try to measure the resonance parameters of the $\rho(1300)$, the spin 1 intensity was fit again with the $\rho(1300)$ mass and width free. The fit gives a mass of $(1330 \pm 60)\,\text{MeV/c}^2$ and width of $170^{+120}_{-70}\,\text{MeV/c}^2$. The results are quite consistent with the result from the two pion analysis of Section 7.6.

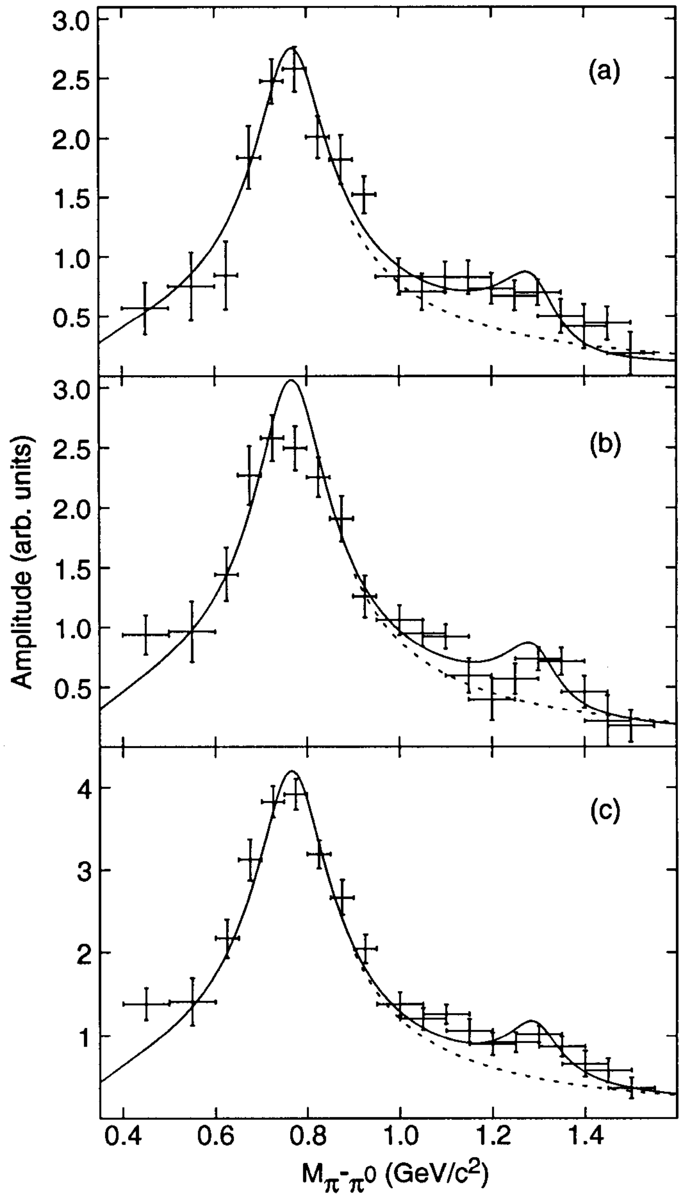

Figure 8.30: The results of independent fits to (a) P_0, (b) P_+, and (c) the total spin 1 amplitude from the partial wave analysis. The extra bins above 1 GeV/c^2 were *not* included in the fit. The dotted curves indicate the tail of the ρ under the second resonance.

8.7 Discussion

The analysis of $K^-p \rightarrow \Lambda\pi^+\pi^-\pi^0$ has shown evidence of resonances in all particle combinations, including clear signals from η and ω in the 3 pion channel. The η cross section was measured as $(3.1 \pm 0.3)\mu$b, all in the forward direction. The t' differential cross section shows a dip around $t' \simeq 0.4\,(\mathrm{GeV/c})^2$, which is reasonably well described by Regge theory. The ω forward cross section was measured as $(3.26 \pm 0.14)\,\mu$b and the backward as $(0.44 \pm 0.05)\,\mu$b, giving a total cross section of $(3.70 \pm 0.15)\,\mu$b. ω production is dominated by natural parity exchange. The differential cross sections are well described by the expected shape (Equation 7.14).

The analysis of the forward $\pi^-\pi^0$ system against $\Sigma^+(1385)$ has provided corroboration of the existence of the $\rho(1300)$. Both σ_0^P and σ_+^P show clear excesses in the tail of the ρ around $1300\,\mathrm{MeV/c^2}$, consistent with the resonance parameters found in the earlier analysis. A fit to the total P-wave amplitude gives a cross section of $(0.031 \pm 0.011)\,\mu$b, corrected for Λ and $\Sigma^+(1385)$ visibilities. A fit with the resonance parameters free yields a mass of $(1330 \pm 60)\,\mathrm{MeV/c^2}$ and width of $170^{+120}_{-70}\,\mathrm{MeV/c^2}$.

Chapter 9

Analyses of Other Channels

This chapter describes surveys of two reactions,

$$K^-p \rightarrow \Lambda\pi^+\pi^-\pi^+\pi^- \tag{9.1}$$

and

$$K^-p \rightarrow \Lambda\pi^+\pi^-\pi^+\pi^-\pi^0. \tag{9.2}$$

All the relevant mass spectra are shown, but the justification and main thrust of the analyses is to check the 4 pion systems for evidence of the $\rho(1300)$. It is hoped that some of the "missing" cross section of the $\rho(1300)$ will be visible in the 4 pion system. However, the complexity of a 4 particle system makes any type of spin separation very difficult. Therefore, if a signal is seen, the identity of the resonance will have to be assumed.

The final section of this chapter looks at a number of meson systems involving kaons, previously analysed by LASS, which might show some signal from $\rho(1300)$ decay.

9.1 $\Lambda\pi^+\pi^-\pi^+\pi^-$ Analysis

9.1.1 Event Selection

Reaction 9.1 is very similar to the 2 pion channel in that there is no missing particle. Therefore, the event selection was essentially the same (see Section 7.1),

Description of Cut	# Events Cut	# Events Remaining
Input events	—	1,498,495
Unsuccessful 4C Fit	1,406,061	92,434
4-C Confidence Level $< 10^{-6}$	45,279	47,155
TOF Particle ID	728	46,427
Cherenkov Particle ID	3,252	43,175
Photon conversion	639	42,536
Lambda Decay Length $< 0.1\,\mathrm{cm}$	1,086	41,450
Output events	—	41,450

Table 9.1: Summary of cuts used in $\Lambda\pi^+\pi^-\pi^+\pi^-$ event selection.

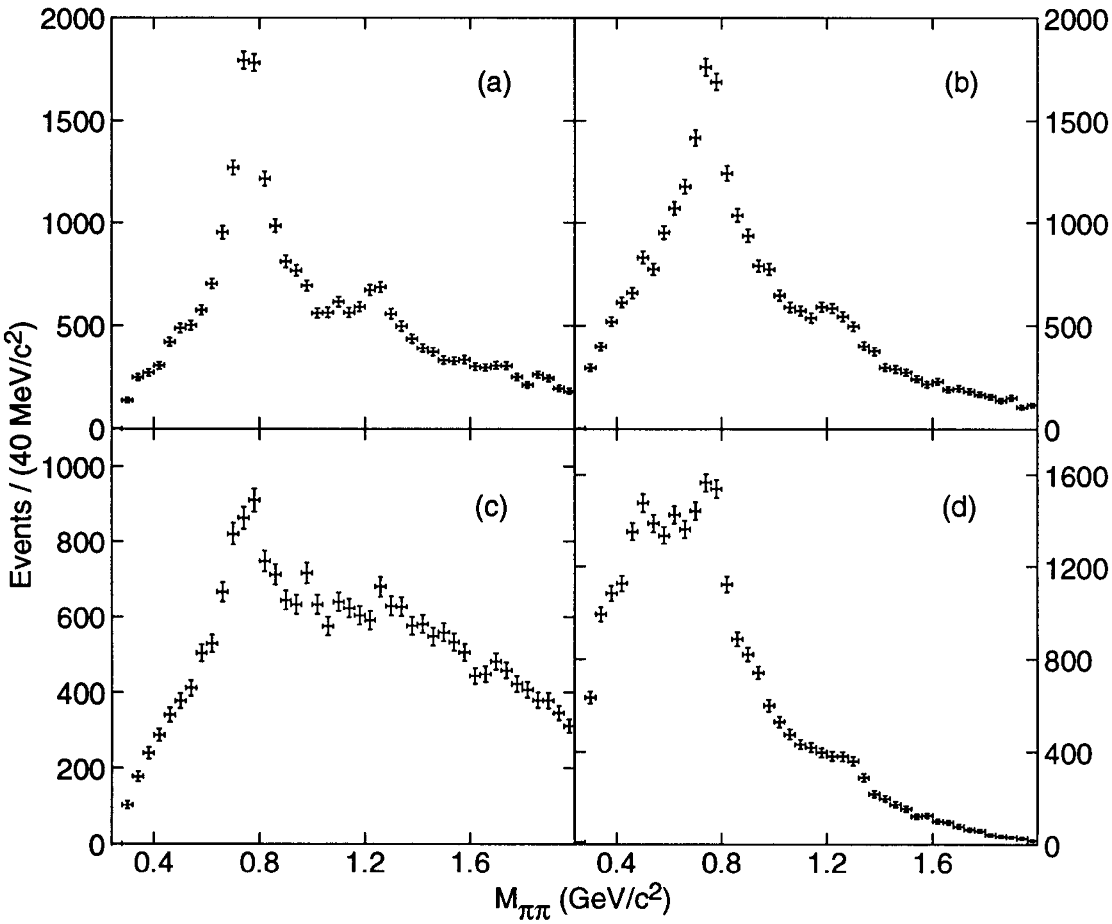

Figure 9.1: The raw $\pi^+\pi^-$ spectra for backward Λ: (a) $\pi_F^+\pi_F^-$, (b) $\pi_F^+\pi_S^-$, (c) $\pi_S^+\pi_F^-$, (d) $\pi_S^+\pi_S^-$.

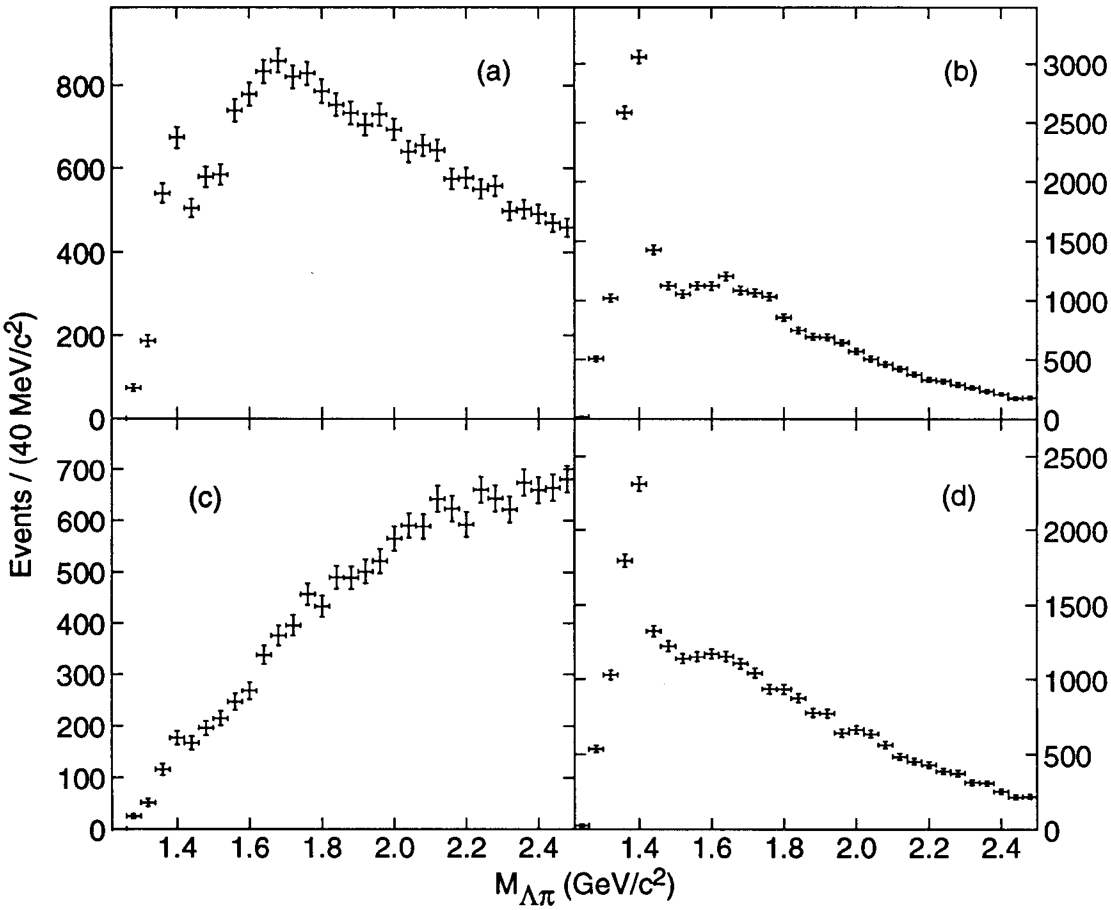

Figure 9.2: The raw $\Lambda\pi$ spectra for backward Λ: (a) $\Lambda\pi^+_F$, (b) $\Lambda\pi^+_S$, (c) $\Lambda\pi^-_F$, (d) $\Lambda\pi^-_S$.

apart from the extra tracks. The 4C Fit confidence level was cut at 10^{-6} and the decay length of the Λ at 0.1 cm. Particle ID cuts were made to all tracks, although there was no evidence of contamination in the dE/dx signals. Electron pairs from photon conversion were also removed. A summary of the cuts made and the number of events removed is given in Table 9.1.

9.1.2 Backward Λ Sample

The mass spectra for the backward Λ sample (selected by cutting on the Feynman x of the Λ) are shown in Figures 9.1 through 9.6. Since there are two pions of

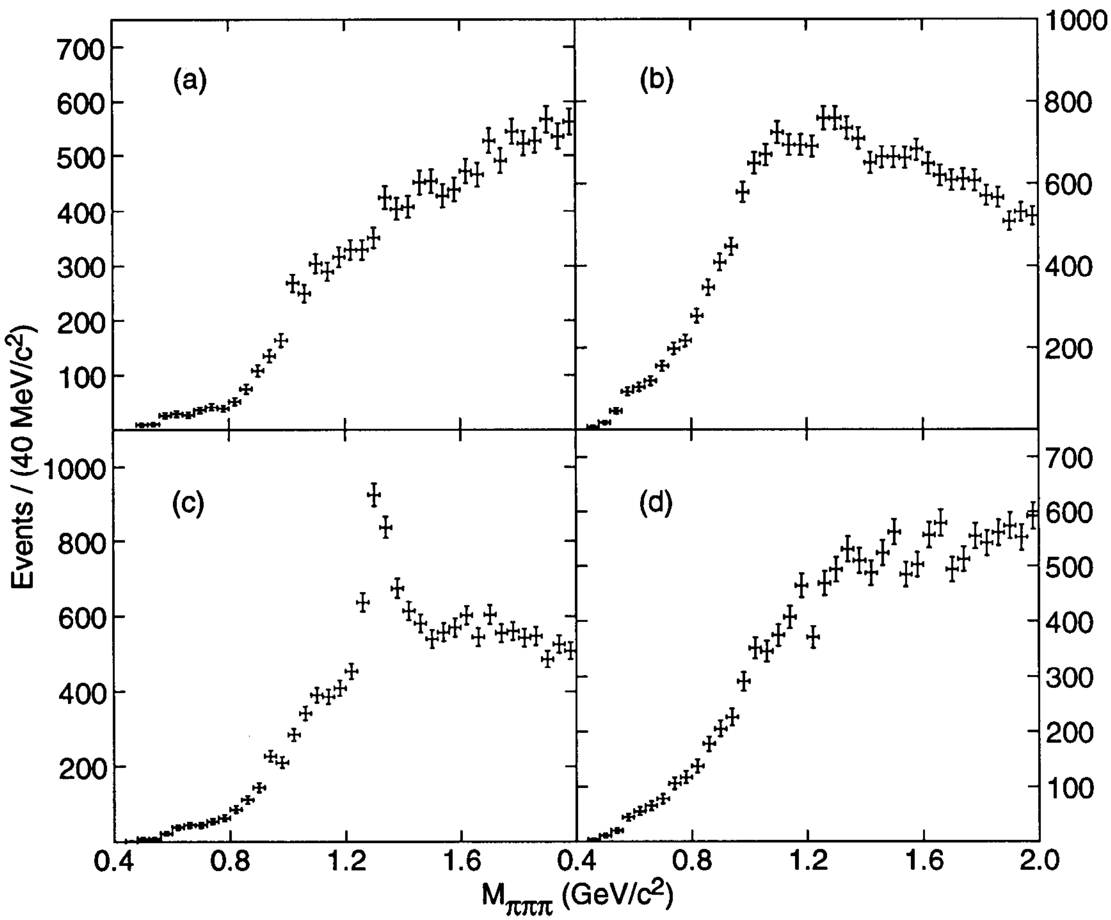

Figure 9.3: The raw 3π spectra for backward Λ: (a) $\pi_F^+\pi_S^+\pi_F^-$, (b) $\pi_F^+\pi_S^+\pi_S^-$, (c) $\pi_F^+\pi_F^-\pi_S^-$, (d) $\pi_S^+\pi_F^-\pi_S^-$.

each charge, the pions of the same charge have been labelled as "fast" or "slow" (designated by subscripts "F" and "S", respectively) as determined by their relative momenta. This designation is somewhat artificial, but it does enhance some of the features in the mass spectra.

The $\pi^+\pi^-$ spectra are shown in Figure 9.1. Both the ρ and $f_2(1270)$ are evident in all combinations, but are much stronger when π_F^+ is used. Some of the pairs, particularly $\pi_S^+\pi_S^-$, show clear evidence of the decay $K_S^0 \to \pi^+\pi^-$ around 500 MeV/c^2.

The spectra for $\Lambda\pi$ are shown in Figure 9.2. $\Sigma(1385)$ is evident in all four

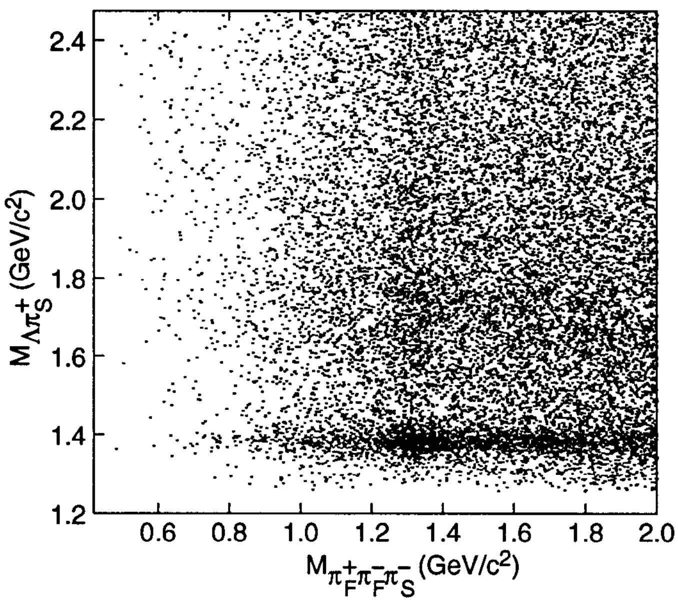

Figure 9.4: The correlation between $a_2(1320)$ production in $\pi_F^+\pi_F^-\pi_S^-$ and Σ resonances in $\Lambda\pi_S^+$.

combinations, but is very much stronger in the two involving the slow pions. This is a consequence of the kinematics of the reaction; the Σ is preferentially produced backward in the center of mass system, and therefore, the pion from its decay will be moving relatively slowly in the lab frame. The higher mass Σs in the range 1.6–1.9 GeV/c^2 seen in the previously described channels are also present here.

Figure 9.3 shows the charged 3 pion spectra. The steep rise in the cross section starting at about 0.8 GeV/c^2 is due to the kinematic turn-on of the two ρs in the neutral sub-channels. The $a_2(1320)$ is evident in $\pi_F^+\pi_F^-\pi_S^-$ but almost completely missing from the other combinations. It is interesting to check the connection between the $a_2(1320)$ and the complementary $\Lambda\pi$ combination. It is evident from Figure 9.4 that the production of $a_2(1320)$ is strongly correlated with Σ^+ production, both $\Sigma^+(1385)$ and the higher mass resonances.

The neutral $\Lambda\pi\pi$ spectra for a backward Λ are shown in Figure 9.5. The $\Lambda\pi_S^+\pi_S^-$ spectrum, in particular, shows evidence for three resonances. Because of their masses, widths and decay mode, they are most likely the $\Lambda(1520)$, $\Lambda(1690)$ and $\Lambda(1810)$.

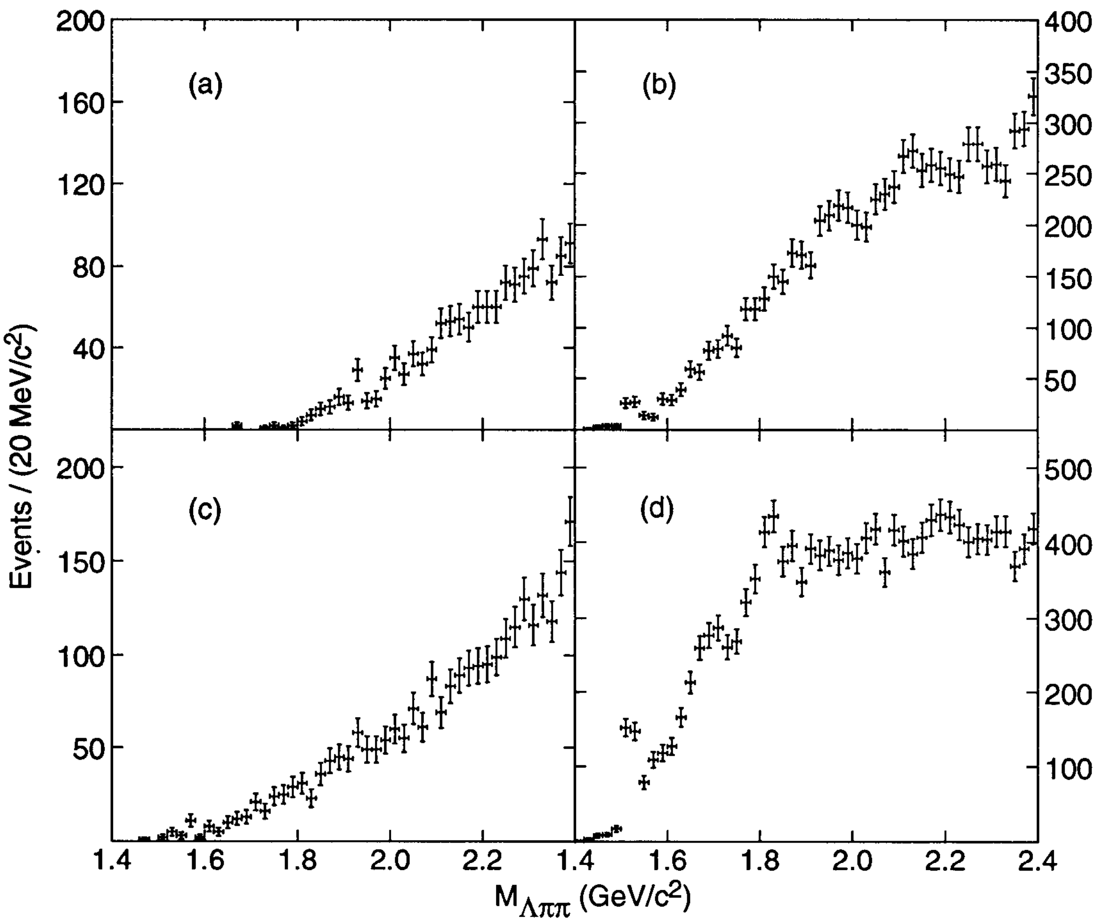

Figure 9.5: The raw $\Lambda\pi^+\pi^-$ spectra for backward Λ: (a) $\Lambda\pi_F^+\pi_F^-$, (b) $\Lambda\pi_F^+\pi_S^-$, (c) $\Lambda\pi_S^+\pi_F^-$, (d) $\Lambda\pi_S^+\pi_S^-$.

Finally, the 4 pion spectrum against a backward Λ is shown in Figure 9.6. There appears to be a small bump around 1300 MeV/c^2, which could be evidence of $f_2(1270)$ or $\rho(1300)$. The only obvious feature is the peak at about 860 MeV/c^2. Unfortunately, this is, in fact, contamination from the decay $\eta' \rightarrow \eta\pi^+\pi^- \rightarrow \pi^+\pi^-\pi^+\pi^-(\pi^0/\gamma)$, where the π^0 or γ is very slow, allowing the 4C Fit to succeed. The 5 pion spectrum is shown in Figure 9.7; the momenta are from the GeoFit quantities, with the missing momentum assigned to the π^0. The low mass bump now peaks at 950 MeV/c^2, the mass of the η'. There are about 60 events in the peak.

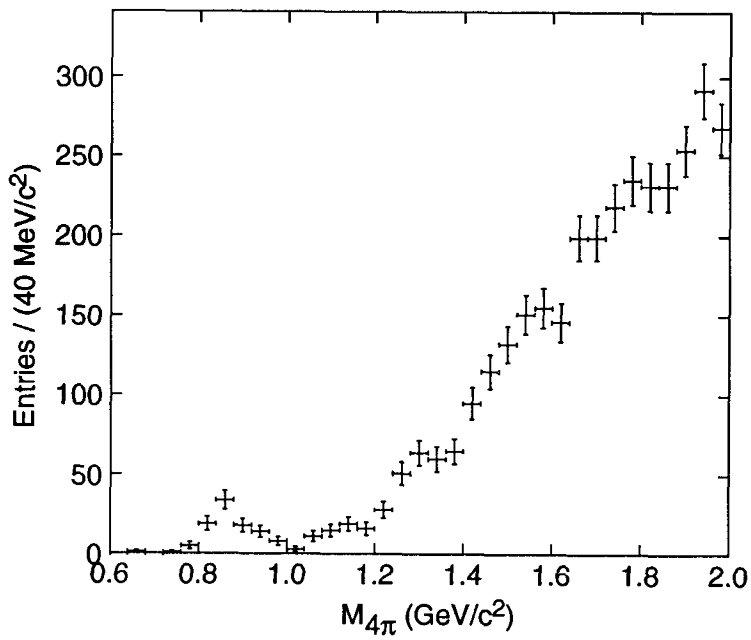

Figure 9.6: The raw 4π spectrum for backward Λ. The peak around $800\,\mathrm{MeV/c^2}$ is due to $\eta' \to 4\pi(\pi^0/\gamma)$ events (see Figure 9.7).

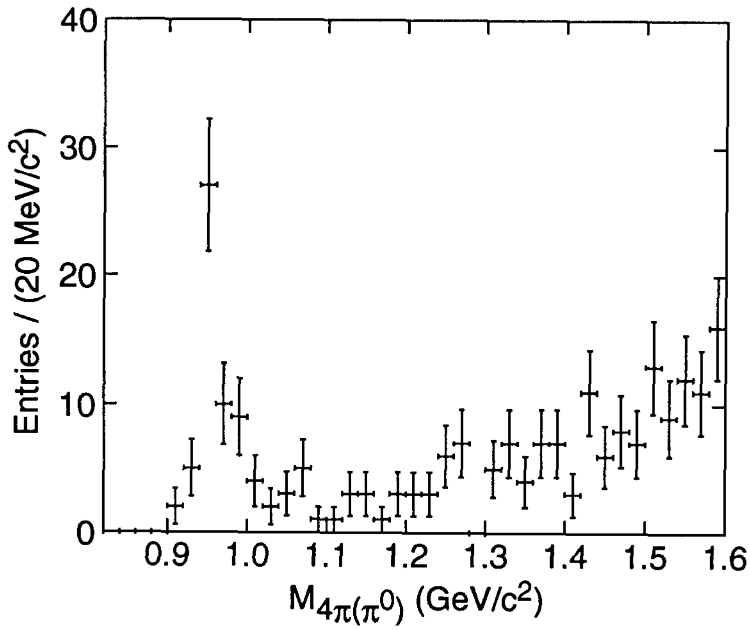

Figure 9.7: The raw $4\pi(\pi^0)$ spectrum for backward Λ. The momenta of the particles come from the GeoFit, with the missing momentum assigned to the π^0.

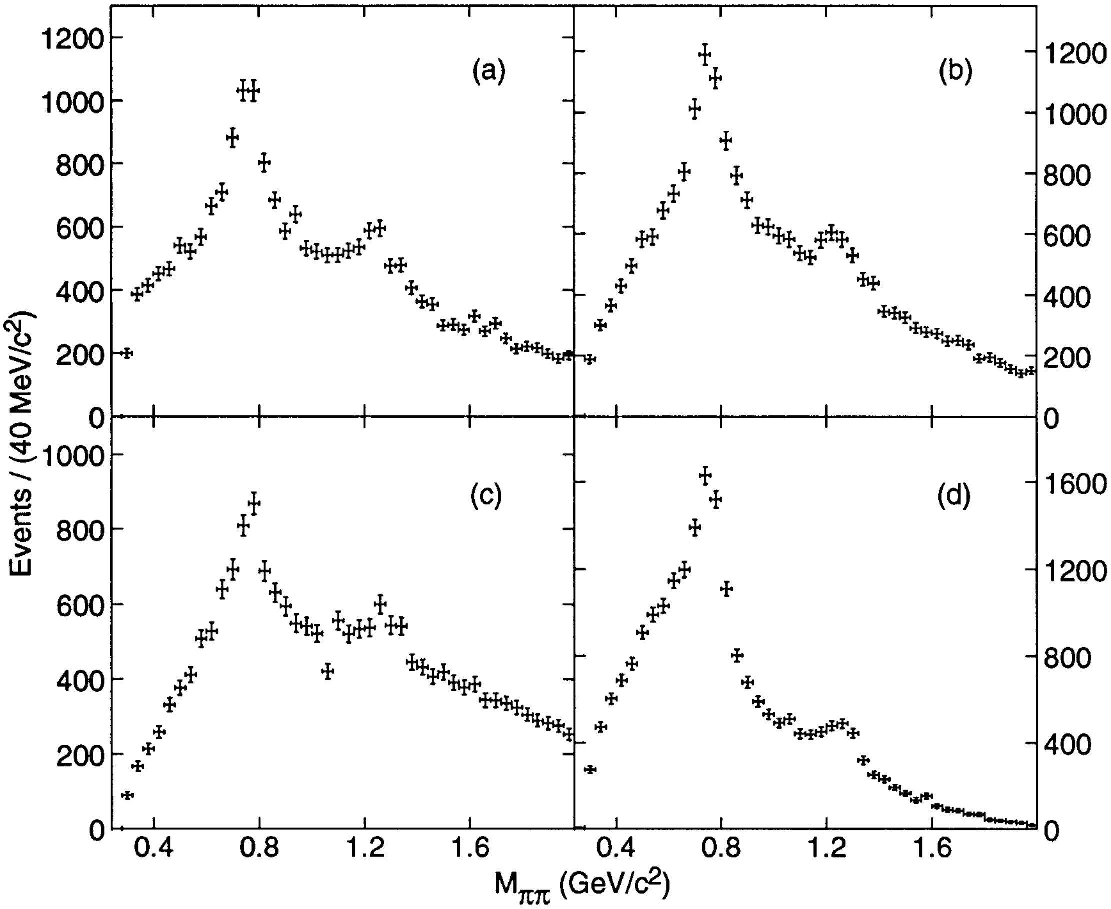

Figure 9.8: The raw $\pi^+\pi^-$ spectra for forward Λ: (a) $\pi_F^+\pi_F^-$, (b) $\pi_F^+\pi_S^-$, (c) $\pi_S^+\pi_F^-$, (d) $\pi_S^+\pi_S^-$.

9.1.3 Forward Λ Sample

Figure 9.8 shows the 2 pion spectra against a forward Λ. The ρ and $f_2(1270)$ show strong signals in all particle combinations. There does not appear to be a very significant signal from K^0_S decay.

The $\Lambda\pi$ spectra in Figure 9.9 show signals from $\Sigma(1385)$ and higher Σs in all combinations. The $\Sigma(1385)$ signals are relatively smaller than in the backward Λ sample.

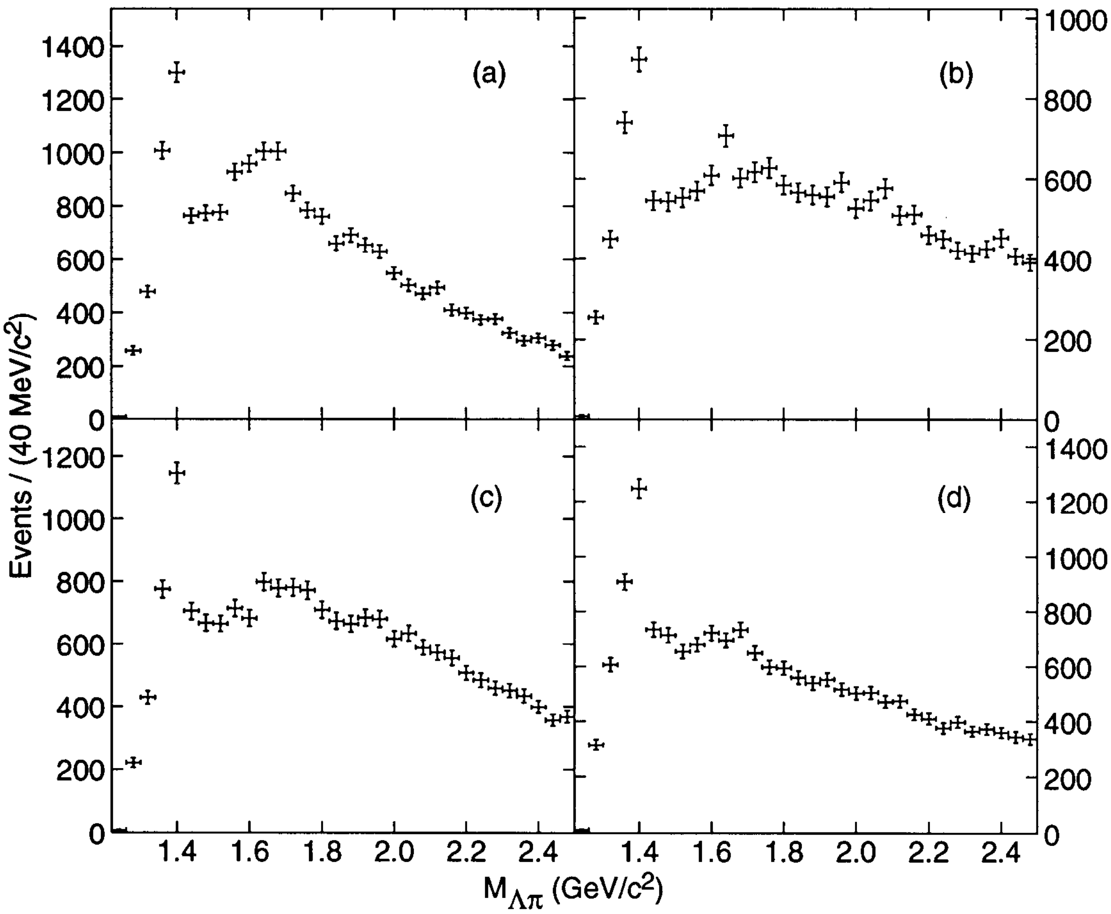

Figure 9.9: The raw $\Lambda\pi$ spectra for forward Λ: (a) $\Lambda\pi_F^+$, (b) $\Lambda\pi_S^+$, (c) $\Lambda\pi_F^-$, (d) $\Lambda\pi_S^-$.

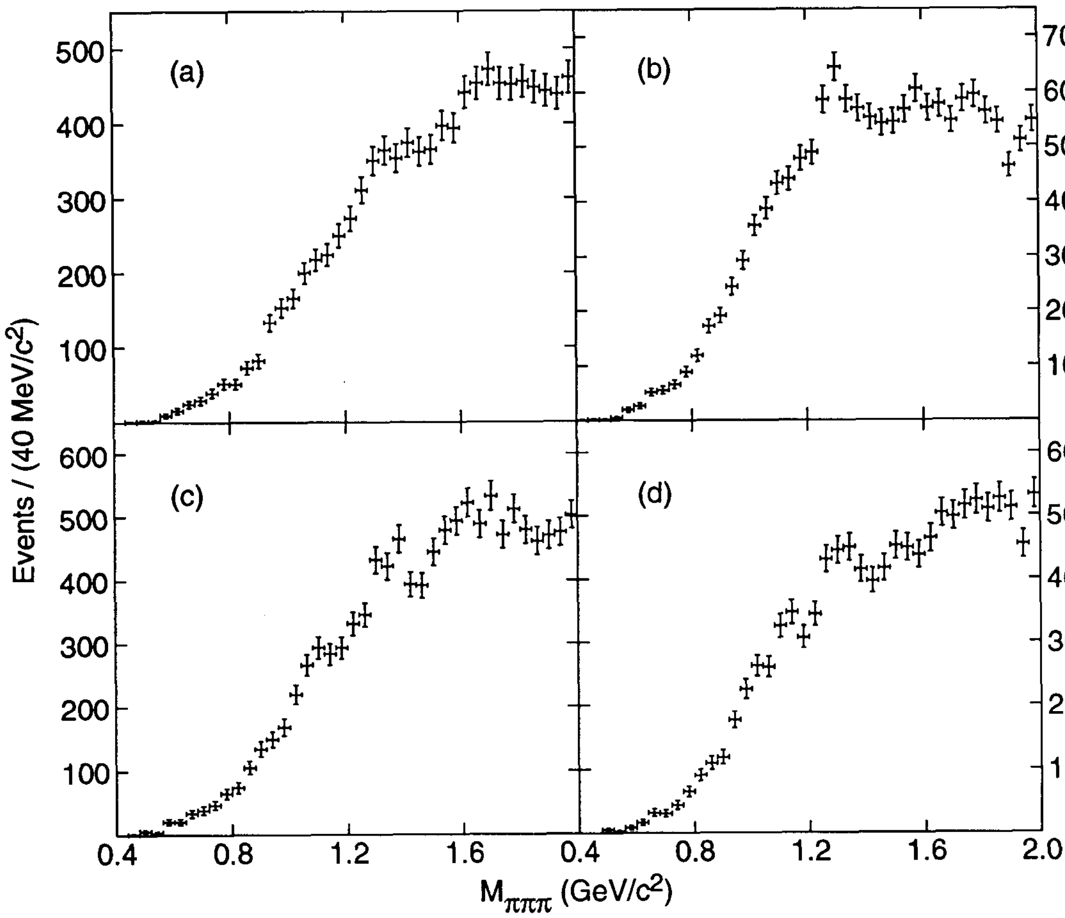

Figure 9.10: The raw 3π spectra for forward Λ: (a) $\pi_F^+\pi_S^+\pi_F^-$, (b) $\pi_F^+\pi_S^+\pi_S^-$, (c) $\pi_F^+\pi_F^-\pi_S^-$, (d) $\pi_S^+\pi_F^-\pi_S^-$.

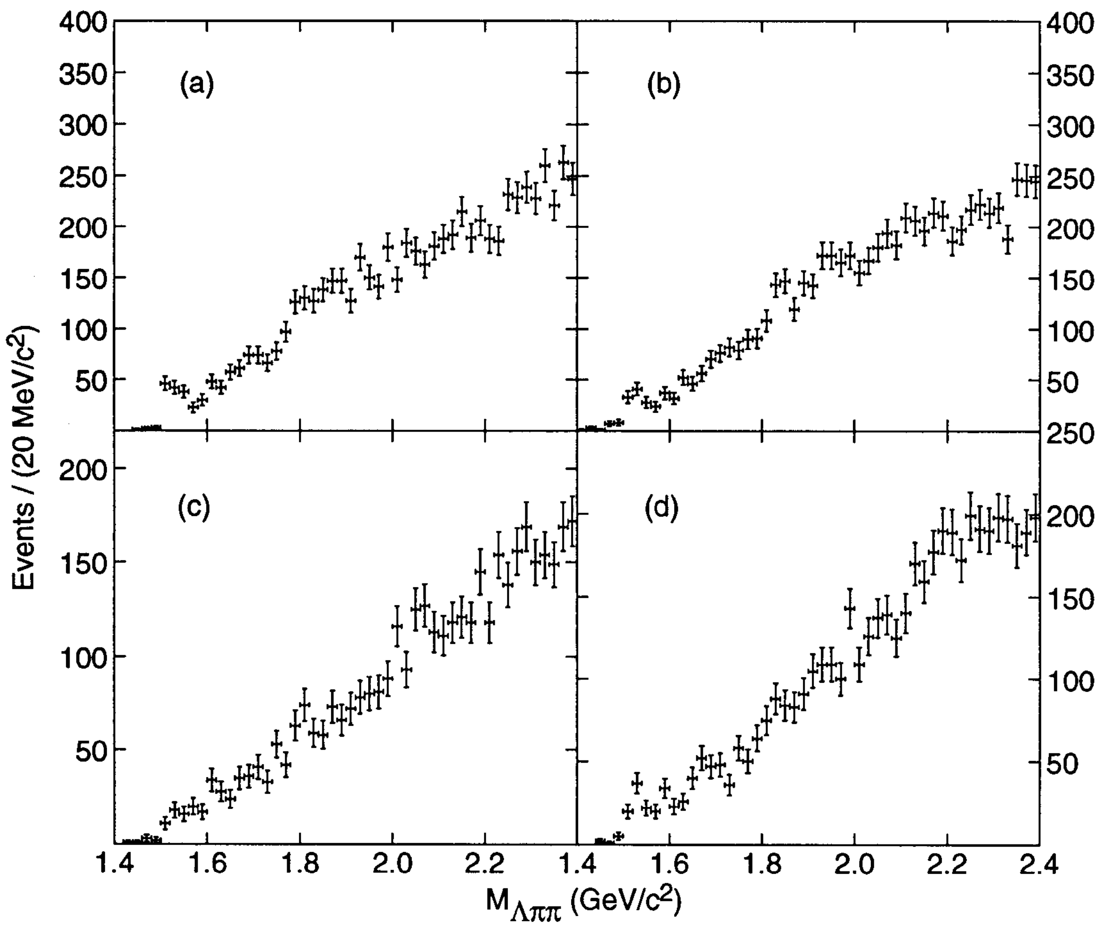

Figure 9.11: The raw $\Lambda\pi^+\pi^-$ spectra for forward Λ: (a) $\Lambda\pi_F^+\pi_F^-$, (b) $\Lambda\pi_F^+\pi_S^-$, (c) $\Lambda\pi_S^+\pi_F^-$, (d) $\Lambda\pi_F^+\pi_S^-$.

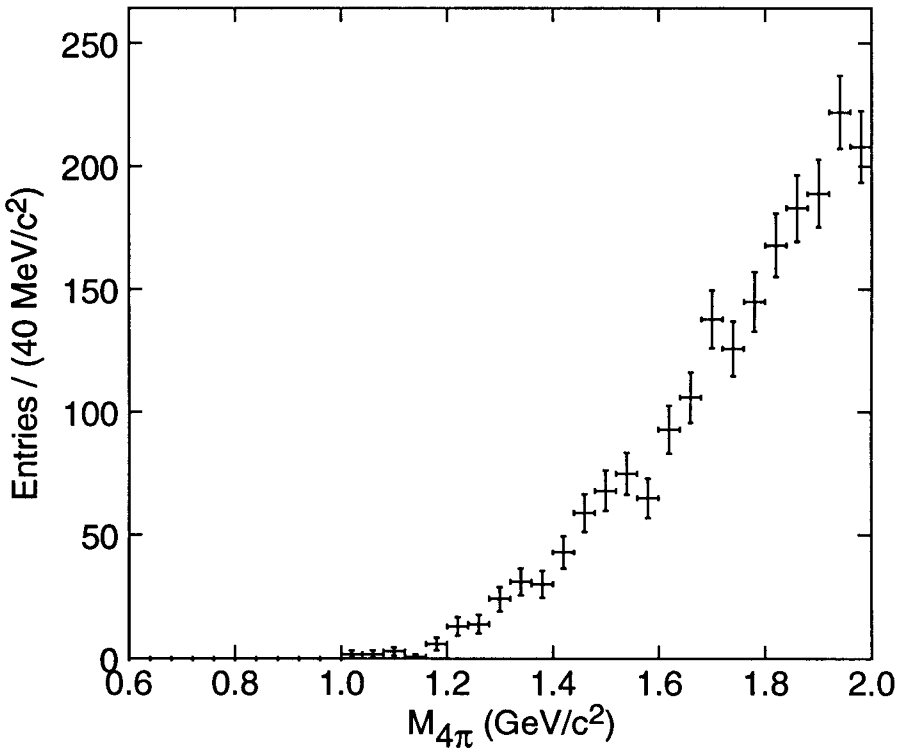

Figure 9.12: The raw $\pi^+\pi^-\pi^+\pi^-$ spectrum for forward Λ.

Figure 9.10 shows the 3 pion spectra. The steep rise due to the kinematic threshold for ρ in the 2 pion sub-channel is evident in all combinations. There appears to be some signal from $a_2(1320)$ in three of the combinations, but the bumps are small.

The spectra for $\Lambda\pi^+\pi^-$ are shown in Figure 9.11. The $\Lambda(1520)$ is evident, though small. There are small structures in some of the combinations which could be due to $\Lambda(1690)$ and $\Lambda(1810)$.

The 4 pion spectrum against a forward Λ is shown in Figure 9.12. It increases smoothly from 1.1 GeV/c^2 and does not have any significant structure.

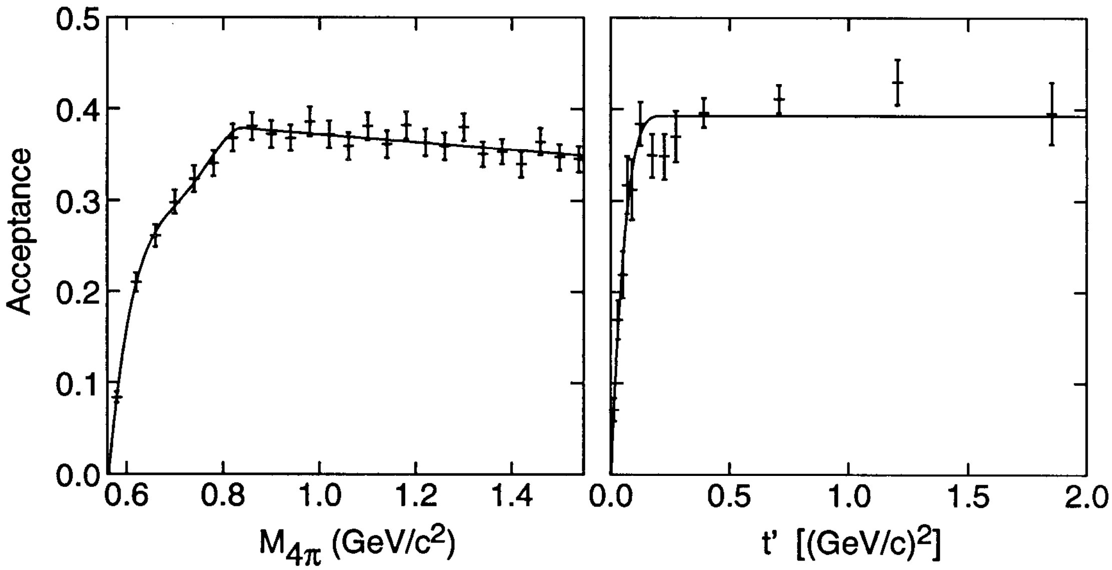

Figure 9.13: The mass and t' dependence of the acceptance for the 4 pion system. The curves are the parametrizations discussed in the text.

9.1.4 Analysis of 4π System

While $\rho(1300) \to \pi^+\pi^-\pi^+\pi^-$ is a possible decay mode for the $\rho(1300)$, it is a very difficult channel to analyse definitively. The number of degrees of freedom in the 4 pion system means that substantially more data is needed than in the 2 pion analysis. In addition, the number of possible decay sub-channels (*e.g.* $\rho^0\pi^+\pi^-$) means that any analysis will be somewhat model dependent.

To find the acceptance for the 4 pion system, 60,000 Monte Carlo events were thrown with the 4 pion system following 4 particle phase space. After reconstruction and selection, the events were binned in mass and t', and the acceptance was parametrized. The mass and t' dependences, along with their fits, are shown in Figure 9.13. The curves used for the parametrization were a quartic below a certain point (0.84 GeV/c^2 for mass and 0.25 (GeV/c)^2 for t') and a straight line above; the two sections were required to be smooth and continuous at the transition. It should be noted that this is only an approximate acceptance. Since the Monte Carlo sample was not thrown to mimic the data, the acceptance would have to be parametrized in all kinematic variables of the 4 pion system. However, it is expected that the acceptance parametrized in mass and t' will correct the data to within a few percent since the LASS detector is quite uniform and mass and t' effects dominate the acceptance.

To find the cross section due to $\rho(1300)$, the 4 pion mass spectrum was fit with a spin 1 Breit–Wigner plus a background function. The mass and width of the Breit–Wigner were fixed to the values for the $\rho(1300)$, specifically 1300 MeV/c^2 and 120 MeV/c^2. $\Sigma(1385)$ was removed from all $\Lambda\pi$ combinations by cutting events with $1.30 < m_{\Lambda\pi} < 1.47$ GeV/c^2 before the acceptance correction. Also, events with $m_{4\pi\pi^0} < 1.1$ GeV/c^2 were cut to remove the η' contamination.

Figure 9.14 shows three fits to the acceptance corrected mass spectrum, each using a different background shape. The solid curves are the total shape; the Breit–Wigner is shown as a dashed curve while the background is shown as a dotted curve. Figure 9.14a shows a fit to the region 1.0–1.6 GeV/c^2 with a cubic background. The resulting cross section for the Breit–Wigner is $(0.10 \pm 0.04)\mu$b. The χ^2 is 14.8 for 10 degrees of freedom as opposed to 18.2 for 11 for the best fit without the Breit–Wigner.

The correlation between the 4 pion mass and one of its neutral sub-channels is shown in Figure 9.15. The kinematic turn-on of the ρ in the sub-channel occurs between 1.2 and 1.3 GeV/c^2, and contributes significantly to the 4 pion cross section. Therefore, in order to approximate the ρ turn-on, the fit shown in Figure 9.14b uses a background which is a straight line plus a cubic, where the cubic is cut off when it tries to go below 0. The fit to the mass range 0.92–2.0 GeV/c^2 results in a cross section of $(0.10 \pm 0.03)\mu$b with a χ^2 of 26.0 for 20 degrees of freedom versus 28.8 for 21 without the Breit–Wigner.

The fit of Figure 9.14c uses an exponential growth curve to represent the ρ turn-on, *i.e.* $1 - \exp(b(m - m_0))$ above $m = m_0$ and 0 below. This shape gave a reasonable fit to the turn-on when a narrow region of $\pi_F^+\pi_F^-$ mass around the ρ was selected. The fit of Figure 9.14c gives a cross section of $(0.26 \pm 0.05)\mu$b. The χ^2 is 23.4 for 21 degrees of freedom versus 33.8 for 22 for the best fit without the resonance. This cross section corresponds to roughly all the events in the range 1.2 to 1.36 GeV/c^2 being attributed to the resonance.

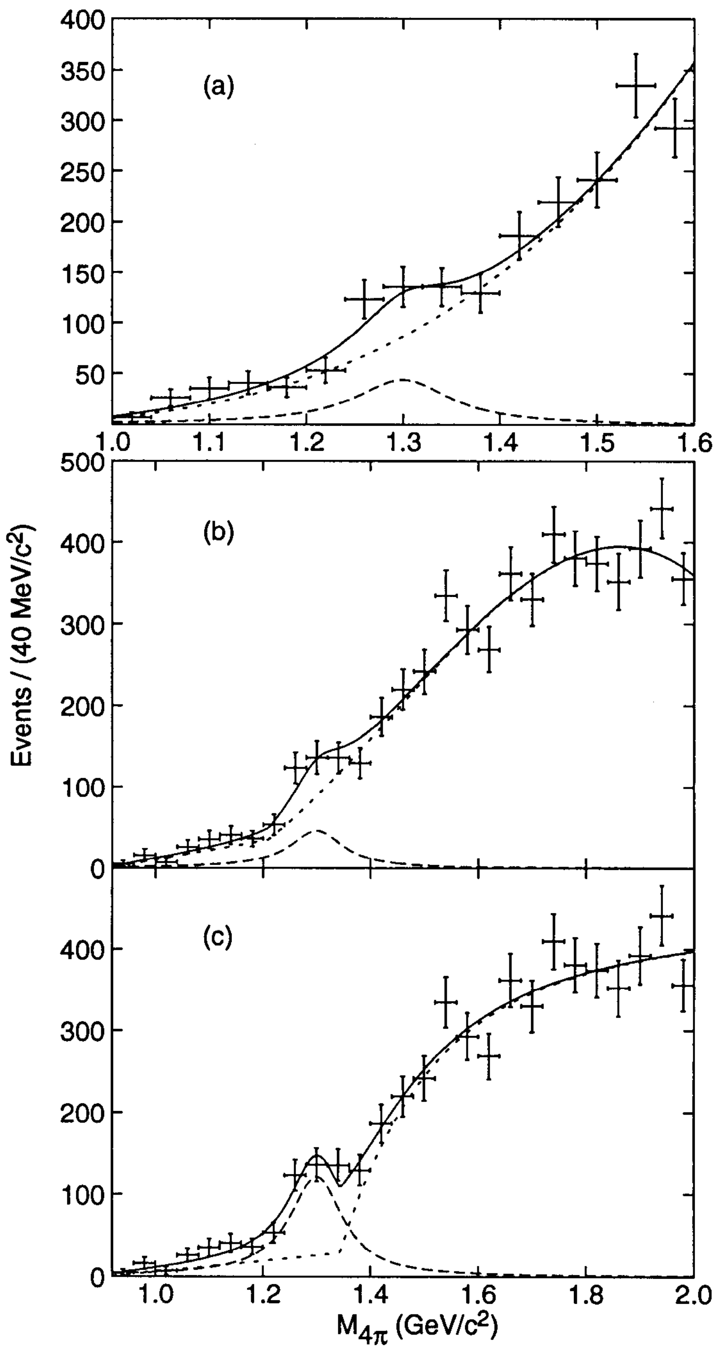

Figure 9.14: Fits of a $\rho(1300)$ Breit–Wigner plus various backgrounds to the 4 pion mass spectrum. The solid curves show the result of the fits described in the text. The dashed curves show the Breit–Wigner contribution while the dotted curves show the background shape. The background shapes are described in the text.

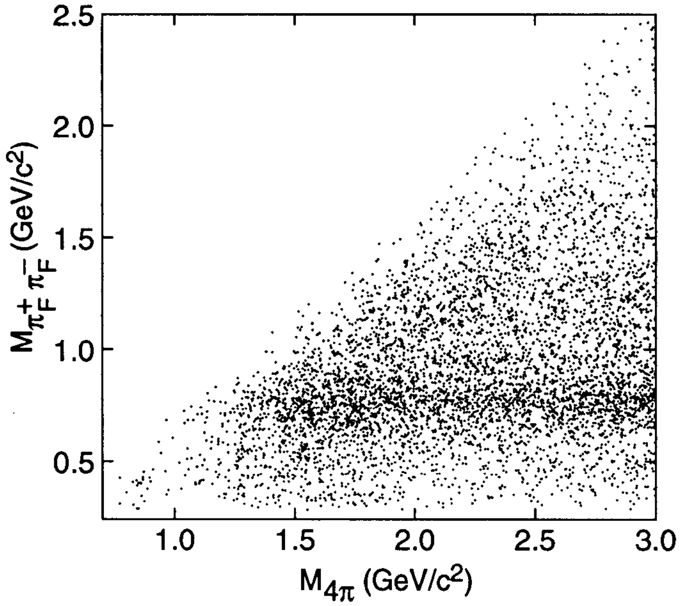

Figure 9.15: The correlation between ρ production in the $\pi_F^+\pi_F^-$ system and 4π mass.

The one definite source of background to the $\rho(1300)$ in this channel is the $f_2(1270)$. Using the Particle Data Group values,[30] the 4π branching ratio is

$$\frac{\sigma(f_2(1270) \rightarrow \pi^+\pi^-\pi^+\pi^-)}{\sigma(f_2(1270) \rightarrow \pi^+\pi^-)} = 0.050 \pm 0.007.$$

Combining this with the cross section measured in Section 7.9, the expected $f_2(1270)$ cross section in the all-charged 4 pion channel is $(0.075 \pm 0.013)\mu$b. However, because the experiments which measured the 4 pion cross sections did not do any spin analyses, this may be significantly over-estimated.

To get an upper limit, the entire cross section from the fit shown in Figure 9.14c is attributed to the $\rho(1300)$. The 90% confidence level upper limit is $\sigma(\rho(1300) \rightarrow \pi^+\pi^-\pi^+\pi^-) < 0.32\,\mu$b. This implies that the upper limit on the branching ratio is

$$\frac{\sigma(\rho(1300) \rightarrow \pi^+\pi^-\pi^+\pi^-)}{\sigma(\rho(1300) \rightarrow \pi^+\pi^-)} < 3.$$

Description of Cut	Events Cut	Events Remaining
Input Events	—	1,481,270
Unsuccessful 1C Fit	970,844	510,426
4C Events	63,857	446,569
Unsuccessful GeoFit	216	446,353
Missing P_t–P_z	23,941	422,412
ΔP_{est} cut	33,549	388,863
dE/dx Particle ID	4,547	384,316
ToF Particle ID	38,700	345,616
Cherenkov Particle ID	47,541	298,075
Photon conversion	10,866	287,209
$MM^2 > 0.08\,(\mathrm{GeV/c^2})^2$	143,717	143,492
Λ Helicity cut	4,669	138,823
Lambda Decay length $< 0.1\,cm$	8,338	130,485
1C Confidence Level $< 10^{-2}$	41,475	89,010
Final Sample	—	89,010

Table 9.2: Summary of cuts used in $\Lambda\pi^+\pi^-\pi^+\pi^-\pi^0$ event selection.

9.2 $\Lambda\pi^+\pi^-\pi^+\pi^-\pi^0$ Analysis

This channel has been studied by LASS previously,[16] but only in the specialized mode $\mathrm{K^-p} \to \Lambda\eta\pi^+\pi^-$. The following discussion presents a more general survey of the channel.

9.2.1 Event Selection

The event selection of Reaction 9.2 was nearly identical to that of the 3 pion channel, apart from the extra two tracks (see Section 8.1). Any event with a successful 4C 4 pion fit were removed (a 4C 4 kaon fit had not been done on the sample). The cut in the missing $p_t - p_z$ plane was changed to $p_t < 0.06\,\mathrm{GeV/c}$ and $p_z < 0.3\,\mathrm{GeV/c}$, since the cluster of 4C events was more concentrated near 0 than in the 3 pion channel. Particle ID cuts were made to all tracks, and electron pairs from photon conversion were removed. The missing mass squared was cut at $-1.0 < (MM)^2 < 0.08\,(\mathrm{GeV/c^2})^2$. The 1C Fit confidence level was cut at 10^{-2}

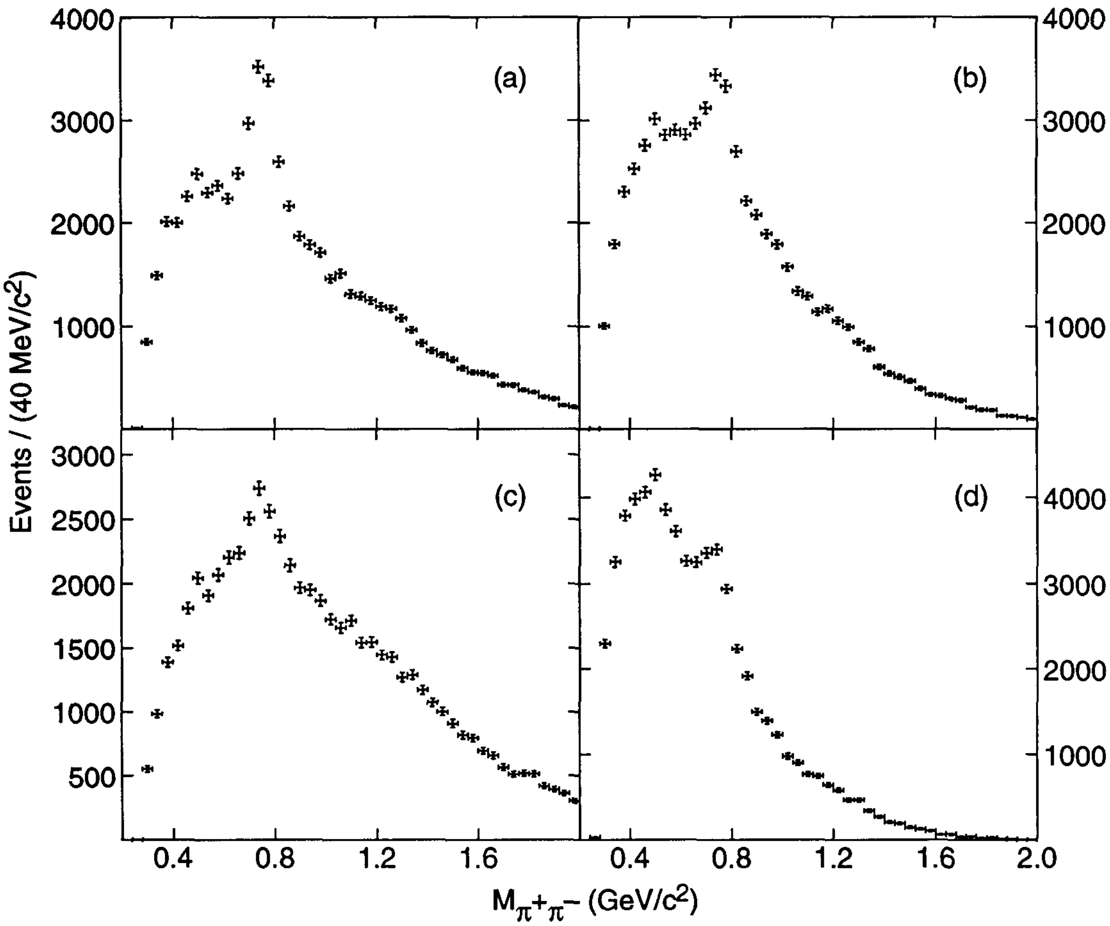

Figure 9.16: The $\pi^+\pi^-$ spectra for a backward Λ: (a) $\pi_F^+\pi_F^-$, (b) $\pi_F^+\pi_S^-$, (c) $\pi_S^+\pi_F^-$, (d) $\pi_S^+\pi_S^-$.

and the decay length of the Λ at 0.1 cm. A summary of the cuts made and the number of events removed is given in Table 9.2.

9.2.2 Backward Λ Sample

The various raw mass spectra for events with a backward Λ are shown in Figures 9.16 through 9.24. As with the 4π channel, the charged pions are labelled as fast ("F") and slow ("S"), depending on their relative momenta.

The four neutral 2π spectra are shown in Figure 9.16. There is a strong ρ signal in all combinations. Also, all combinations show some signal from K^0 decays.

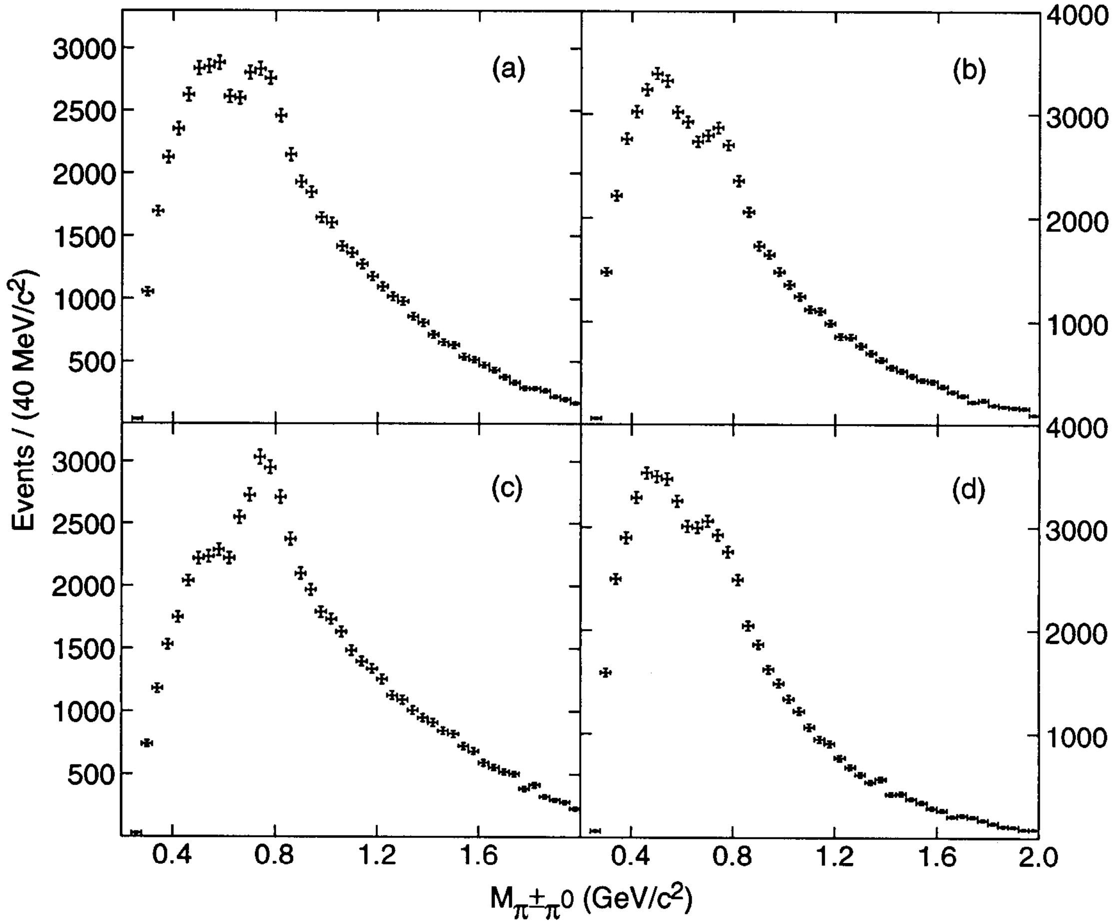

Figure 9.17: The $\pi^\pm\pi^0$ spectra for a backward Λ: (a) $\pi_F^+\pi^0$, (b) $\pi_S^+\pi^0$, (c) $\pi_F^-\pi^0$, (d) $\pi_S^-\pi^0$.

There are small enhancements around 1.3 GeV/c^2, due to $f_2(1270)$ and possibly $\rho(1300)$.

The charged 2π spectra are shown in Figure 9.17. ρ is evident in all combinations. There is no clear evidence for any other signal.

Figure 9.18 shows the $\Lambda\pi$ spectra for a backward Λ. The $\Sigma(1385)$ is evident in all the combinations; however, the signals are much stronger when the slow π^+ or π^- are used. This is consistent with baryons being produced in the backward direction. The threshold enhancement in $\Lambda\pi^0$ is due to decays $\Sigma \to \Lambda\gamma$, with the photon mis-identified as a pion. The higher mass Σ^*s seen in the previous channels

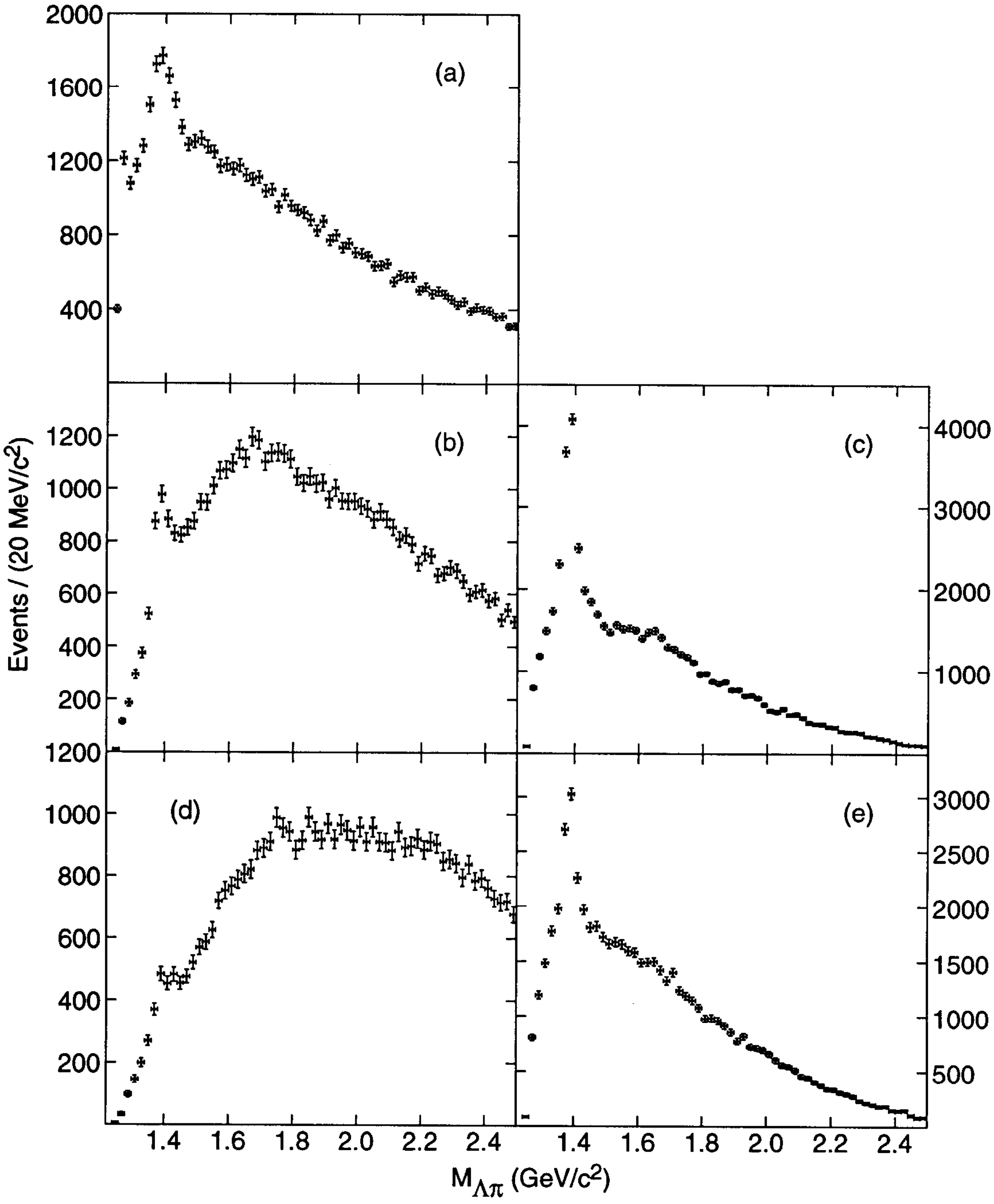

Figure 9.18: The $\Lambda\pi$ spectra for a backward Λ: (a) $\Lambda\pi^0$, (b) $\Lambda\pi_F^+$, (c) $\Lambda\pi_S^+$, (d) $\Lambda\pi_F^-$, (e) $\Lambda\pi_S^-$.

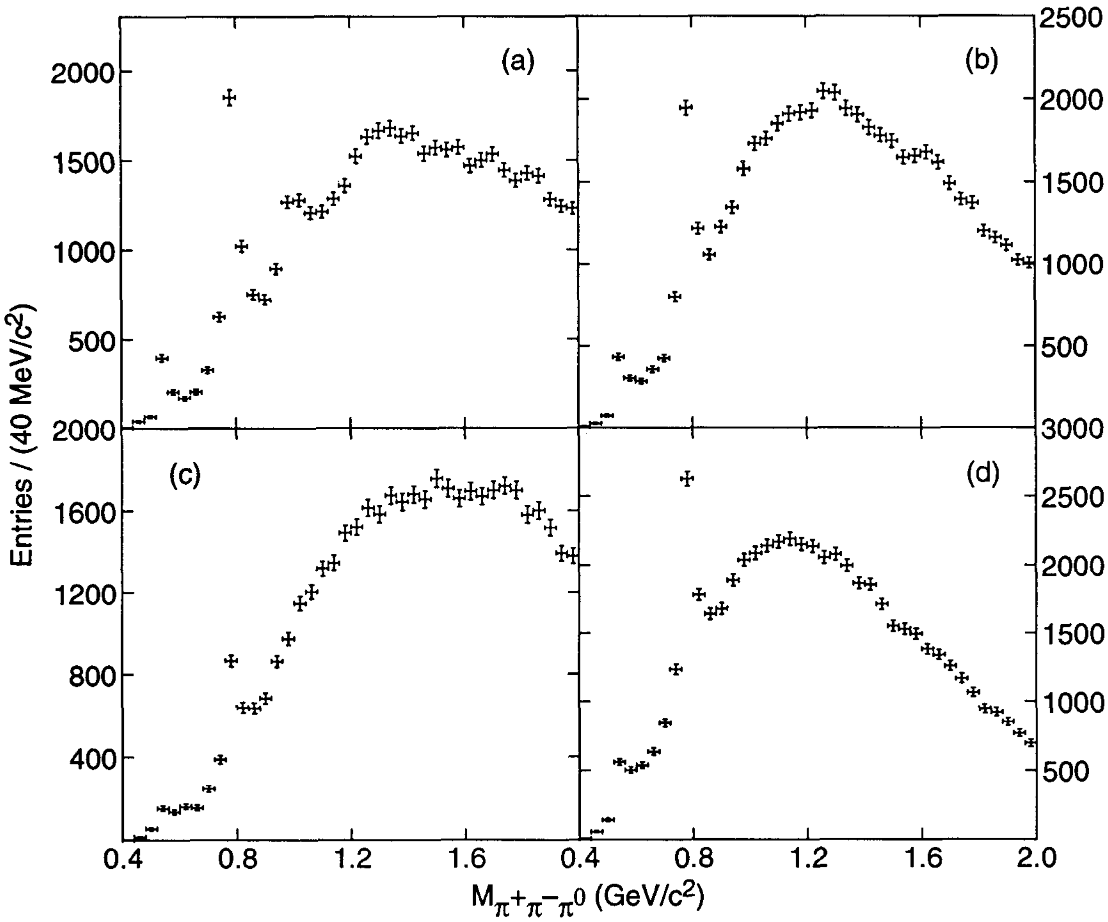

Figure 9.19: The $\pi^+\pi^-\pi^0$ spectra for a backward Λ: (a) $\pi_F^+\pi_F^-\pi^0$, (b) $\pi_F^+\pi_S^-\pi^0$, (c) $\pi_S^+\pi_F^-\pi^0$, (d) $\pi_S^+\pi_S^-\pi^0$.

are not very evident, although there is some evidence in $\Lambda\pi_S^+$.

Figure 9.19 shows the neutral 3π spectra for a backward Λ. Both the η and ω are visible in all four spectra. The peak in $\pi_F^+\pi_F^-\pi^0$ around 1 GeV/c^2 is most likely a mixture of ϕ and η', with the photon from the η' decay mis-identified. The steep rise starting at about 0.8 GeV/c^2 is due to the turn-on of the ρ in the 2π subchannels. The charged 3π spectra, shown in Figure 9.20, are mostly featureless. There is, however, a small enhancement around 1300 MeV/c^2, which may be due to the $a_2(1320)$.

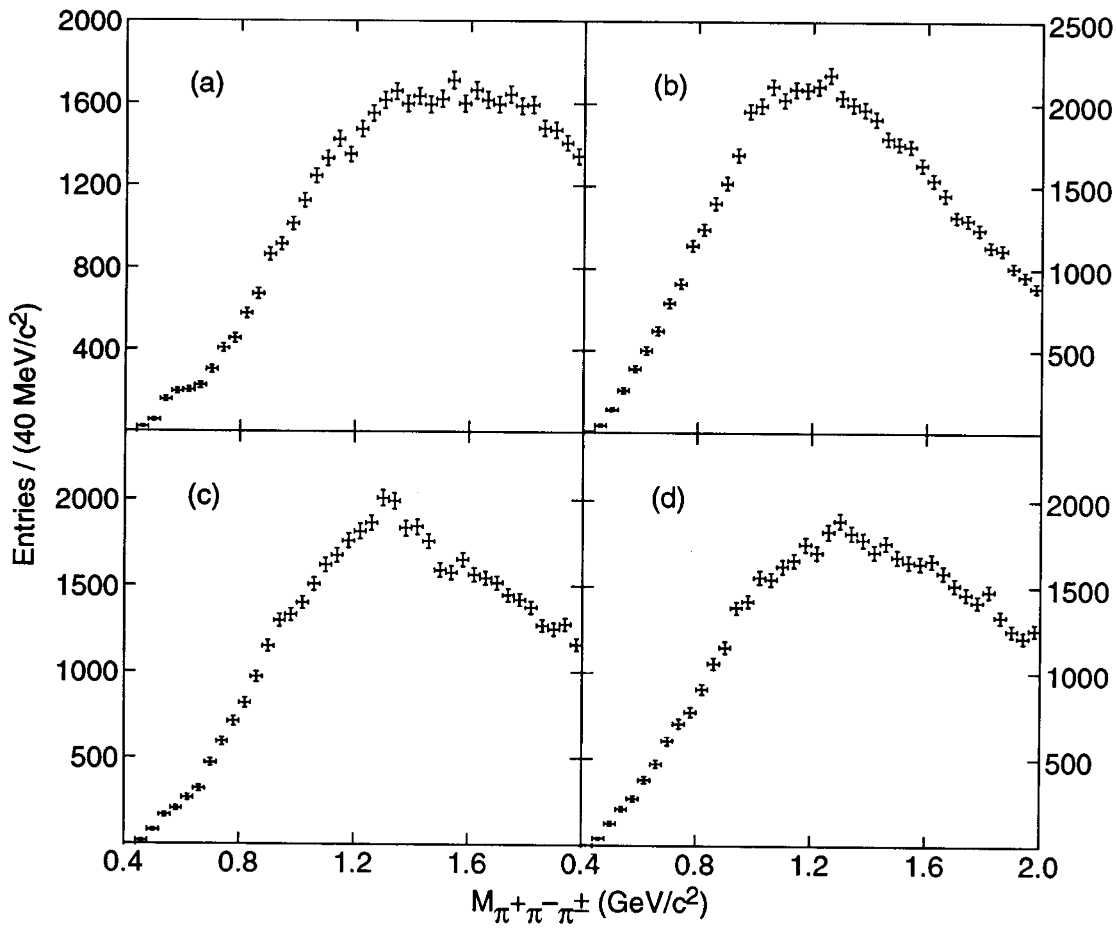

Figure 9.20: The $\pi^+\pi^-\pi^\pm$ spectra for a backward Λ: (a) $\pi_F^+\pi_S^+\pi_F^-$, (b) $\pi_F^+\pi_S^+\pi_S^-$, (c) $\pi_F^+\pi_F^-\pi_S^-$, (d) $\pi_S^+\pi_F^-\pi_S^-$.

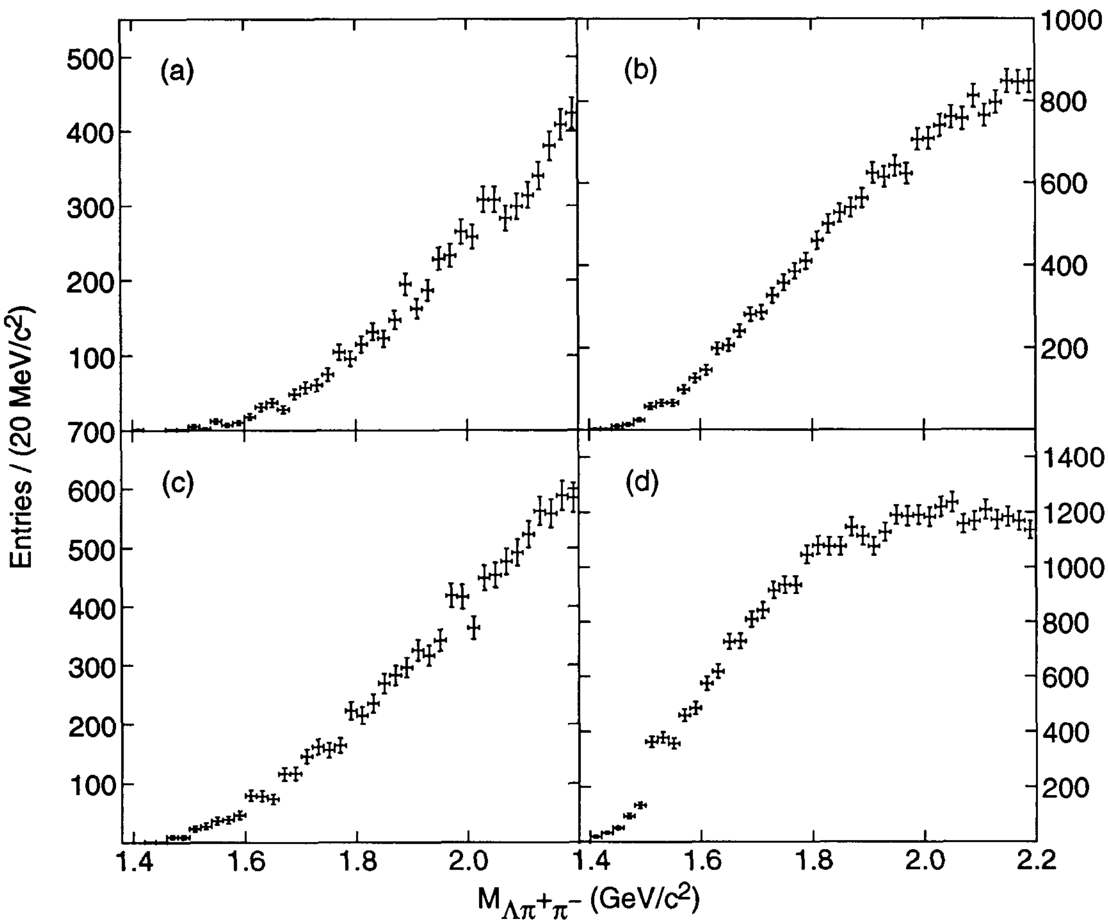

Figure 9.21: The $\Lambda\pi^+\pi^-$ spectra for a backward Λ: (a) $\Lambda\pi_F^+\pi_F^-$, (b) $\Lambda\pi_F^+\pi_S^-$, (c) $\Lambda\pi_S^+\pi_F^-$, (d) $\Lambda\pi_S^+\pi_S^-$.

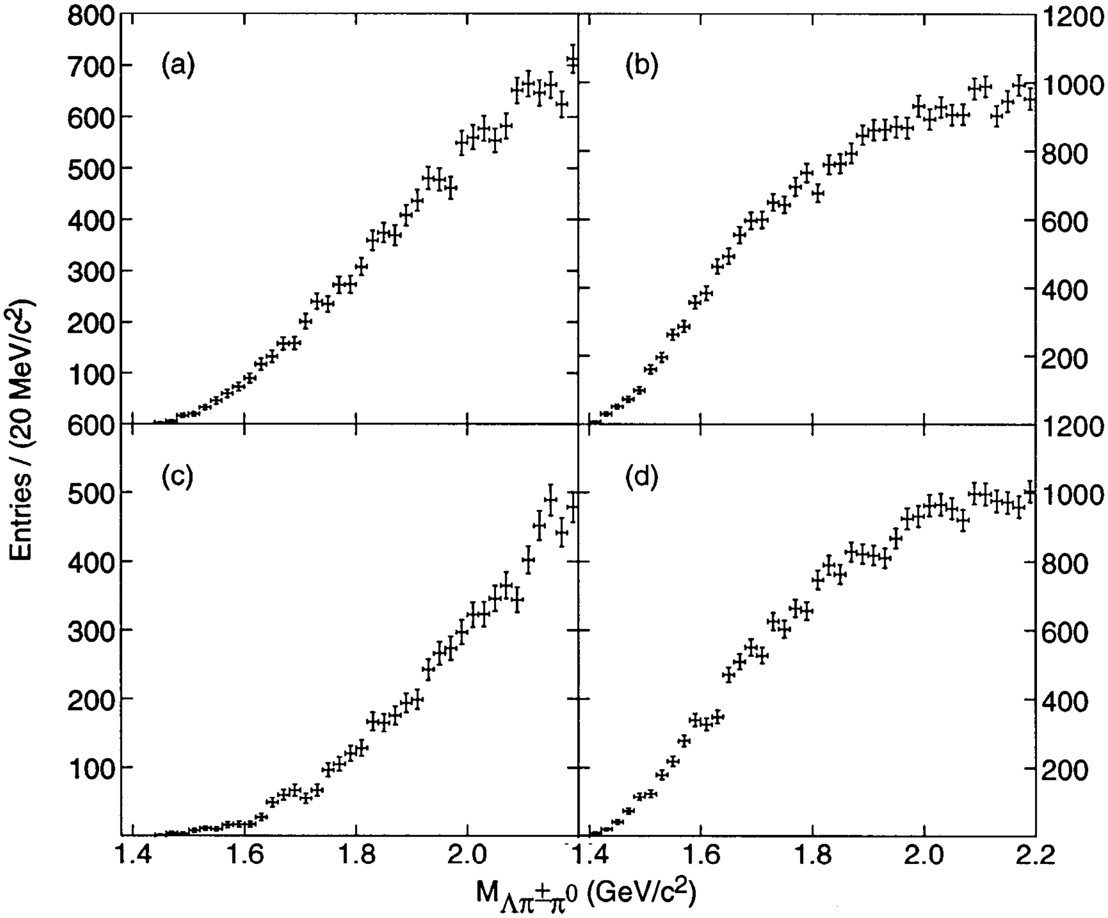

Figure 9.22: The $\Lambda\pi^{\pm}\pi^0$ spectra for a backward Λ: (a) $\Lambda\pi^+_F\pi^0$, (b) $\Lambda\pi^+_S\pi^0$, (c) $\Lambda\pi^-_F\pi^0$, (d) $\Lambda\pi^-_S\pi^0$.

The $\Lambda\pi^+\pi^-$ spectra are shown in Figure 9.21, while Figure 9.22 shows the charged $\Lambda\pi^{\pm}\pi^0$ spectra. The only significant feature is some signal from $\Lambda(1520)$ decay in $\Lambda\pi^+_S\pi^-_S$. There does appear to be a bump around 1.7 GeV/c^2 in $\Lambda\pi^-_F\pi^0$, but it is not clear what this state could be.

The five 4π spectra for a backward Λ are shown in Figure 9.23. The most notable feature is the bump in all five combinations around 800 MeV/c^2. This is due to the decay of η' to 5 pions. Omitting one pion causes the peak to move down about 100 MeV/c^2 and broaden significantly. The broad peak around 1250 MeV/c^2

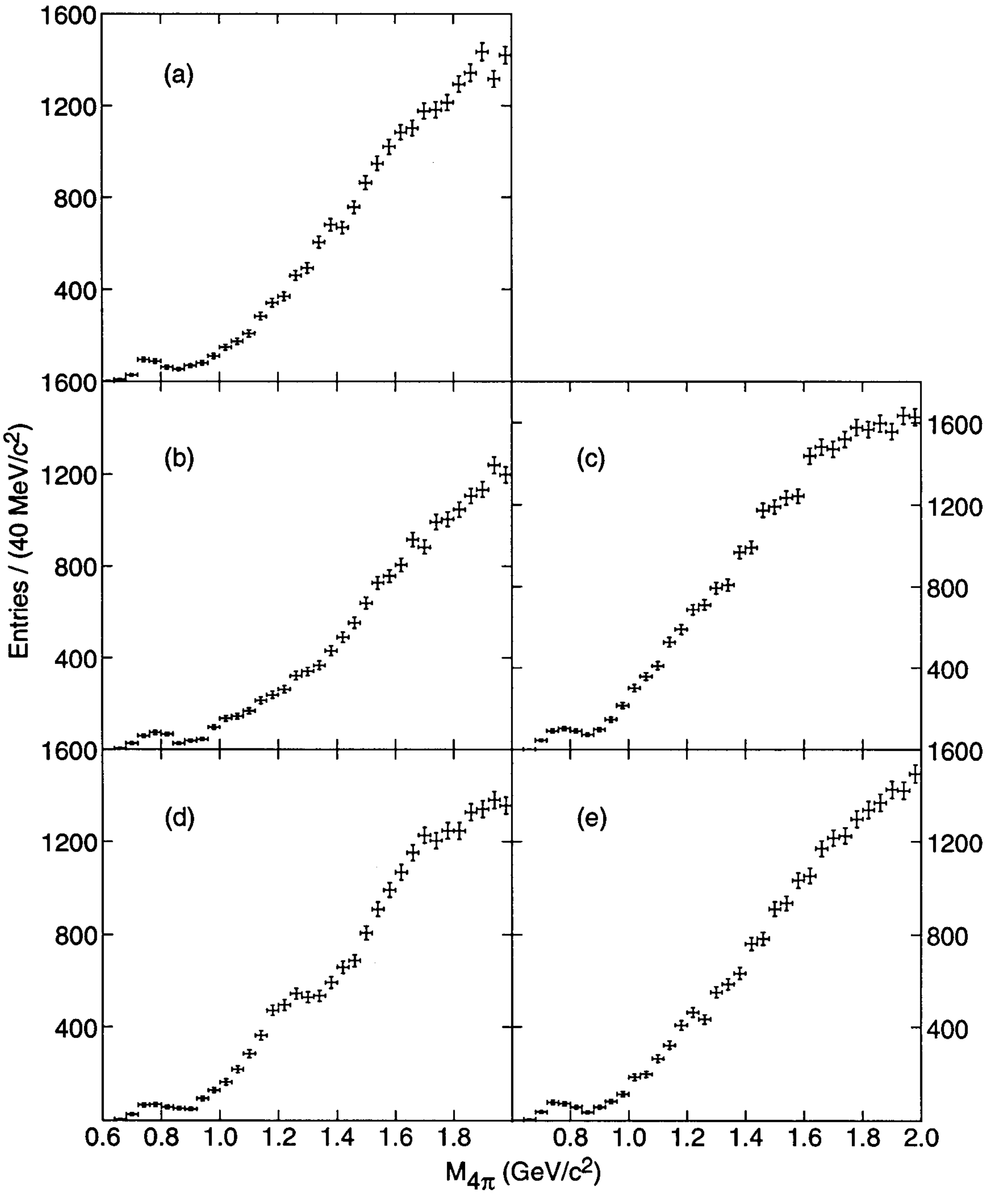

Figure 9.23: The 4π spectra for a backward Λ: (a) $\pi_F^+\pi_S^+\pi_F^-\pi_S^-$, (b) $\pi_F^+\pi_S^+\pi_F^-\pi^0$, (c) $\pi_F^+\pi_S^+\pi_S^-\pi^0$, (d) $\pi_F^+\pi_F^-\pi_S^-\pi^0$, (e) $\pi_S^+\pi_F^-\pi_S^-\pi^0$.

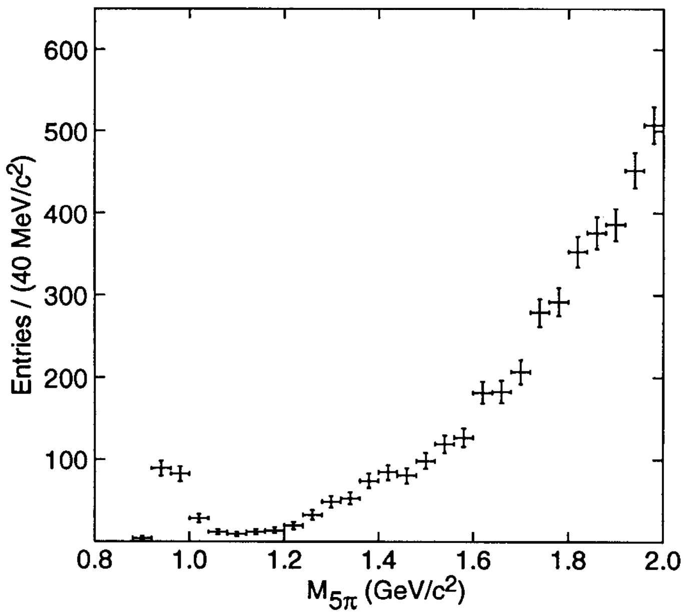

Figure 9.24: The 5π spectra for a backward Λ.

in $\pi_F^+\pi_F^-\pi_S^-\pi^0$ is most likely due to $b_1(1235)$ and will be investigated in a following section.

Finally, the 5π spectrum is shown in Figure 9.24. The η' peak is evident just below $1\,\mathrm{GeV/c^2}$. The subchannel $\mathrm{K^-p} \rightarrow \Lambda\eta\pi^+\pi^-$ has been investigated thoroughly in a previous LASS analysis.[16]

9.2.3 Forward Λ Sample

The mass spectra for the events with a forward-going Λ are shown in Figures 9.25 through 9.33. The neutral 2π mass spectra are shown in Figure 9.25. The ρ is fairly strong in all combinations. The $f_2(1270)$ bump at about $1300\,\mathrm{MeV/c^2}$ is more evident than in the backward Λ sample, probably because of the lower background. The steep increase around $500\,\mathrm{MeV/c^2}$ may indicate the presence of $\mathrm{K^0}$.

Figure 9.26 shows the charged 2π spectra. The ρ peak is wider than in the neutral spectra due to the poorer resolution of the π^0. There are no clear bumps around $1300\,\mathrm{MeV/c^2}$.

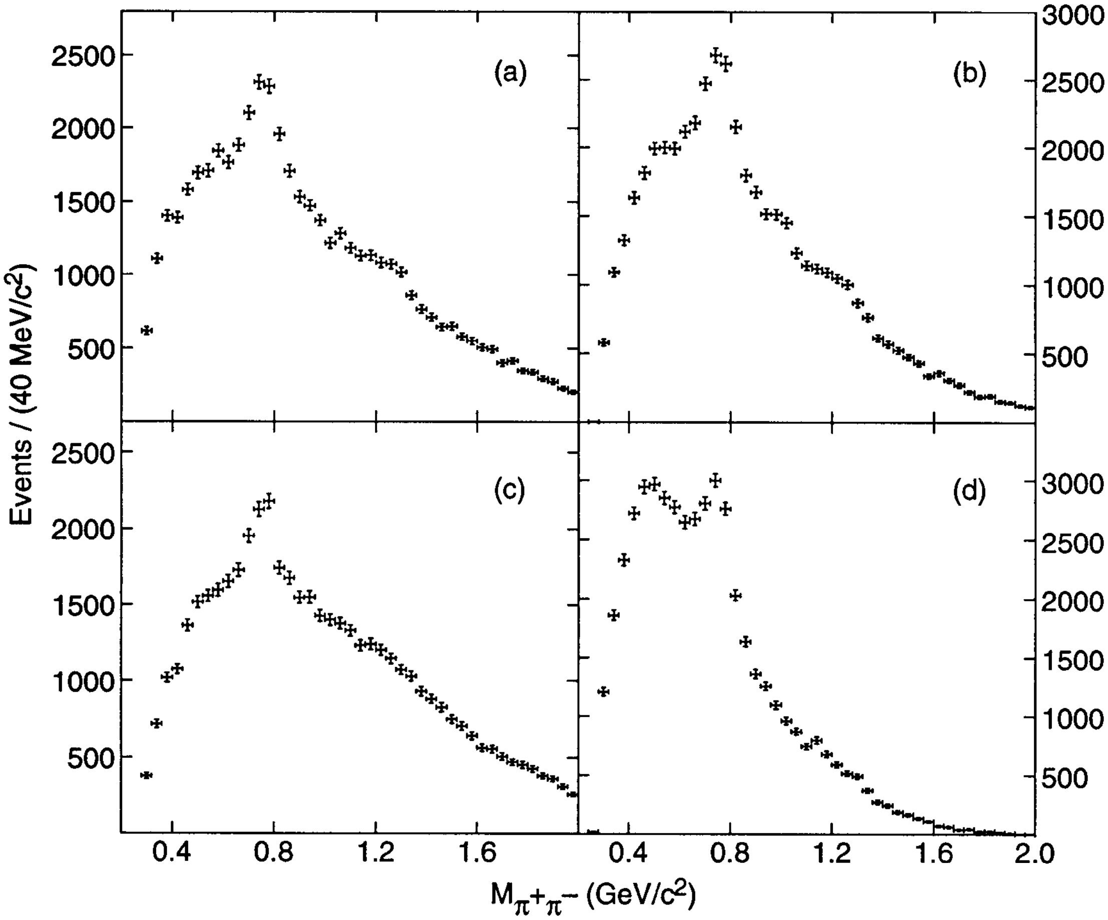

Figure 9.25: The $\pi^+\pi^-$ spectra for a forward Λ: (a) $\pi_F^+\pi_F^-$, (b) $\pi_F^+\pi_S^-$, (c) $\pi_S^+\pi_F^-$, (d) $\pi_S^+\pi_S^-$.

Figure 9.27 shows the $\Lambda\pi$ spectra. $\Sigma(1385)$ are present in all combinations. The higher mass Σ^* are evident in all charged spectra, although they are more strongly produced with respect to the "fast" pions. The threshold rise in the $\Lambda\pi^0$ is caused by $\Sigma \to \Lambda\gamma$, with the photon mis-identified.

The neutral 3π spectra from the forward Λ sample are shown in Figure 9.28. The ω meson is clearly seen in all particle combinations, and there is also a small η signal in each. A possible mass bump around 1300 MeV/c^2 is seen in the $\pi_F^+\pi_S^-\pi^0$ combination.

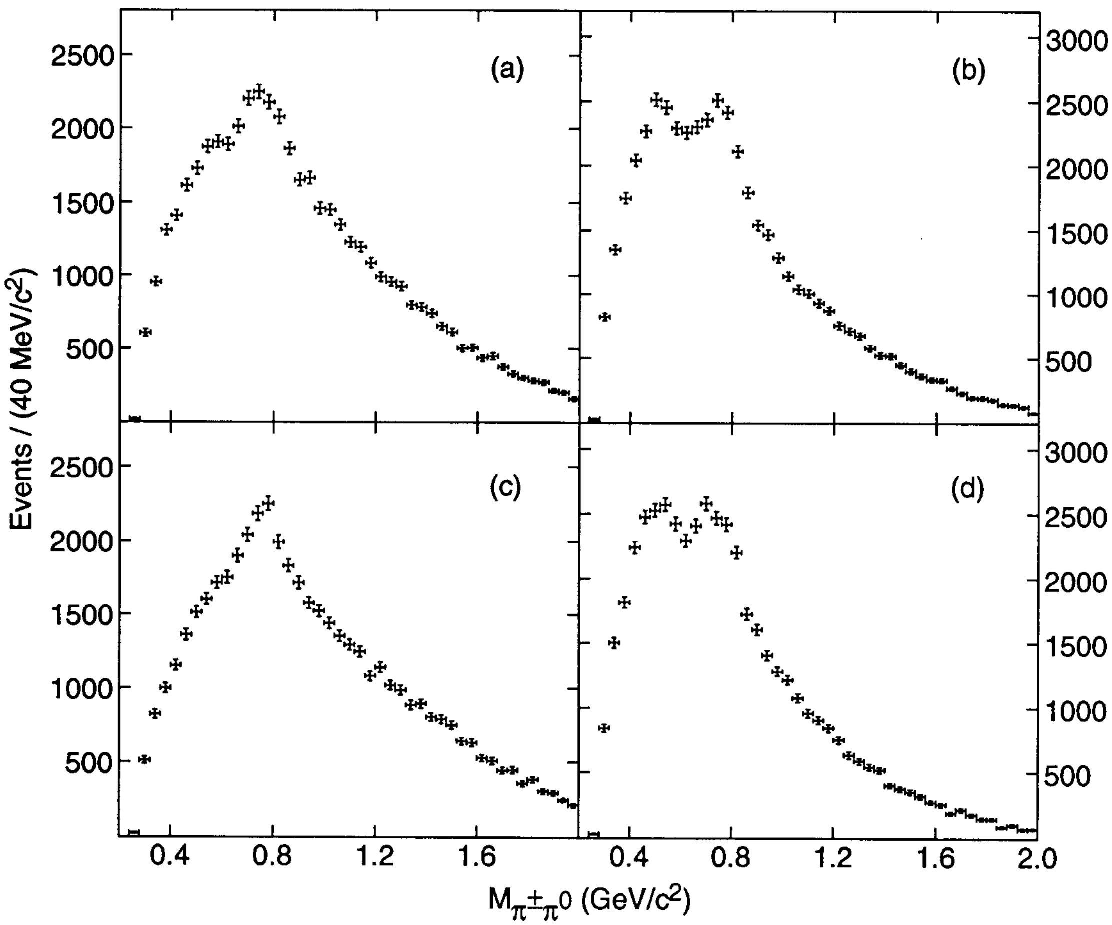

Figure 9.26: The $\pi\pi^0$ spectra for a forward Λ: (a) $\pi_F^+\pi^0$, (b) $\pi_S^+\pi^0$, (c) $\pi_F^-\pi^0$, (d) $\pi_S^-\pi^0$.

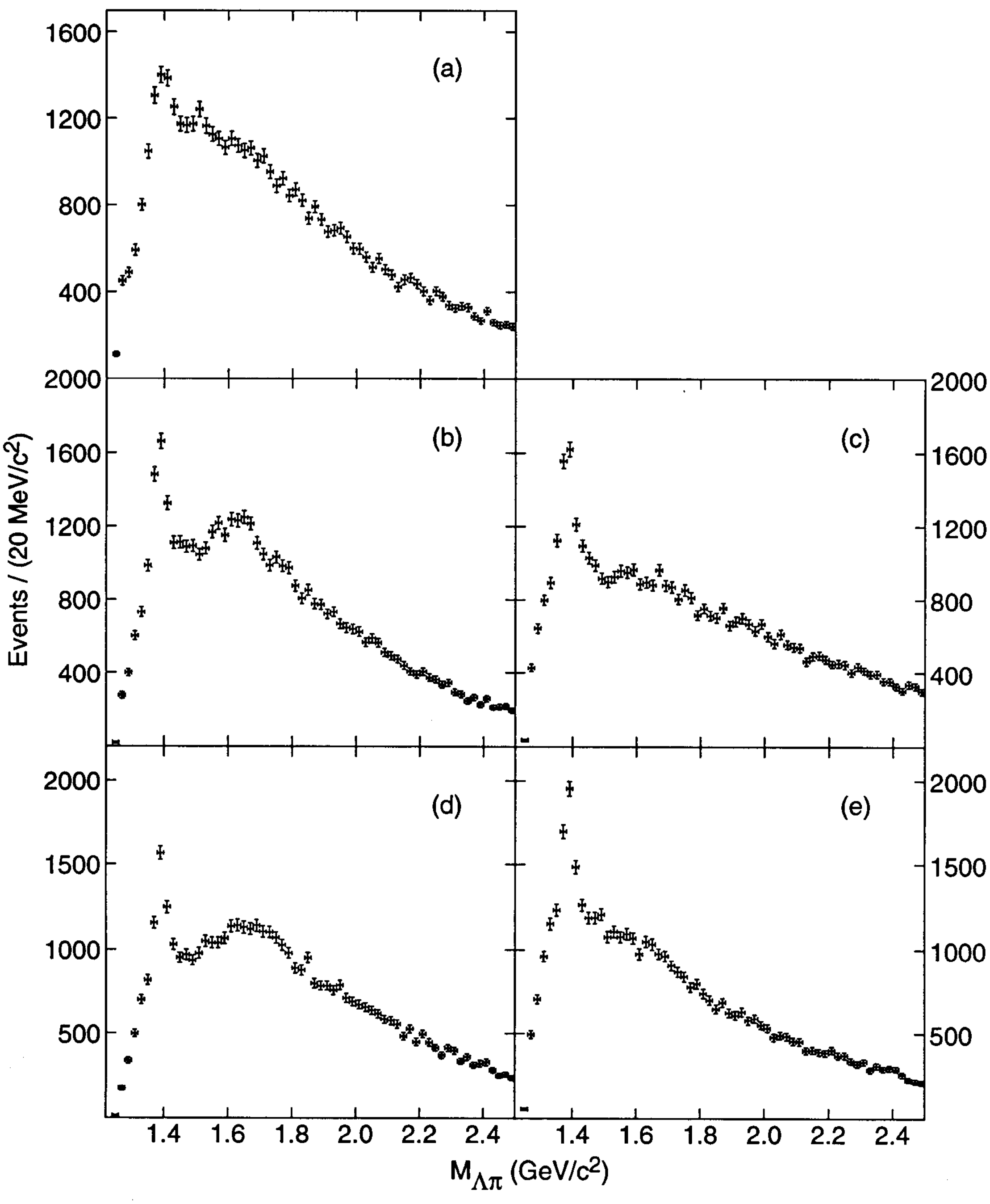

Figure 9.27: The $\Lambda\pi$ spectra for a forward Λ: (a) $\Lambda\pi^0$, (b) $\Lambda\pi_F^+$, (c) $\Lambda\pi_S^+$, (d) $\Lambda\pi_F^-$, (e) $\Lambda\pi_S^-$.

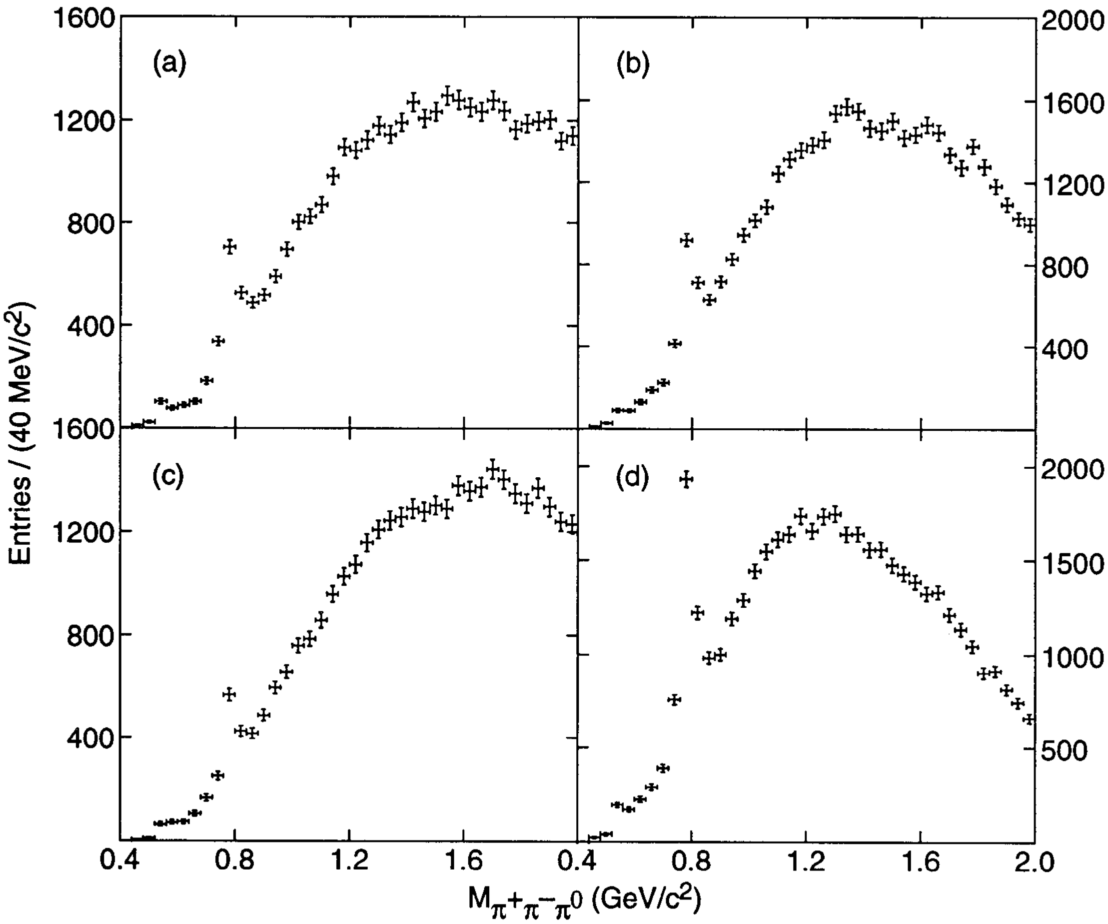

Figure 9.28: The $\pi^+\pi^-\pi^0$ spectra for a forward Λ: (a) $\pi^+_F\pi^-_F\pi^0$, (b) $\pi^+_F\pi^-_S\pi^0$, (c) $\pi^+_S\pi^-_F\pi^0$, (d) $\pi^+_S\pi^-_S\pi^0$.

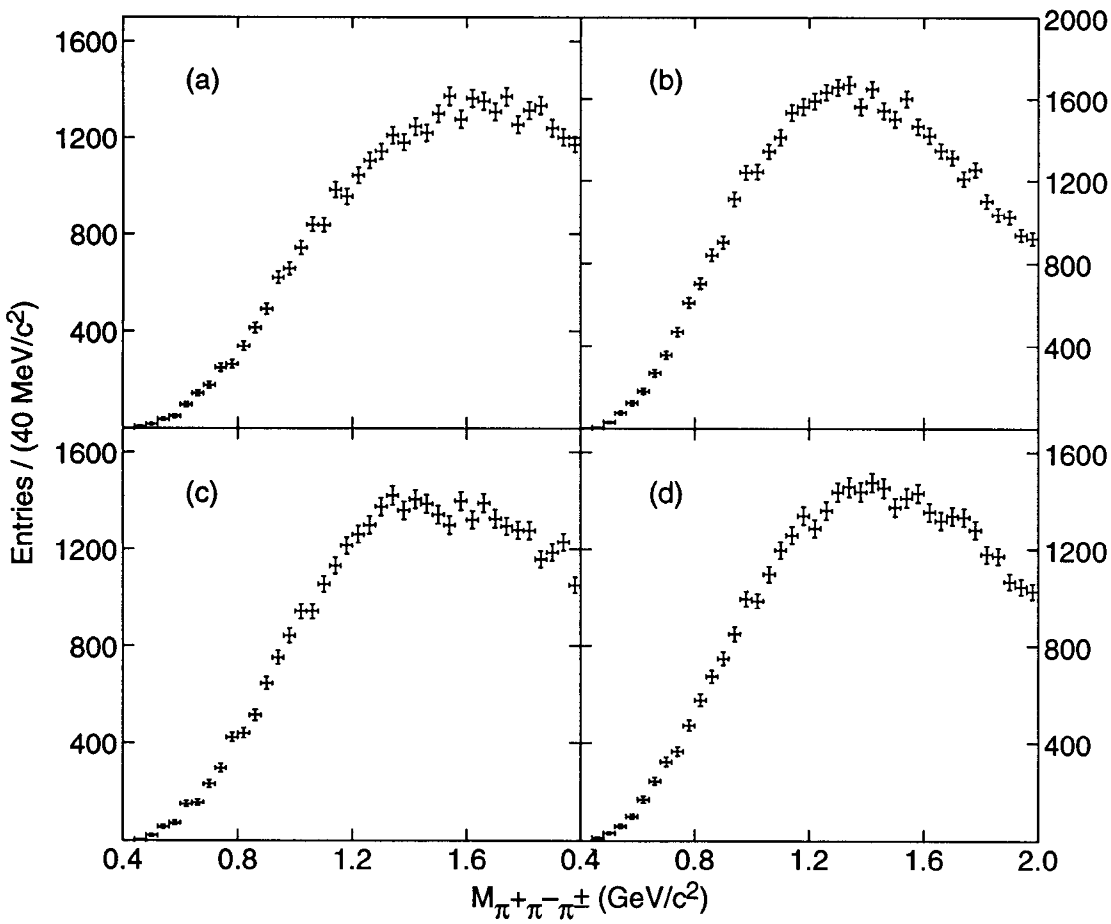

Figure 9.29: The $\pi^+\pi^-\pi^\pm$ spectra for a forward Λ: (a) $\pi_F^+\pi_S^+\pi_F^-$, (b) $\pi_F^+\pi_S^+\pi_S^-$, (c) $\pi_F^+\pi_F^-\pi_S^-$, (d) $\pi_S^+\pi_F^-\pi_S^-$.

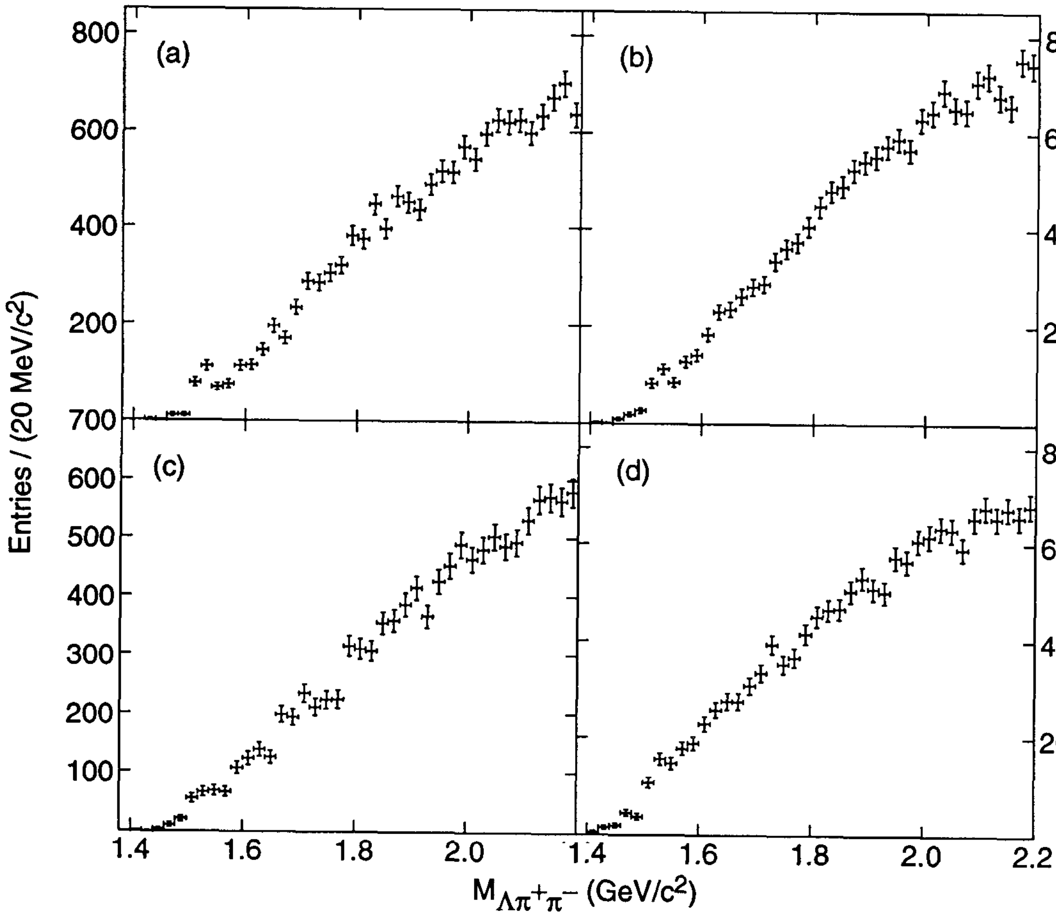

Figure 9.30: The $\Lambda\pi^+\pi^-$ spectra for a forward Λ: (a) $\Lambda\pi_F^+\pi_F^-$, (b) $\Lambda\pi_F^+\pi_S^-$, (c) $\Lambda\pi_S^+\pi_F^-$, (d) $\Lambda\pi_S^+\pi_S^-$.

Figure 9.29 shows the singly charged 3π spectra. The spectra are featureless except for rapid increase around 1 GeV/c^2 due to the kinematic turn-on of the ρ in the various sub-channels.

The $\Lambda\pi^+\pi^-$ spectra, shown in Figure 9.30, are mostly featureless. A small $\Lambda(1520)$ signal is visible in some, possible all, of the channels. The charged $\Lambda\pi\pi^0$ spectra, shown in Figure 9.31, are also quite featureless. The is some evidence for a resonant behaviour around 1650 MeV/c^2 in $\Lambda\pi_S^\pm\pi^0$.

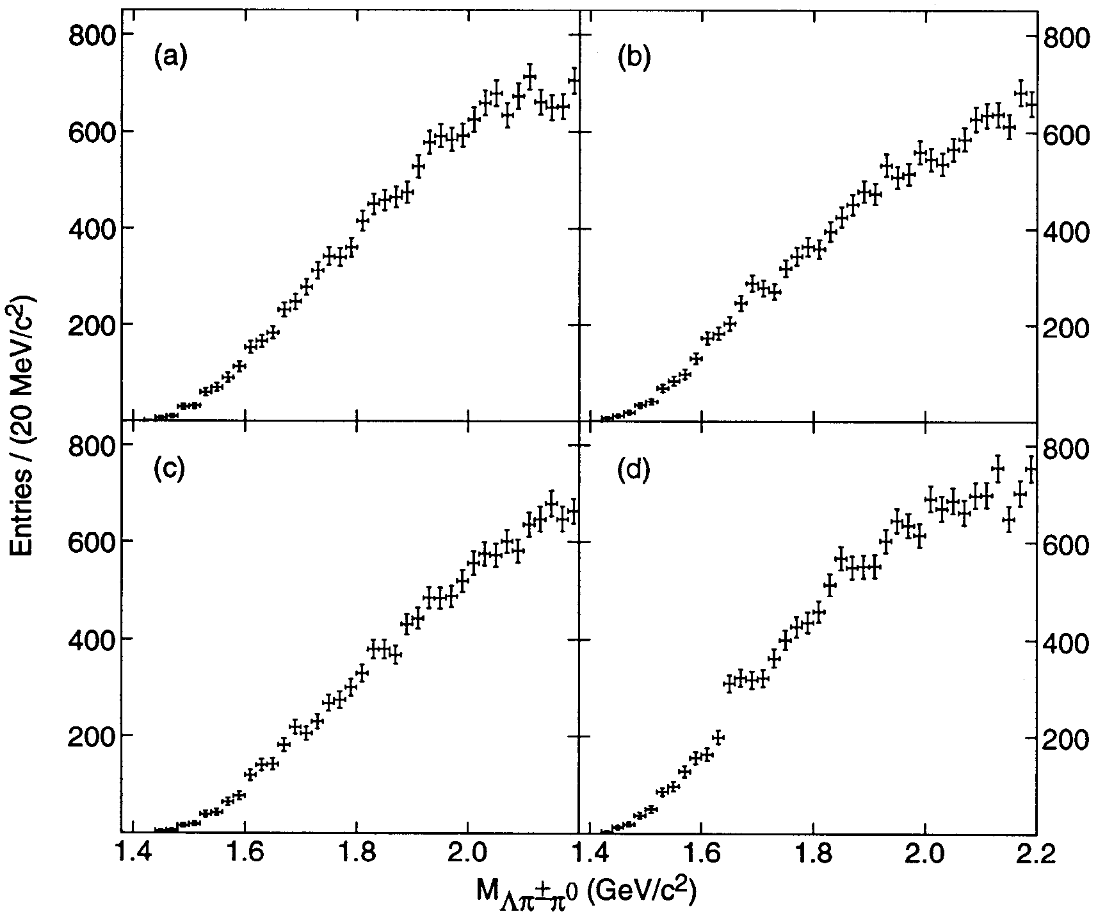

Figure 9.31: The $\Lambda\pi^{\pm}\pi^{0}$ spectra for a forward Λ: (a) $\Lambda\pi^{+}_{F}\pi^{0}$, (b) $\Lambda\pi^{+}_{S}\pi^{0}$, (c) $\Lambda\pi^{-}_{F}\pi^{0}$, (d) $\Lambda\pi^{-}_{S}\pi^{0}$.

Figure 9.32 shows the 4π spectra from the event sample with a forward-going Λ. Except for a more rapid increase starting near 1.4 GeV/c^2 due to ρ production, the plots are generally featureless. There may be a small signal from $b_1(1235)$ in $\pi^{+}_{F}\pi^{+}_{S}\pi^{-}_{S}\pi^{0}$.

Finally, the 5π mass spectrum against a forward Λ is shown in Figure 9.33. The spectrum is quite ragged, but there is no clear evidence of resonance production. As opposed to the backward Λ sample, there is no evidence of η' production.

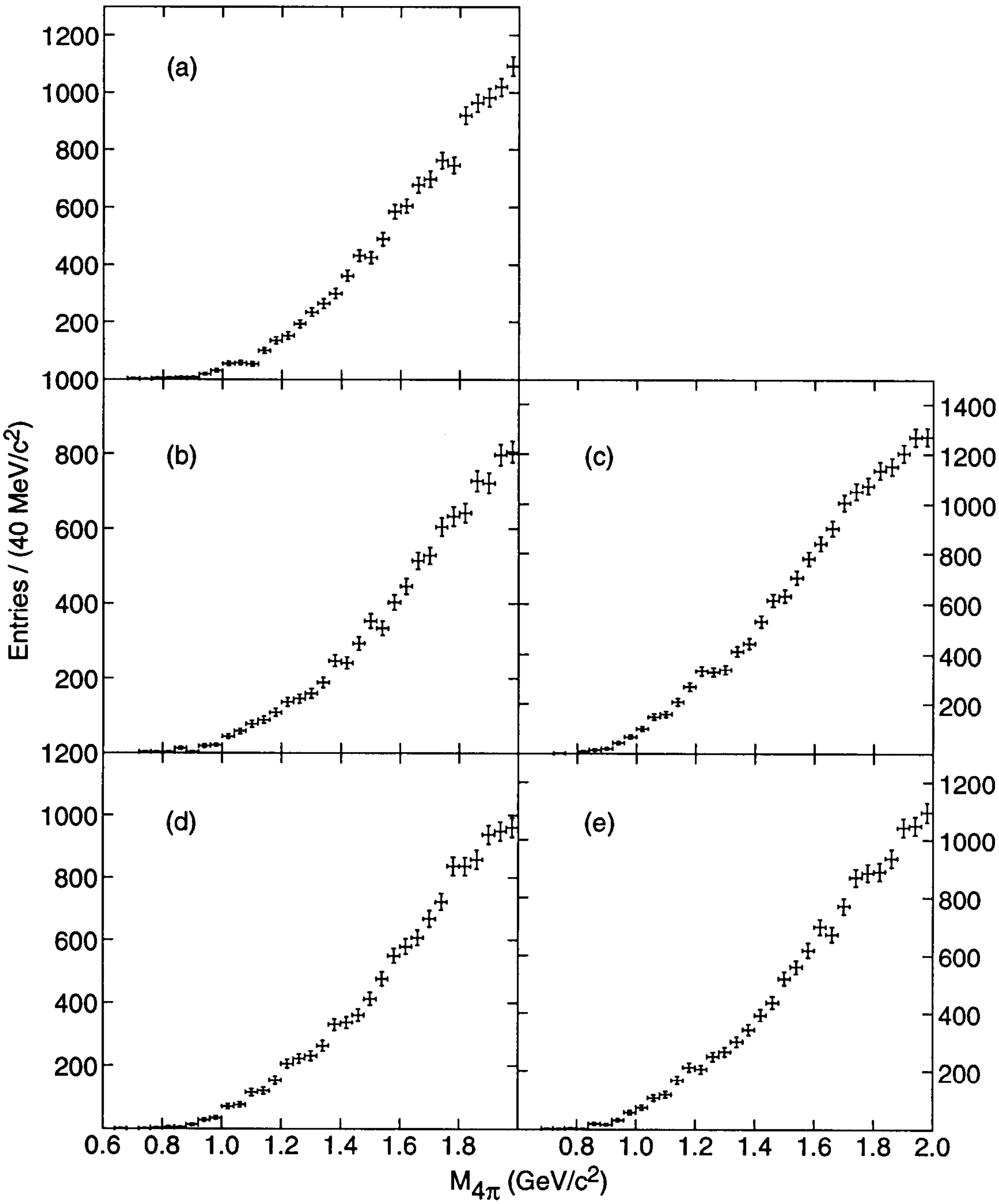

Figure 9.32: The 4π spectra for a forward Λ: (a) $\pi_F^+\pi_S^+\pi_F^-\pi_S^-$, (b) $\pi_F^+\pi_S^+\pi_F^-\pi^0$, (c) $\pi_F^+\pi_S^+\pi_S^-\pi^0$, (d) $\pi_F^+\pi_F^-\pi_S^-\pi^0$, (e) $\pi_S^+\pi_F^-\pi_S^-\pi^0$.

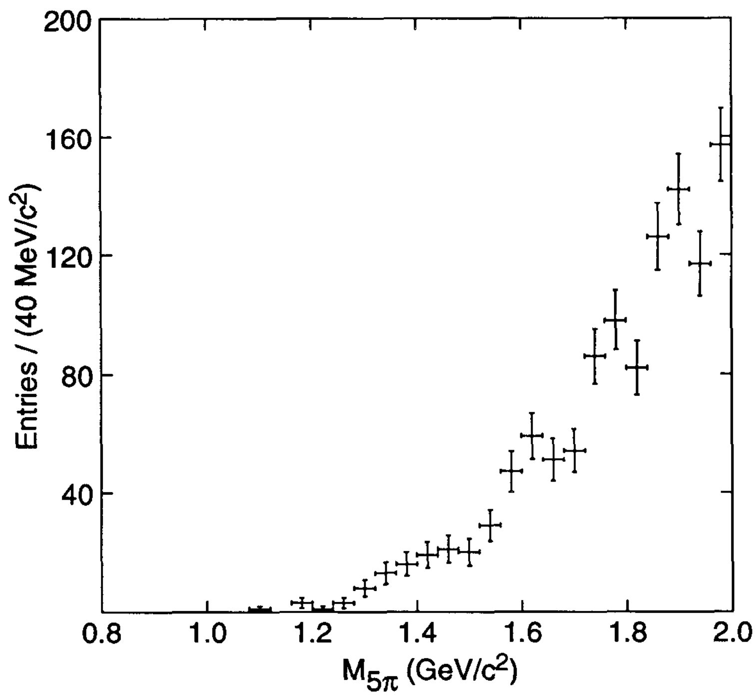

Figure 9.33: The 5π spectra for a forward Λ.

9.2.4 Analysis of $\Sigma^+(1385)\pi^+\pi^-\pi^-\pi^0$

Like the $\Sigma^+(1385)\pi^-\pi^0$ system analysed previously, the 4π system against a backward $\Sigma^+(1385)$ is a good candidate for a $\rho(1300)$ decay mode. If the $\rho(1300)$ prefers to decay to $\rho\rho$, then $\rho^0(1300)$ would have to decay to $\rho^+\rho^-$ because of the Clebsch–Gordan coefficients involved; therefore, the $\rho(1300)$ would not be seen in significant numbers in $\pi^+\pi^-\pi^+\pi^-$. The $\rho^-(1300)$, however, can decay $\rho^-(1300) \to \rho^-\rho^0 \to \pi^+\pi^-\pi^-\pi^0$, making it visible against $\Sigma^+(1385)$.

Unfortunately, unlike the $\pi^-\pi^0$ system where there are no other resonances expected around 1300 MeV/c^2, the 4π system will contain a signal from $b_1(1235)$. The b_1's dominant decay mode is $\omega\pi$, which is an unlikely decay mode for the $\rho(1300)$ because the ω and π would be in a relative $L = 1$ state. However, since an isobar analysis, which can separate different decay modes, is beyond the scope of this analysis, the search for a $\rho(1300)$ signal will again be limited to fitting the mass spectrum.

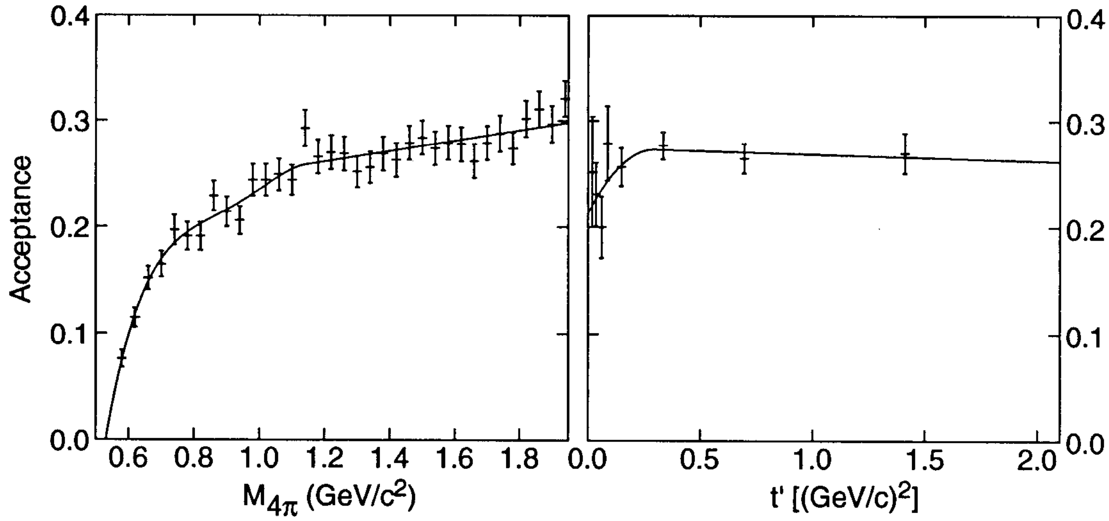

Figure 9.34: The mass and t' dependences of the $\pi^+\pi^-\pi^-\pi^0$ acceptance. The curves represent the parametrizations described in the text.

The mass and t' dependences of the acceptance of $\Sigma^+(1385)\pi^+\pi^-\pi^-\pi^0$ are shown in Figure 9.34. The acceptance was determined from a sample of 50,000 Monte Carlo events, where the $\Lambda\pi^+$ mass was thrown to follow a $\Sigma^+(1385)$ Breit–Wigner shape. Similar to the previous neutral 4π channel, the acceptance was binned in mass and t'. The mass dependence was fit with a quartic plus a line smoothly joined at a point, while the t' shape was fit with a quadratic plus a line, as shown in Figure 9.34. Unlike the previous channel, the acceptance does not fall to zero near $t' = 0$ because the recoil system, the $\Sigma^+(1385)$, has a higher mass than the Λ. The q and t_{min} of the $\Sigma^+(1385)$ decay gives the Λ an extra boost so that the daughter proton is not stopped in the target.

The forward going, acceptance corrected 4π mass spectrum, with the $\Sigma^+(1385)$ background removed by sideband subtraction, is shown in Figure 9.35. The regions used for the $\Sigma^+(1385)$ are the same as those in the $\Sigma^+(1385)\pi^-\pi^0$ analysis, specifically 1.340–1.430 GeV/c^2 for the signal region and 1.265–1.310 and 1.460–1.505 GeV/c^2 for the sidebands. The principal feature of the 4π spectrum is the large bump around 1.2 GeV/c^2, which, as shown below, is mainly due to the decay $b_1^-(1235) \to \omega\pi^-$.

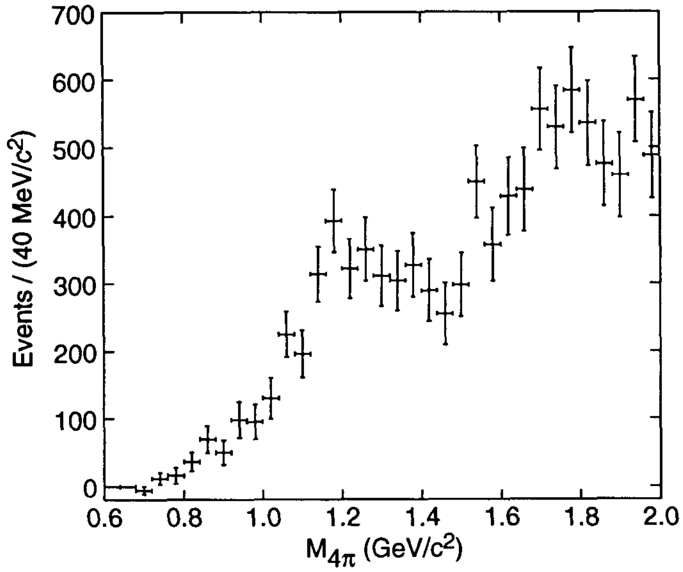

Figure 9.35: The 4π acceptance corrected mass spectrum against a backward-going $\Sigma^+(1385)$.

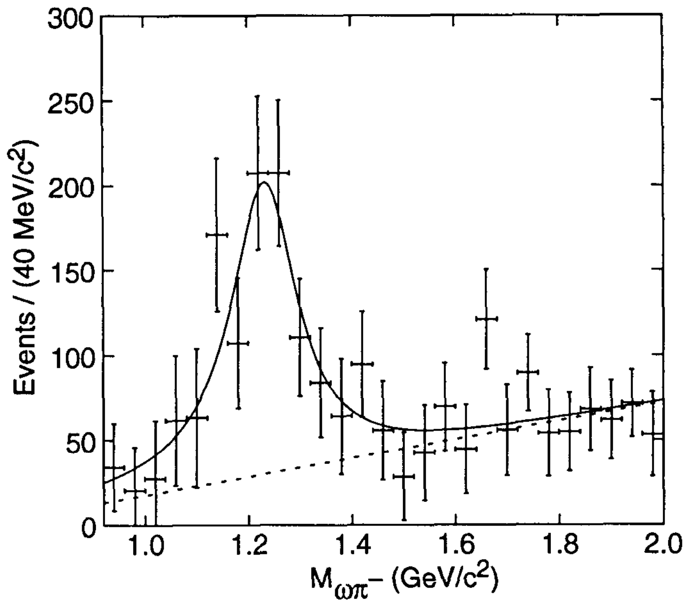

Figure 9.36: The $\omega\pi^-$ spectrum against a backward-going $\Sigma^+(1385)$. The solid curve shows the fit to the $b_1(1235)$ shape with a linear background, shown by the dotted curve.

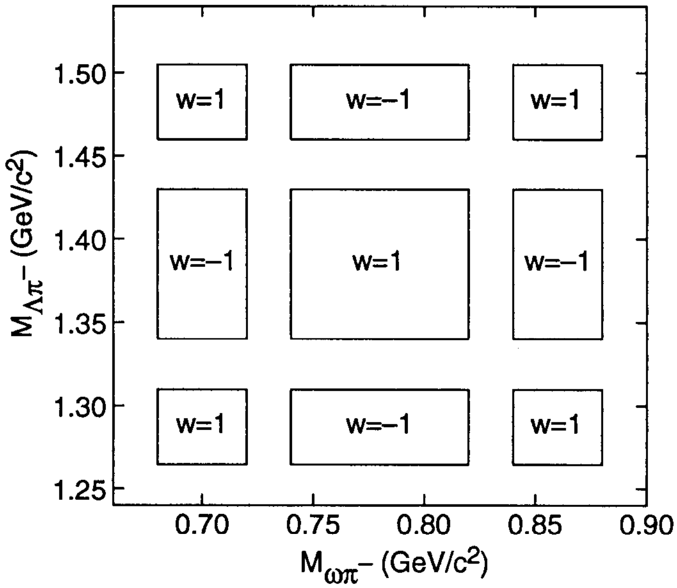

Figure 9.37: The 2D sideband regions used to analyze $\Sigma^+(1385)\omega\pi^-$. The weights for each region are indicated in the boxes; the weight for any event outside a box is 0.

The $\omega\pi^-$ spectrum against a backward $\Sigma^+(1385)$ is shown in Figure 9.36. The $\omega\pi^-$ spectrum was computed using a 2 dimensional sideband subtraction. The 1 dimensional signal and sideband regions for the two quantities in question define a 2D grid of 9 regions, as shown in Figure 9.37. The weight for each region, indicated in the figure as w, is the product of the two 1D sideband weights. This satisfies the criteria that the weighted integral of the regions is 0 for a planar background and 1 for a distribution restricted to the central 2D signal region. The signal region for the ω was 740–820 MeV/c^2, while the sidebands were 680–720 MeV/c^2 and 840–880 MeV/c^2. The $\omega\pi^-$ spectrum was computed for both $\pi^+\pi^-\pi^0$ combinations and the two spectra were summed. The result is shown in Figure 9.36 and contains a strong b_1 signal. The spectrum was fit with a Breit–Wigner shape with the parameters of a b_1 meson,[30] namely $m = 1232\,\mathrm{MeV/c^2}$ and $\Gamma = 155\,\mathrm{MeV/c^2}$, plus a linear background. The fit, also shown in Figure 9.36, is quite good, giving a χ^2 of 15 for 24 degrees of freedom. The measured cross section for the $b_1 \to \omega\pi^-$ against a backward $\Sigma^+(1385)$ is $(0.61 \pm 0.11 \pm 0.03)\mu$b, where the 0.03μb systematic

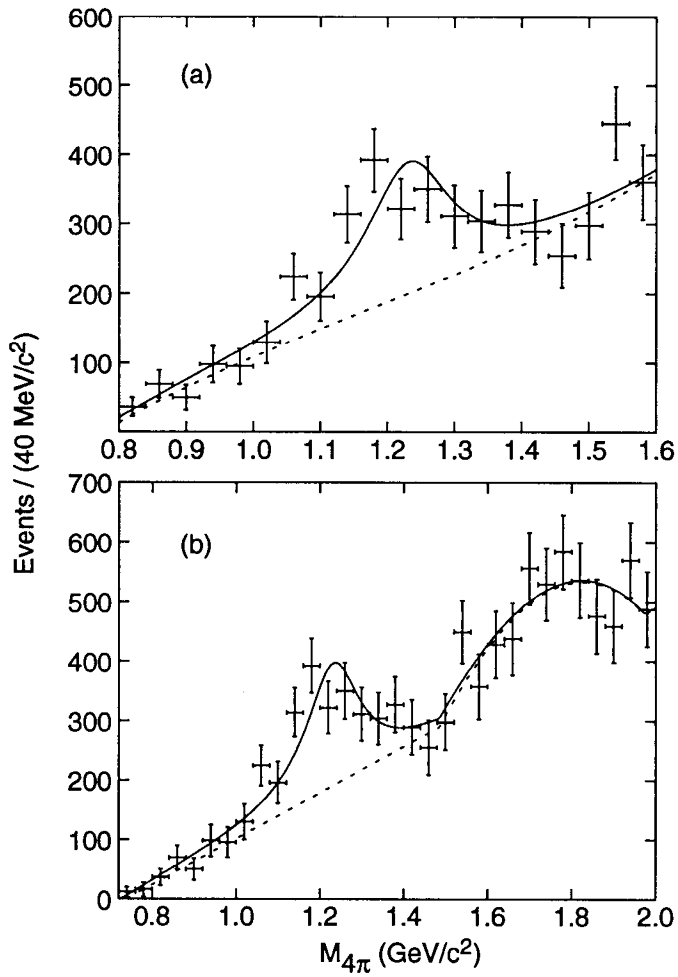

Figure 9.38: Fits to the 4π mass spectrum. The dotted curves shows the background shape. The intensity contributions due to the $\rho(1300)$ are driven to zero in both fits.

uncertainty is added to account for possible double counting of events. The cross section has been corrected for the $\Sigma^+(1385)$, Λ, and ω visibilities. There is no evidence for $\rho(1300)$ in the spectrum.

Two fits to the 4π mass spectrum are shown in Figure 9.38. Both fit shapes consist of a b_1 and a $\rho(1300)$ Breit–Wigner plus a background. The background in 9.38a is a cubic polynomial while that of 9.38b consists of a straight line plus a cubic which is cut off when it tries to go below zero, as in Figure 9.14b. The

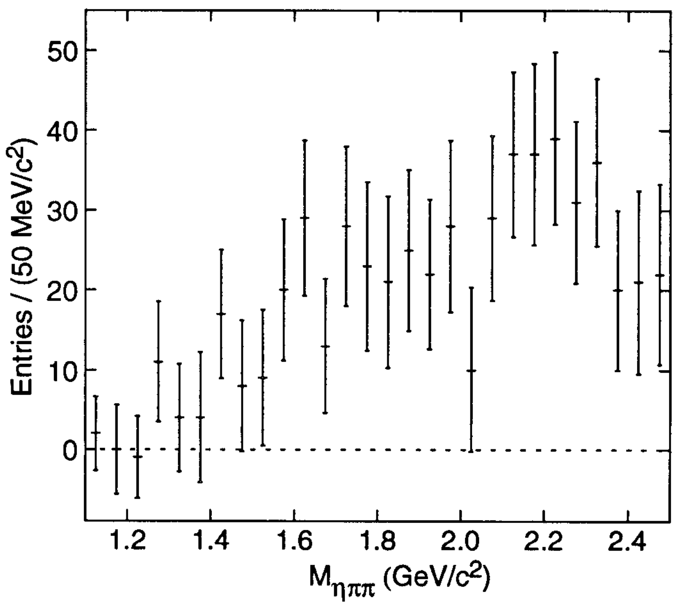

Figure 9.39: The $\eta\pi^+\pi^-$ mass spectrum with $m_{\eta\pi^+\pi^-} > 1.1\,\mathrm{GeV/c^2}$ and $-t_{p\to\Lambda} < 1.0\,(\mathrm{GeV/c})^2$, from Reference [16].

fits describe the data reasonably well. The dotted curves in Figure 9.38 show the contribution from the background. The $b_1(1235)$ cross section from the fit (a) is $(0.57 \pm 0.11)\mu$b, while (b) gives $(0.62 \pm 0.12)\mu$b (corrected only for baryon visibilities). The uncertainty is statistical only. Both fits indicate that no $\rho(1300)$ contribution is required. Using the larger of the uncertainties from the two fits, the 90% confidence level upper limit on the $\rho(1300)$ cross section is $0.10\,\mu$b, giving an upper limit on the branching ratio of

$$\frac{\sigma(\rho(1300) \to \pi^+\pi^-\pi^-\pi^0)}{\sigma(\rho(1300) \to \pi^-\pi^0)} < 6.$$

9.2.5 $\eta\pi^+\pi^-$ Sample

The channel $K^-p \to \eta\pi^+\pi^-$, with $\eta \to \pi^+\pi^-\pi^0$, previously has been analysed in detail by LASS.[16] The observed mass spectrum with $m_{\eta\pi^+\pi^-} > 1.1\,\mathrm{GeV/c^2}$ and $-t_{p\to\Lambda} < 1.0\,(\mathrm{GeV/c})^2$ (*i.e.* a backward Λ) is shown in Figure 9.39. There is clearly no evidence for any significant production of the $\rho(1300)$ meson.

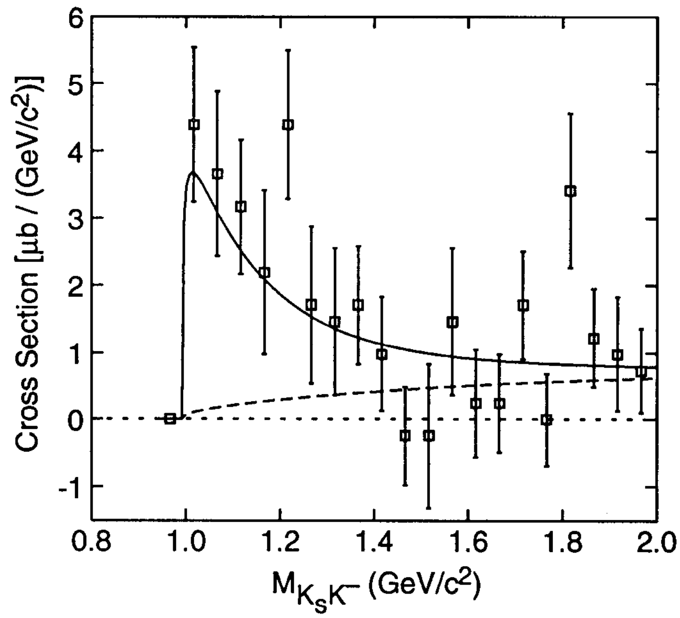

Figure 9.40: The $K^0_S K^-$ mass spectrum from the reaction $K^- p \to \Sigma^+(1385) K^0_S K^-$, from Reference [16]. The solid curve shows the contribution of $a_0(980)$, while the dashed curve indicates the background. The points below zero are due to the background subtraction of the $\Sigma^+(1385)$.

9.3 $K\overline{K}$ Channels

Previous analyses of LASS data have looked at $K^- p \to \Sigma^+(1385) K^0_S K^-$, $K^- p \to \Lambda K^+ K^-$, and $K^- p \to \Lambda K^* K$. The analyses are described in detail in References [16], [59], and [60], respectively.

The $K^0_S K^-$ mass spectrum against a backward $\Sigma^+(1385)$ is shown in Figure 9.40. The background under the $\Sigma^+(1385)$ has been subtracted using one sideband. The threshold enhancement is due to the $a_0(980)$ meson. The curve represents a fit to the data of the $a_0(980)$ shape, using a model where the $K^0_S K^-$ decay momentum is analytically continued below threshold.[61] The curve clearly represents the data very well. There is no evidence for any $\rho(1300)$ in this channel.

The $K^+ K^-$ system in the reaction $K^- p \to \Lambda K^+ K^-$ was analysed using a partial wave analysis essentially the same as in the present analysis. The total P-wave intensity is shown in Figure 9.41 in $4\,\mathrm{MeV/c^2}$ bins from 1.0 to $1.04\,\mathrm{GeV/c^2}$ and

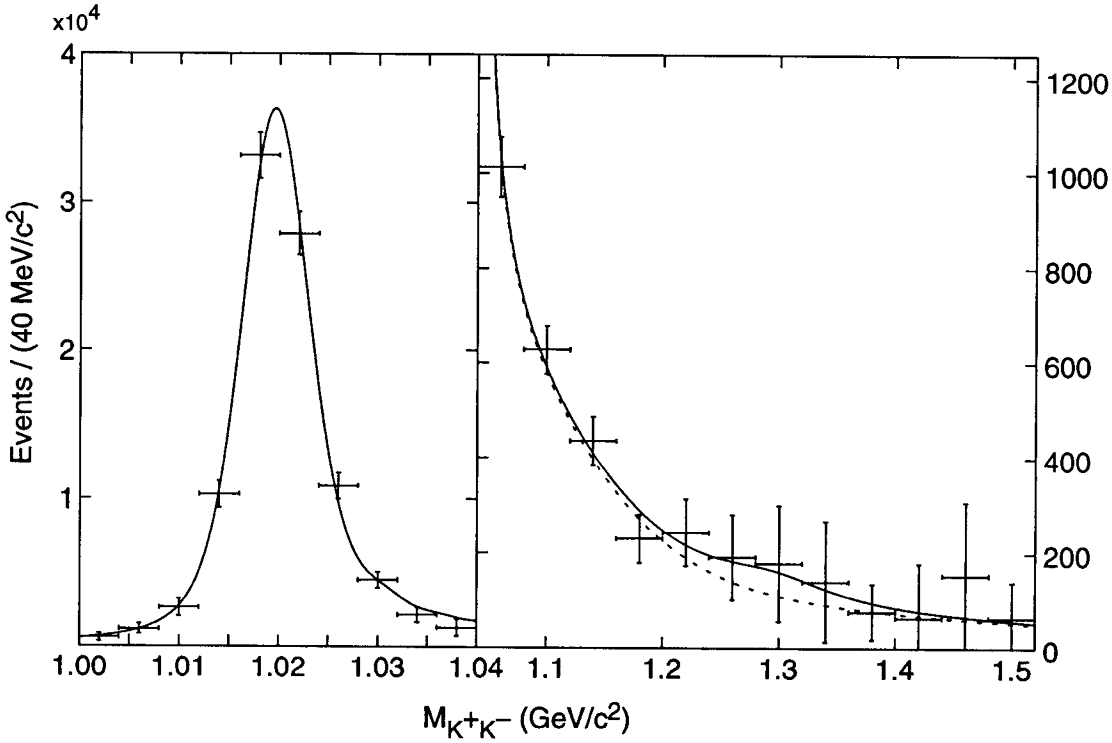

Figure 9.41: The total P-wave intensity in the K^+K^- from the reaction $K^-p \rightarrow \Lambda K^+K^-$, from Reference [59]. The solid curve represents the fit described in the text, with the dotted curve showing the same fit without the contribution of the $\rho(1300)$.

in 40 MeV/c^2 bins from 1.04 to 1.52 GeV/c^2. The points below 1.04 GeV/c^2 have been renormalized to a 40 MeV/c^2 bin width. While the lower mass data are well described by a ϕ Breit–Wigner smeared by the detector resolution, the data in the upper region are significantly higher than the tail of the ϕ. In order to fit the tail, the shape needs to include the contribution of the $\rho(770)$. This effect has also been seen in the data from $e^+e^- \rightarrow K^+K^-$.[62,63]

The data of Figure 9.41 were fit with a shape composed of a ϕ Breit–Wigner, the ρ tail, and a Breit–Wigner with the parameters of the $\rho(1300)$, all interfering. The ρ shape above K^+K^- threshold was approximated by using the decay momentum q from $\rho \rightarrow \pi^+\pi^-$ when calculating the mass variation of the total width and q from $\rho \rightarrow K^+K^-$ for the partial width. The curve was smeared by a resolution

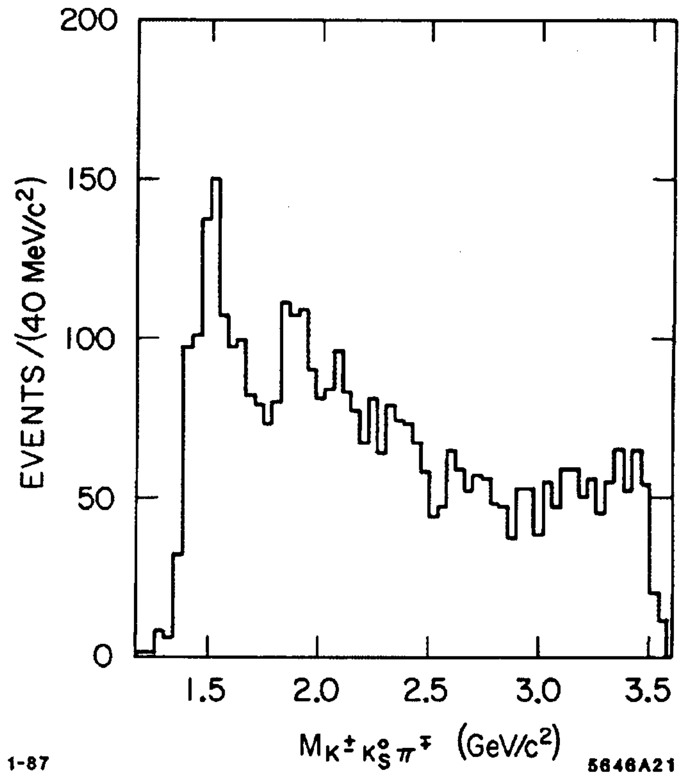

Figure 9.42: The $\overline{\mathrm{K}}^0\mathrm{K}^{\pm}\pi^{\mp}$ mass spectrum from Reference [60].

function consisting of two Gaussians of different amplitudes but having the same mean. Because the tail of the ρ is important when fitting the high mass data, several values of the barrier factor R were tried. An acceptable fit was achieved with $R = 20\,\mathrm{GeV}^{-1}$. The fit is shown as the solid curve in Figure 9.41; the dotted curve gives the shape without the $\rho(1300)$. From the fit, the $\rho(1300)$ cross section is $(0.01 \pm 0.03)\mu$b. The χ^2 of the fit is 7.70 for 14 degrees of freedom versus 7.89 for 16 degrees of freedom from the best fit without the $\rho(1300)$. Obviously, there is no clear evidence for $\rho(1300)$ production in this channel. The 90% confidence level upper limit on the cross section is $0.084\,\mu$b, where the phase of the $\rho(1300)$ was allowed to vary freely. This gives an upper limit on the $\mathrm{K}^+\mathrm{K}^-$ branching ratio of

$$\frac{\sigma(\rho(1300) \to \mathrm{K}^+\mathrm{K}^-)}{\sigma(\rho(1300) \to \pi^+\pi^-)} < 0.7.$$

The $\overline{\mathrm{K}}^0\mathrm{K}^{\pm}\pi^{\mp}$ mass spectrum is shown in Figure 9.42. There are very few events below 1.34 GeV/c^2. The small bump around 1.3 GeV/c^2 is consistent with the decay $f_1(1285) \rightarrow a_0\pi \rightarrow \overline{\mathrm{K}}^0\mathrm{K}\pi$, which is significantly narrower than the $\rho(1300)$. There is also no evidence of $\rho(1300)$ production in the K*K spectrum from a 3-body PWA.[60]

9.4 Discussion

Basic analyses of the $\mathrm{K}^-\mathrm{p} \rightarrow \Lambda\pi^+\pi^-\pi^+\pi^-$ and $\mathrm{K}^-\mathrm{p} \rightarrow \Lambda\pi^+\pi^-\pi^+\pi^-\pi^0$ channels have been performed with an emphasis on obtaining evidence for $\rho(1300)$ decay. Because of the complexity of a 4 particle system and insufficient statistics, no spin separation analysis was performed.

The 4π system in $\Lambda\pi^+\pi^-\pi^+\pi^-$ shows a bump in the mass spectrum around 1.3 GeV/c^2. Estimates of the cross section attributable to this bump range from 0.10 ± 0.04 to $(0.26 \pm 0.05)\mu$b, depending on the background shape used. The expected $f_2(1270)$ contribution, using the PDG all-charged 4π branching fraction of $(2.8 \pm 0.4)\%$, is $(0.075 \pm 0.013)\mu$b, although this may be an overestimate. Therefore, there is no clear evidence for $\rho(1300)$ in $\pi^+\pi^-\pi^+\pi^-$. The number of events in the region indicates that the all-charged 4π branching ratio is

$$\frac{\sigma(\rho(1300) \rightarrow \pi^+\pi^-\pi^+\pi^-)}{\sigma(\rho(1300) \rightarrow \pi^+\pi^-)} < 3.$$

The analysis of the 4π system against a backward $\Sigma^+(1385)$ shows a significant number of events from $b_1^-(1235) \rightarrow \omega\pi^-$. The cross section for this channel is $(0.54 \pm 0.10 \pm 0.03)\mu$b. A fit to the overall 4π mass spectrum gives no evidence of $\rho(1300)$ production. The 90% confidence level upper limit on the $\rho(1300) \rightarrow \pi^+\pi^-\pi^-\pi^0$ cross section is 0.10 μb, giving an upper limit on the branching ratio of

$$\frac{\sigma(\rho(1300) \rightarrow \pi^+\pi^-\pi^-\pi^0)}{\sigma(\rho(1300) \rightarrow \pi^-\pi^0)} < 6.$$

An examination of channels previously analysed by LASS provided no evidence for $\rho(1300)$ decays to $\eta\pi^+\pi^-$, $\mathrm{K}^+\mathrm{K}^-$, $\mathrm{K}^0_S\mathrm{K}^-$, and $\overline{\mathrm{K}}^0\mathrm{K}^{\pm}\pi^{\mp}$. A fit to the $\mathrm{K}^+\mathrm{K}^-$

Fit	Mass (MeV/c^2)	Width (MeV/c^2)
$\pi^+\pi^-$ "Fit A"	1290 ± 30	90^{+40}_{-30}
$\pi^+\pi^-$ "Fit B"	1290^{+20}_{-30}	120^{+60}_{-50}
$\pi^-\pi^0$	1330 ± 60	170^{+120}_{-70}

Table 9.3: A summary of the $\rho(1300)$ resonance parameters. The results of the first two fits are not independent of each other.

spectrum gives an upper limit on the branching ratio of

$$\frac{\sigma(\rho(1300) \to \mathrm{K}^+\mathrm{K}^-)}{\sigma(\rho(1300) \to \pi^+\pi^-)} < 0.7.$$

The total picture of the $\rho(1300)$ presented by this thesis is confused. The 2π systems in $\Lambda\pi^+\pi^-$ and $\Sigma^+(1385)\pi^-\pi^0$ show clear evidence of a resonance at 1300 MeV/c^2 with a width of 100–200 MeV/c^2. Using the amplitude relative to the ρ, the elasticity is estimated as $\sim 5\%$. However, there is no evidence for any other significant decay mode of the $\rho(1300)$ in the channels accessible to LASS.

There are two possible explanations for the observed data. The preferred decay mode may be $\rho(1300) \to \rho\rho$, in which case, $\rho^0(1300)$ would been seen in $\pi^+\pi^-\pi^0\pi^0$ because of the Clebsch–Gordan coefficient involved. This channel cannot be analysed by LASS because of the two neutral particles in the final state. It is also a very difficult decay mode to observe; because the 2π masses will be very low compared to the nominal ρ mass, the channel *must* be analysed in a way which identifies the ρ's by their decay distributions, not by a background subtraction method, and this will require an unprecedented number of events. The data from the 4π system against $\Sigma^+(1385)$, however, does not show any significant signal for the $\rho(1300)$.

Another possibility is that the $\rho(1300)$ is not a $q\bar{q}$ state, but rather a $q\bar{q}q\bar{q}$ state, as suggested by Donnachie, Kalashnikova, and Clegg.[51,52] In this case, the quoted elasticity is meaningless. However, the t' differential cross section seen in $\pi^+\pi^-$ is not steeper than the the ρ, as one would expect from a physically extended 4-quark state.

In summary, evidence has been found for an isospin 1, P-wave state around 1.3 GeV/c^2. Table 9.3 presents a summary of the different measurements of the resonance parameters of this state. The 2π elasticity is estimated as $\sim 5\%$, assuming the ρ and $\rho(1300)$ production amplitudes are the same. There is no definite evidence of $\rho(1300)$ in the analysed 4π states. The branching ratio of $\pi^+\pi^-\pi^+\pi^-$ to $\pi^+\pi^-$ is less than 3. From the 5π channel, the branching ratio of $\pi^+\pi^-\pi^-\pi^0$ to $\pi^-\pi^0$ is less than 6. There is no evidence for significant cross section in the decay modes $\eta\pi\pi$, $K\overline{K}$, and $K\overline{K}\pi$. This means that, assuming the $\rho(1300)$ is a normal $q\overline{q}$ state, the channels examined in this thesis can account for at most 25% of the cross section.

Appendix A

Moment–Amplitude Relations

Shown here are the relations between the moments, through $L = 6$, and the underlying amplitudes, through F-wave. A factor of $\sqrt{2L+1}$ is implicit in each amplitude. Because the strong interaction conserves parity, each expression consists only of bilinear products where both terms are either natural or unnatural parity exchange.

$$
\begin{aligned}
t_{00} &= |S_0|^2 + |P_0|^2 + |P_-|^2 + |P_+|^2 + \\
&\quad |D_0|^2 + |D_-|^2 + |D_+|^2 + |F_0|^2 + |F_-|^2 + |F_+|^2 \\
t_{10} &= 2|S_0||P_0|\cos(\phi_S - \phi_{P_0}) + \frac{4}{\sqrt{5}}|P_0||D_0|\cos(\phi_{P_0} - \phi_{D_0}) + \\
&\quad 2\sqrt{\frac{3}{5}}\left[|P_+||D_+|\cos(\phi_{P_+} - \phi_{D_+}) + |P_-||D_-|\cos(\phi_{P_-} - \phi_{D_-})\right] \\
&\quad +6\sqrt{\frac{3}{35}}|D_0||F_0|\cos(\phi_{D_0} - \phi_{F_0}) \\
&\quad +4\sqrt{\frac{6}{35}}\left[|D_+||F_+|\cos(\phi_{D_+} - \phi_{F_+}) + |D_-||F_-|\cos(\phi_{D_-} - \phi_{F_-})\right] \\
t_{11} &= \sqrt{2}|S_0||P_-|\cos(\phi_S - \phi_{P_-}) \\
&\quad +\sqrt{\frac{6}{5}}|P_0||D_-|\cos(\phi_{P_0} - \phi_{D_-}) - \sqrt{\frac{2}{5}}|P_-||D_0|\cos(\phi_{P_-} - \phi_{D_0}) \\
&\quad +\frac{6}{\sqrt{35}}|D_0||F_-|\cos(\phi_{D_0} - \phi_{F_-}) - 3\sqrt{\frac{2}{35}}|D_-||F_0|\cos(\phi_{D_-} - \phi_{F_0})
\end{aligned}
$$

$$
\begin{aligned}
t_{20} &= 2|S_0||D_0|\cos(\phi_S - \phi_{D_0}) + \frac{2}{\sqrt{5}}|P_0|^2 - \frac{1}{\sqrt{5}}\left[|P_+|^2 + |P_-|^2\right] \\
&\quad + \frac{2\sqrt{5}}{7}|D_0|^2 + \frac{\sqrt{5}}{7}\left[|D_+|^2 + |D_-|^2\right] \\
&\quad + \frac{4}{3\sqrt{5}}|F_0|^2 + \frac{1}{\sqrt{5}}\left[|F_+|^2 + |F_-|^2\right] \\
&\quad + 6\sqrt{\frac{3}{35}}|P_0||F_0|\cos(\phi_{P_0} - \phi_{F_0}) \\
&\quad + 6\sqrt{\frac{2}{35}}\left[|P_+||F_+|\cos(\phi_{P_+} - \phi_{F_+}) + |P_-||F_-|\cos(\phi_{P_-} - \phi_{F_-})\right] \\
t_{21} &= +\sqrt{2}|S_0||D_-|\cos(\phi_S - \phi_{D_-}) + \sqrt{\frac{6}{5}}|P_0||P_-|\cos(\phi_{P_0} - \phi_{P_-}) \\
&\quad + \frac{\sqrt{10}}{7}|D_0||D_-|\cos(\phi_{D_0} - \phi_{D_-}) + \frac{2\sqrt{5}}{15}|F_0||F_-|\cos(\phi_{F_0} - \phi_{F_-}) \\
&\quad + 4\sqrt{\frac{3}{35}}|P_0||F_-|\cos(\phi_{P_0} - \phi_{F_-}) - 3\sqrt{\frac{2}{35}}|P_-||F_0|\cos(\phi_{P_-} - \phi_{F_0}) \\
t_{22} &= -\sqrt{\frac{3}{10}}\left[|P_+|^2 - |P_-|^2\right] - \frac{\sqrt{15}}{7\sqrt{2}}\left[|D_+|^2 - |D_-|^2\right] \\
&\quad - \sqrt{\frac{2}{15}}\left[|F_+|^2 - |F_-|^2\right] \\
&\quad + \sqrt{\frac{3}{35}}\left[|P_+||F_+|\cos(\phi_{P_+} - \phi_{F_+}) - |P_-||F_-|\cos(\phi_{P_-} - \phi_{F_-})\right] \\
t_{30} &= 2|S_0||F_0|\cos(\phi_S - \phi_{F_0}) + 6\sqrt{\frac{3}{35}}|P_0||D_0|\cos(\phi_{P_0} - \phi_{D_0}) \\
&\quad - \frac{6}{\sqrt{35}}\left[|P_+||D_+|\cos(\phi_{P_+} - \phi_{D_+}) + |P_-||D_-|\cos(\phi_{P_-} - \phi_{D_-})\right] \\
&\quad + \frac{8\sqrt{5}}{15}|D_0||F_0|\cos(\phi_{D_0} - \phi_{F_0}) \\
&\quad + \frac{2\sqrt{10}}{15}\left[|D_+||F_+|\cos(\phi_{D_+} - \phi_{F_+}) + |D_-||F_-|\cos(\phi_{D_-} - \phi_{F_-})\right]
\end{aligned}
$$

$$
\begin{aligned}
t_{31} &= \sqrt{2}|S_0||F_-|\cos(\phi_S - \phi_{F_-}) \\
&\quad +4\sqrt{\frac{3}{35}}|P_0||D_-|\cos(\phi_{P_0} - \phi_{D_-}) + \frac{6}{\sqrt{35}}|P_-||D_0|\cos(\phi_{P_-} - \phi_{D_0}) \\
&\quad +\sqrt{\frac{2}{5}}|D_0||F_-|\cos(\phi_{D_0} - \phi_{F_-}) + \frac{2\sqrt{5}}{15}|D_-||F_0|\cos(\phi_{D_-} - \phi_{F_0}) \\
t_{32} &= -\sqrt{\frac{6}{7}}\left[|P_+||D_+|\cos(\phi_{P_+} - \phi_{D_+}) - |P_-||D_-|\cos(\phi_{P_-} - \phi_{D_-})\right] \\
&\quad -\sqrt{\frac{1}{3}}\left[|D_+||F_+|\cos(\phi_{D_+} - \phi_{F_+}) - |D_-||F_-|\cos(\phi_{D_-} - \phi_{F_-})\right] \\
t_{40} &= \frac{6}{7}|D_0|^2 - \frac{4}{7}\left[|D_+|^2 + |D_-|^2\right] + \frac{6}{11}|F_0|^2 - \frac{1}{11}\left[|F_+|^2 + |F_-|^2\right] \\
&\quad +\frac{8}{\sqrt{21}}|P_0||F_0|\cos(\phi_{P_0} - \phi_{F_0}) \\
&\quad -2\sqrt{\frac{2}{7}}\left[|P_+||F_+|\cos(\phi_{P_+} - \phi_{F_+}) + |P_-||F_-|\cos(\phi_{P_-} - \phi_{F_-})\right] \\
t_{41} &= 5\sqrt{\frac{2}{35}}|P_0||F_-|\cos(\phi_{P_0} - \phi_{F_-}) + 2\sqrt{\frac{5}{21}}|P_-||F_0|\cos(\phi_{P_-} - \phi_{F_0}) \\
&\quad +\frac{2\sqrt{15}}{7}|D_0||D_-|\cos(\phi_{D_0} - \phi_{D_-}) + \frac{\sqrt{30}}{11}|F_0||F_-|\cos(\phi_{F_0} - \phi_{F_-}) \\
t_{42} &= -\frac{\sqrt{10}}{7}\left[|D_+|^2 - |D_-|^2\right] - \frac{\sqrt{10}}{11}\left[|F_+|^2 - |F_-|^2\right] \\
&\quad -\sqrt{\frac{5}{7}}\left[|P_+||F_+|\cos(\phi_{P_+} - \phi_{F_+}) - |P_-||F_-|\cos(\phi_{P_-} - \phi_{F_-})\right] \\
t_{50} &= \frac{20\sqrt{5}}{3\sqrt{77}}|D_0||F_0|\cos(\phi_{D_0} - \phi_{F_0}) \\
&\quad -\frac{10\sqrt{10}}{3\sqrt{77}}\left[|D_+||F_+|\cos(\phi_{D_+} - \phi_{F_+}) + |D_-||F_-|\cos(\phi_{D_-} - \phi_{F_-})\right] \\
t_{51} &= \frac{10}{\sqrt{77}}|D_0||F_-|\cos(\phi_{D_0} - \phi_{F_-}) + \frac{20\sqrt{2}}{3\sqrt{77}}|D_-||F_0|\cos(\phi_{D_-} - \phi_{F_0}) \\
t_{52} &= -\frac{5}{\sqrt{33}}\left[|D_+||F_+|\cos(\phi_{D_+} - \phi_{F_+}) - |D_-||F_-|\cos(\phi_{D_-} - \phi_{F_-})\right] \\
t_{60} &= \frac{100}{33\sqrt{13}}|F_0|^2 - \frac{25}{11\sqrt{13}}\left[|F_+|^2 + |F_-|^2\right]
\end{aligned}
$$

SLAC–421
UC–414
(E / I)

ERRATA

SINGLE ELECTRON DETECTION FOR SLD CRID AND MULTI-PION SPECTROSCOPY IN $K^{-}p$ INTERACTIONS AT 11 GeV/c*

Paul Elliot Rensing
Stanford Linear Accelerator Center
Stanford University, Stanford, CA 94309

Due to an error by the author, the page numbers of some of the references were omitted. Below are the corrected references.

[5] I. M. Frank and Ig. Tamm, Doklady Akad. Nauk., SSSR **14(3)** (1937) 109.

[8] A. Roberts, NIM **9** (1960) 55.

[9] J. Seguinot and T. Ypsilantis, NIM **142** (1977) 377.

[10] T. Ypsilantis, Phys. Scr. **23** (1981) 371.

[14] E. Spencer *et al.*, IEEE Trans. Nucl. Sci. **35** (1988) 231, also SLAC-PUB-4404.

[15] P. Antilogus *et al.*, IEEE Trans. Nucl. Sci. **38** (1991) 408, also, SLAC–PUB–5120.

[18] P. Battaiotto, NIM **A269** (1988) 538.

[19] P. Antilogus *et al.*, NIM **A293** (1990) 136, also, SLAC-PUB-5105.

[34] J. M. Blatt and V. F. Weisskopf, *Theoretical Nuclear Physics*, John Wiley & Sons, New York, 1952, p. 361.

SLAC–Report–421
October 1993

*Work supported by the Department of Energy under contract number DE–AC03–76SF00515

Bibliography

[1] *SLD Design Report*, SLAC-273, 1984.

[2] *SLC Conceptual Design Report*, SLAC-Report-229, 1980.

[3] I. Peruzzi *et al.*, in *Proceedings of the Kirkwood SLD Physics Meeting*, volume SLAC-Report-354, 1989, also C. Baltay, G. Eigen, and M. H. Kelsey; and P. Antilogus.

[4] P. A. Cerenkov, Izvestiya AN, SSSR, Seriya Fiz., OMEN (1937).

[5] I. M. Frank and Ig. Tamm, Doklady Akad. Nauk., SSSR **14(3)** (1937).

[6] J. V. Jelley, *Cerenkov Radiation, and its Applications*, Pergamon Press, 1958.

[7] J. D. Jackson, *Classical Electrodynamics*, John Wiley & Sons, 1975.

[8] A. Roberts, NIM **9** (1960).

[9] J. Seguinot and T. Ypsilantis, NIM **142** (1977).

[10] T. Ypsilantis, Phys. Scr. **23** (1981).

[11] K. Abe *et al.*, NIM **A300** (1991) 501, also, SLAC–PUB–5199.

[12] J. Va'vra *et al.*, SLAC-PUB-5214, 1990.

[13] M. Gaillard, CRID Note #24, SLAC, 1986.

[14] E. Spencer *et al.*, IEEE Trans. Nucl. Sci. **35** (1988), also SLAC-PUB-4404.

[15] P. Antilogus *et al.*, IEEE Trans. Nucl. Sci. **38** (1991), also, SLAC–PUB–5120.

[16] T. L. Bienz, *Strangeonium Spectroscopy at 11 GeV/c and Cherenkov Ring Imaging at the SLD*, PhD thesis, Stanford University, 1990, also, SLAC-369.

[17] D. Sherden, SLAC-PUB-4297, 1987, also D. Sherden, SLAC-PUB-4786, 1988.

[18] P. Battaiotto, NIM **A269** (1988).

[19] P. Antilogus *et al.*, NIM **A293** (1990), also, SLAC-PUB-5105.

[20] D. Aston *et al.*, NIM **A283** (1989) 590, also, SLAC–PUB–4875.

[21] C. F. G. Delaney, *Electronics for the Physicist*, Ellis Horwood, Chichester, West Sussex, UK, 1980.

[22] J. Va'Vra, *Total Wire Gain Calibration, Single Electron Pulse Height Spectra, Noise and Cross-talk Measurements in the CRID Single Electron Detector*, CRID Note #50, SLAC, 1988, unpublished.

[23] J. Va'vra, IEEE Trans. Nucl. Intr. **NS–34** (1987) 486.

[24] S. Dasu, P. E. Rensing, and J. Va'vra, *CRID High Voltage System*, CRID Note #73, 1992, unpublished.

[25] J. Va'vra *et al.*, IEEE Trans. Nucl. Intr. **NS–35** (1988) 487, also CRID Note #36, 1987, unpublished.

[26] L. Malter, Phys. Rev. **50** (1936), and Güntherschultze, Z. Phys., **86**, (1933) 778.

[27] P. Antilogus *et al.*, *Component and System Tests of the SLD Cerenkov Ring Imaging Detector*, SLAC–PUB–5365-Rev., 1991.

[28] S. Gadomski *et al.*, Nucl. Instrum. Meth. **A320** (1992) 217, also, CERN–PPE-92-70, April 1992.

[29] W. E. Ramsey, Phys. Rev. **57** (1940) 1022, and G. R. Ricker and J. J. Gomes, Rev. Sci. Intr. **40** (1969) 227.

[30] Particle Data Group, Phys. Rev. **D45** (1992).

[31] Stephen Godfrey and Nathan Isgur, Phys. Rev. **D32** (1985) 189.

[32] D. Aston *et al.*, *The LASS Spectrometer*, SLAC–REP–298, 1986.

[33] W. H. Press *et al.*, *Numerical Recipes in C*, Cambridge University Press, 1988.

[34] J. M. Blatt and V. F. Weisskopf, *Theoretical Nuclear Physics*, John Wiley & Sons, New York, 1952.

[35] G. Costa *et al.*, Nucl. Phys. **B175** (1980) 402.

[36] S. O. Holmgren *et al.*, Phys. Lett. **B66** (1977) 191.

[37] M. J. Losty *et al.*, Nucl. Phys. **B133** (1978) 38.

[38] M. Aguilar-Benitez *et al.*, Z. Phys. **C8** (1981) 313.

[39] M. Baubillier *et al.*, Z. Phys. **C23** (1984) 213.

[40] P. F. Bird, *Cerenkov Ring Imaging and Spectroscopy of Charged KStar Interactions at 11 GeV/c*, PhD thesis, Stanford University, 1988, also, SLAC-332.

[41] S. L. Glashow, Phys. Rev. Lett. **7** (1961) 469.

[42] S. Coleman and S. L. Glashow, Phys. Rev. **B134** (1964) 671.

[43] S. Coleman *et al.*, *Electromagnetic Mass Differences of Strongly Interacting Particles*, in *Proceedings of the XII International Conference on High Energy Physics, Dubna, 1964*, volume 1, pages 785–787, Atomizdat,Moscow, 1966.

[44] A. S. Goldhaber, G. C. Fox, and C. Quigg, Phys. Lett. **B30** (1969) 249.

[45] R. Gatto, Nuovo Cim. **28** (1963) 658.

[46] V. Flaminio *et al.*, *Compilation of Cross-sections II: K^+ and K^- Induced Reactions*, CERN–HERA 83–02, 1983.

[47] S. N. Ganguli *et al.*, Nuovo Cim. **44A** (1978) 345.

[48] B. Hyams *et al.*, Nucl. Phys. **B64** (1973) 134.

[49] W. Dunwoodie, *The Status of Strange Meson Spectroscopy*, in *Proceedings of the Rheinfels Workshop on the Hadron Spectrum, St. Goar, Germany, September 3–6, 1990*, pages 16–24, North Holland, 1991.

[50] A. Donnachie and H. Mirzaie, Z. Phys. **C33** (1987) 407.

[51] A. Donnachie and Yu. S. Kalashnikova, *Four-quark and hybrid mixing in the light-quark vector sector*, M–C–TH–93–02, 1993.

[52] A. Donnachie, Yu. S. Kalashnikova, and A. B. Clegg, *A candidate for a four-quark vector-meson?*, M–C–TH–93–10, 1993.

[53] J.-P. K. Sinervo, *A Study of the Strange Meson Spectrum as Observed in the Reaction* $\mathrm{K^-p \rightarrow \bar{K}^0\pi^+\pi^-n}$ *at 11 GeV/c*, PhD thesis, Stanford University, 1986, SLAC–299.

[54] M. Perl, *High Energy Hadron Physics*, John Wiley and Sons, New York, 1974.

[55] F. Marzano *et al.*, Nucl. Phys. **B123** (1977) 203.

[56] S. al Harran *et al.*, Nucl. Phys. **B183** (1981) 269.

[57] J. D. Jackson, *Particle and Polarization Angular Distributions for Two and Three Body Decays*, in *High Energy Physics*, pages 327–365, Gordon and Breach, New York, 1965.

[58] T. Regge, Nuovo Cim. **14** (1959) 951.

[59] H. Ozaki, *A Study of the* $\mathrm{K^-K^+}$ *System in the Reaction* $\mathrm{K^-p \rightarrow K^-K^+\Lambda}$ *at 11 GeV/c*, PhD thesis, Nagoya University, 1988.

[60] D. Aston *et al.*, Phys. Lett. **B201** (1988) 573.

[61] S. Flatté, Phys. Lett. **B63** (1976) 224.

[62] P. M. Ivanov *et al.*, Phys. Lett. **B107** (1981) 297.

[63] D. Bisello *et al.*, **C39** (1988) 13.